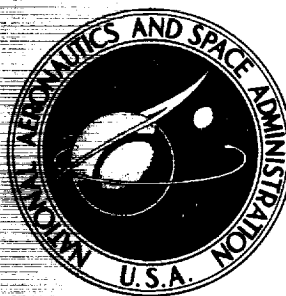


**NASA TECHNICAL
MEMORANDUM**



NASA TM X-2329

NASA TM X-2329

**CASE FILE
COPY**

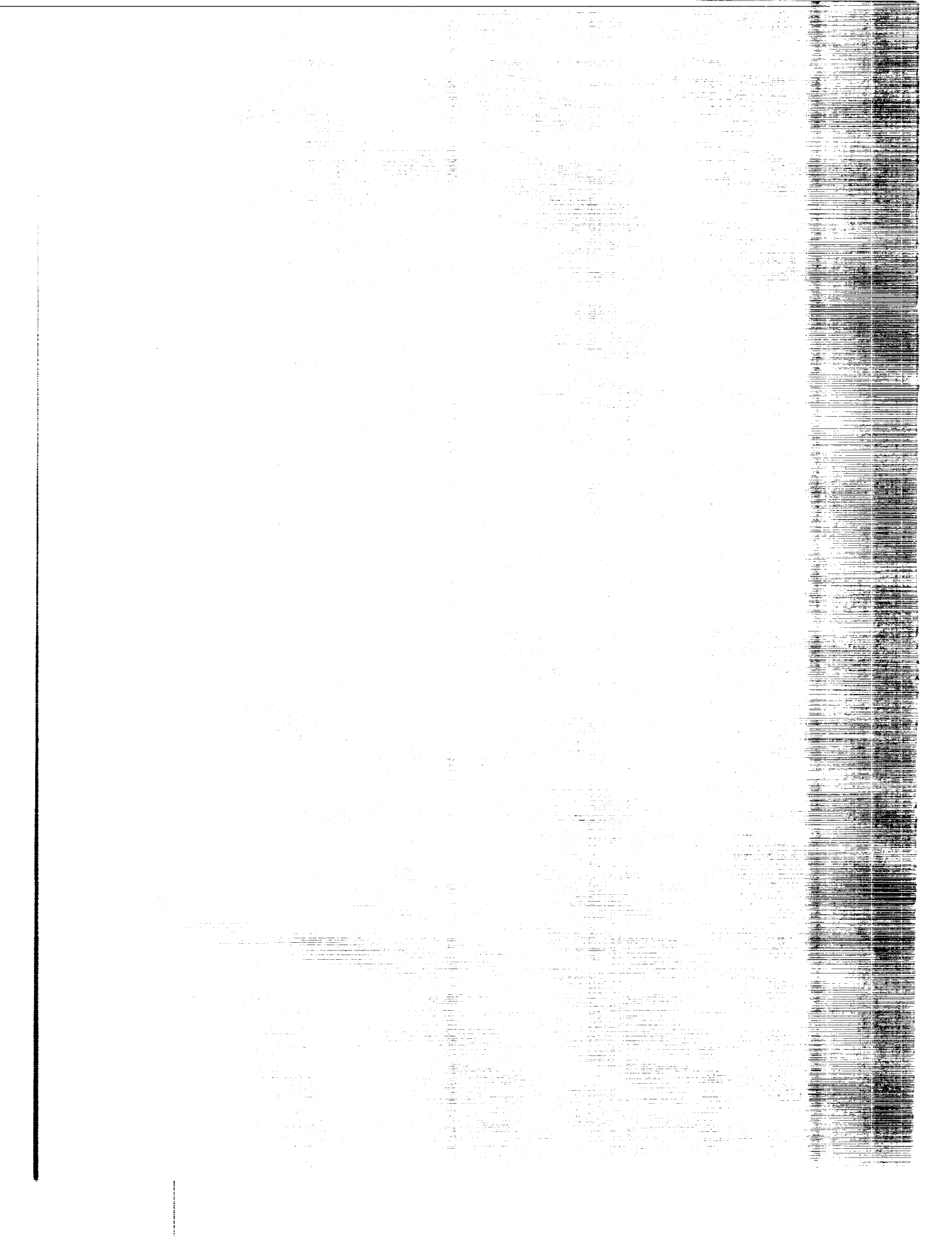
**PERFORMANCE OF CLOSELY SPACED
TWIN-JET AFTERBODIES WITH
DIFFERENT INBOARD-OUTBOARD
FAIRING AND NOZZLE SHAPES**

by Edwin E. Lee, Jr., and Jack F. Runckel

Langley Research Center

Hampton, Va. 23365

NATIONAL AERONAUTICS AND SPACE ADMINISTRATION • WASHINGTON, D. C. • SEPTEMBER 1971



1. Report No. NASA TM X-2329	2. Government Accession No.	3. Recipient's Catalog No.	
4. Title and Subtitle PERFORMANCE OF CLOSELY SPACED TWIN-JET AFTER- BODIES WITH DIFFERENT INBOARD-OUTBOARD FAIRING AND NOZZLE SHAPES		5. Report Date September 1971	6. Performing Organization Code
		8. Performing Organization Report No. L-7759	10. Work Unit No. 136-63-02-18
7. Author(s) Edwin E. Lee, Jr., and Jack F. Runckel		11. Contract or Grant No.	
		13. Type of Report and Period Covered Technical Memorandum	
9. Performing Organization Name and Address NASA Langley Research Center Hampton, Va. 23365		14. Sponsoring Agency Code	
		12. Sponsoring Agency Name and Address National Aeronautics and Space Administration Washington, D.C. 20546	
15. Supplementary Notes			
16. Abstract <p>Thrust-minus-drag forces and pressure distributions were obtained on the afterbody and nozzle sections of various fuselage closures at Mach numbers from 0.60 to 2.01. Four interfairing contours were investigated: a circular-arc, an elliptical, and a blunt configuration, all ending at the nozzle attachment station; and one blunt-based type extending between the nozzles. Also, limited data were obtained with tail booms of circular or oval cross section extending from the sides of the afterbody past the nozzles. Propulsive-nozzle shapes represented variable-geometry iris and convergent-divergent types with circular-arc and conical boattailing, respectively. Each was configured for minimum and maximum throat area (dry and augmented power) and operated with compressed air at pressure ratios up to 20, depending on Mach number.</p>			
17. Key Words (Suggested by Author(s)) Twin-jet afterbodies Jet interference Afterbody drag Nozzle-boattail drag		18. Distribution Statement Unclassified - Unlimited	
19. Security Classif. (of this report) Unclassified	20. Security Classif. (of this page) Unclassified	21. No. of Pages 151	22. Price* \$3.00

|

PERFORMANCE OF CLOSELY SPACED TWIN-JET AFTERBODIES
WITH DIFFERENT INBOARD-OUTBOARD FAIRING
AND NOZZLE SHAPES

By Edwin E. Lee, Jr., and Jack F. Runckel
Langley Research Center

SUMMARY

The effects of interfairing, tail-boom, and nozzle shapes on thrust-minus-drag performance of afterbodies with closely spaced twin jets were studied at Mach numbers from 0.60 to 2.01. Four interfairing contours were used: a circular-arc, an elliptical, and a blunt configuration, all ending at the nozzle-attachment station; and a blunt type extending between the nozzles. Also, limited results were obtained with tail booms of circular and oval cross sections extending from the sides of the afterbody past the nozzles. The propulsive nozzles represented variable-geometry iris and convergent-divergent types with circular-arc and conical boattailing, respectively. Each type was configured for minimum and maximum throat-area (dry and augmented) power settings. Exhaust flow was simulated with compressed air at pressure ratios up to 20, depending upon Mach number.

At scheduled pressure ratios assumed for a turbofan engine, the results show (1) that interfairings of the circular-arc and elliptical type caused the least subsonic nozzle drag by ventilating the inboard region of the boattails and allowing pressure to recover inboard as well as outboard; (2) that reducing the boattail angle of the nozzles for augmented power at transonic speeds pressurized the elliptical interfairing and made its supersonic performance comparable to that of the blunt and extended shapes; (3) that tail booms increased both afterbody and nozzle drag at subsonic and transonic speeds; and (4) that curved-nozzle boattailing generally caused somewhat less external drag than the conical type, but the convergent-divergent nozzle had the highest internal performance at supersonic speeds.

INTRODUCTION

Past research conducted with powered models of aircraft having twin engines mounted in the aft end of the fuselage has revealed that thrust-minus-drag performance losses may be associated with such installations because of the complex flow field and local aerodynamic interferences in this region (refs. 1 to 4). In order to establish some of the basic phenomena affecting engine exhaust-airframe interaction, engine placement

(refs. 5 to 7), nozzle type, and afterbody shape (refs. 6 and 8) have been studied at the Langley Research Center. The closely spaced twin-engine fuselage configuration is one concept that offers the advantages of compact afterbody structure, minimum centerbody and base area, and the possibility of lower drag. A previous investigation with clustered jets (ref. 9) had indicated the importance of the shape of the interfairing between closely spaced nozzles on the performance of the afterbody-nozzle combination.

The present paper presents the results of an investigation of a closely spaced twin-jet powered afterbody model. The profile shape and length of the interfairing were varied on a smoothly faired afterbody in combination with two types of nozzles. Investigated were circular-arc, elliptical, and blunt interfairings which terminated at the nozzle-attachment location and an extended interfairing with a small flat base located behind the nozzle exits. Four shapes of streamline fairings located along the outboard sides of the afterbody and nozzles were also studied, primarily at supersonic speeds. The concepts leading to the close-spaced twin-jet design and some preliminary results from the present investigation have been reported in reference 10.

Tests were conducted at zero angle of attack in the Langley 16-foot transonic tunnel and 4- by 4-foot supersonic pressure tunnel at Mach numbers from 0.60 to 1.30 and 2.01 over a jet-pressure-ratio range from jets off to 20, depending on Mach number.

SYMBOLS

A	cross-sectional area, m^2
A_b	area at the base of one nozzle, $\pi d_b^2/4$, m^2
A_e	exit area of one nozzle, m^2
A_{max}	maximum cross-sectional area of afterbody, $0.030851 m^2$
A_n	maximum cross-sectional area of one nozzle, $\pi d_n^2/4$, m^2
A_O	internal area of one afterbody-nozzle opening (fig. 4), m^2
A_{seal}	cross-sectional area enclosed by metric-gap seal (fig. 4), m^2
A_t	throat area of one nozzle, m^2
$C_{A,a}$	axial-force coefficient of afterbody including nozzle-clearance annuli, positive downstream, $F_{A,a}/q_\infty A_{max}$

$$\Delta C_{A,a,j} = (C_{A,a})_{\text{jet-on}} - (C_{A,a})_{\text{jet-off}}$$

$C_{A,n}$ axial-force coefficient of both nozzles, $F_{A,n}/q_{\infty}A_{\text{max}}$

$C_{A,\beta}$ combined pressure axial-force coefficient of both nozzles, $\frac{-2}{A_{\text{max}}} \int_{A_e}^{A_n} C_{p,n} dA$

$$\Delta C_{A,\beta,j} = (C_{A,\beta})_{\text{jet-on}} - (C_{A,\beta})_{\text{jet-off}}$$

$C_{p,a}$ afterbody surface-pressure coefficient

$C_{p,n}$ nozzle surface-pressure coefficient

$C_{T,i}$ aerodynamic ideal-thrust coefficient, $F_i/q_{\infty}A_{\text{max}}$

c strut-support local chord, parallel to free stream, m

d_b nozzle base diameter, m

d_e nozzle exit diameter, m

d_{eq} equivalent diameter corresponding to A_{max} , m

d_n nozzle maximum diameter, m

d_t nozzle throat diameter, m

$F_{A,a}$ axial force on afterbody, including nozzle-clearance annuli, N

$F_{A,n}$ axial force on both nozzles (external drag), N

$F_{A,t}$ total axial force of afterbody plus nozzles, N

$F_{\text{bal},a}$ force measured by afterbody drag balance, positive downstream, N

$F_{\text{bal},j}$ force measured by thrust-minus-drag balance, positive upstream, N

F_i ideal thrust for isentropic expansion of measured total mass-flow rate to

$$\text{free-stream static pressure, } \dot{m}_j \sqrt{\frac{2\gamma}{\gamma-1} RT_{t,j} \left[1 - \left(\frac{p_{\infty}}{p_{t,j}} \right)^{\gamma-1/\gamma} \right]}, \text{ N}$$

F_j	gross thrust of both nozzles, positive upstream, N
h	maximum height of afterbody (fig. 3), m
L	model length from nose to afterbody-nozzle interface, 1.3208 m
l_n	nozzle-boattail axial length, m
M	free-stream Mach number
\dot{m}_i	ideal total mass-flow rate, kg/s
\dot{m}_j	measured total mass-flow rate, kg/s
p_{an}	static pressure in nozzle-clearance annuli (fig. 4), N/m ²
p_{ej}	ejector-cavity static pressure for shrouded iris nozzles (fig. 6), N/m ²
p_{es}	static pressure in metric gap, external to seal (fig. 4), N/m ²
p_i	internal static pressure of afterbody (fig. 4), N/m ²
$p_{t,j}$	jet total pressure, N/m ²
p_∞	free-stream or ambient static pressure, N/m ²
q_∞	free-stream dynamic pressure, N/m ²
R	gas constant ($\gamma = 1.4$), 287.3 N-m/kg-K
r	radius, m
S	lateral distance between nozzle center lines (fig. 4), m
s	axial distance from nozzle throat to exit (fig. 6), m
$T_{t,j}$	jet stagnation temperature, K
V_l	local velocity in boundary layer, m/s

V_δ	velocity at outer edge of boundary layer, m/s
V_∞	free-stream velocity, m/s
w	maximum width of afterbody (fig. 3), m
X	axial distance from model nose, m
x	axial distance from afterbody-nozzle interface, m
y,z	rectangular coordinates
α	nozzle divergence half-angle, deg
β	boattail angle, deg
γ	ratio of specific heats
δ	boundary-layer thickness, m
ϵ_e	nozzle-expansion ratio, A_e/A_t
ϕ	meridian angle about nozzle axis, deg

A bar over a symbol denotes an average value.

APPARATUS AND METHODS

Wind Tunnels and Tests

The present investigation was conducted in both the Langley 16-foot transonic tunnel and the Langley 4- by 4-foot supersonic pressure tunnel. The 16-foot transonic tunnel is a single-return, atmospheric facility with continuous-air-exchange capability and a slotted octagonal test section. Mach number can be varied continuously from 0.20 to 1.30 by varying fan drive speed. The 4- by 4-foot supersonic pressure tunnel is a single-return, continuous-flow facility with a stagnation-pressure range from 0.2758×10^5 N/m² to 2.0684×10^5 N/m². Mach numbers ranging from 1.25 to 2.20 are obtained by mechanically deflecting the tunnel floor and ceiling between fixed side walls 1.37 m apart, thereby forming a series of two-dimensional nozzles of rectangular cross section.

Data on the closely spaced twin-jet afterbody models of this report were taken at Mach numbers from 0.60 to 1.30 in the 16-foot tunnel, where the average Reynolds number per meter ranged from 10.82×10^6 at $M = 0.60$ to 13.77×10^6 at $M = 1.3$. In the 4- by 4-foot supersonic pressure tunnel, data were recorded at $M = 2.01$ only. The stagnation pressure was 1.234×10^5 N/m², the stagnation temperature was 311 K, and the Reynolds number per meter was 13.77×10^6 . The model angle of attack was zero degrees in both facilities, and the jet total-to-free-stream static-pressure ratio was varied from approximately one at the jet-off condition to 20, depending on Mach number and model nozzle configuration. The general procedure used was to investigate configurations with cruise-power nozzles (minimum throat area) at Mach numbers from 0.60 to 0.95 only and those with augmented nozzles (maximum throat area) over the full speed range.

Model and Support System

Photographs of the model installed in the Langley 16-foot transonic tunnel are shown in figure 1 and photographs of the model taken in the Langley 4- by 4-foot supersonic pressure tunnel are shown in figure 2. A sketch of the air-powered twin-jet model and support system is presented in figure 3. The model in the 16-foot transonic tunnel was supported from a vertical floor mounted strut which attached to the forebody. The interference of this support with afterbody pressure measurements is discussed in appendix B of reference 11, which shows that the strut slightly reduces local static pressures near the model at transonic speeds. It is felt that these small perturbations would not change the relative data levels of the various configurations very much, thereby providing good comparative results, which were of primary interest. In the 4- by 4-foot supersonic pressure tunnel the model was mounted from a fixed side wall with a shorter strut identical in cross section to the 16-foot transonic tunnel support. (See figs. 2 and 3.)

The twin-jet air-powered model system was similar to those reported in references 5 to 8. The afterbody of the model began 83.82 cm from the nose and was attached to a drag balance which in turn was attached in tandem to a thrust-minus-drag balance as shown in figure 3. A teflon strip inserted into grooves machined into the afterbody shell and forebody was used as a seal to prevent internal flow in the model. The teflon strip, because of its low coefficient of friction, minimized restraint on the two balances. The afterbody terminated at station 132.08 cm and had an annular clearance gap between the afterbody and nozzles to prevent fouling of the afterbody balance (fig. 4). The afterbody width-to-height ratio w/h was 2.0 at the separation station, and the cross-sectional area was maximum at this point. Transition was fixed at the nose of the model with a strip of No. 180 carborundum grit 0.25 cm wide located 2.54 cm from the nose of the model.

High-pressure air was used to simulate the exhaust of a twin-jet configuration. The apparatus, shown schematically in figure 4, introduced compressed air radially into a

plenum to eliminate incoming axial momentum. The air was ducted from the plenum chamber to twin tailpipes, which incorporated perforated flow smoothing plates, and exhausted through interchangeable nozzles.

Sketches of the afterbodies and outboard fairings or tail booms are presented in figure 5. The side and planform profile shapes were identical for all of the basic afterbodies. Each body had boattail angles of 3° in the nacelle vertical center planes and 6° along the sides approaching the nozzles. Only the central contours varied, and the four different interfairing shapes investigated are shown in figure 5(a). The interfairing profiles at the model vertical center line had circular-arc, elliptical, and blunt shape, all terminating at the afterbody-nozzle-interface station 132.08 cm. The blunt interfairing had a flat base (fig. 5(b)). The fourth interfairing was an extension of the blunt interfairing and terminated at station 141.48 cm in a small flat base. The maximum cross-sectional shape of the afterbody and details of the blunt-interfairing base and blunt-interfairing extension are given in figure 5(b), and afterbody cross-section contours are sketched in figure 5(c). Contours outboard of the nozzle vertical center planes were identical for all afterbodies.

The detachable outboard fairings or tail booms were tested only on the afterbody with the extended interfairing and are shown in figures 5(d) and 5(e). Tail-boom configuration 1 had circular cross sections and was investigated at all Mach numbers. Tail-boom configurations 2, 3, and 4 had generally rectangular or flat sided cross sections and were tested at $M = 2.01$ only. Configuration 2 was the basic shape of the latter group (fig. 5(e)). Configuration 3 was generated from configuration 2 by adding volume inboard adjacent to the nozzle, leaving the outboard-planform profile unchanged. Configuration 4 was obtained by removing volume along the outboard side of configuration 2, leaving the inboard planform virtually unchanged.

Two variable-geometry nozzle designs, one iris and the other convergent-divergent, were each simulated at minimum throat area for dry power and at maximum throat area for augmented power. In a given power mode, the throat areas of the two types were equal. Five fixed-geometry model nozzles were used to simulate these conditions and are shown in figure 6, together with pertinent geometric ratios and pressure orifice locations. The iris configurations in figure 6(a) represented a three-position nozzle whose circular-arc boattail sections would translate along the arc path to provide minimum throat area when fully extended (dry iris). When the boattail sections were fully retracted for maximum augmentation, the nozzle would shorten to its minimum length and have maximum convergent throat area (augmented iris). This concept included another feature, used in the augmented mode, in that an extensible outer shroud would be translated rearward to form a zero secondary flow ejector with uncontrolled expansion from throat to exit (shrouded augmented iris). This configuration is similar to the zero secondary flow ejectors of references 12 to 14. The nozzles in figure 6(b) represented the two extreme positions of a

continuously variable-geometry convergent-divergent design, which provided controlled internal expansion in the augmented power mode. This design also had a conical boattail with an angle of 14° at dry power, and 3.6° when fully augmented. Moreover, the conically divergent internal expansion section of the augmented configuration had an area ratio ϵ_e of 1.41, which was identical to the exit-to-primary area ratio of the shrouded augmented iris. In concept, the convergent-divergent nozzle was similar to those reported in reference 11.

Cross-sectional-area distributions are shown in figure 7(a) for afterbodies with different interfairings and nozzles and in figure 7(b) for different tail booms combined with the extended interfairing and shrouded iris nozzles. The forebody ahead of the seal station ($X = 83.82$ cm) was identical for all configurations and had an area distribution similar to that shown in reference 7.

Instrumentation

Each afterbody was instrumented with several rows of surface-pressure orifices as shown in figure 8. Because of model symmetry they are illustrated in the sketch as being on the right side of the model. Row 1 extended along the top of the left nacelle vertical center line and was in line with the $\phi = 0^\circ$ orifice row of pressure taps on the nozzles, which are shown in figure 6 and are repeated in figure 8 as noted. Afterbody row 2 was along the upper right-hand shoulder of the afterbody, and row 3 was on the left horizontal model center line and in line with the $\phi = 90^\circ$ orifice row on the left nozzles. Row 4 was on the vertical center line of the model and extended to the termination of the interfairing. Rows 5 and 6 were axial rows outboard of the model center line. A total of 42 pressure taps were employed on the afterbody shell. Afterbody-pressure-orifice rows 1, 3, and 5 were actually on the left side of the body and nozzle orifice rows at $\phi = 0^\circ$, 90° , and 300° were located on the left nozzle. As previously noted, nozzle rows at $\phi = 0^\circ$, 90° , and 300° were installed on the left nozzle and rows at $\phi = 45^\circ$, 270° , and 330° were on the right nozzle. To indicate nozzle pressure distributions and obtain pressure drag integrations, all rows have been combined in figure 8 as if located on the right nozzle, giving a total of 42 pressure measurements. The shrouded-augmented iris nozzles also included four static-pressure taps on the internal shroud surface which are designated p_{ej} in figure 6(a).

Six internal pressures were measured in the afterbody cavity at the seal-gap station and along the length of the afterbody as shown in figure 4. In addition, the annulus base pressure was measured with three orifices on each side installed in line with the nozzle pressure rows. Eight external static pressures (p_{es}) were measured with orifices located in the afterbody seal gap. These pressure measurements were used for axial-force corrections. The total pressure and stagnation temperature of the exhaust flow were measured in each tailpipe as shown in figure 4.

Boundary-layer rakes were installed at model station 124.41 in line with the nozzle top center line and side center line, as shown in figure 9. Five total pressure probes and one static-pressure probe were included on each rake at positions parallel to the surface, as indicated in the figure. The afterbody boundary-layer rakes were installed on the configuration with the circular-arc interfairing and dry iris nozzles only.

Forces and moments on the metric portions of the model (see fig. 4) were measured with balances mounted in tandem. The main balance $F_{bal,j}$ measured gross thrust minus the combined axial forces of the afterbody and nozzles. The lower capacity axial-force balance $F_{bal,a}$ measured forces and moments on the afterbody shell only. The tandem-balance arrangement and the pressure measurements provide a means for separating the component forces so that the influence of interfairing-shape variations on the performance of the afterbody, the nozzles, and the combination of the two can be isolated. A magnetic turbine flowmeter with electrical readout was used to measure the total air-mass-flow rate to the nozzles.

Data obtained in the Langley 16-foot transonic tunnel were recorded simultaneously on magnetic tape and were reduced to coefficient form by use of a computer. Approximately five frames of data were taken over a time period of 1 second for each data point, and the average was used for computations. Data obtained in the Langley 4- by 4-foot supersonic pressure tunnel were transmitted to self-balancing potentiometers, digitized, and punched into computer cards. Electrical scanning valves were used for measuring and recording the internal and external pressures.

Data Reduction

The recorded data were used to compute standard force and pressure coefficients. Desired axial and thrust-minus-drag forces were determined by correcting balance readings for the pressure tare forces on the afterbody forward rim just outside the metric-gap seal, and on the inside of the afterbody shell (see fig. 4). The corrections were obtained by multiplying the axial projection of these areas by the average difference between local and free-stream static pressures.

Afterbody axial force (drag) was obtained from the rear tandem balance as follows:

$$F_{A,a} = F_{bal,a} - (\bar{p}_{es} - p_{\infty})(A_{max} - A_{seal}) - (\bar{p}_i - p_{\infty})(A_{seal} - 2A_O) - 2(\bar{p}_{an} - p_{\infty})(A_O - A_n) \quad (1)$$

The balance output $F_{bal,a}$ (positive downstream) contains all pressure and friction forces acting on the afterbody shell; and the second and third terms correct for forward rim and interior pressure forces, respectively. The fourth term is a fictitious external base-pressure drag acting on the open clearance annuli where the nozzles emerge from

the afterbody shell. Although this force was not physically sensed by the afterbody balance, it has been charged to afterbody drag throughout this report. This was done to partially account for the small additional external drag that would have been measured had the afterbody shell not been truncated slightly for clearance with the nozzles.

Gross thrust minus total axial force on the afterbody and nozzles was computed from the forward balance output using the relation:

$$F_j - F_{A,t} = F_{bal,j} + (\bar{p}_{es} - p_\infty)(A_{max} - A_{seal}) + (\bar{p}_i - p_\infty)(A_{seal} - 2A_O) + 2(\bar{p}_i - p_\infty)A_n + 2(\bar{p}_{an} - p_\infty)(A_O - A_n) \quad (2)$$

where $F_{bal,j}$ (positive upstream) includes all pressure and viscous forces, internal and external, on both the afterbody and thrust systems (see fig. 4). In equation (2) the second and third terms are identical to those in equation (1), except for signs. The fourth term in equation (2) is the pressure force on exposed surfaces of the thrust system inside the afterbody (plenum and tailpipes); and the last term is the annulus drag, which was not sensed by the main balance, and must be added.

Results from equations (1) and (2) were then combined to get the gross thrust minus total axial force of both nozzles, given by

$$F_j - F_{A,n} = (F_j - F_{A,t}) + F_{A,a} = F_{bal,j} + F_{bal,a} + 2(\bar{p}_i - p_\infty)A_n \quad (3)$$

The internal pressure-force term in the above equations was, on occasion, quite sizable and approached the afterbody drag-balance readings in magnitude. However, internal pressures were always quite steady, uniform, and virtually identical, indicating no significant gradients or flow inside the afterbody shell. Furthermore, annulus pressures p_{an} were only very slightly lower than internal pressures p_i indicating no significant leakage flow around the nozzles – only the small, local influence of steady-state recirculation (ring vortices) just behind the clearance steps.

Single-probe jet total-pressure readings in each tailpipe were corrected to the integrated average throat value of the nozzle as determined from individual pretest rake surveys behind each exit. Only the dry iris, augmented iris, and dry convergent-divergent (C-D) nozzles were surveyed directly; and data from the augmented iris were used for the shrouded iris and augmented C-D nozzles. The maximum nonuniformity correction was approximately 3 percent of the nominal total-pressure setting. The two corrected values (right and left) were then averaged to obtain the ratios of jet total pressure to free-stream static pressure shown in the data figures. Total pressures in the two tailpipes generally differed by less than 1 percent of nominal setting (flow balance). Averaged total

pressures and temperatures were also used with total measured mass flow and total throat area to calculate ideal thrust and mass flow, respectively.

It should be noted that nozzle axial-force coefficient $C_{A,\beta}$, as presented in this paper, is the combined pressure drag of both nozzles and does not include the relatively small skin-friction drag on the nozzle boattails. As a check on the pressure integrations, total nozzle axial force (including skin friction) was also computed directly from force data by the equation

$$F_{A,n} = \left(\frac{F_j}{F_i} \right)_{M=0} F_i - (F_j - F_{A,t}) - F_{A,a} \quad (4)$$

Here, gross thrust (first term) was obtained by multiplying calculated ideal-thrust values for tunnel-on data points by the statically determined thrust ratios shown in figure 11. The second and third terms are tunnel-on results from equations (2) and (1), respectively. A sample of force-derived $C_{A,n}$ values from equation (4) is compared with pressure-integrated $C_{A,\beta}$ values in figure 10. Good agreement is indicated, with pressure-drag coefficients slightly lower than force-data values, as would be expected.

RESULTS

The results of the investigation are presented in the following figures:

	Figure
Comparison of nozzle drag from force and pressure measurements	10
Nozzle internal performance	11 and 12
Afterbody boundary-layer profiles	13
Effect of interfairing shape	14 to 17
Effect of tail booms	18
Effect of nozzle shape	19 to 21
Assumed variation of jet-pressure ratio with Mach number	22
Ideal aerodynamic thrust coefficients	23
Performance comparisons with various interfairings	24
Jet interference increment with various interfairings	25
Performance comparisons with and without booms	26
Performance comparisons with various nozzles	27
Afterbody pressure distributions with various interfairings	28 and 29
Effect of tail booms on afterbody pressure distribution	30
Effect of jet operation on afterbody pressures	31 and 32
Nozzle pressure distributions with various interfairings	33 and 34

Effect of booms on nozzle pressure distribution	35
Jet effects on nozzle pressure distribution	36 and 37

Figure

DISCUSSION

Nozzle Internal Performance

The static performance of the nozzles is given in figure 11. These values were obtained with the tunnel off, and the pressure instrumentation indicated no external drag from jet entrainment, and so forth. The data symbols represent static tests with various afterbody interfairings, as well as repeat runs. The thrust ratios of the dry and augmented iris and the dry convergent-divergent nozzles followed expected trends for convergent nozzles. At pressure ratios below the critical, data scatter increases for both thrust ratio and mass-flow ratio due to inherent inaccuracies of measuring equipment in the low output range. The shrouded-augmented iris nozzle shows the underexpansion and jet detachment phenomena with decreasing jet-pressure ratio typical of ejector nozzles with no secondary flow (ref. 12). The mass-flow ratio for the dry convergent-divergent nozzle (fig. 11(b)) is lower than that of the dry iris nozzle due to the internal cylindrical section producing a thicker internal boundary layer. The augmented convergent-divergent iris-nozzle thrust ratio is tending to peak near a jet-pressure ratio of 5, which is close to the design pressure ratio of the nozzle.

The pressures in the ejector cavity of the shrouded-augmented iris nozzle (see fig. 6(a)) are presented in figure 12. The no-flow ejector characteristics are presented in a manner similar to those shown in reference 15. The data at the top of figure 12 indicate that the internal normal shock was at the exit for a jet-pressure ratio of about 3 and that variation of the external Mach number had no effect on the ejector-cavity pressures.

Afterbody Boundary-Layer Surveys

The representative velocity profiles in figure 13(a) were obtained from boundary-layer rake surveys near the rear of the afterbody with circular-arc interfairing and dry iris nozzles (see fig. 9 also). Velocities were calculated from pressure data using the standard Mach number relations, assuming free-stream stagnation temperature through the boundary layer. Moreover, constant static pressure through the boundary layer was indicated experimentally. Surface pressures without the rake installed were virtually identical to the rake-static-probe values.

It can be seen that the boundary-layer thickness was somewhat larger on the side of the engine compartment than on top and averaged about 1.50 cm subsonically. This difference presumably resulted from the longer surface run and somewhat different

pressure-gradient history in the horizontal plane of the model compared to the vertical. Velocity perturbations in the flow outside the boundary layer were generally small; but the largest occurred in the vertical plane, indicating the flow there may be more nearly two-dimensional.

The velocities were also normalized on the value at the edge of the boundary layer to estimate the profile power laws involved. Figure 13(b) indicates corresponding exponents of about 1/4 and 1/6 for the side and top profiles, respectively. The denominators of these exponents are somewhat lower than those obtained for flat plates without pressure gradients (see ref. 16).

Effect of Interfairing Shape on Axial-Force Coefficients

Jet-off axial-force variation with Mach number.- The fact that the interfairing can have a significant effect on the flow field over the afterbody and nozzles can be seen from the jet-off variation of axial-force coefficient with Mach number in figure 14. Data for the afterbody axial-force coefficient $C_{A,a}$ generally indicate that afterbody drag increases as the interfairing is changed from the extended to circular-arc, blunt, and elliptical shapes. Pressure-distribution measurements obtained on the afterbody (fig. 28) confirm these results in that: the extended interfairing is the only centerbody that shows a pressure-recovery tendency, and the elliptical interfairing generally has the lowest level of pressures over the rear portion of the afterbody.

The more boattailed nozzles are very sensitive to interfairing contour; the most favorable shapes for the iris nozzles were the elliptical and circular-arc shapes ($C_{A,\beta}$ curves). These interfairings blend in well with the curved nozzle boattails and permit the external flow to close in the vertical plane between the nozzles; this promotes pressure recovery at subsonic speeds (ref. 17). The blunt interfairings, in contrast, tend to block this flow ventilation between the nozzles. The nozzle pressure distributions of figure 33 show that the boattailed iris nozzles (dry and augmented) with elliptical and circular-arc interfairings have the highest pressure levels whereas the blunt and extended interfairings tend to depress the pressures on these nozzles.

When the afterbody and nozzle axial-force coefficients are added to obtain the total-axial-force coefficient $C_{A,a} + C_{A,\beta}$, the relative order of merit for the interfairings tends to change from that for the afterbody alone (fig. 14(a)). At subsonic speeds the longer circular-arc nozzles in combination with interfairings having vertical closure have the lowest total-axial-force coefficients. The short augmented iris nozzles (fig. 14(b)) combined with the extended interfairing appear to have the best jet-off flow-field environment; this is also the case with the shrouded-augmented iris nozzles. Little difference is noticed for the various interfairings at a Mach number of 2.0.

Effect of jet-pressure ratio.- The effect of jet exhaust on axial-force coefficients and thrust-minus-axial-force ratios for the iris nozzles and various interfairings is presented in figures 15 to 17. The effects of changing interfairing shape on the relative magnitude of the axial-force coefficients are similar to those found for the jet-off data of figure 14. The thrust-minus-axial-force ratios on the plots reflect both the favorable jet interference effect on drag and the increase in thrust with jet-pressure ratio. The same conclusions regarding the more favorable shapes of interfairings can be inferred from either the drag or thrust plots. The thrust-minus-drag curves for the shrouded iris nozzle (fig. 17) include the internal performance variation with jet-pressure ratio that would be expected of a no-flow ejector (refs. 13 and 14).

Afterbody pressure distributions for the various interfairings with iris nozzles are shown in figure 29. The jet-pressure ratios for the various Mach numbers approximate those of the schedule given in figure 22. The largest influence of jet operation appears along the center of the afterbodies in row 4. Similar jet-on pressure distributions on the nozzles are presented in figure 34. The pressure data emphasize the strong effect of a centerbody shape on afterbody and installed-nozzle pressure distributions for a close-spaced nozzle-afterbody combination. In going from the side of the model to the interfairing center line, the local pressures on both the afterbody and nozzle become more influenced by the shape of the interfairing. Since the flow field produced by the various types of interfairings can affect aft-end components in different ways, the interfairing results emphasize the difficulty of predicting installed-nozzle performance and aft-end drag, even for simplified configurations.

Effect of Tail Booms

The addition of outboard booms or streamline fairings extending downstream of the nozzle exits was shown to have detrimental effect on nozzle performance for dry-power nozzles in reference 17. This unfavorable effect diminished as the nozzle shape became more cylindrical. A brief study of the effect of outboard booms on the afterbody with extended interfairing and the shrouded augmented nozzles was included in the present investigation and the results are shown in figure 18. The addition of the number 1 booms to the afterbody increased afterbody, nozzle, and total-axial-force coefficients over the jet-pressure range at subsonic speeds. At supersonic speed the unfavorable effect of the boom addition changes to a favorable effect on the afterbody-axial-force-coefficient measurements at higher pressure ratios. This indicates that the pluming jet exhaust is tending to pressurize the aft-sloping surface of the booms behind the exits (refs. 3, 18, and 19).

The effect of the booms on the pressure-distribution measurements for the outboard rows 1 and 2 is shown in figure 30. At subsonic speeds the booms decreased afterbody pressures locally; at supersonic speeds the presence of the booms indicates a general rise

in afterbody pressure coefficients. The jet-off indication appears contrary to the data of figure 18, but pressures on the booms were not measured and could have a compensating effect. The nozzle pressure distributions with booms on are unfavorably influenced except for some limited regions at the $\phi = 90^\circ$ station (fig. 35).

Effect of Nozzle Shape

A comparison of the axial-force coefficients obtained with the jets off is depicted in figure 19 and indicates the influence of the nozzle shape on the flow field. The two dry-power nozzles, iris and convergent-divergent, have the same fineness ratio and base to maximum nozzle-area ratios; but the combination of the convergent-divergent (C-D) nozzle with this afterbody produces higher drag ($C_{A,a}$) due to the corner expansion of the conical nozzle compared with a curved boattail nozzle (ref. 20). The dry and augmented iris nozzles have an identical influence on the afterbody axial-force coefficient since the shape at the afterbody-nozzle interface was the same for both nozzles. The nozzles with nearly cylindrical shapes produce the lowest jet-off afterbody drag. The jet-off axial-force coefficients for the nozzles $C_{A,\beta}$ generally show that the more boattailed configurations provide thrust recovery at subsonic speeds and the more cylindrical shaped nozzles have the least drag at supersonic speeds, as expected. In terms of the total-axial-force coefficient $C_{A,a} + C_{A,\beta}$ the augmented convergent-divergent nozzle combination had the least drag over the speed range and the augmented iris nozzle had the highest drag.

The effect of jet operation for the types of nozzles appropriate for subsonic speeds is shown in figure 20. The operation of the jets produces a favorable effect on all axial-force components (reduces drag) and the iris nozzles produce the most favorable jet interferences (refs. 17 and 21). When the dry nozzles are operating unchoked, nozzle performance values greater than 1.0 are obtained because of the thrust on the nozzle boattail. Similar results were found in the investigation of reference 6. Generally, similar trends occur for the augmented-nozzle combinations of figure 21. At a Mach number of 2.01 (fig. 21(d)) the combination with the augmented iris nozzle has the lowest total-axial-force coefficient, but the thrust-minus-drag performance is poor because the jet expansion occurs outside the convergent nozzle. The augmented C-D nozzle with some guided internal expansion has the best thrust-minus-drag performance.

The power effects on afterbody pressure distributions for various types of nozzles are depicted in figures 31 and 32. The most noticeable result of jet operation is that jet-interference effects are propagated well forward of the nozzle and over an appreciable portion of the rear of the afterbody. Although the jet-interference effects are mainly confined to the region of the interfairing channel, the jets can influence the pressures over as much as 15 percent of the afterbody (augmented iris nozzles at subsonic speeds).

The effect of jet operation on installed-nozzle pressure distributions is shown in figures 36 and 37. The values of pressure coefficient located at $\frac{x}{d_n} = 0$ are measurements obtained in the afterbody-nozzle clearance annulus at each row station and are indicative of the effect of the small aft-facing step on the nozzle pressure measurements. When compared to the last pressure measurement on corresponding rows of the afterbody (fig. 31) the annulus pressures generally indicate a small corner expansion at the nozzle-attachment point. The annulus pressures at nozzle row $\phi = 270^\circ$ next to the interfairing are somewhat lower than those at the other peripheral positions for dry iris nozzles. Nozzle pressure distributions at peripheral stations $\phi = 45^\circ$ and $\phi = 90^\circ$ (figs. 36(a) and 36(b)) should be the least affected by centerbody contouring, and the shapes of these pressure distributions are similar for those found on isolated nozzles with circular-arc boattails (refs. 11 and 20). However, for the long iris nozzles, the afterbody boattailing ahead of the nozzles tends to increase the installed pressure level above typical values for isolated nozzles. The presence of the interfairing ($\phi = 270^\circ$) tends to make the adjacent pressures on the nozzles more positive (ref. 10). Also observed in figure 36 are the large favorable jet-interference effects that extend forward over the entire nozzle, particularly noticeable for the augmented-iris configuration (figs. 36(c) and 36(d)). The convergent-divergent nozzles (fig. 37) exhibit generally similar trends due to jet operation.

CONFIGURATION PERFORMANCE

The performance of the various afterbody-nozzle combinations may be summarized by presenting the performance parameters at a typical turbofan pressure-ratio schedule with Mach number. The selected jet pressure-ratio schedule is shown in figure 22 and is the same as that used in reference 7. To permit conversion of axial-force coefficients to thrust ratios, figure 23 has been prepared for dry-power and augmented-power nozzle configurations.

Performance Comparisons of Afterbody Variations

Effect of interfairing shape at scheduled jet-pressure ratios.- A summary of the influence of interfairing contour on axial-force coefficients is given in figure 24. The afterbody with the extended interfairing had the lowest afterbody drag with all iris nozzles and the elliptical interfairing generally had the highest afterbody drag. A generally opposite trend exists for the nozzle axial-force coefficients where the curved interfairings promote pressure recovery on the boattailed nozzle giving thrust while the blunt interfairings produce nozzle drag at subsonic speeds. The total-axial-force coefficients of the afterbody plus nozzle also show that the elliptical and circular-arc interfairings with iris nozzles had the least drag at subsonic speeds. These interfairing shapes promote ventilation between the nozzles leading to better pressure recovery over the entire circumference

of the nozzle boattails. The difference in total-axial-force coefficient between the blunt and elliptical interfairings for the dry iris nozzles represents a change in drag coefficient of about 40 percent (ref. 21). This is a significant difference, since for a typical fighter aircraft this could be equivalent to a change in afterbody drag of about 4 to 8 percent at subsonic cruise. Figure 24(b) again shows the largest drag changes due to centerbody shaping occur on the nozzles. Thrust exists on the augmented iris nozzles at subsonic speeds with all interfairings. The difference in total-axial-force coefficient between the blunt and elliptical interfairing amounts to about 30 percent at a Mach number of 0.80. At supersonic Mach numbers and augmented power (figs. 24(b) and 24(c)), the performance of the elliptical interfairing was comparable to that of the blunt and extended configurations. The large augmented nozzles separated the flow behind the ellipse, reducing afterbody drag as if the interfairing slopes had been physically reduced. (See, for example, figs. 29(d) and 29(e).)

The incremental change in axial-force coefficients due to jet operation is presented in figure 25. The increments represent the difference between the scheduled-pressure-ratio data of figure 24 and the jet-off variations with Mach number of figure 14. Generally small, favorable increments are observed for the various interfairings on the afterbody and nozzle. The augmented iris nozzles which had the shortest length and largest jet diameters produced the most jet interference. The incremental total-axial-force coefficients (fig. 25(c)) generally show more favorable jet interferences for the afterbody with the elliptical interfairing.

Effect of tail booms at scheduled pressure ratios.- Figure 26 reveals that the addition of outboard booms to the clean afterbody with extended interfairing increased all axial-force coefficients at subsonic and transonic speeds. For the selected pressure-ratio schedule, no beneficial effects resulted at supersonic speeds even when the nozzle was operating underexpanded (fig. 18(i)).

Performance Comparisons of Nozzle Configurations

The effect of nozzle type on performance for the afterbody with the elliptical interfairing is presented in figure 27 for the pressure-ratio schedule. The axial-force coefficients of figure 27(a) indicate the nozzle-shape effects on the components of the afterbody-nozzle combination for two power settings. The dry-power nozzles both had the same fineness ratio and exit area. Although all nozzles have thrust on the external surface at subsonic speeds, the augmented C-D nozzle has the least favorable interference due to being operated overexpanded and because of the low boattailing (ref. 11). The better performance of the curved dry iris nozzle compared with the equivalent conical boattail C-D nozzle would be expected, based on isolated nozzle results (ref. 22). The afterbody-axial-force-coefficient trends are generally similar to the jet-off flow-field effects of figure 19, but jet operation has a stronger influence on the afterbody drag with the short augmented-

iris nozzle. When combined with the afterbody having an elliptical interfairing, the dry iris nozzles with circular-arc boattails produced less total subsonic drag and higher thrust-minus-drag values (fig. 27(b)) than conically boattailed nozzles with the same throat area. At supersonic speeds the shrouded iris nozzles caused less total drag than the augmented convergent-divergent nozzles. However, the latter gave higher internal performance and thrust-minus-drag for the same throat area and expansion ratio.

CONCLUDING REMARKS

The performance of closely spaced twin-jet afterbodies with different interfairing, tail-boom, and nozzle shapes was determined at Mach numbers from 0.60 to 2.01. Four interfairing shapes were studied: circular arc, elliptical, and blunt, all ending at the nozzle attachment station; and one blunt-based type extending between the nozzles. Results were also obtained with tail booms of circular or oval cross section extending from the sides of the afterbody past the nozzles. Propulsive-nozzle shapes represented variable-geometry iris and convergent-divergent types with circular-arc and conical boattails, respectively. These were operated in both minimum and maximum throat-area modes at pressure ratios from jets off to 20, depending on Mach number.

At scheduled pressure ratios assumed for a turbofan engine, the power-on results indicate the following:

1. The circular-arc and elliptical interfairings ventilated the inboard regions of the dry-power nozzles causing full-circumferential high-pressure recovery and much lower subsonic nozzle drag than the blunt or extended interfairings.

2. At supersonic Mach numbers and augmented power, there was no significant difference in performance between configurations with elliptical, blunt, and extended interfairings. The large augmented nozzles separated the flow behind the ellipse, reducing afterbody drag as if the interfairing slopes had been physically reduced.

3. Tail booms increased both the afterbody and nozzle drag at subsonic and transonic speeds.

4. When combined with the elliptical interfairing, the dry-iris nozzles with circular-arc boattails produced less total subsonic drag and higher thrust-minus-drag values than conically boattailed nozzles with the same throat area. At supersonic speeds the shrouded iris nozzles (no-flow ejector) caused less total drag than the convergent-divergent nozzles. However, the latter gave higher internal performance and thrust-minus-drag for the same throat area and expansion ratio.

Langley Research Center,
National Aeronautics and Space Administration,
Hampton, Va., July 27, 1971.

REFERENCES

1. Runckel, Jack F.: Jet-Exit and Airframe Interference Studies on Twin-Engine-Fuselage Aircraft Installations. NASA TM X-1274, 1966.
2. Schmeer, James W.; Lauer, Rodney F., Jr.; and Berrier, Bobby L.: Performance of Blow-In-Door Ejector Nozzles Installed on a Twin-Jet Variable-Wing-Sweep Fighter Airplane Model. NASA TM X-1383, 1967.
3. Wilmoth, Richard G.; Norton, Harry T., Jr.; and Corson, Blake W., Jr.: Effect of Engine-Interfairing Modifications on the Performance of a Powered Twin-Jet Fighter-Airplane Model at Mach 1.20. NASA TM X-1534, 1968.
4. Mercer, Charles E.; Pendergraft, Odis C., Jr.; and Berrier, Bobby L.: Effect of Geometric Variations on Performance of a Twin-Jet Blow-In-Door Ejector Nozzle Installation. NASA TM X-1633, 1968.
5. Berrier, Bobby Lee; and Wood, Frederick H., Jr.: Effect of Jet Velocity and Axial Location of Nozzle Exit on the Performance of a Twin-Jet Afterbody Model at Mach Numbers up to 2.2. NASA TN D-5393, 1969.
6. Mercer, Charles E.; and Berrier, Bobby L.: Effect of Afterbody Shape, Nozzle Type, and Engine Lateral Spacing on the Installed Performance of a Twin-Jet Afterbody Model. NASA TM X-1855, 1969.
7. Maiden, Donald L.; and Runckel, Jack F.: Effect of Nozzle Lateral Spacing on Afterbody Drag and Performance of Twin-Jet Afterbody Models With Convergent Nozzles at Mach Numbers up to 2.2. NASA TM X-2099, 1970.
8. Pendergraft, Odis C., Jr.: Performance of Twin D Nozzle-Afterbody With Wedge-Type Interfairings at Mach Numbers to 2.2. NASA TM X-2100, 1970.
9. Kirkham, Frank S.; Lee, Edwin E., Jr.; and Lauer, Rodney F., Jr.: Afterbody Drag of Several Clustered Jet-Exit Configurations at Transonic Speeds. NASA TM X-1216, 1966.
10. Thronson, L. W.: Close-Spaced Nozzles Twin Jet Configuration. AIAA Paper No. 70-934, July 1970.
11. Compton, William B., III; and Runckel, Jack F.: Jet Effects on the Boattail Axial Force of Conical Afterbodies at Subsonic and Transonic Speeds. NASA TM X-1960, 1970.
12. Greathouse, W. K.; and Hollister, D. P.: Preliminary Air-Flow and Thrust Calibrations of Several Conical Cooling-Air Ejectors With a Primary to Secondary Temperature Ratio of 1.0. I - Diameter Ratios of 1.21 and 1.10. NACA RM E52E21, 1952.

13. Hearsh, Donald P.; and Valerino, Alfred S.: Thrust and Pumping Characteristics of a Series of Ejector-Type Exhaust Nozzles at Subsonic and Supersonic Flight Speeds. NACA RM E54H19, 1954.
14. Valerino, Alfred S.; and Yeager, Richard A.: External-Stream Effects on Gross Thrust and Pumping Characteristics of Ejectors Operating at Off-Design Mach Numbers. NACA RM E56C14, 1956.
15. Ellis, C. W.; Hollister, D. P.; and Sargent, A. F., Jr.: Preliminary Investigation of Cooling-Air Ejector Performance at Pressure Ratios From 1 to 10. NACA RM E51H21, 1951.
16. Wesoky, Howard L.: Boundary-Layer Measurements in Accelerated Flows Near Mach 1. NASA TN D-3882, 1967.
17. Corson, Blake W., Jr.; and Runckel, Jack F.: Exploratory Studies of Aircraft Afterbody and Exhaust-Nozzle Interaction. NASA TM X-1925, 1969.
18. Pitts, William C.; and Wiggins, Lyle E.: Axial-Force Reduction by Interference Between Jet and Neighboring Afterbody. NASA TN D-332, 1960.
19. Migdal, D.; Miller, E. H.; and Schnell, W. C.: An Experimental Evaluation of Exhaust Nozzle/Airframe Interference. AIAA Paper No. 69-430, June 1969.
20. Shrewsbury, George D.: Effect of Boattail Juncture Shape on Pressure Drag Coefficients of Isolated Afterbodies. NASA TM X-1517, 1968.
21. Runckel, Jack F.: Aerodynamic Interference Between Exhaust System and Airframe. Paper Presented at AGARD Specialists Meeting on "Aerodynamic Interference" (Silver Spring, Md.), Sept. 1970.
22. Bergman, Dave: Effects of Engine Exhaust Flow on Boattail Drag. AIAA Paper No. 70-132, Jan. 1970.



L-68-10 595

(a) Front view.

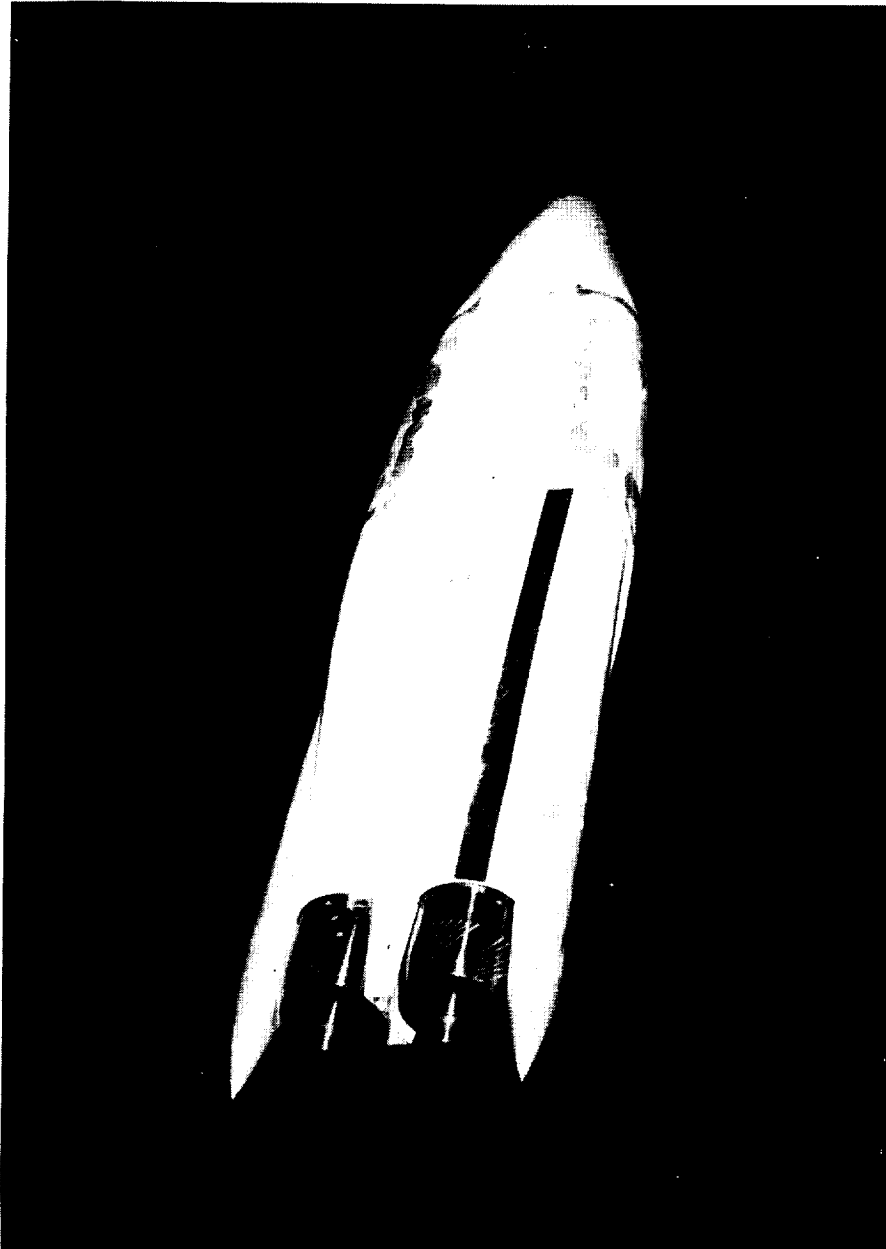
Figure 1.- Photographs of model installation in the Langley 16-foot transonic tunnel.



L-68-10 594

(b) Side view.

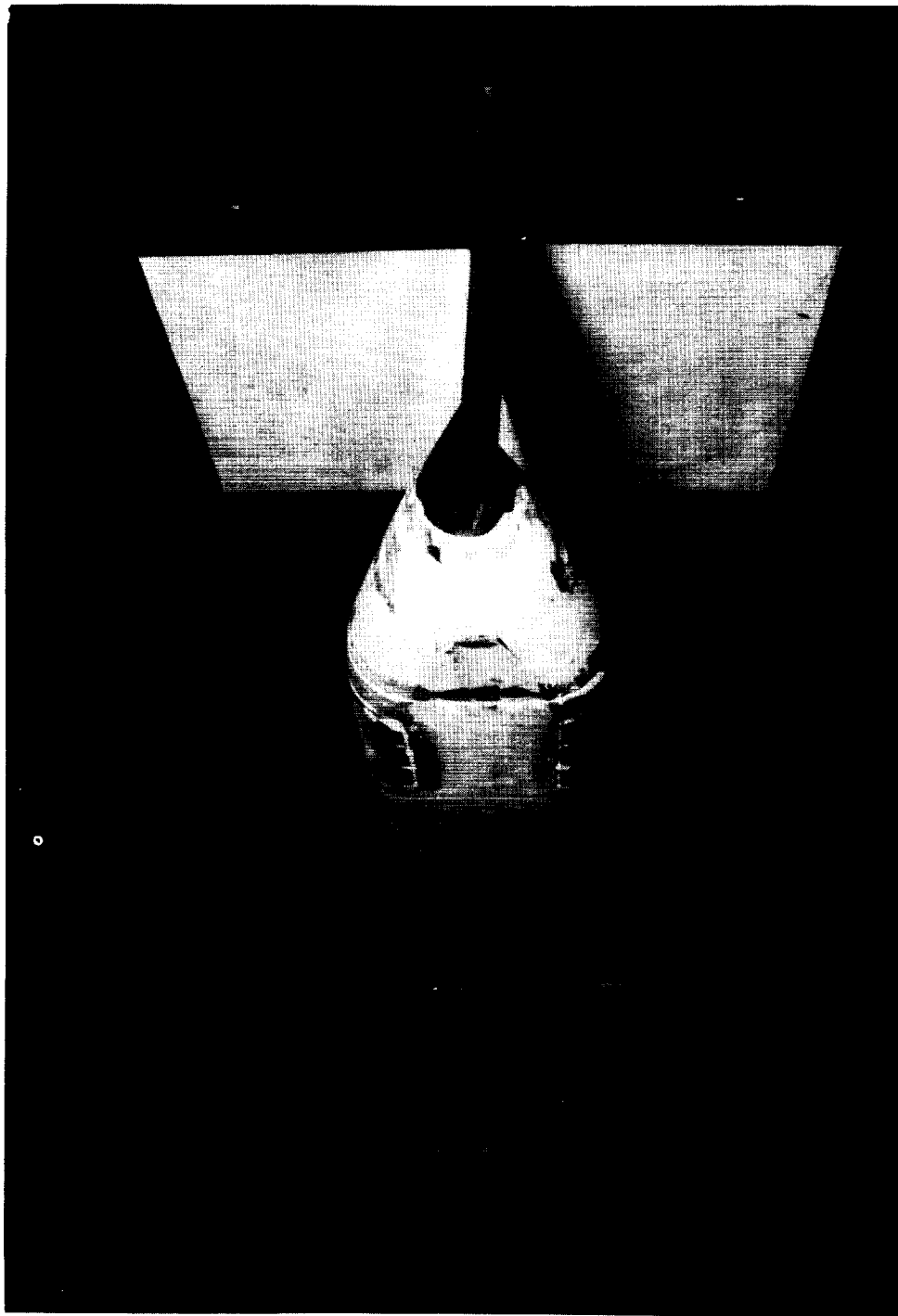
Figure 1.- Continued.



L-68-10 976

(c) Rear view.

Figure 1.- Concluded.



L-71-661

(a) Front view.

Figure 2.- Photographs of model installation in the Langley 4- by 4-foot supersonic pressure tunnel.



L-71-662

(b) Rear view.

Figure 2.- Concluded.

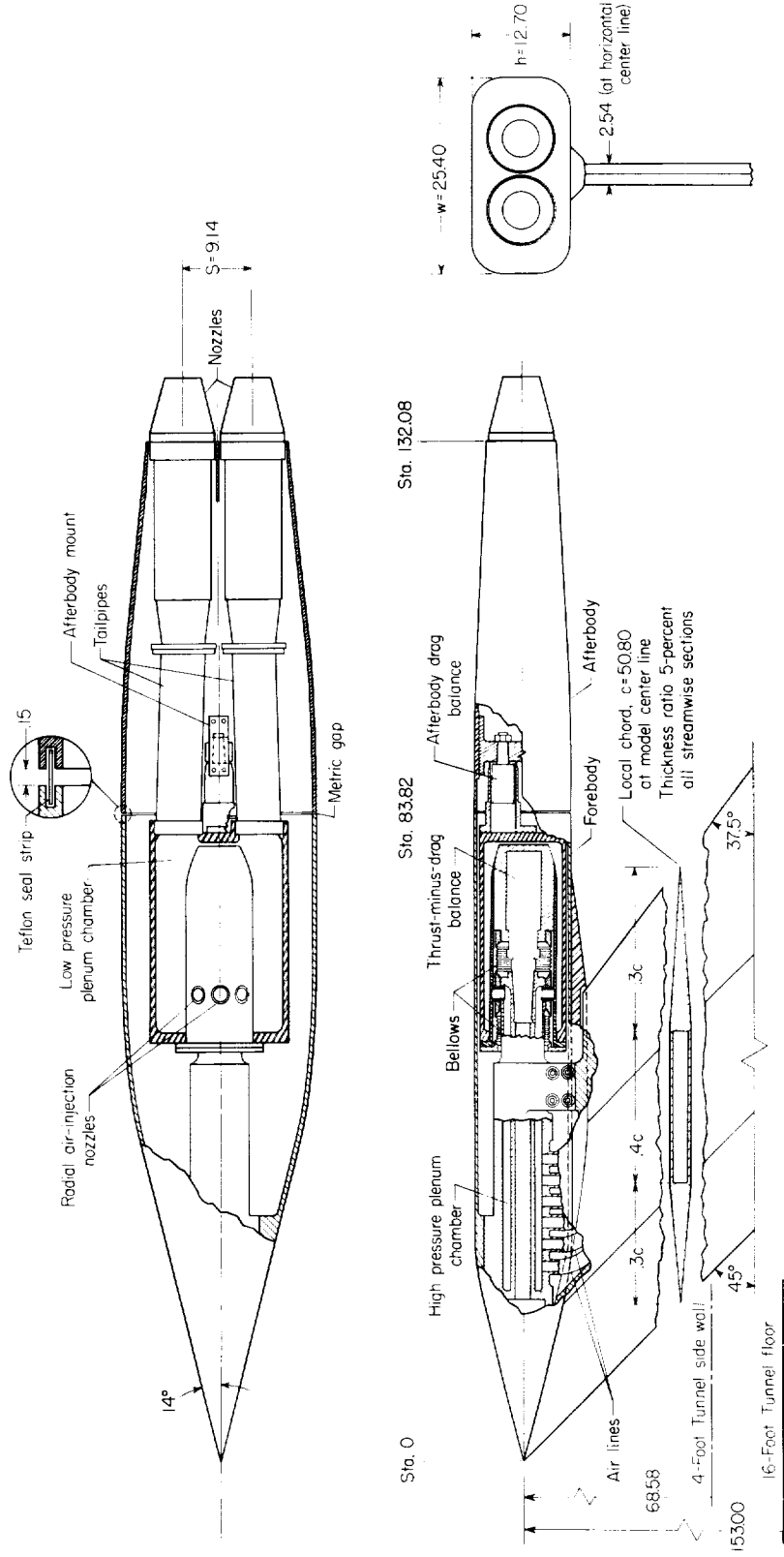


Figure 3.- Sketch of air-powered twin-jet model and strut support system. (All dimensions are in cm unless otherwise noted.)

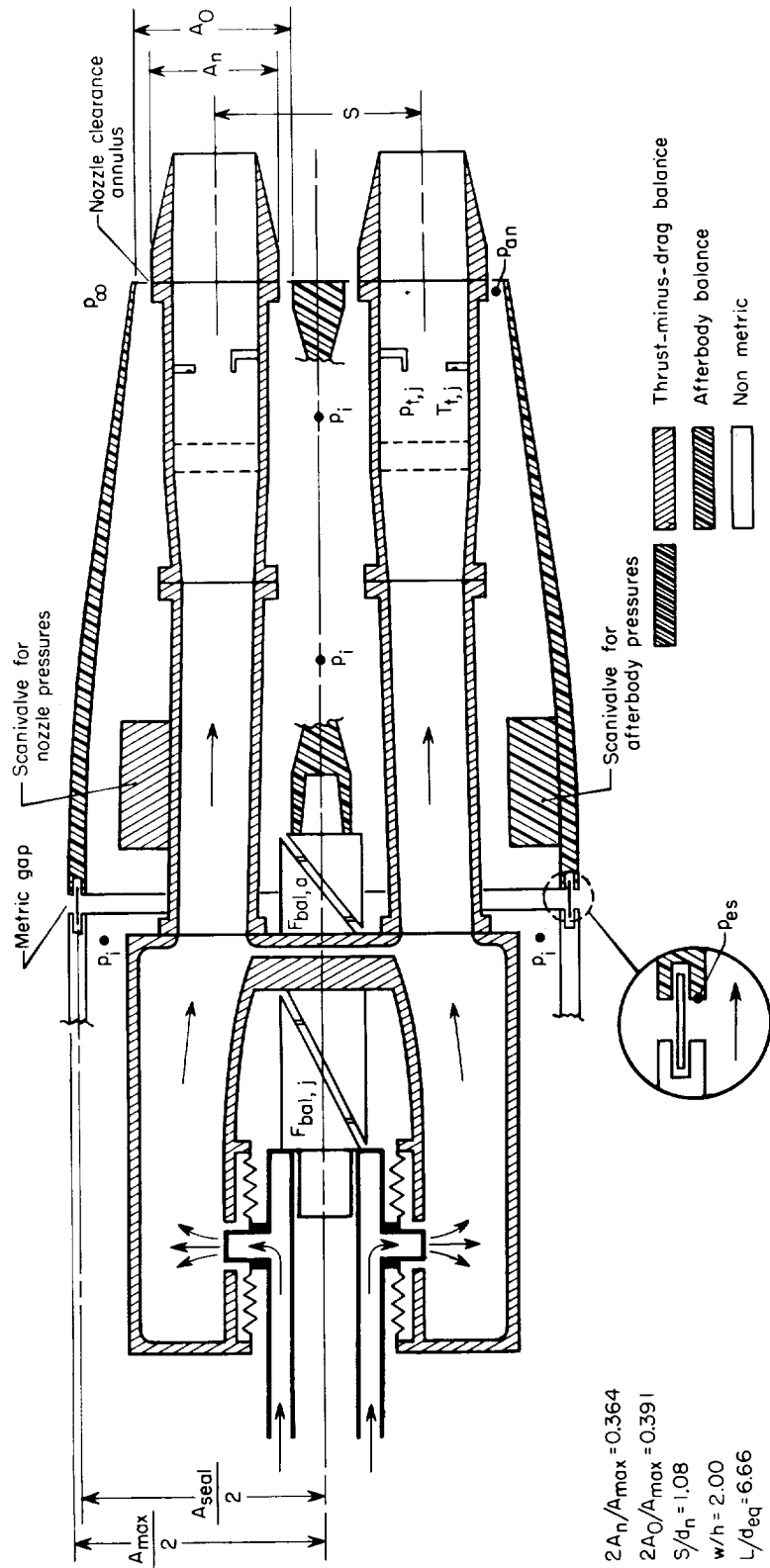
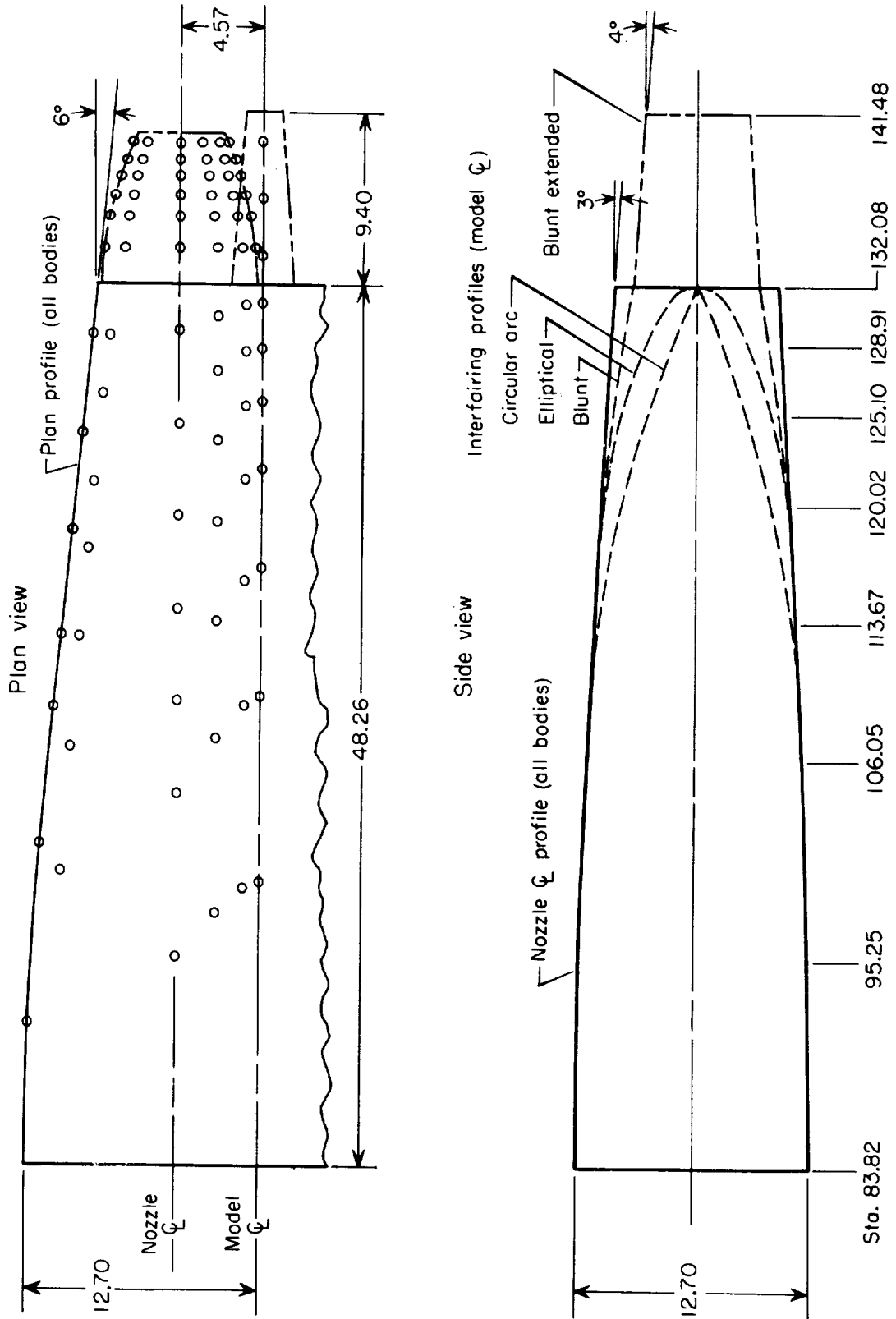


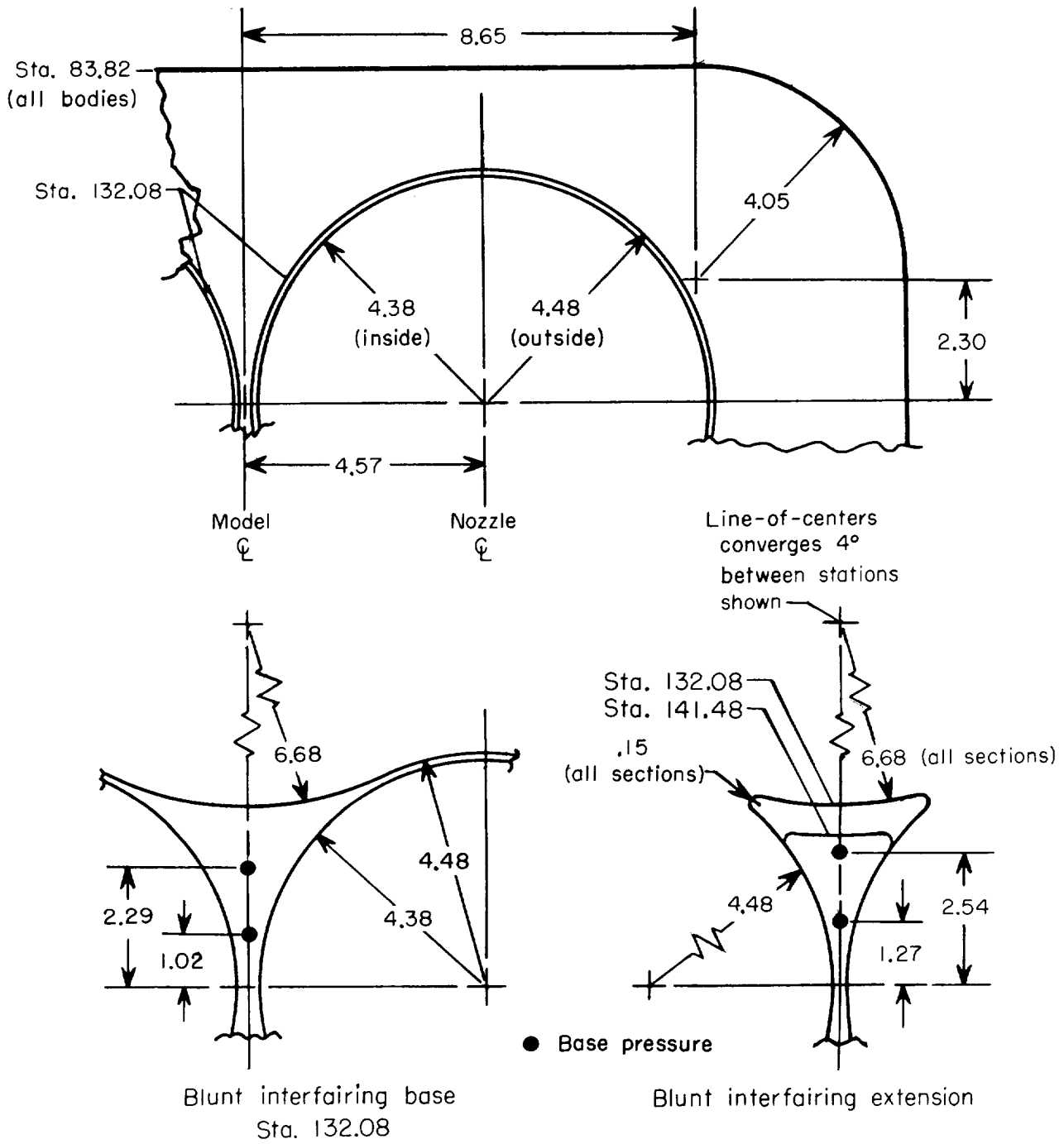
Figure 4.- Schematic sketch of force balance systems.



(a) Plan and side profiles.

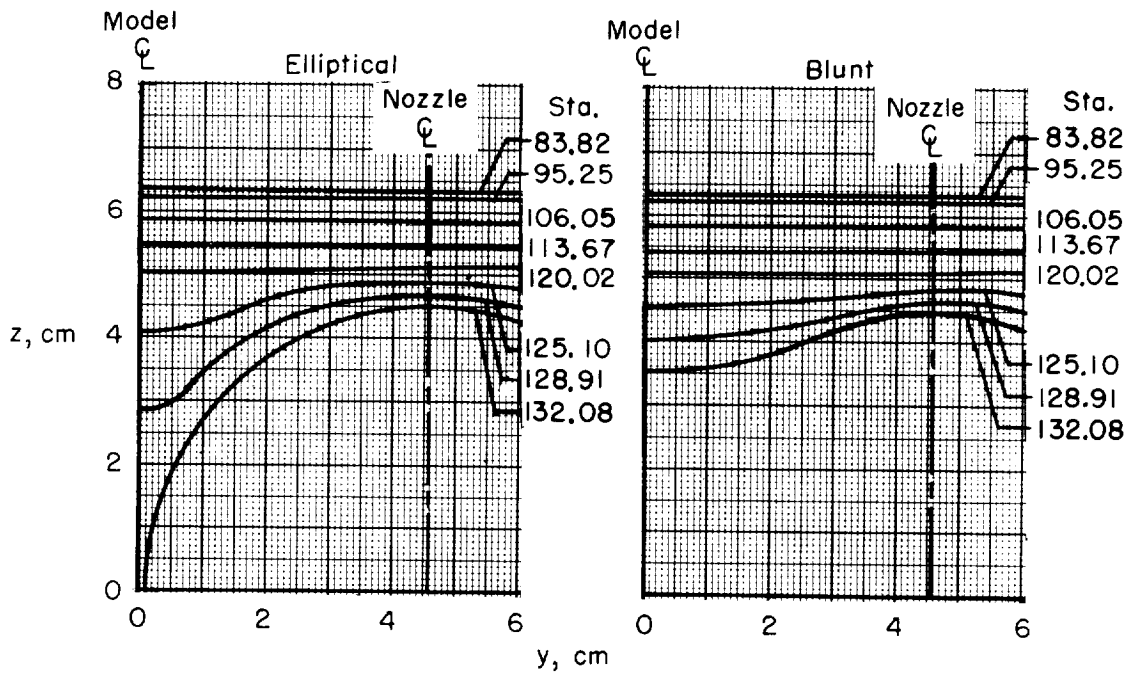
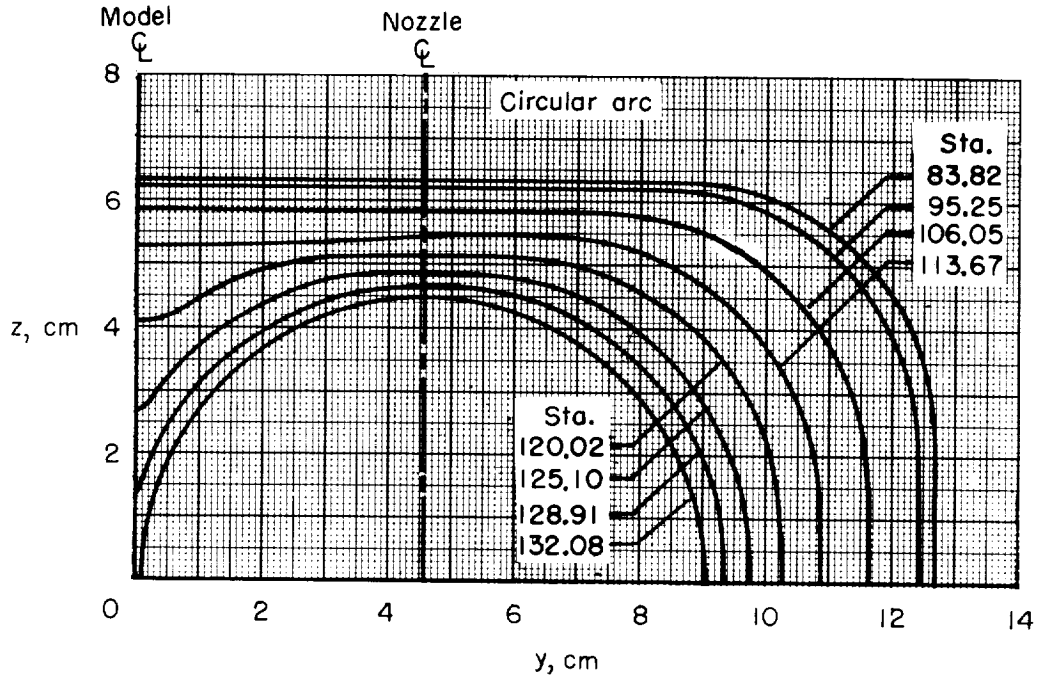
Figure 5.- Twin-jet afterbody models with different interfering profiles and tail-boom shapes.
(All dimensions are in cm.)

Rear view—circular arc and elliptical interfairings



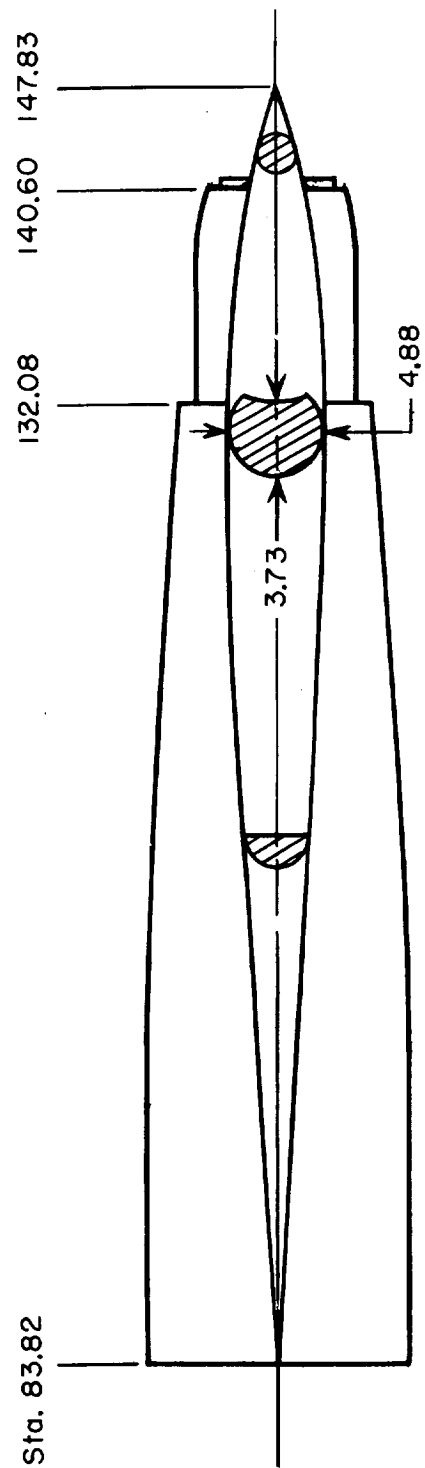
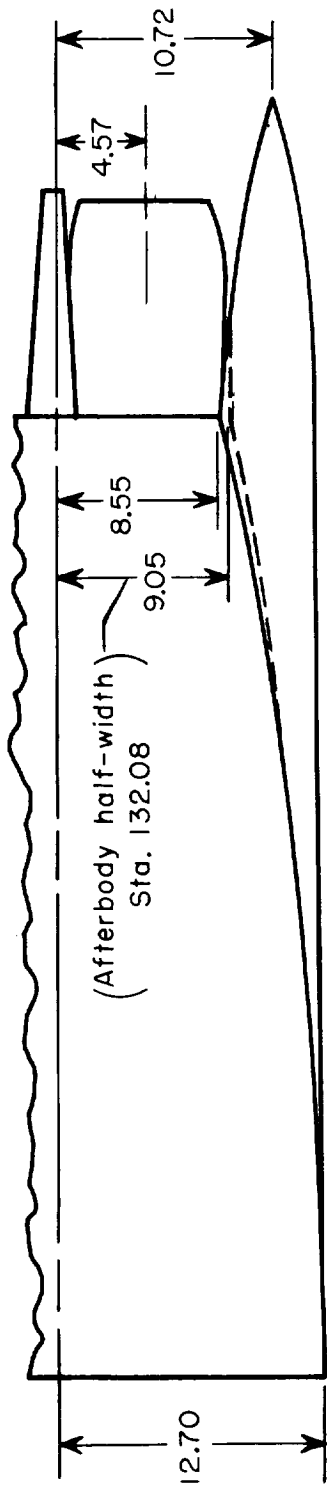
(b) Frontal outline and base details.

Figure 5.- Continued.



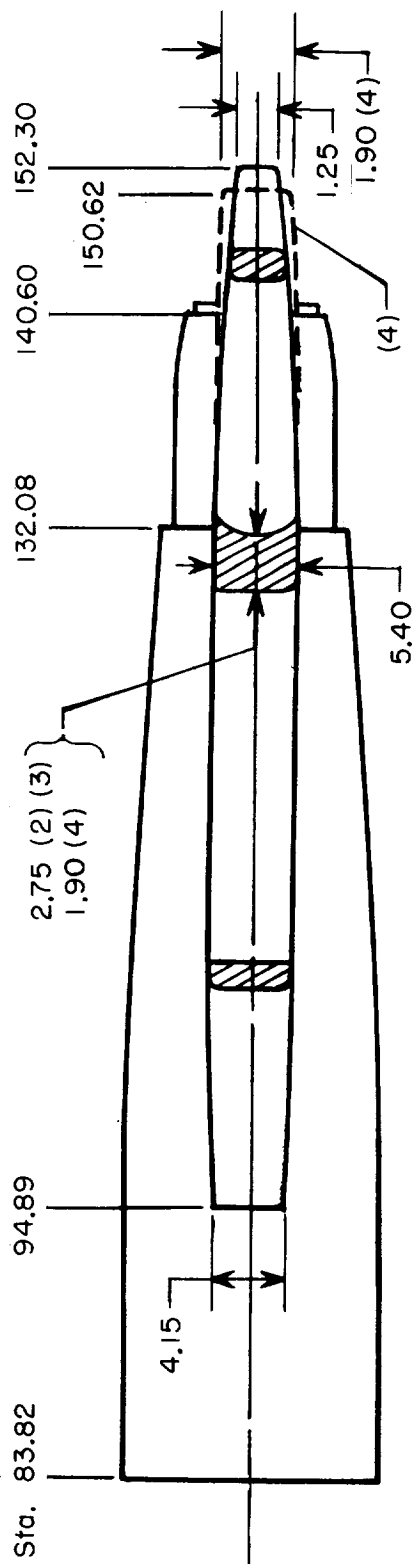
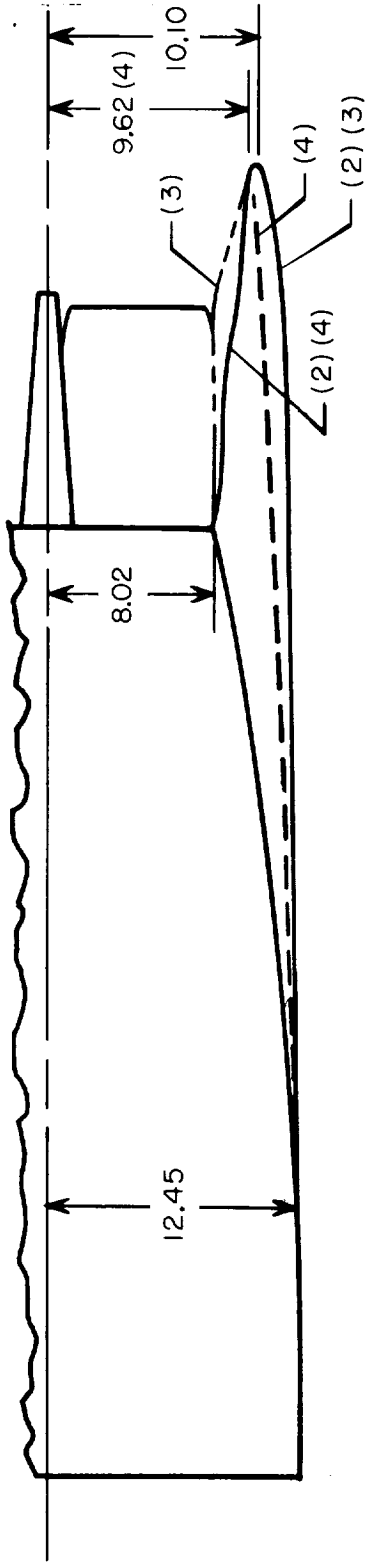
(c) Afterbody cross sections. (Contours outboard of nozzle center line are identical for all bodies.)

Figure 5.- Continued.



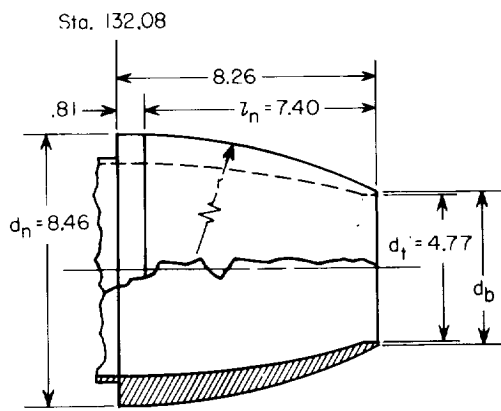
(d) Tail-boom configuration 1; extended interfairing and shrouded iris nozzles.

Figure 5.- Continued.

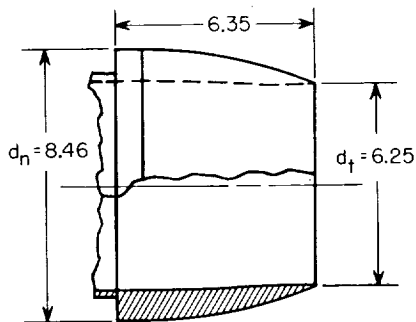
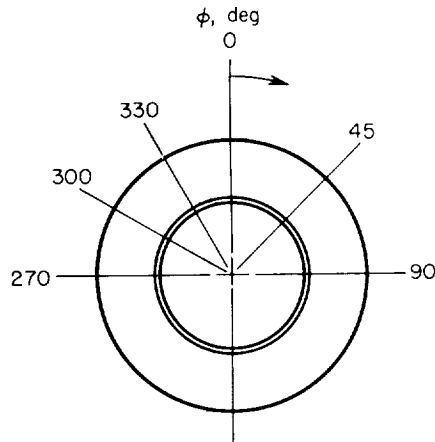


(e) Tail-boom configurations 2, 3, and 4; extended interfering and shrouded iris nozzles.
 (Profiles are identified by numbers in parentheses.)

Figure 5.- Concluded.

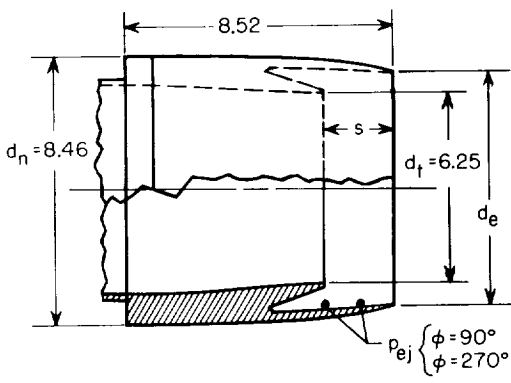


Dry iris nozzle



Augmented iris nozzle

Nozzle Surface Orifice Stations					
Orifice rows located at $\phi = 0^\circ, 45^\circ, 90^\circ, 270^\circ, 300^\circ,$ and 330°					
Dry iris		Augmented iris		Shrouded augmented iris	
x/d_n	X/L	x/d_n	X/L	x/d_n	X/L
0.228	1.016	0.051	1.005	0.100	1.008
.430	1.029	.281	1.019	.668	1.044
.572	1.038	.414	1.028	.758	1.050
.693	1.046	.507	1.034	.827	1.054
.805	1.053	.827	1.039	.886	1.058
.913	1.060	.656	1.043	.937	1.061
		.720	1.047	.984	1.064

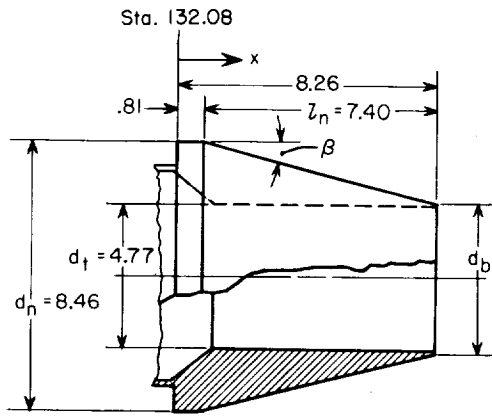


Shrouded augmented iris nozzle

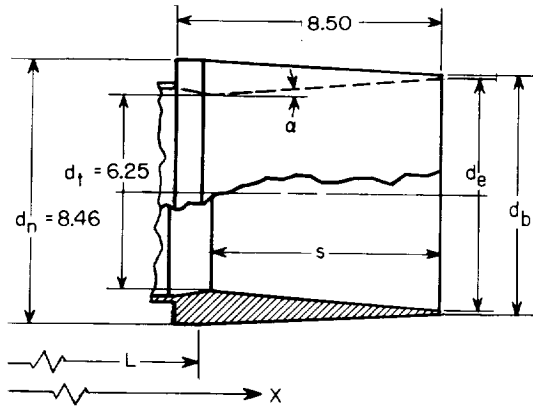
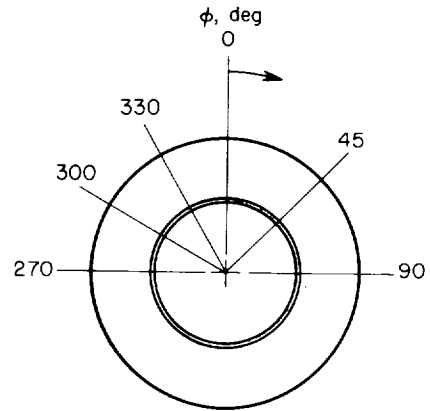
Nozzle Geometry			
	Dry iris	Augmented iris	Shrouded augmented iris
d_e/d_t	1.00	1.00	1.19
ϵ_e	1.00	1.00	1.41
s/d_t	—	—	.35
A_e/A_b	.97	.98	.98
d_e/d_n	.56	.74	.88
A_b/A_n	.32	.56	.79
L_n/d_n	.88	.65	.91
r/d_n	2.66	1.73	2.36
$2A_t/A_{max}$.11	.20	.20

(a) Three-position iris nozzle.

Figure 6.- Nozzle configurations. (All dimensions are in cm unless otherwise noted.)



Dry power nozzle



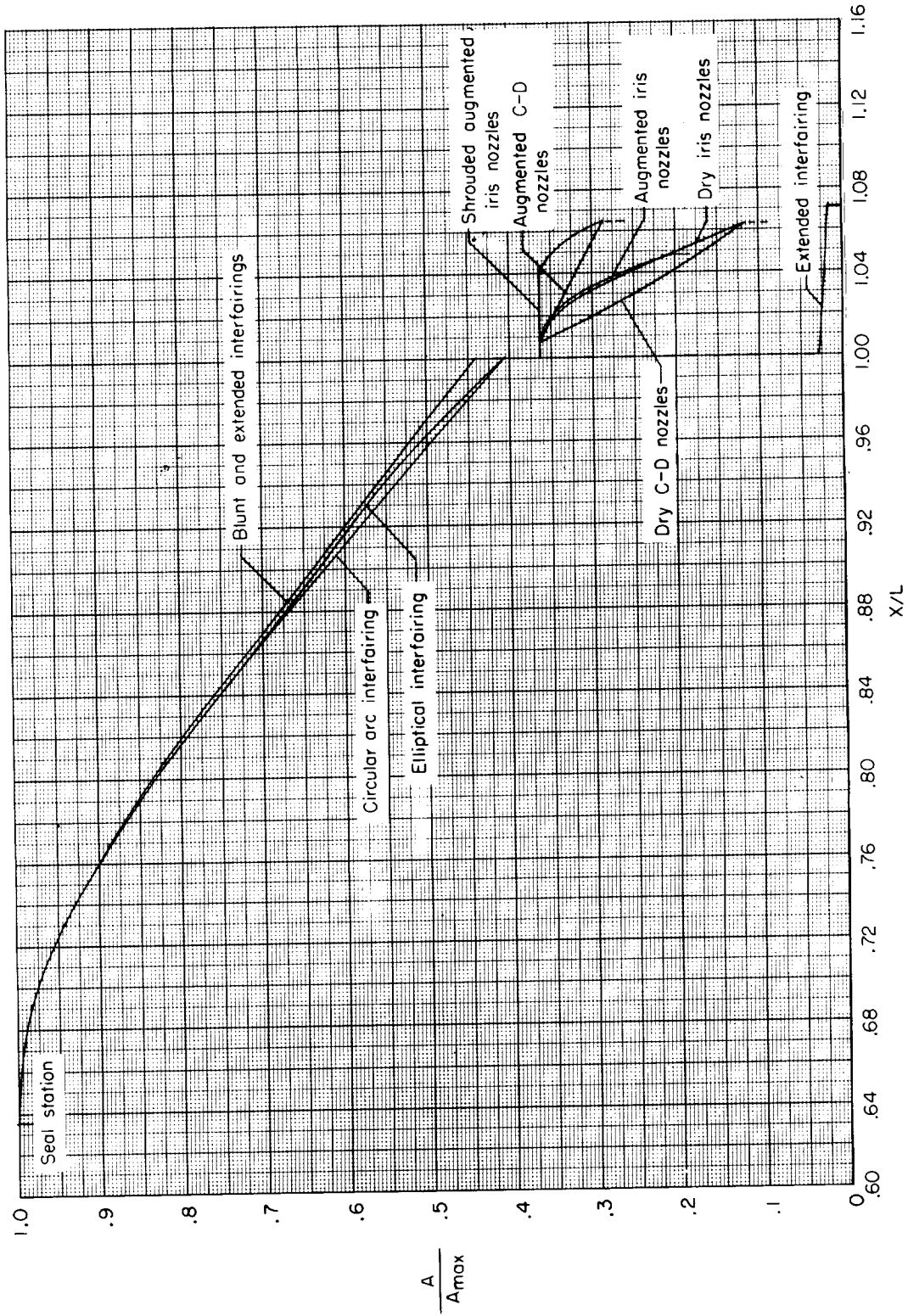
Augmented power nozzle

Nozzle Surface Orifice Stations			
Orifice rows located at $\phi = 0^\circ, 45^\circ, 90^\circ, 270^\circ, 300^\circ,$ and 330°			
Dry power nozzle		Augmented power nozzle	
x/d_n	X/L	x/d_n	X/L
0.051	1.005	0.051	1.005
.160	1.011	.173	1.012
.281	1.019	.317	1.022
.411	1.028	.464	1.031
.551	1.037	.613	1.041
.706	1.040	.766	1.050
.880	1.058	.922	1.060

Nozzle Geometry		
	Dry power nozzle	Augmented power nozzle
d_e/d_t	1.00	1.19
ϵ_e	1.00	1.41
α	0°	4.3°
s/d_t	1.52	1.18
A_e/A_b	.97	.98
d_e/d_n	.56	.88
A_b/A_n	.32	.77
l_n/d_n	.88	.90
β	14.0°	3.6°
$2A_t/A_{max}$.11	.20

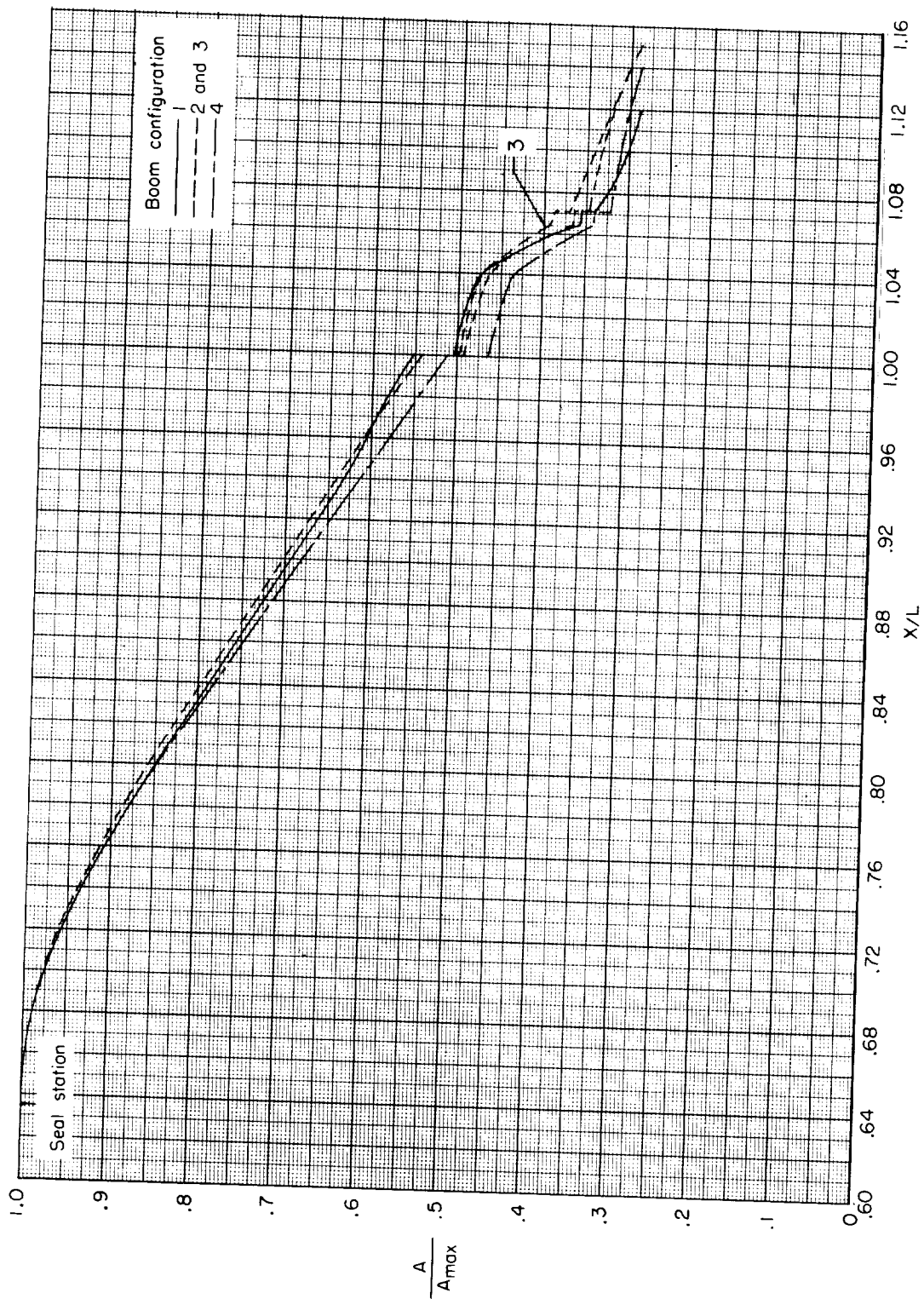
(b) Convergent-divergent nozzles.

Figure 6.- Concluded.



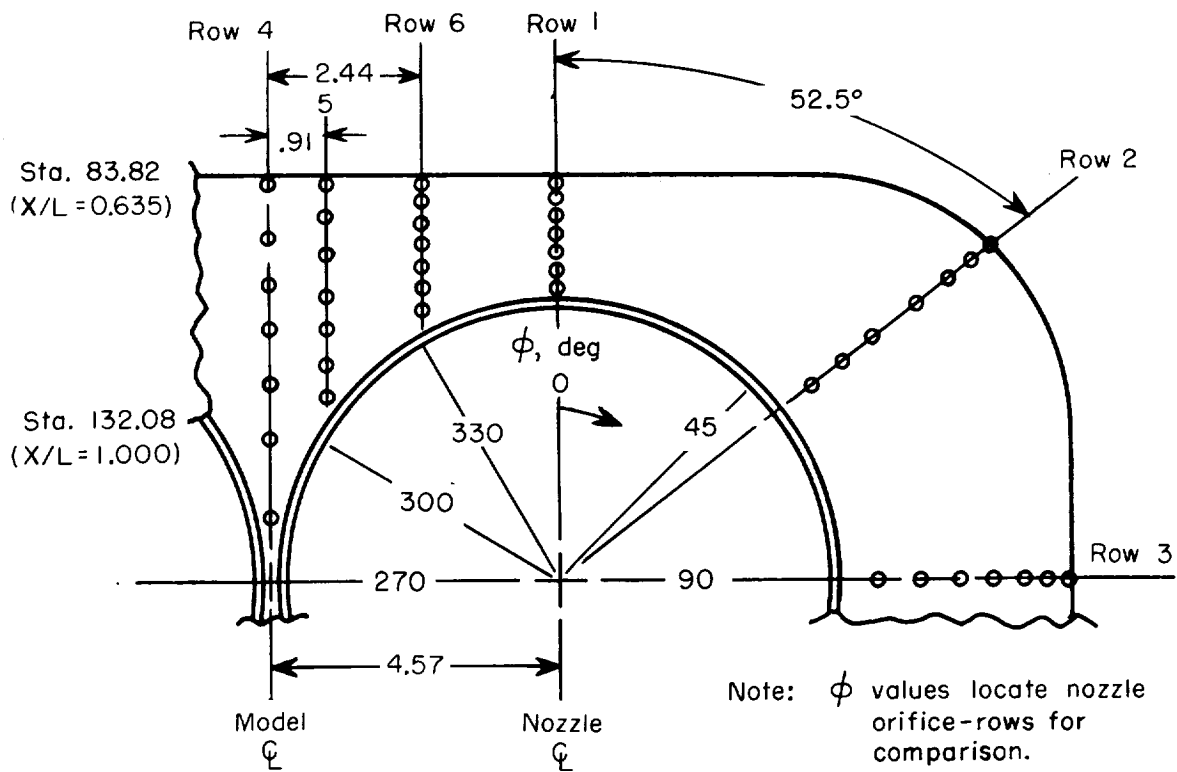
(a) Various interfairing and nozzle shapes.

Figure 7.- Area distributions of twin-jet afterbodies.



(b) Various tail booms; extended interfairing; shrouded-augmented iris nozzles.

Figure 7.- Concluded.

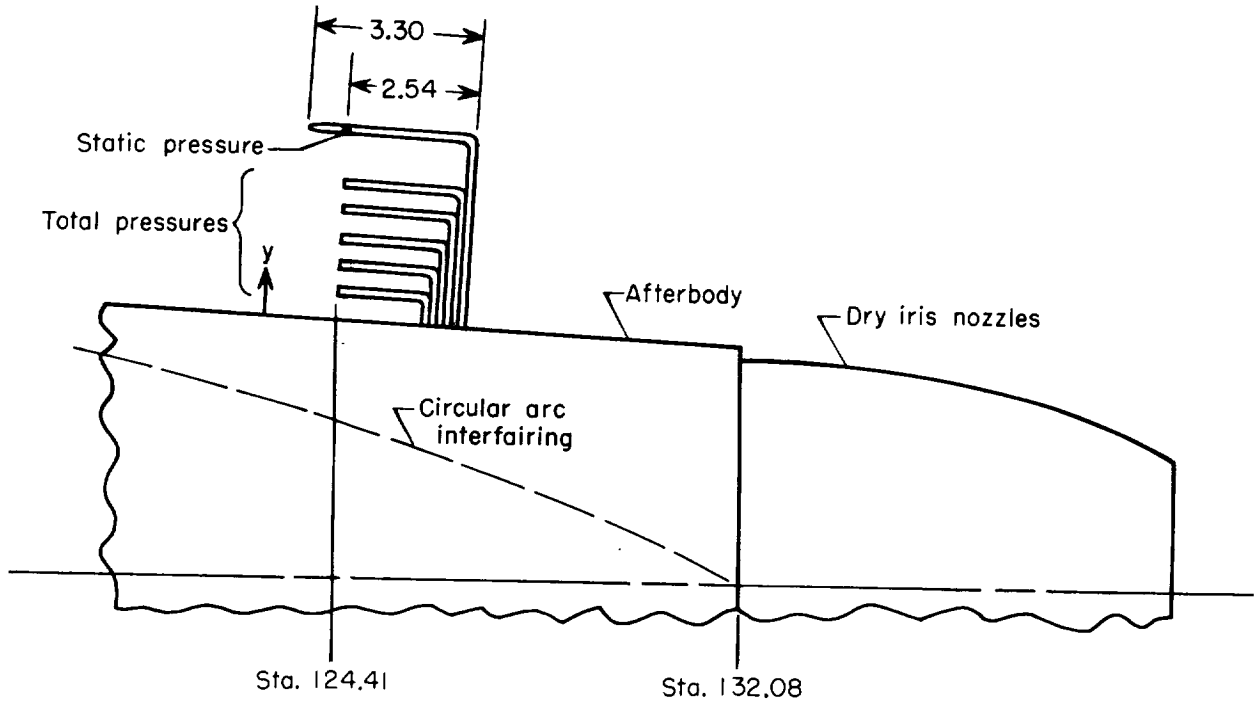


Afterbody pressure orifice locations, X/L											
All bodies			Circular arc			Elliptical			Blunt and extended		
Row			Row			Row			Row		
1	2	3	4	5	6	4	5	6	4	5	6
0.721	0.757	0.694	0.801	0.768	0.736	0.797	0.762	0.737	0.753	0.750	0.740
.788	.808	.768	.878	.841	.805	.912	.848	.807	.829	.825	.812
.827	.854	.815	.912	.880	.852	.947	.910	.861	.882	.877	.861
.865	.891	.855	.936	.912	.894	.970	.937	.905	.923	.919	.902
.904	.918	.898	.958	.938	.928	.985	.958	.938	.951	.950	.935
.942	.954	.939	.976	.964	.959	.995	.974	.967	.973	.972	.964
.981	.978	.980	.992	.988	.986	1.000	.991	.990	.992	.991	.987

Note: X and L measured from model nose. L=132.08 cm.

1.012
1.036
1.059 } Extended inter-fairing only

Figure 8.- Afterbody external-pressure instrumentation. (All absolute dimensions are in cm.)



Rake tube ordinates, y						
Totals						Static
Top	0.38	0.91	1.42	1.93	2.41	3.43
Side	.57	1.08	1.52	2.06	2.79	3.68

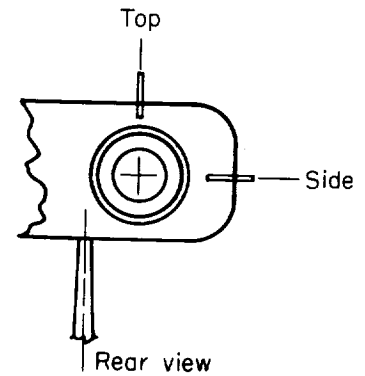


Figure 9.- Afterbody boundary-layer rake installation for circular-arc interfairing and dry iris nozzles only. (All dimensions are in cm.)

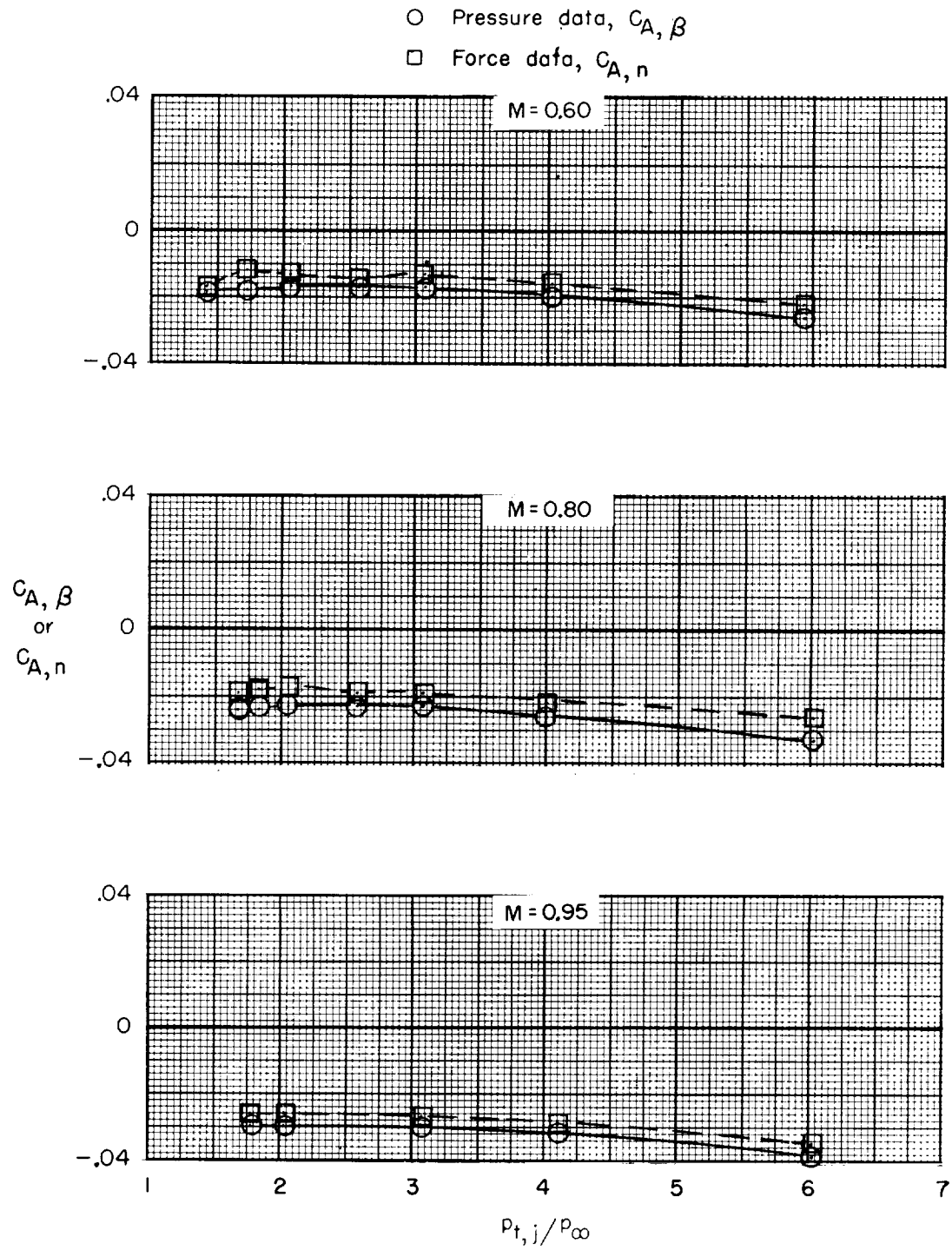
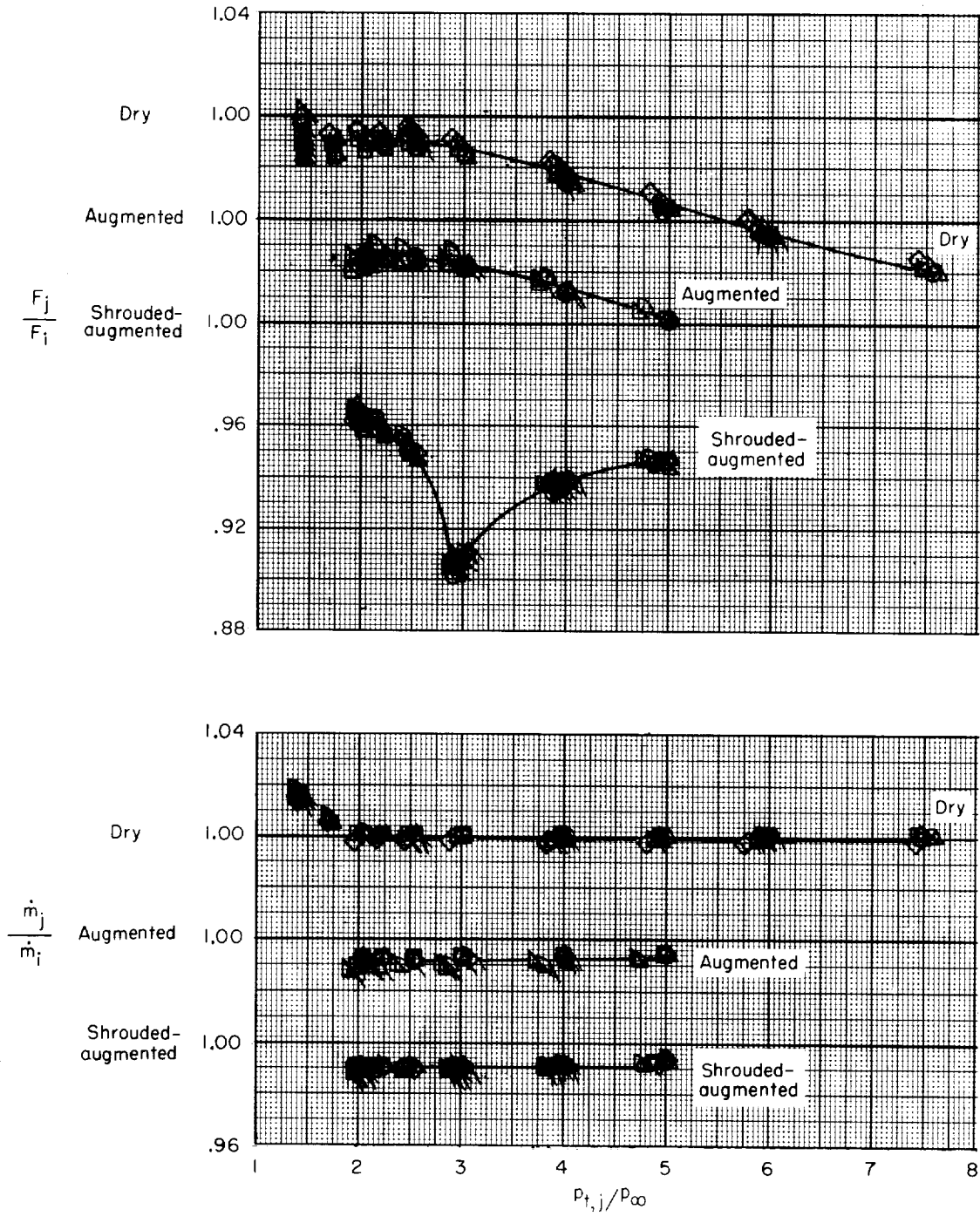
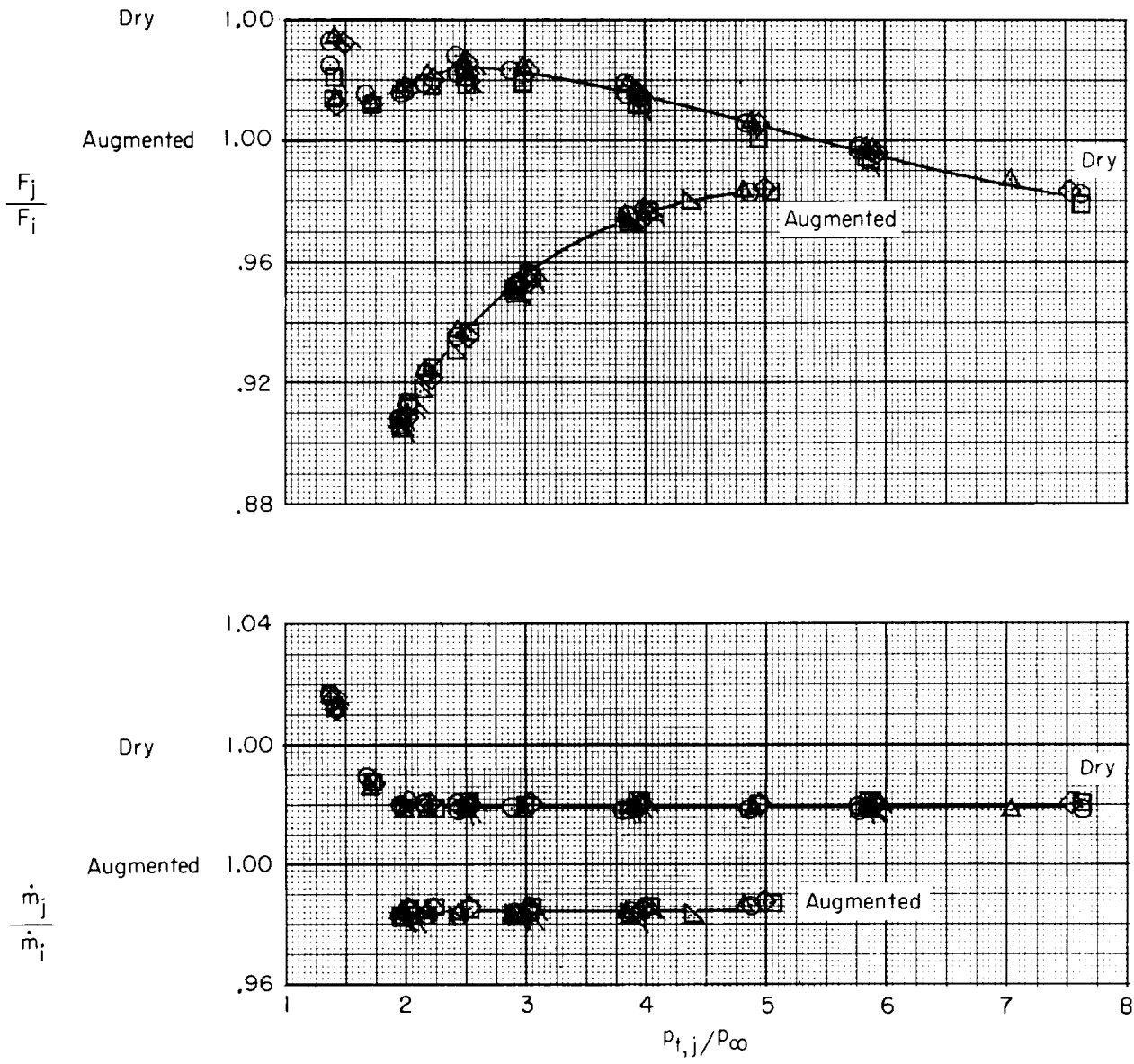


Figure 10.- Comparison of nozzle axial-force coefficients from pressure and force measurements. Dry iris nozzles; elliptical interfairing.



(a) Iris nozzles.

Figure 11.- Nozzle internal performance. (Symbols indicate repeat runs; flagged values denote decreasing pressure ratio.)



(b) Convergent-divergent nozzles.

Figure 11.- Concluded.

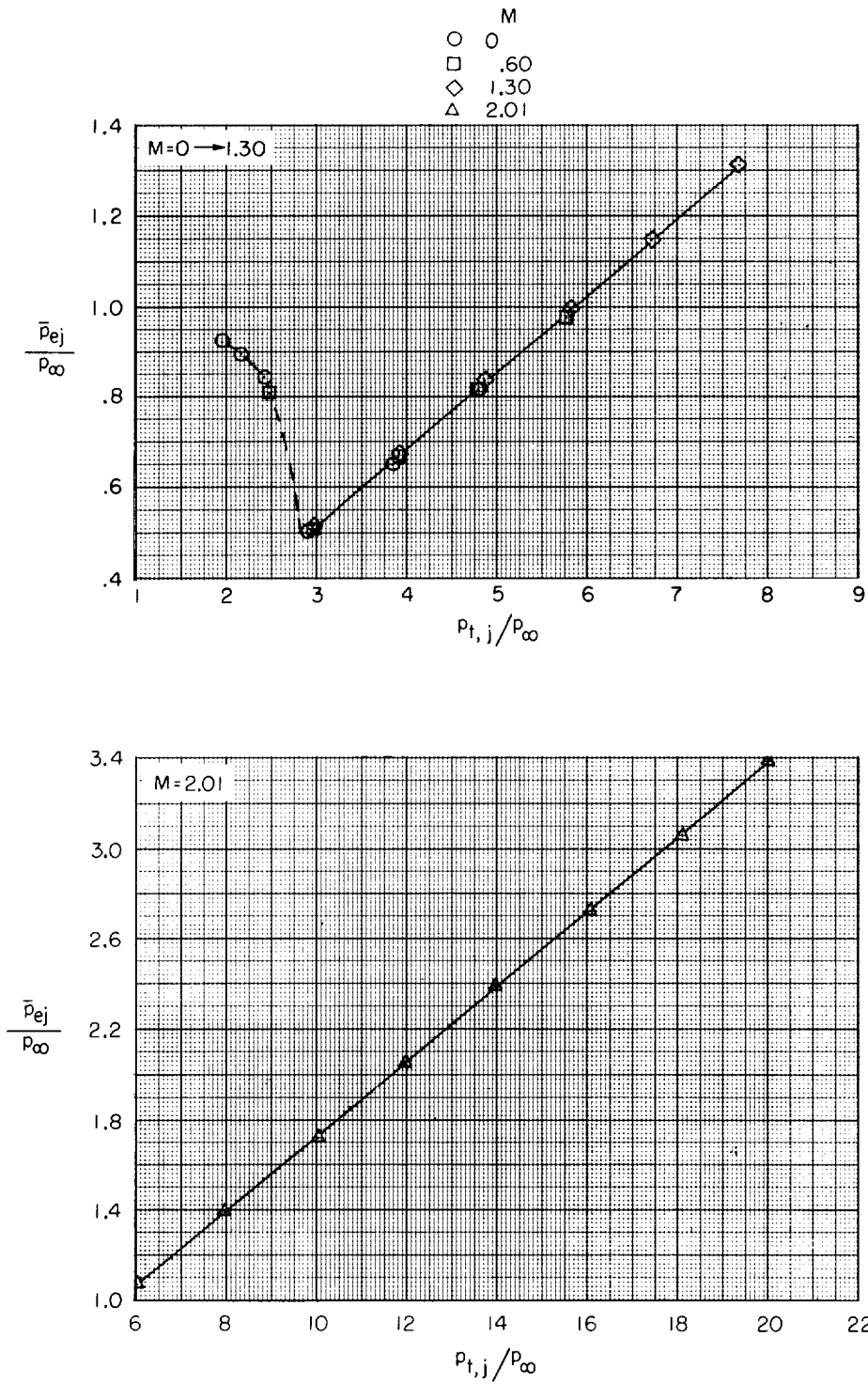
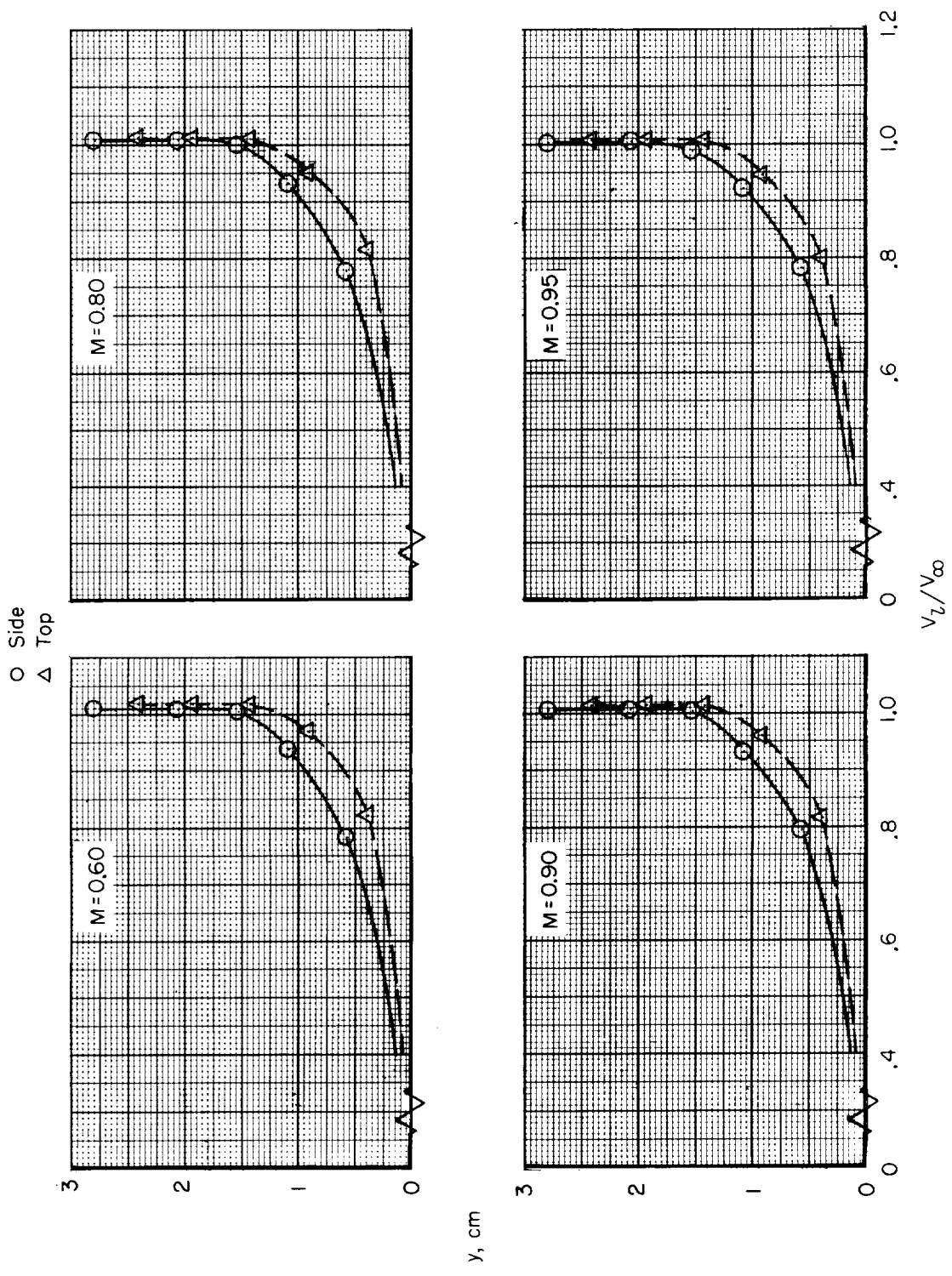
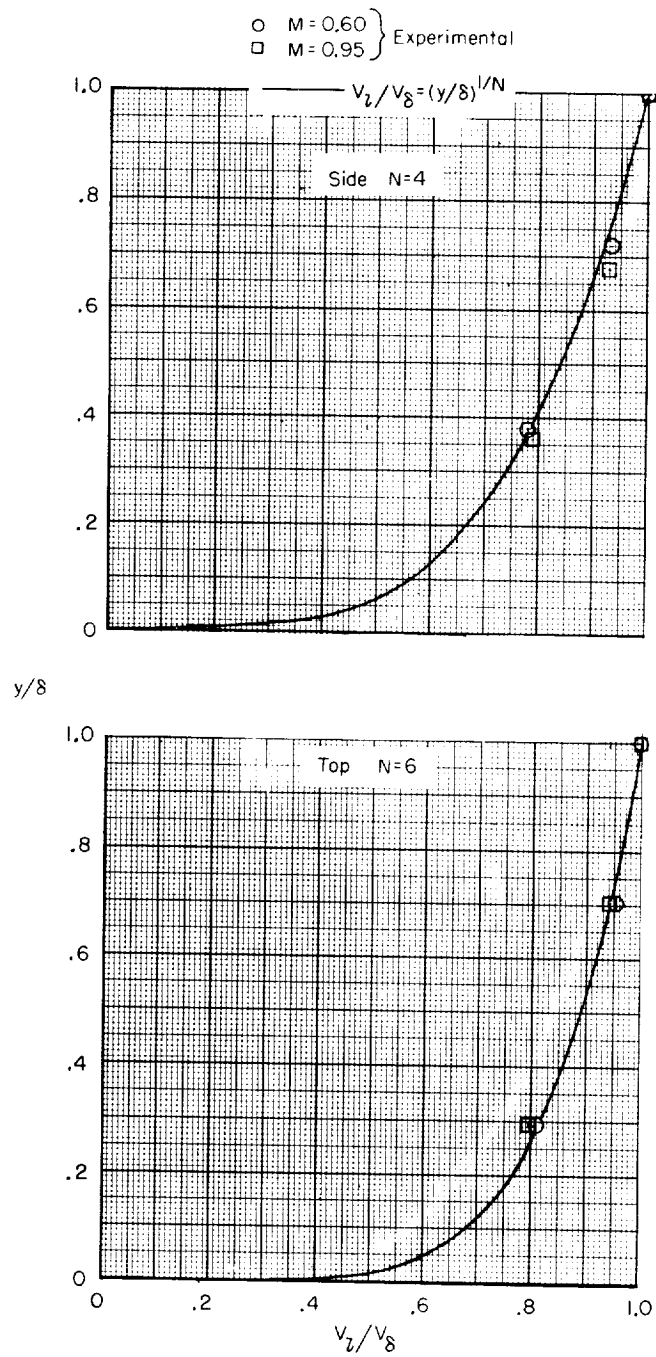


Figure 12.- Variation of average ejector-cavity static pressure with jet-pressure ratio for shrouded iris nozzles and extended interfairing.



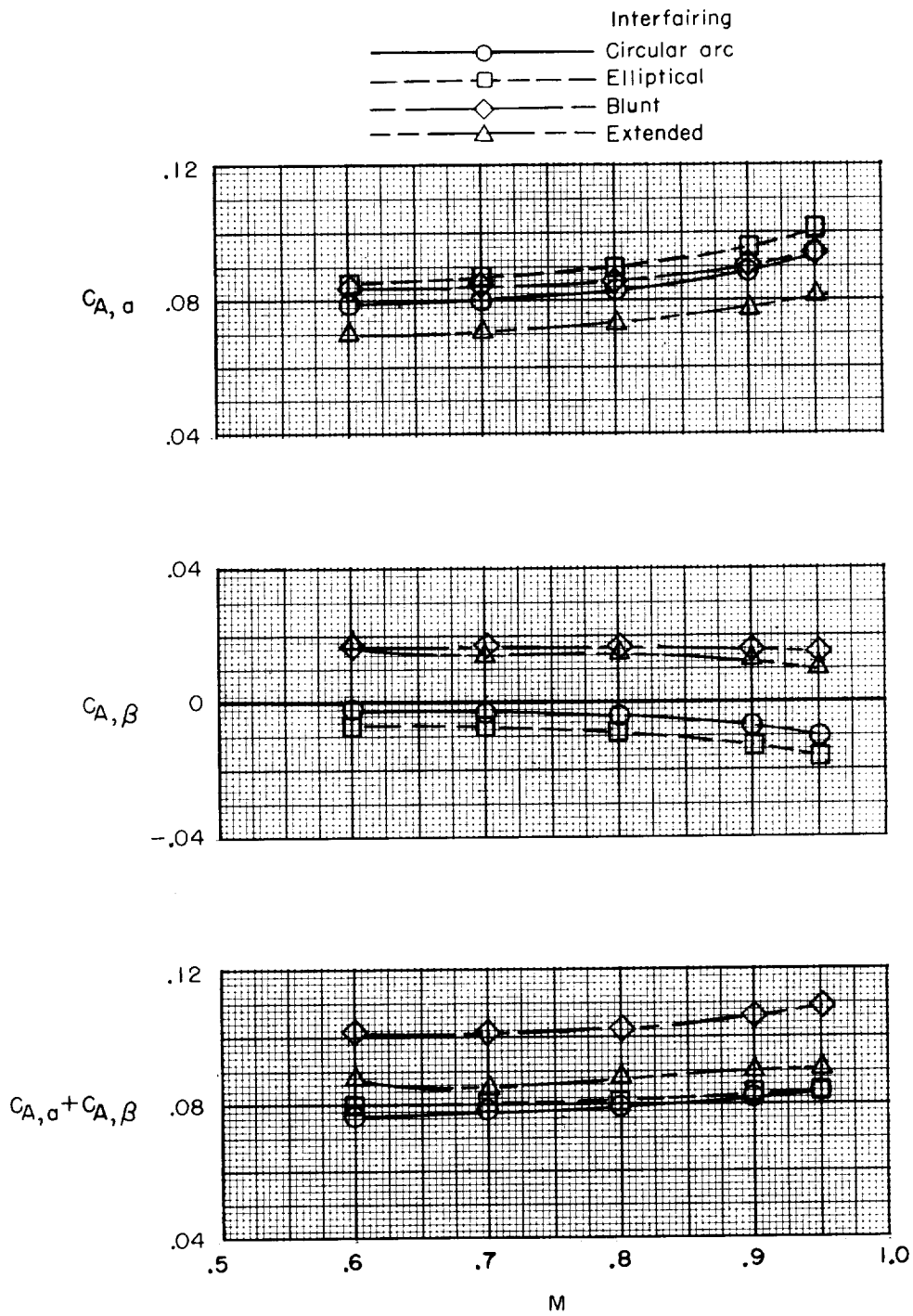
(a) Measurements on top and side of afterbody.

Figure 13.- Boundary-layer velocity profiles for circular-arc interfering and dry iris nozzles with jets off.



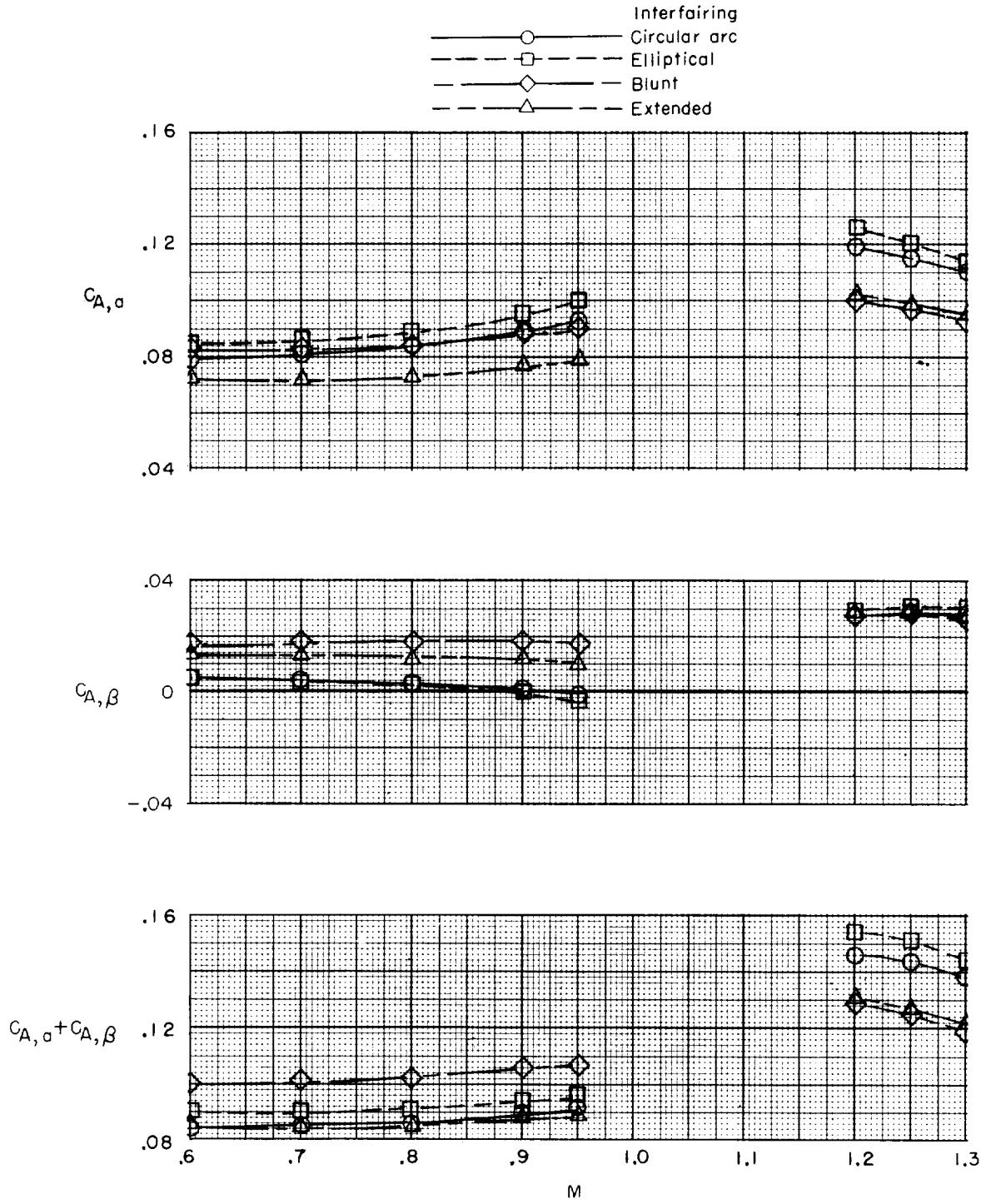
(b) Approximate boundary-layer-profile shapes.

Figure 13.- Concluded.



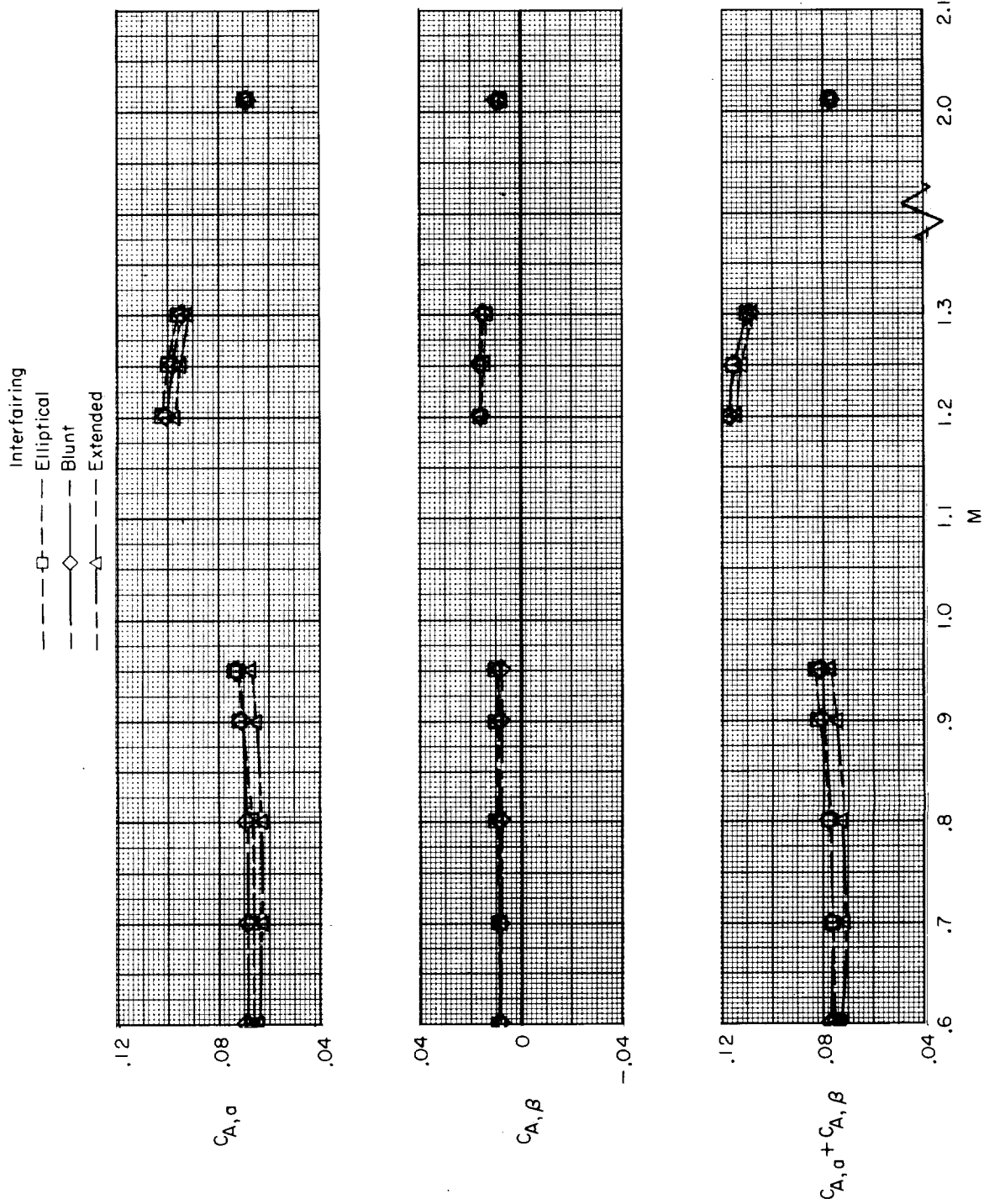
(a) Dry iris nozzles.

Figure 14.- Effect of interfering shape on jet-off axial-force coefficients of configurations with iris nozzles.



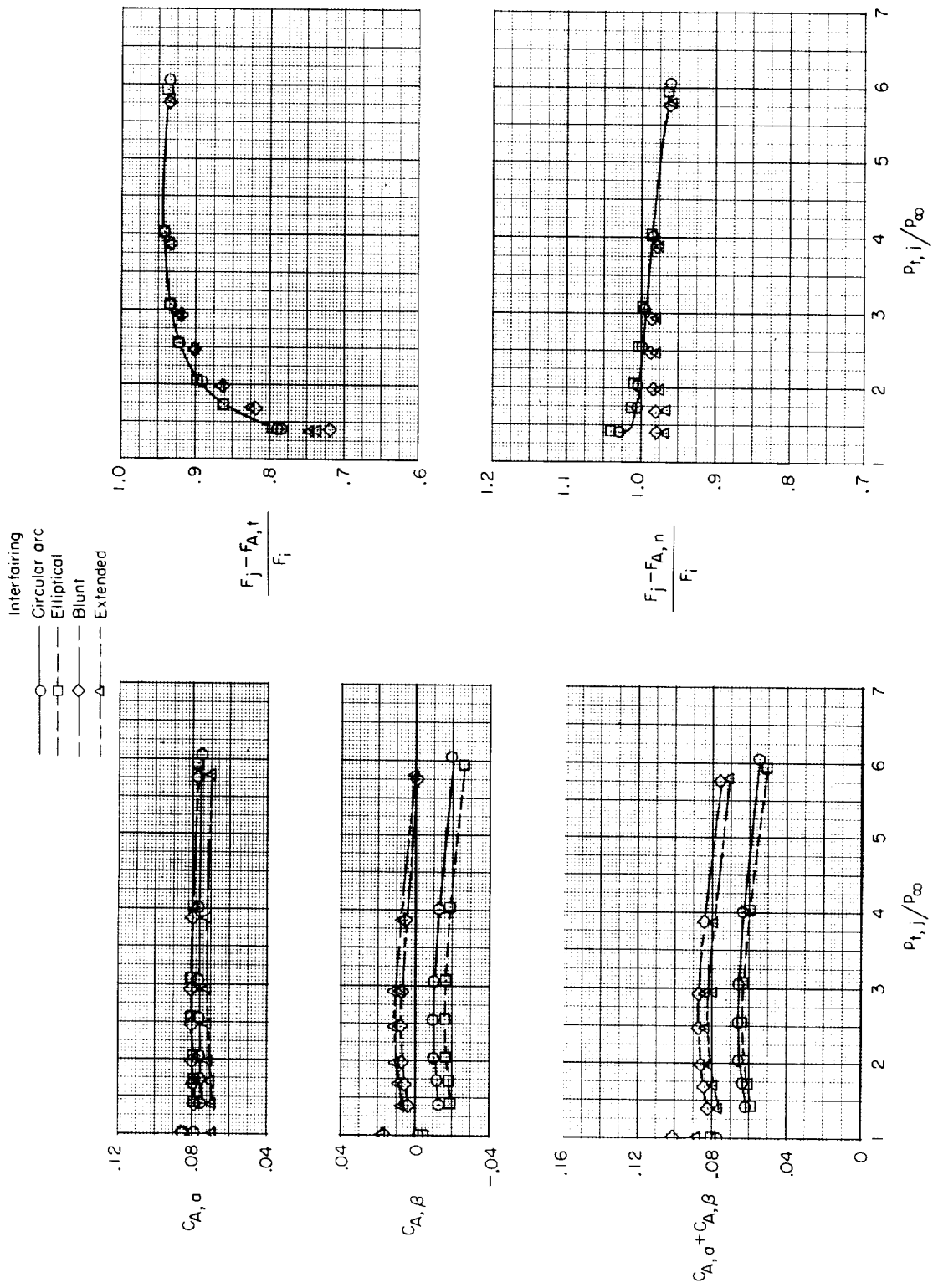
(b) Augmented iris nozzles.

Figure 14.- Continued.



(c) Shrouded-augmented iris nozzles.

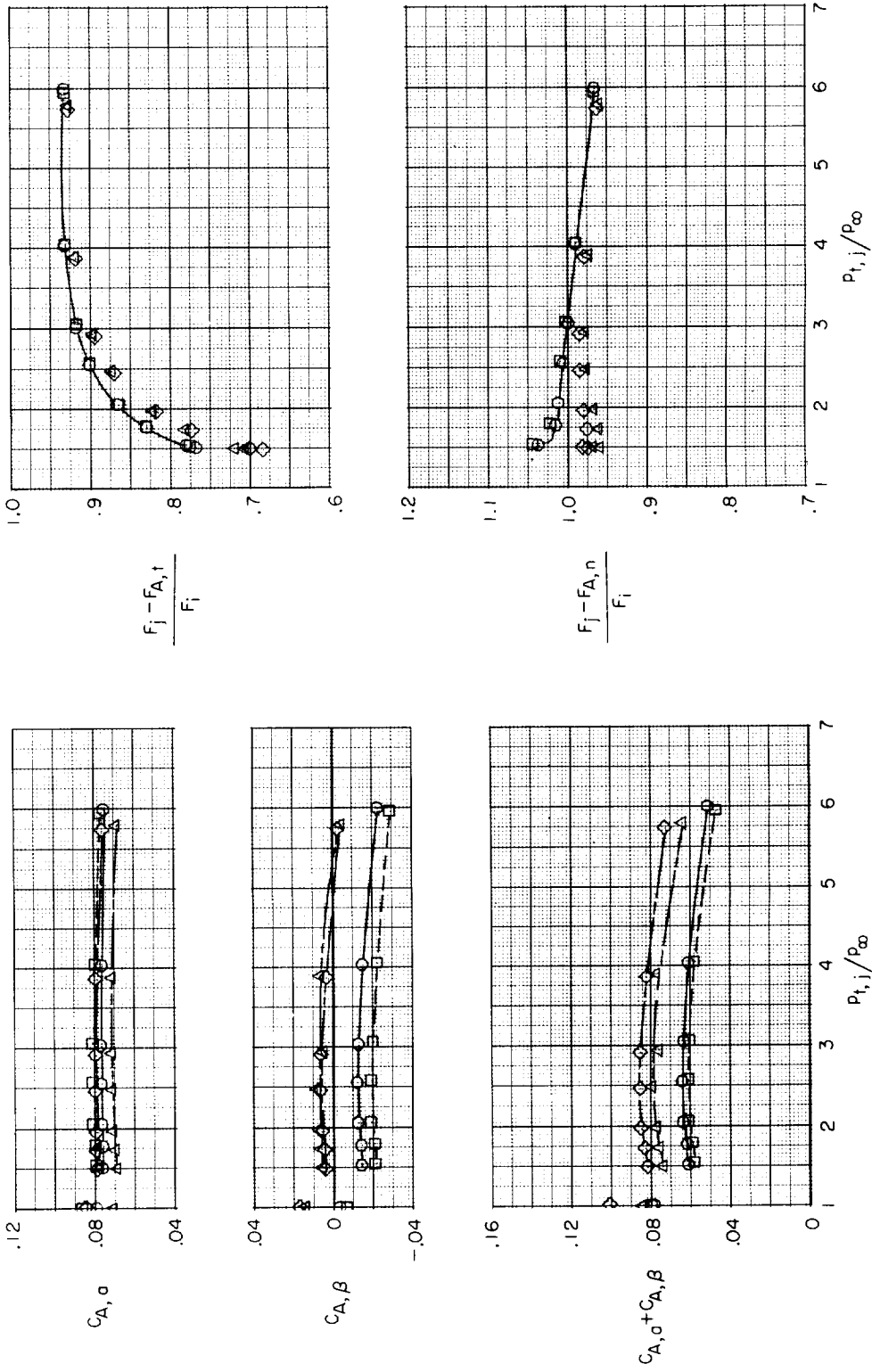
Figure 14.- Concluded.



(a) $M = 0.60$.

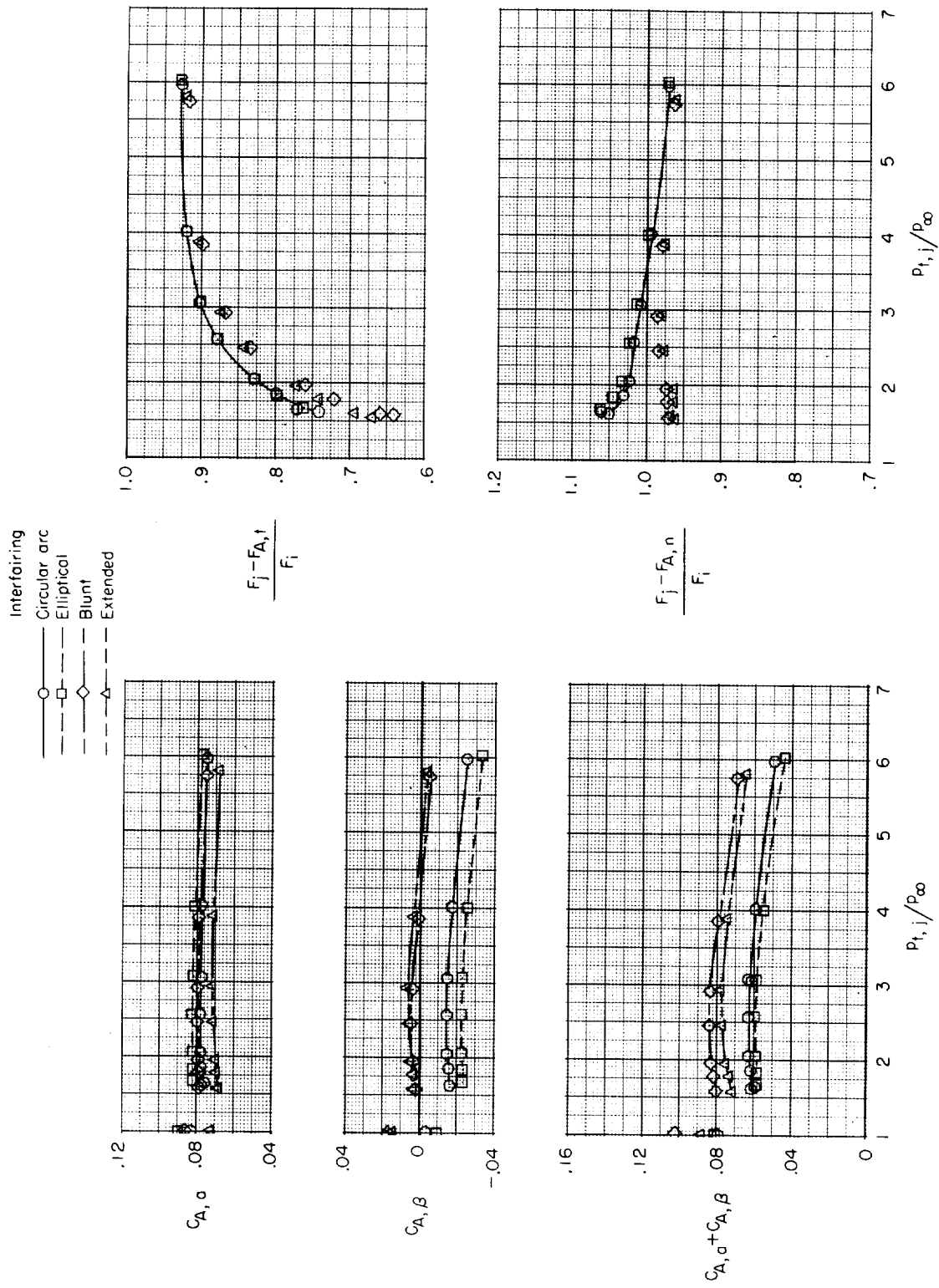
Figure 15.- Effect of interfairing shape on performance of configurations with dry iris nozzles.

Interfering
 Circular arc
 Elliptical
 Blunt
 Extended



(b) $M = 0.70$.

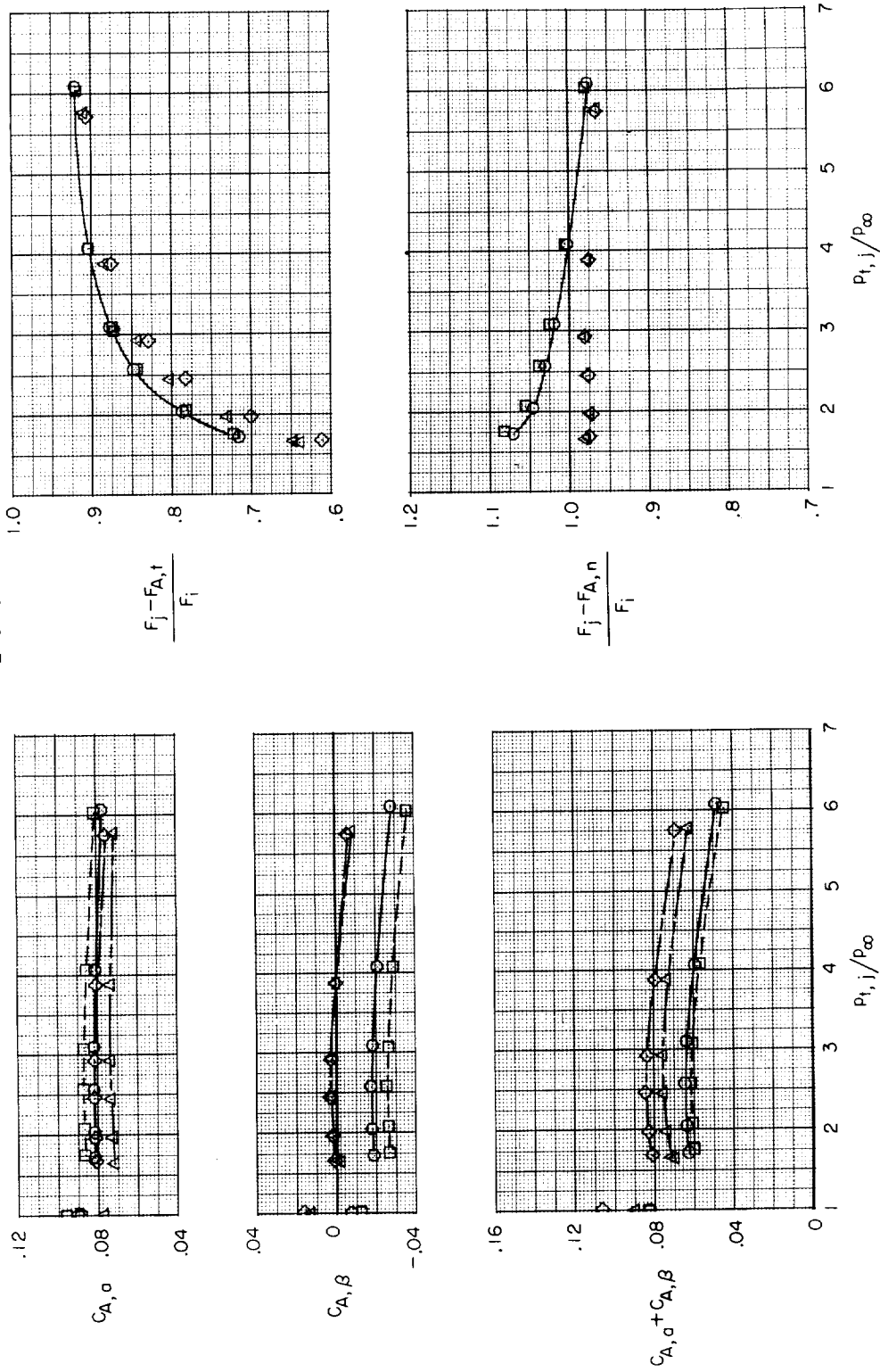
Figure 15.- Continued.



(c) $M = 0.80$.

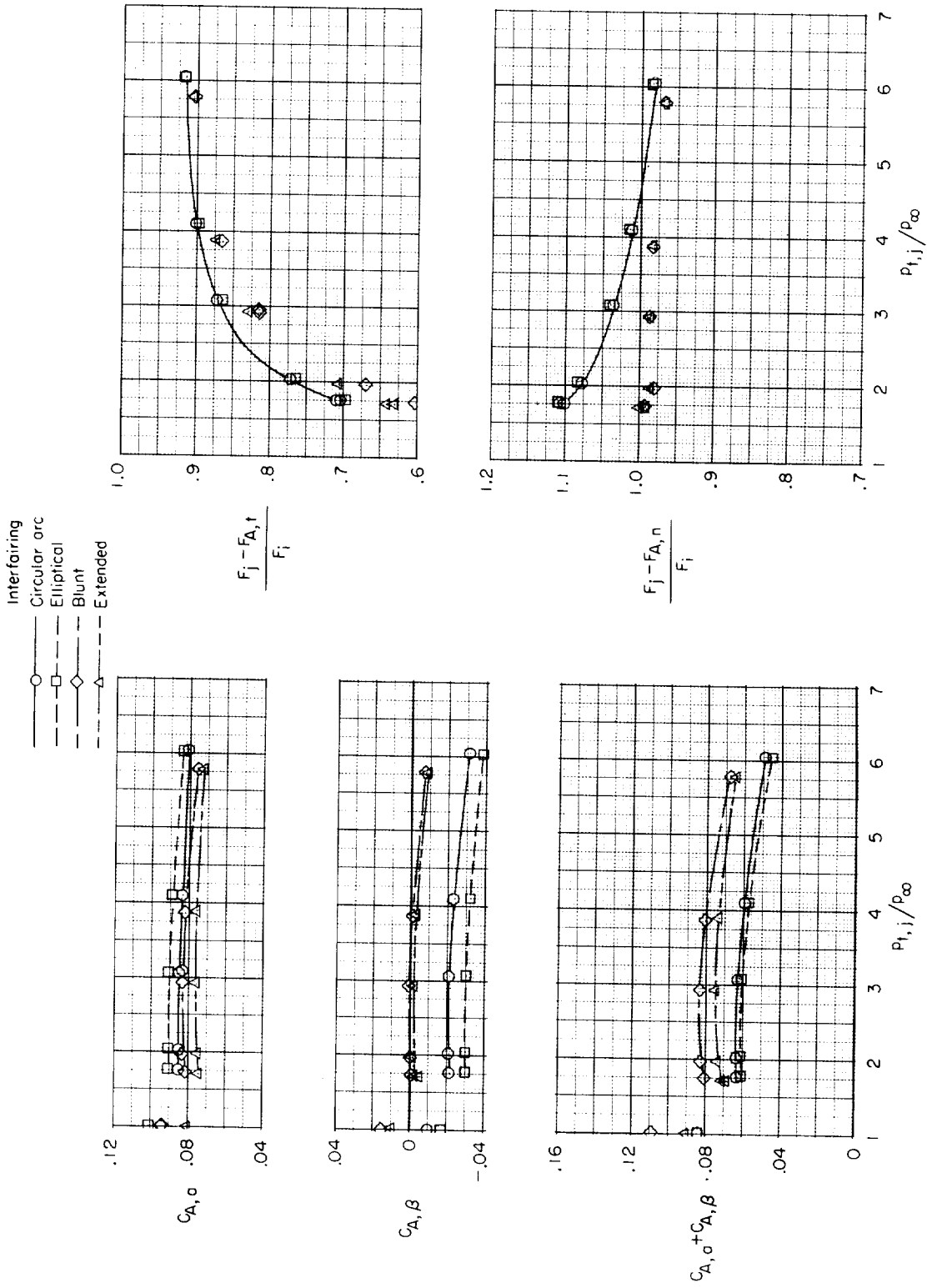
Figure 15.- Continued.

- Interfairing
- Circular arc
- Elliptical
- ◇— Blunt
- △— Extended



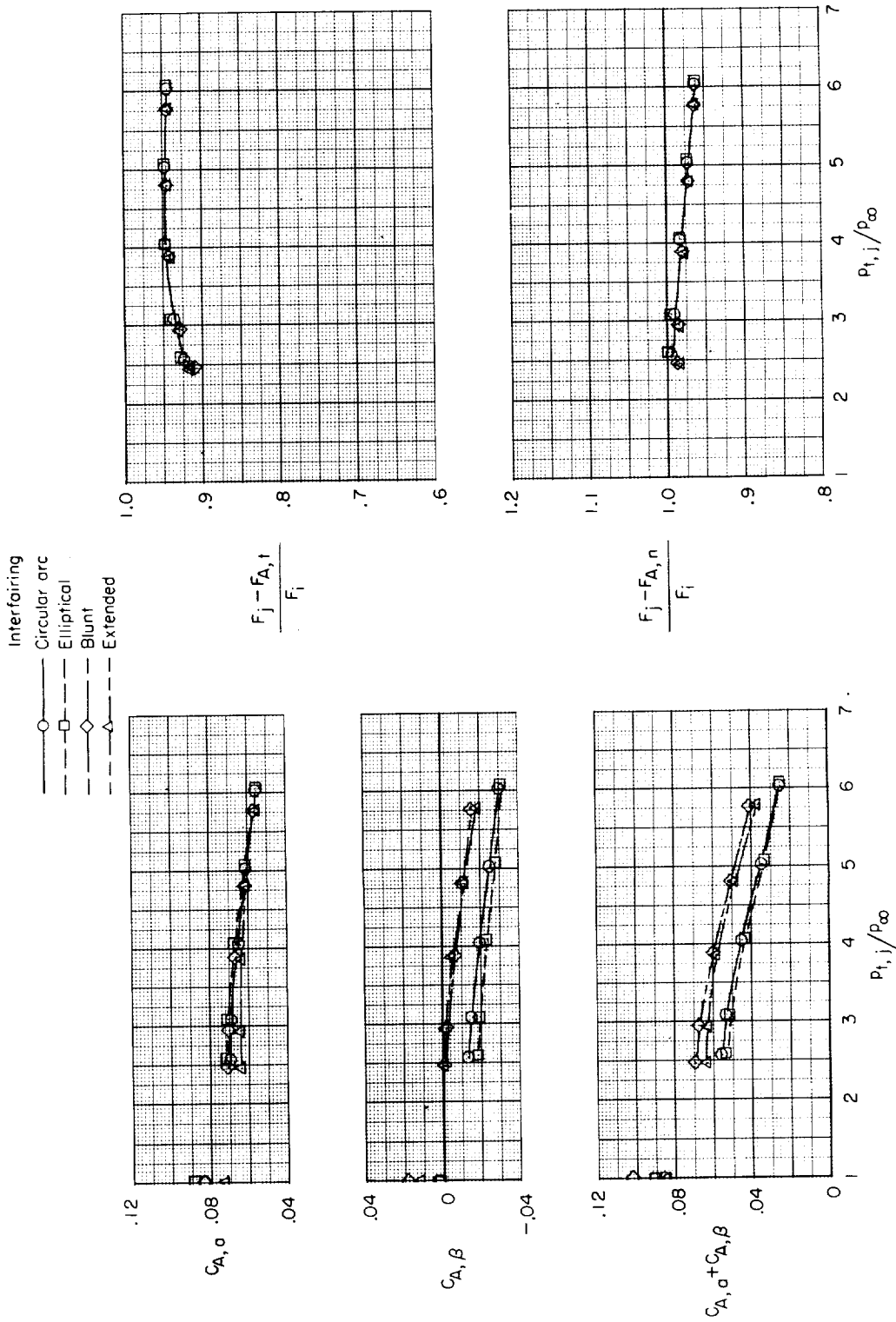
(d) $M = 0.90$.

Figure 15.- Continued.



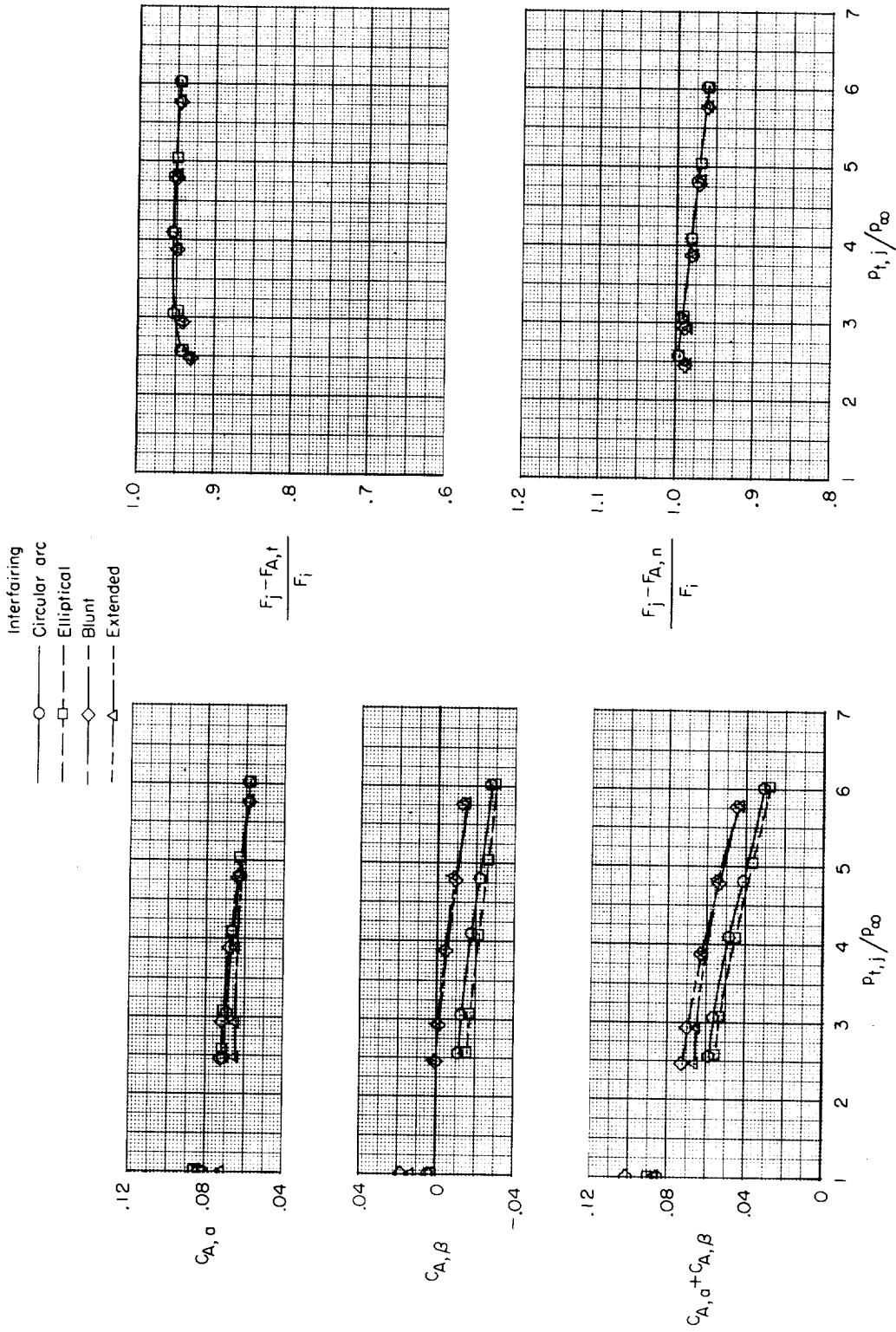
(e) $M = 0.95$.

Figure 15.- Concluded.



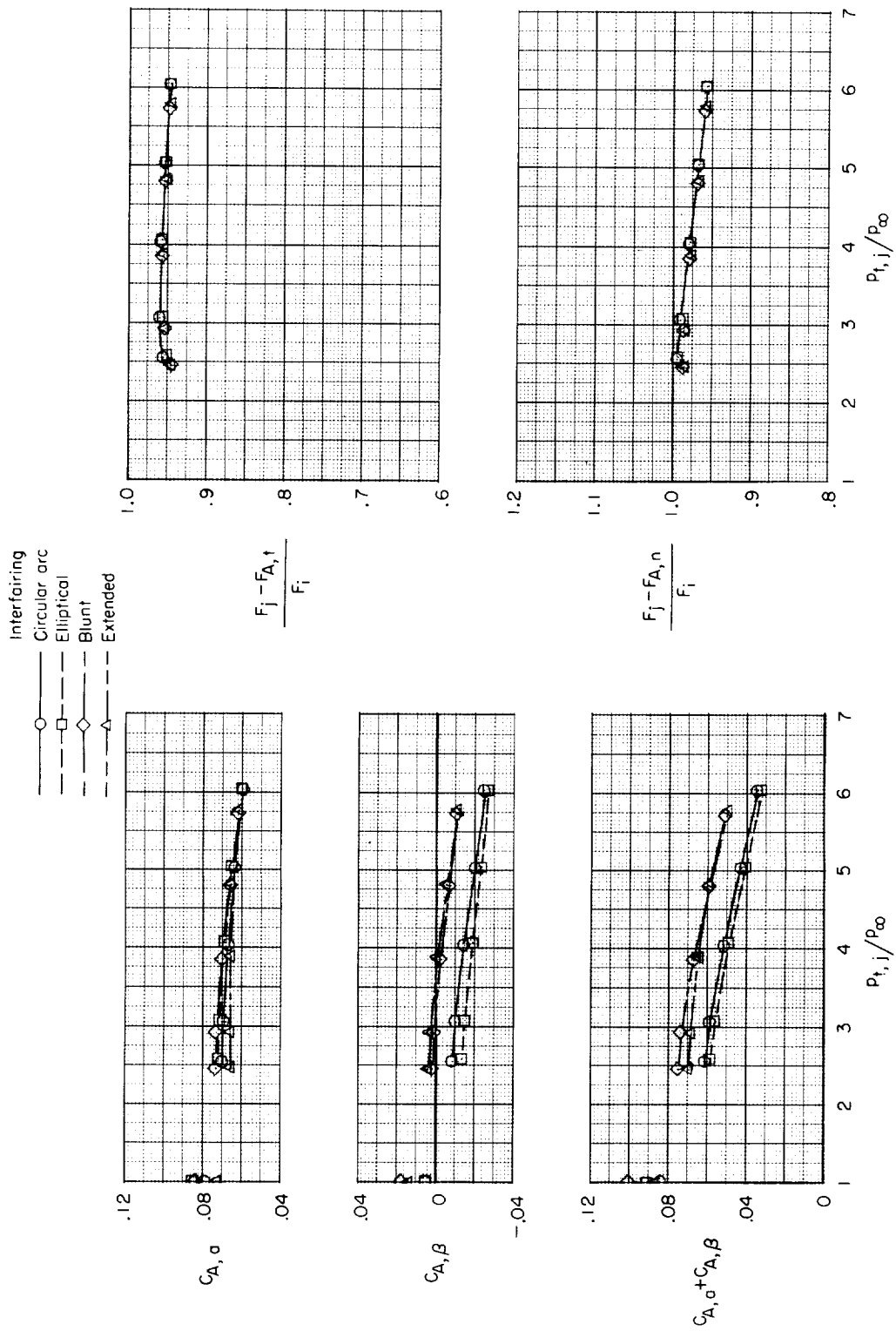
(a) $M = 0.60$.

Figure 16.- Effect of interfairing shape on performance of configurations with augmented iris nozzles.



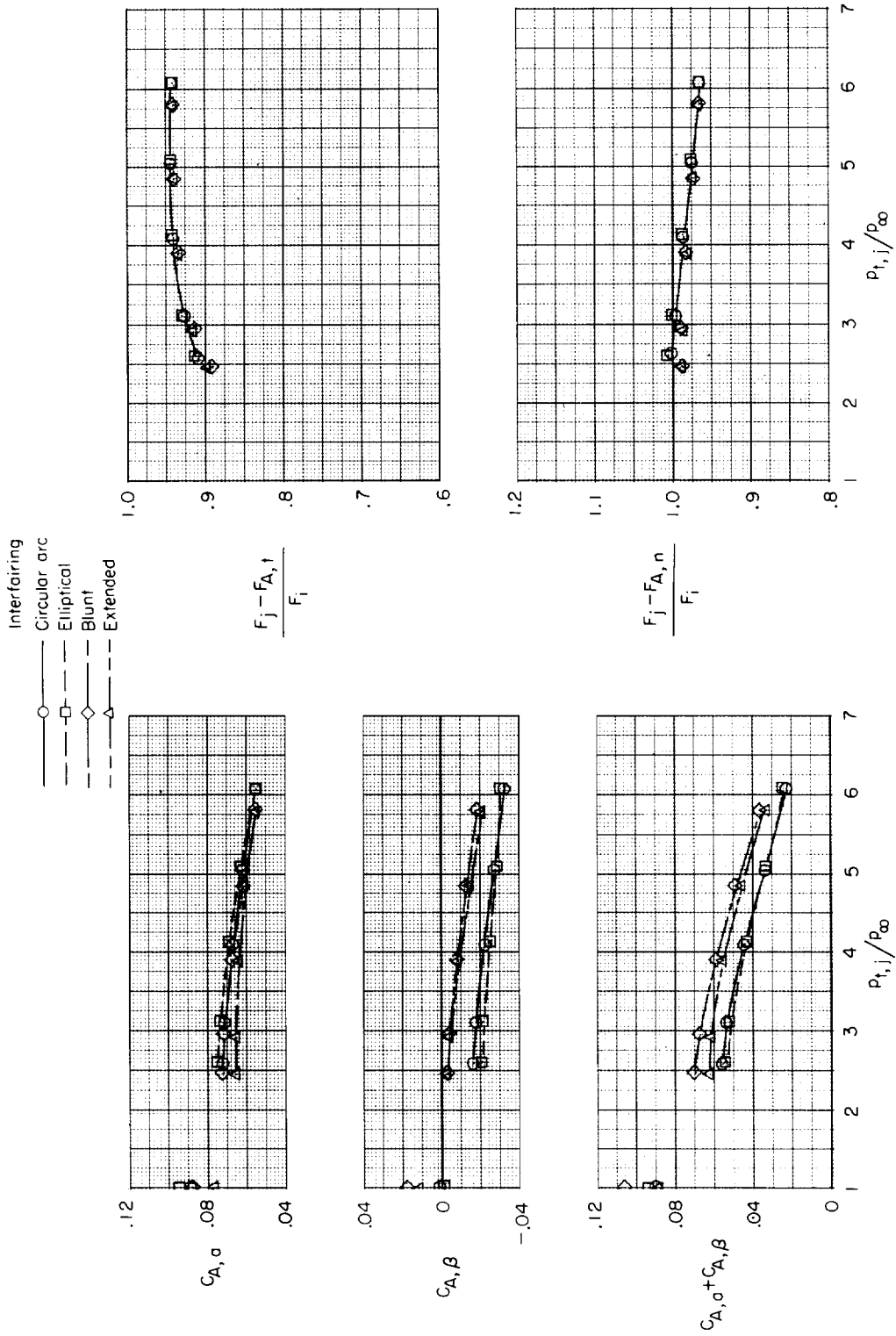
(b) $M = 0.70$.

Figure 16.- Continued.



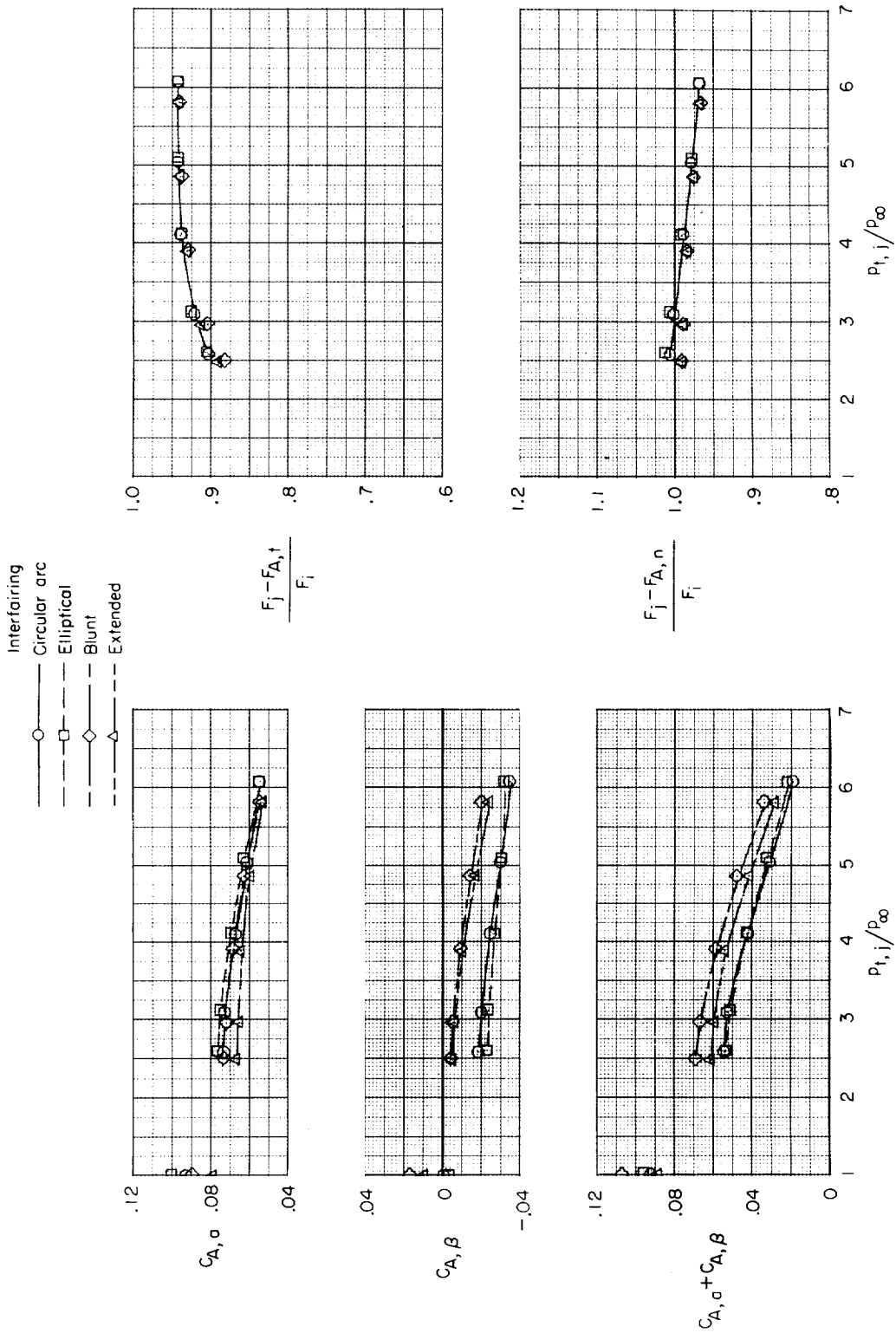
(c) $M = 0.80$.

Figure 16.- Continued.



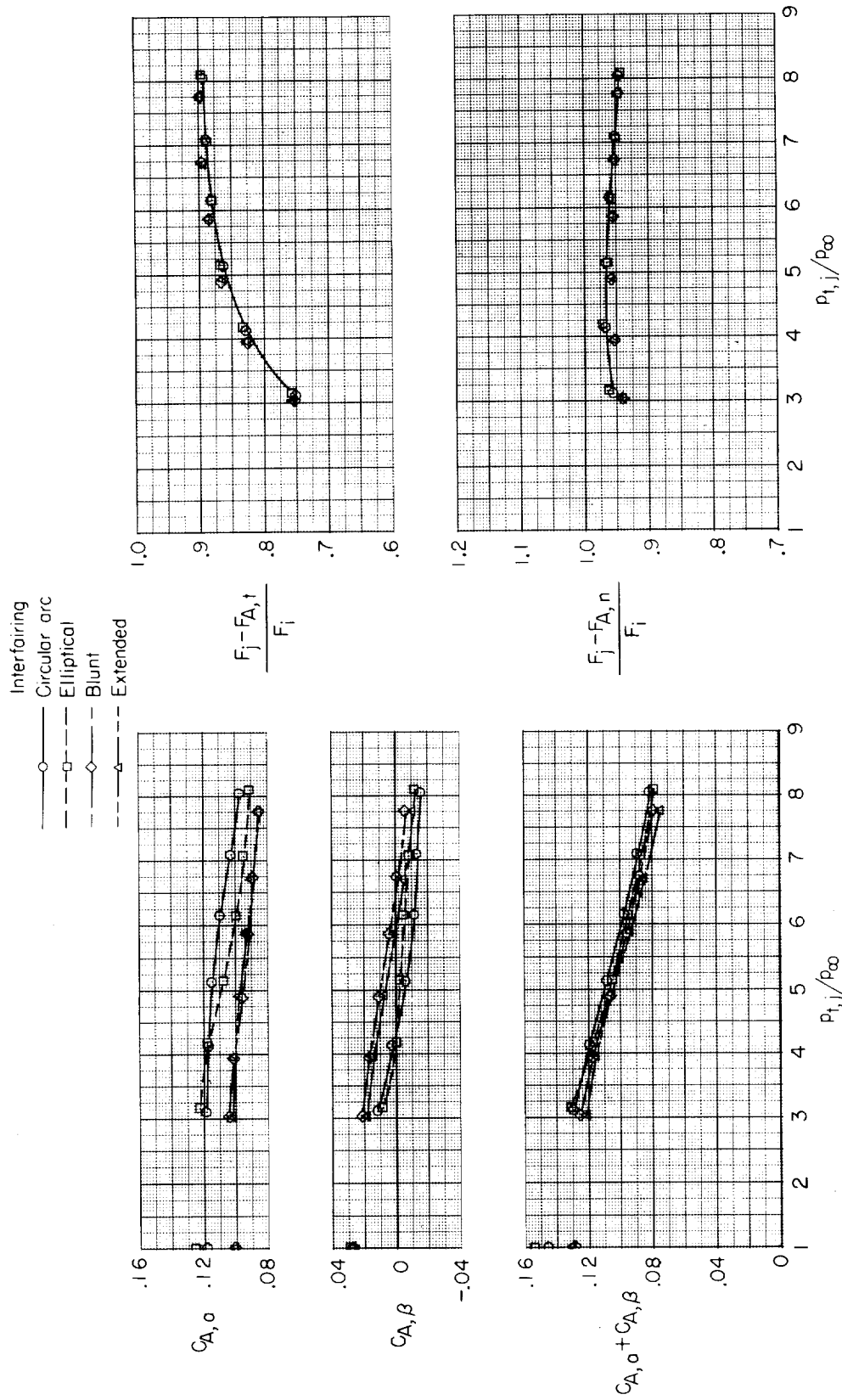
(d) $M = 0.90$.

Figure 16.- Continued.



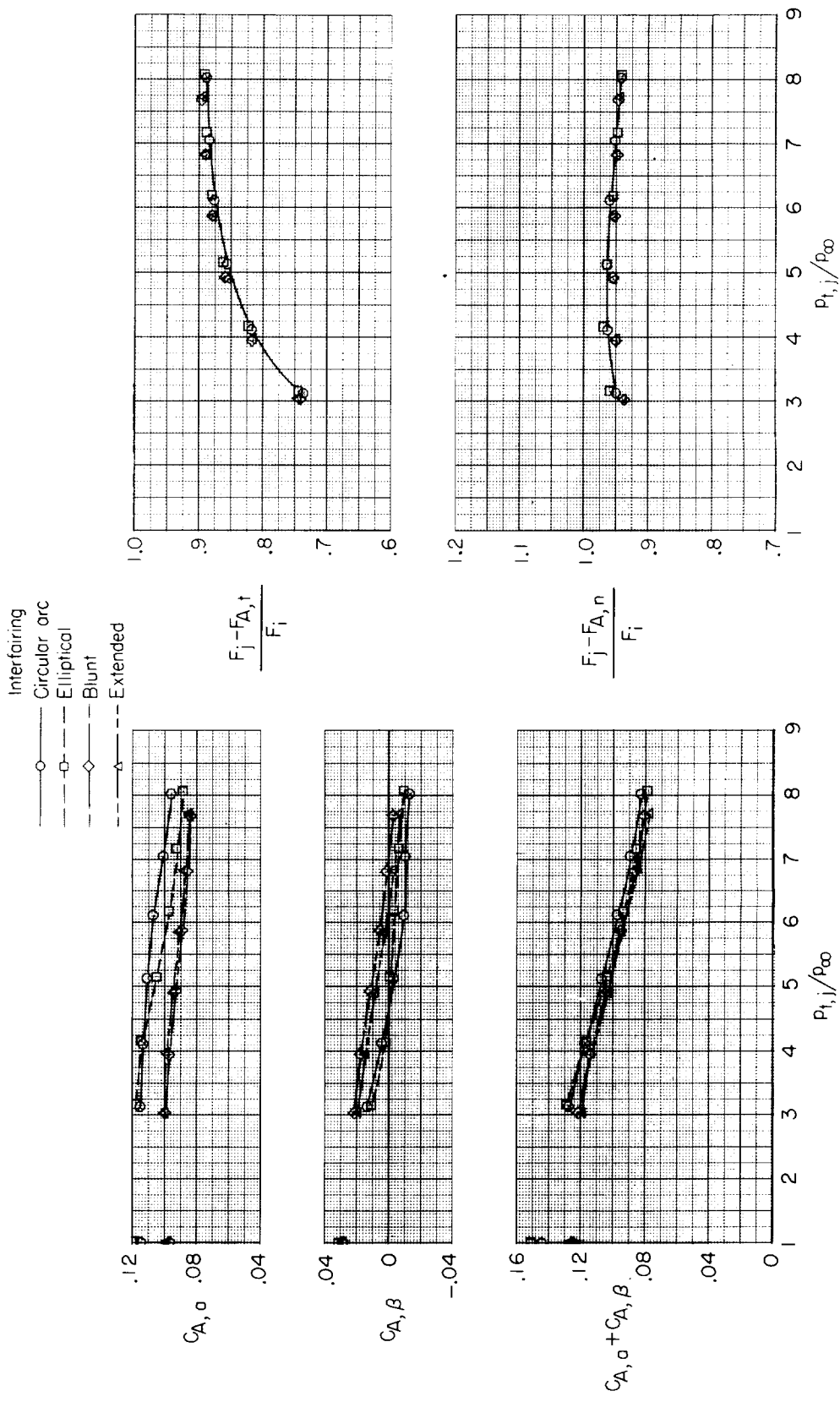
(e) $M = 0.95$.

Figure 16.- Continued.



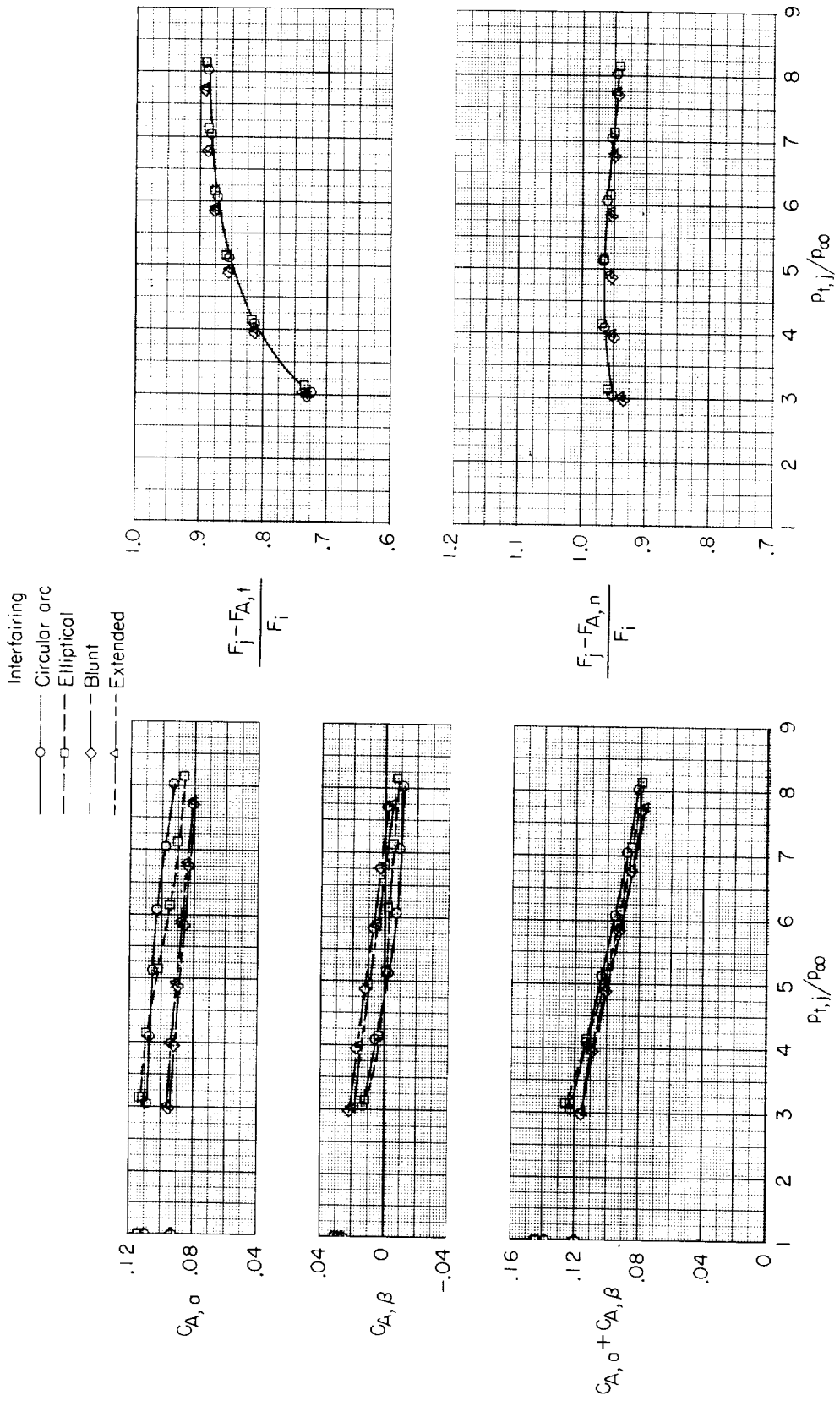
(f) $M = 1.20$.

Figure 16.- Continued.



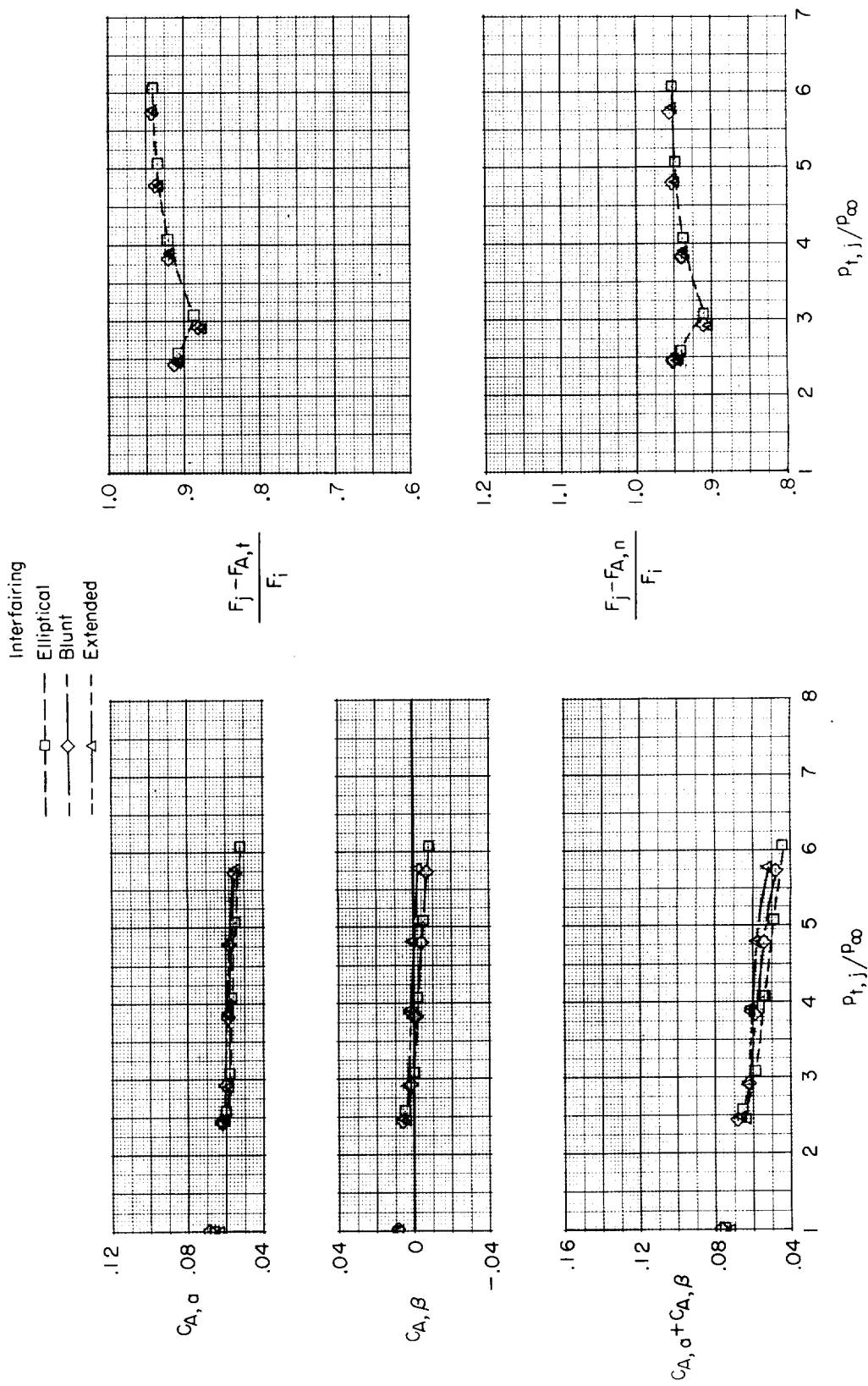
(g) $M = 1.25$.

Figure 16.- Continued.



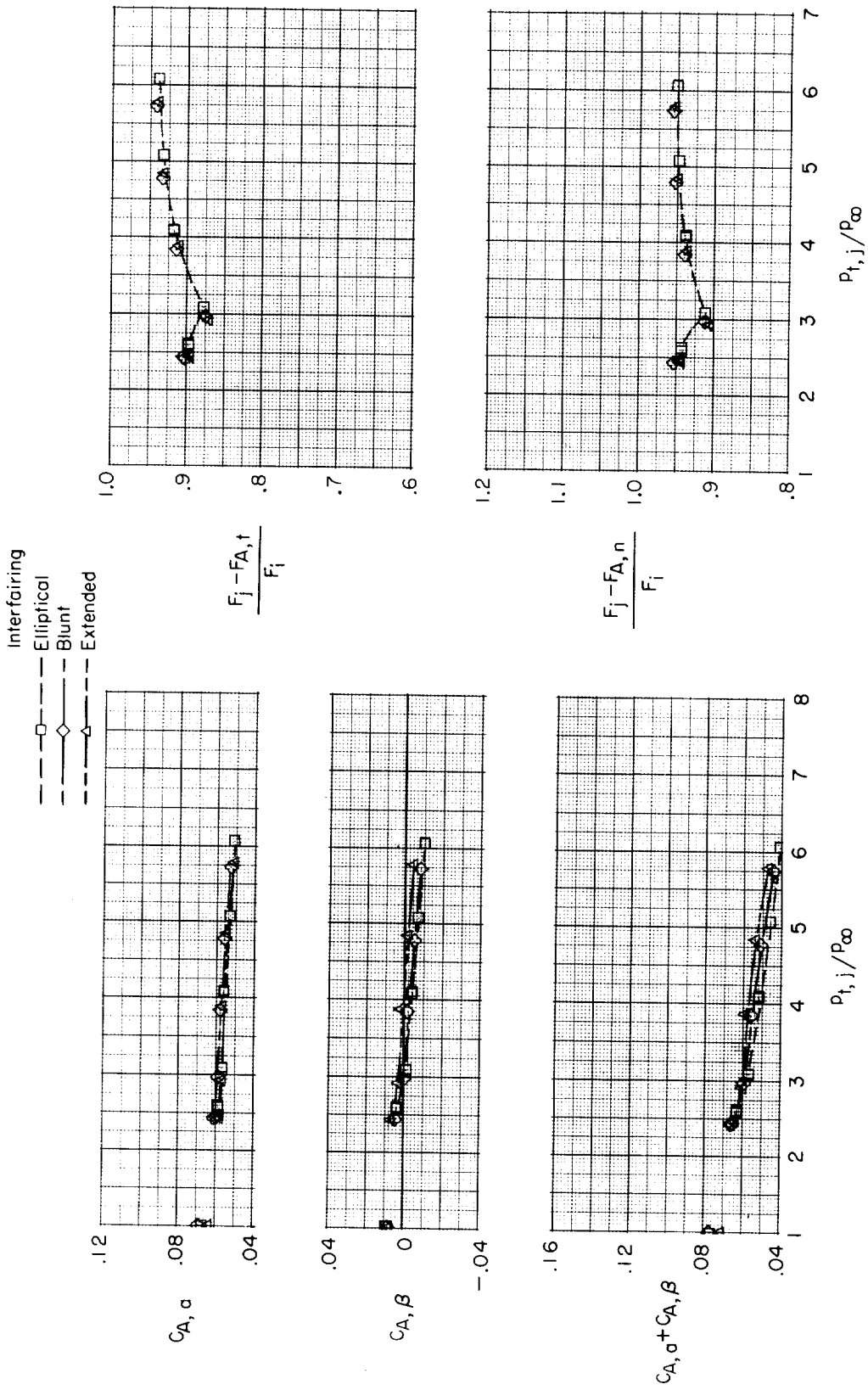
(h) $M = 1.30$.

Figure 16.- Concluded.



(a) $M = 0.60$.

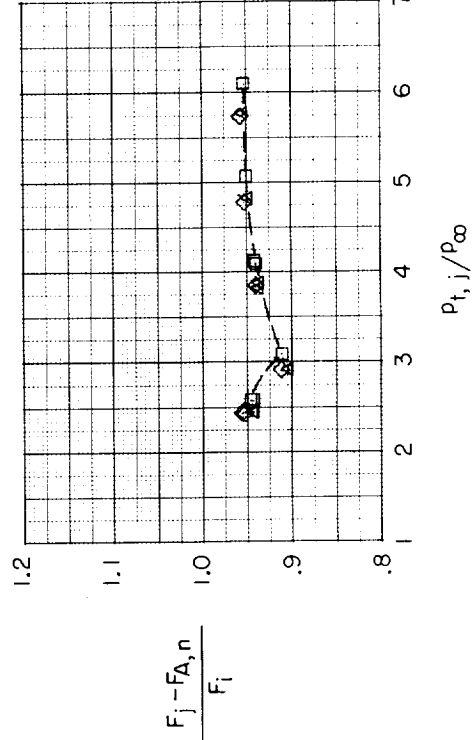
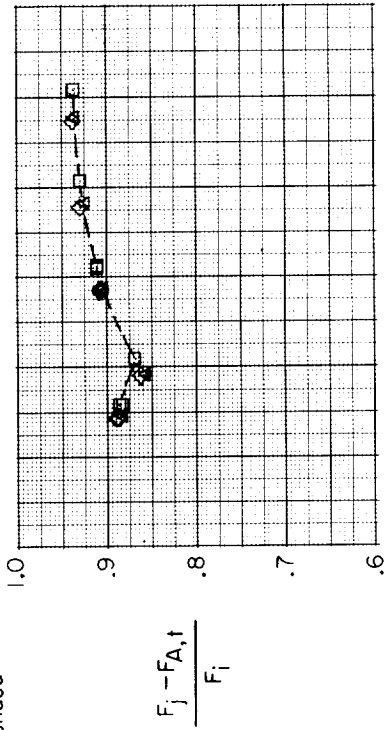
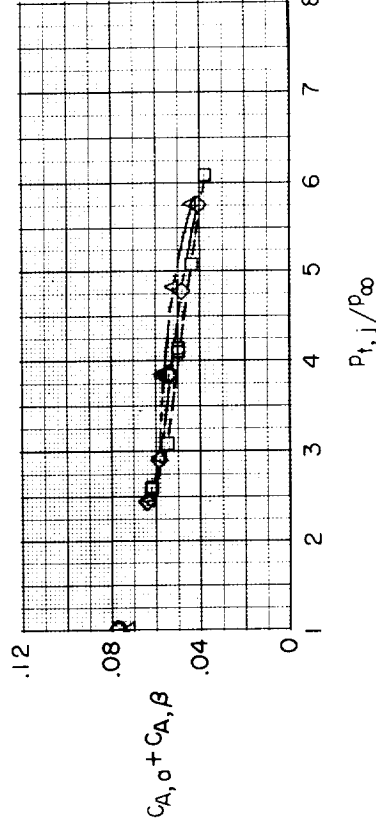
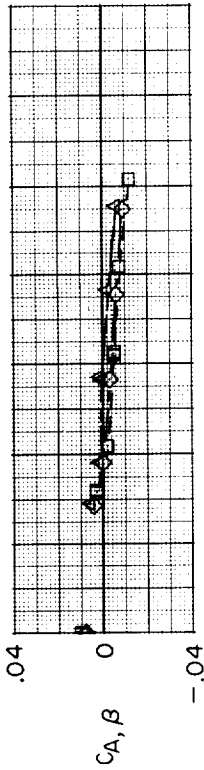
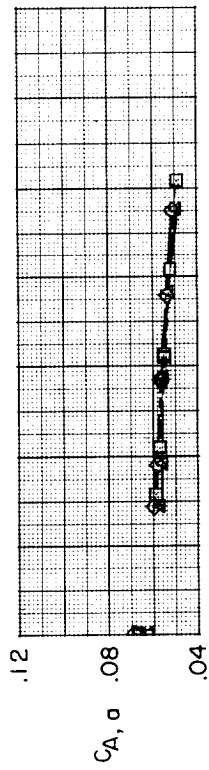
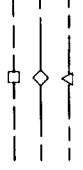
Figure 17.- Performance of afterbodies with shrouded-augmented iris nozzles and various interfairings.



(b) $M = 0.70$.

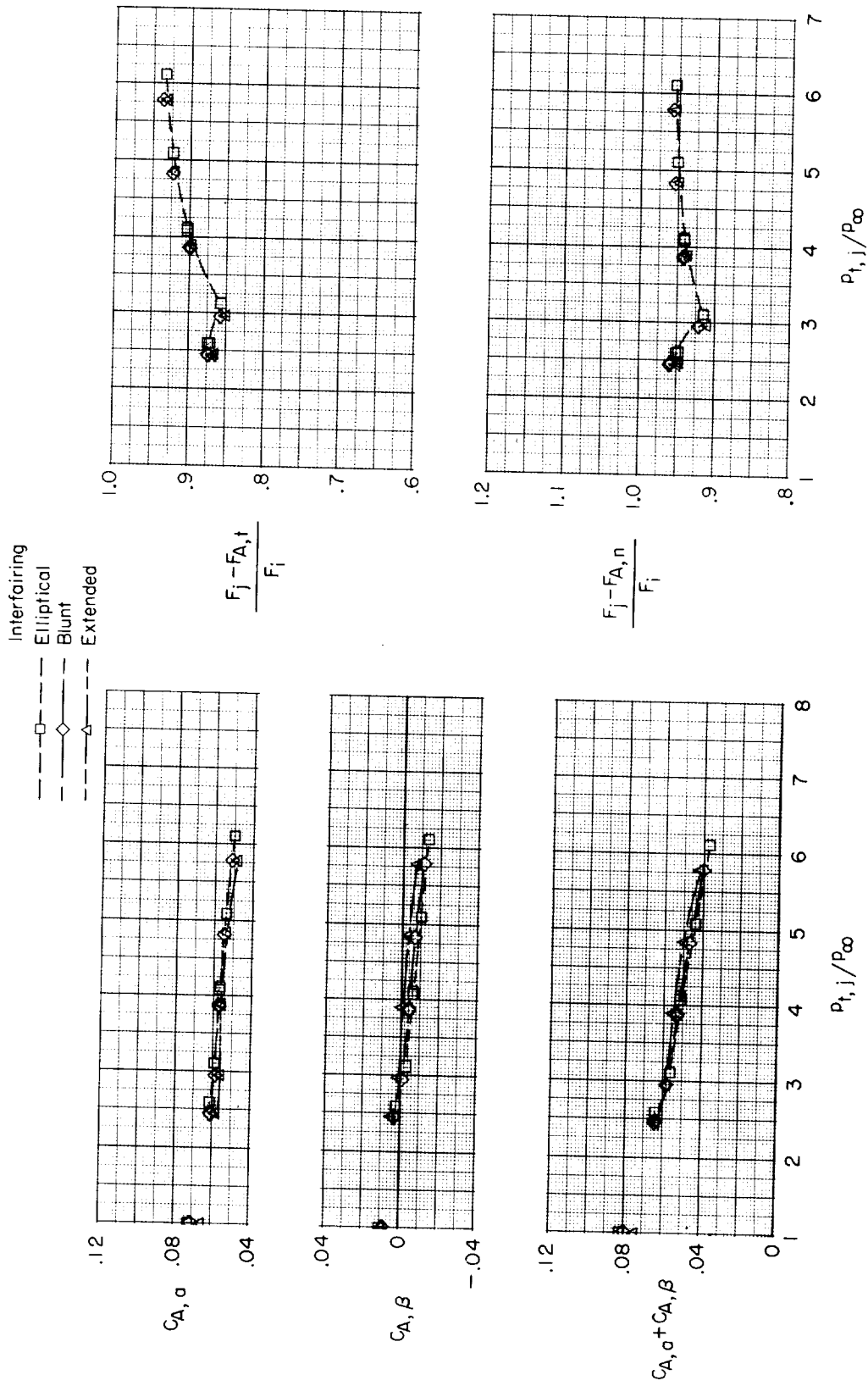
Figure 17.- Continued.

Interfering
 Elliptical
 Blunt
 Extended



(c) $M = 0.80$.

Figure 17.-- Continued.



(d) $M = 0.90$.

Figure 17.- Continued.

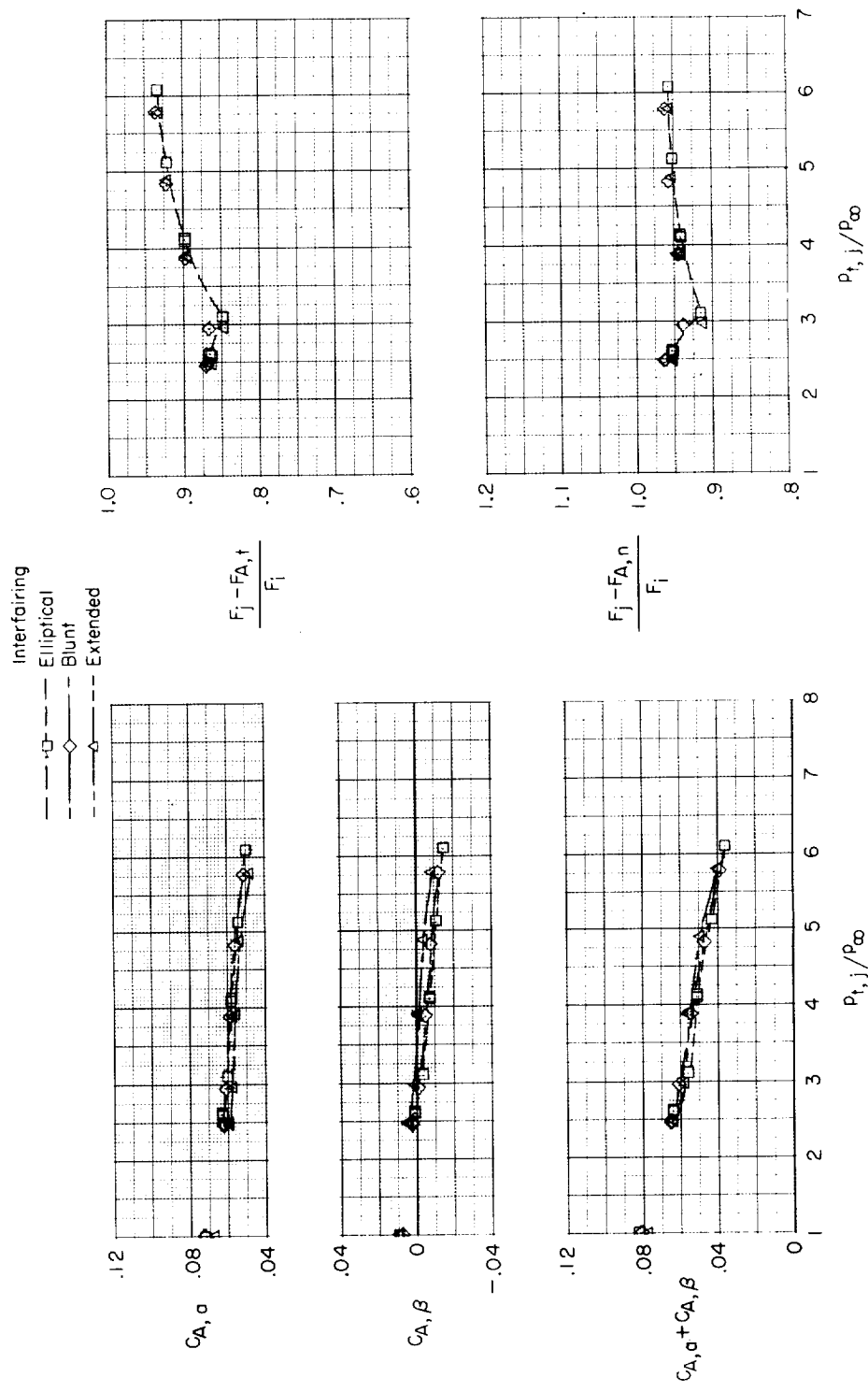


Figure 17.- Continued.

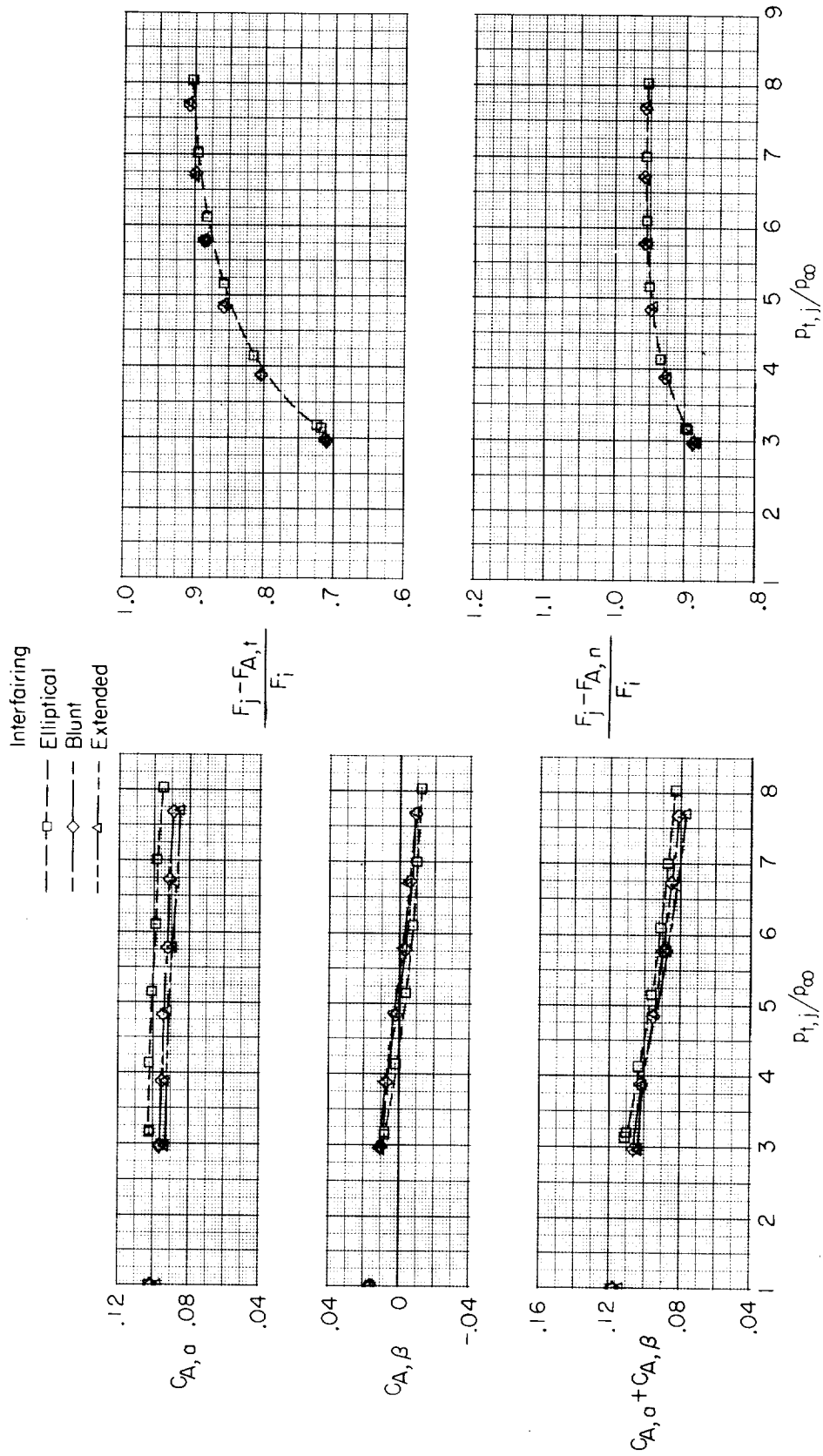
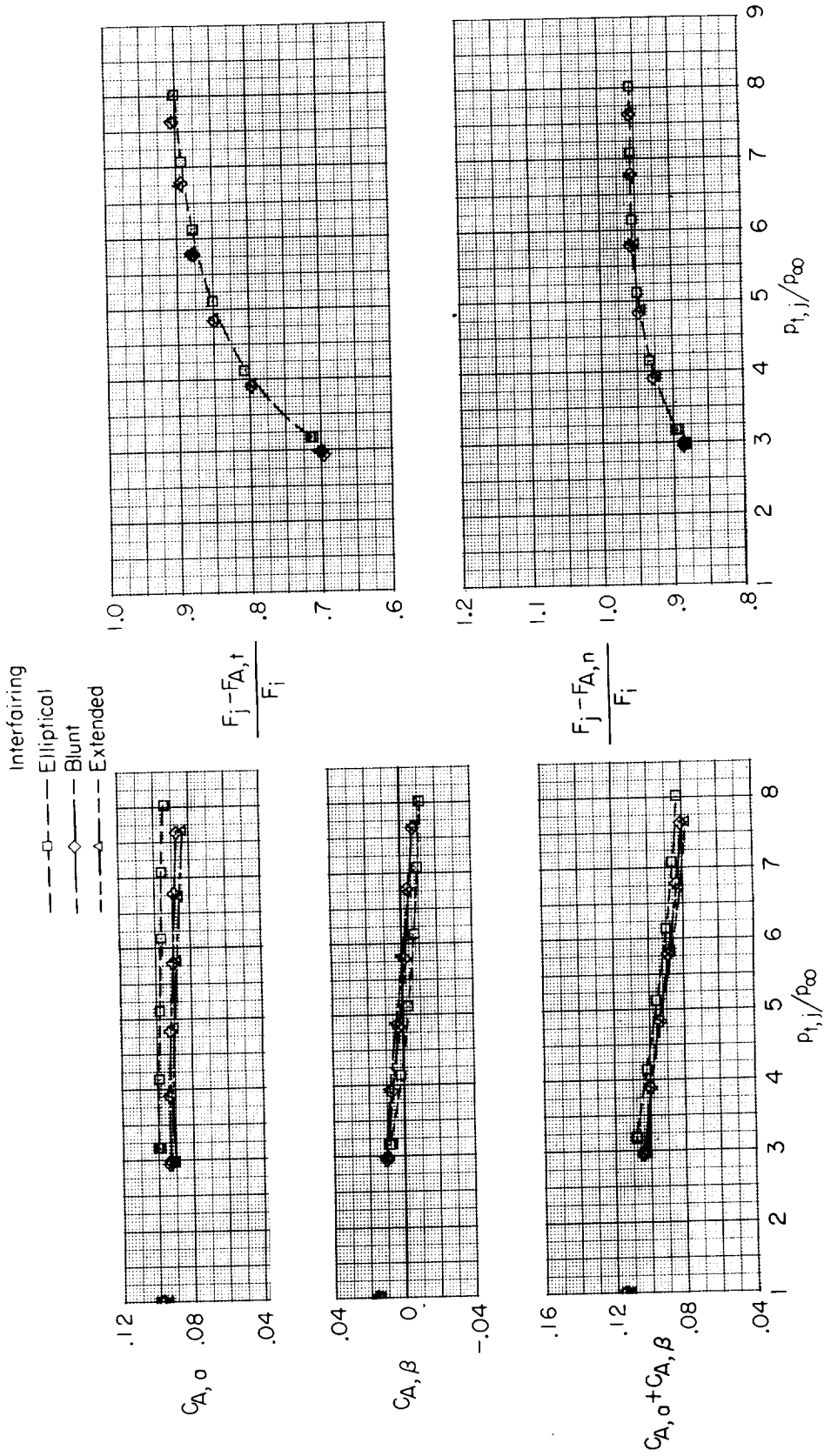
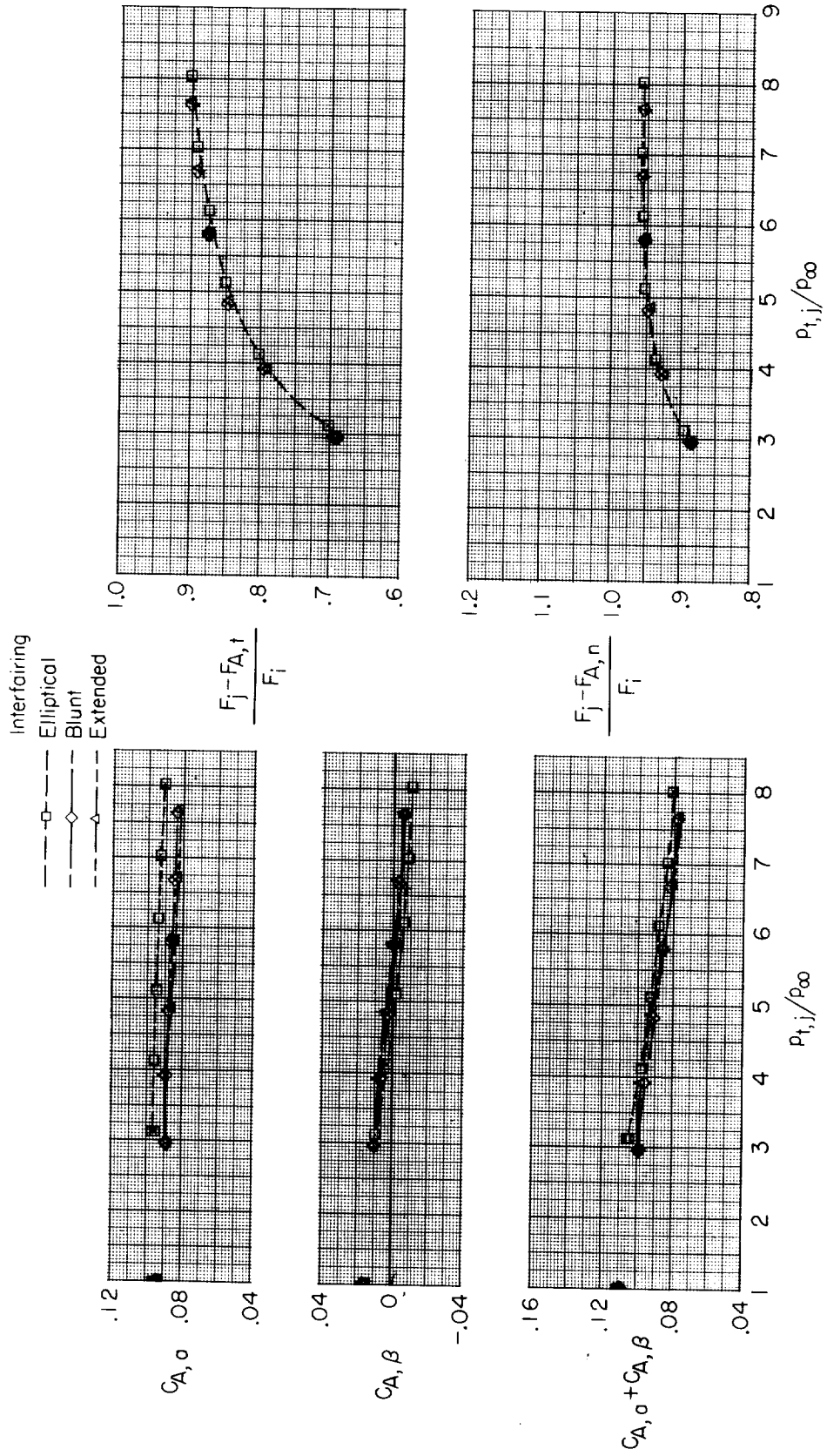


Figure 17.- Continued.



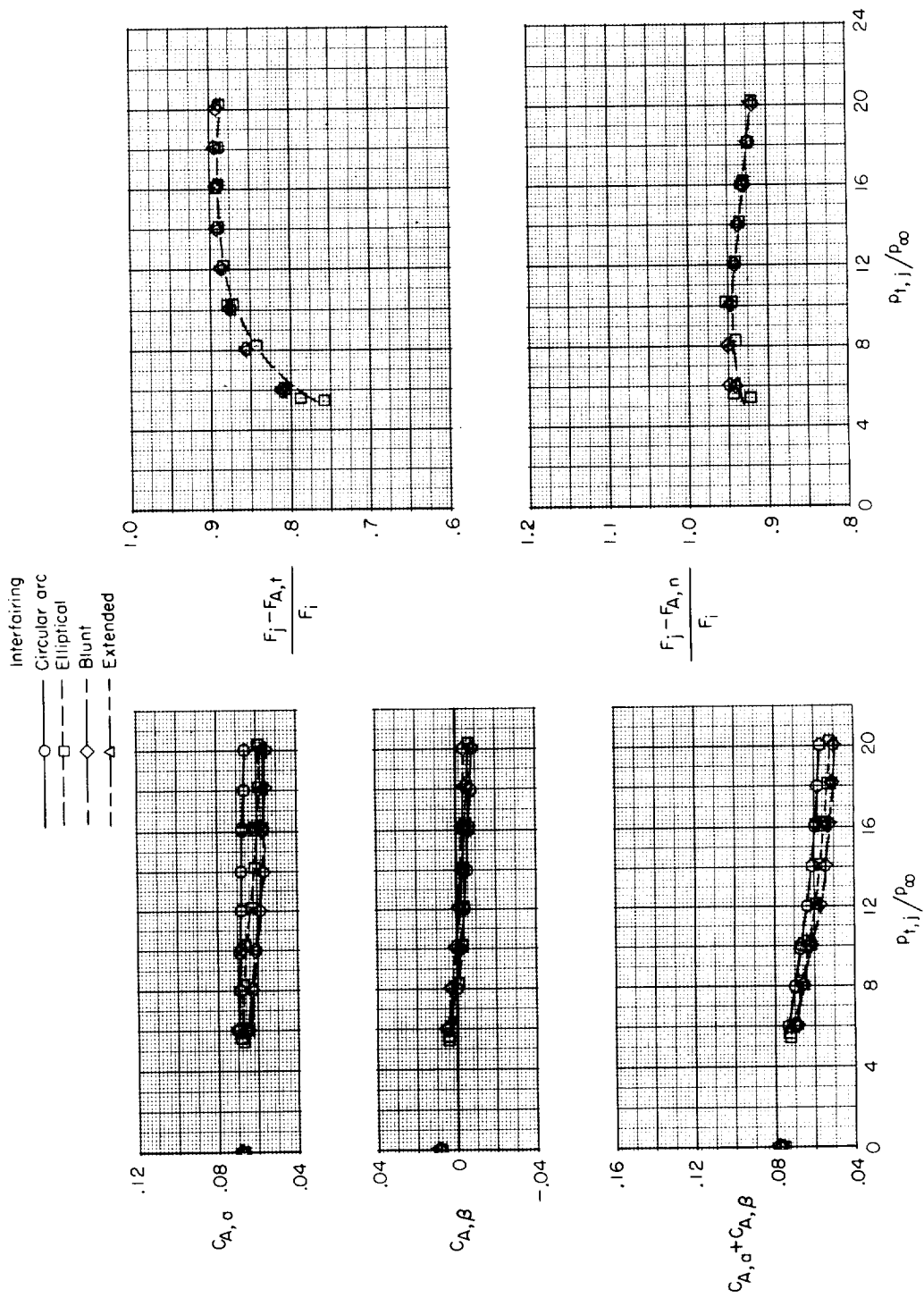
(g) $M = 1.25$.

Figure 17.- Continued.



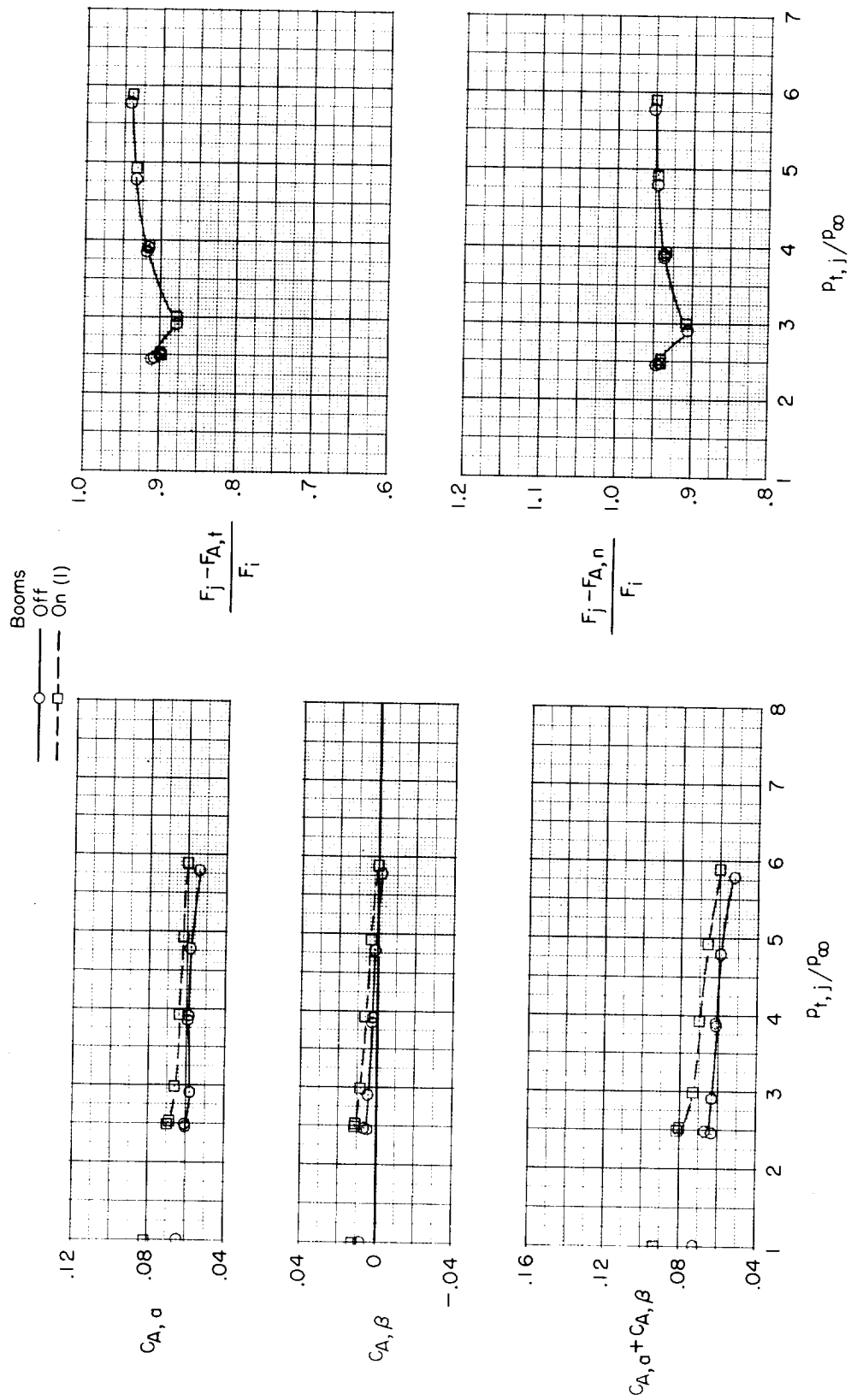
(h) $M = 1.30$.

Figure 17.-- Continued.



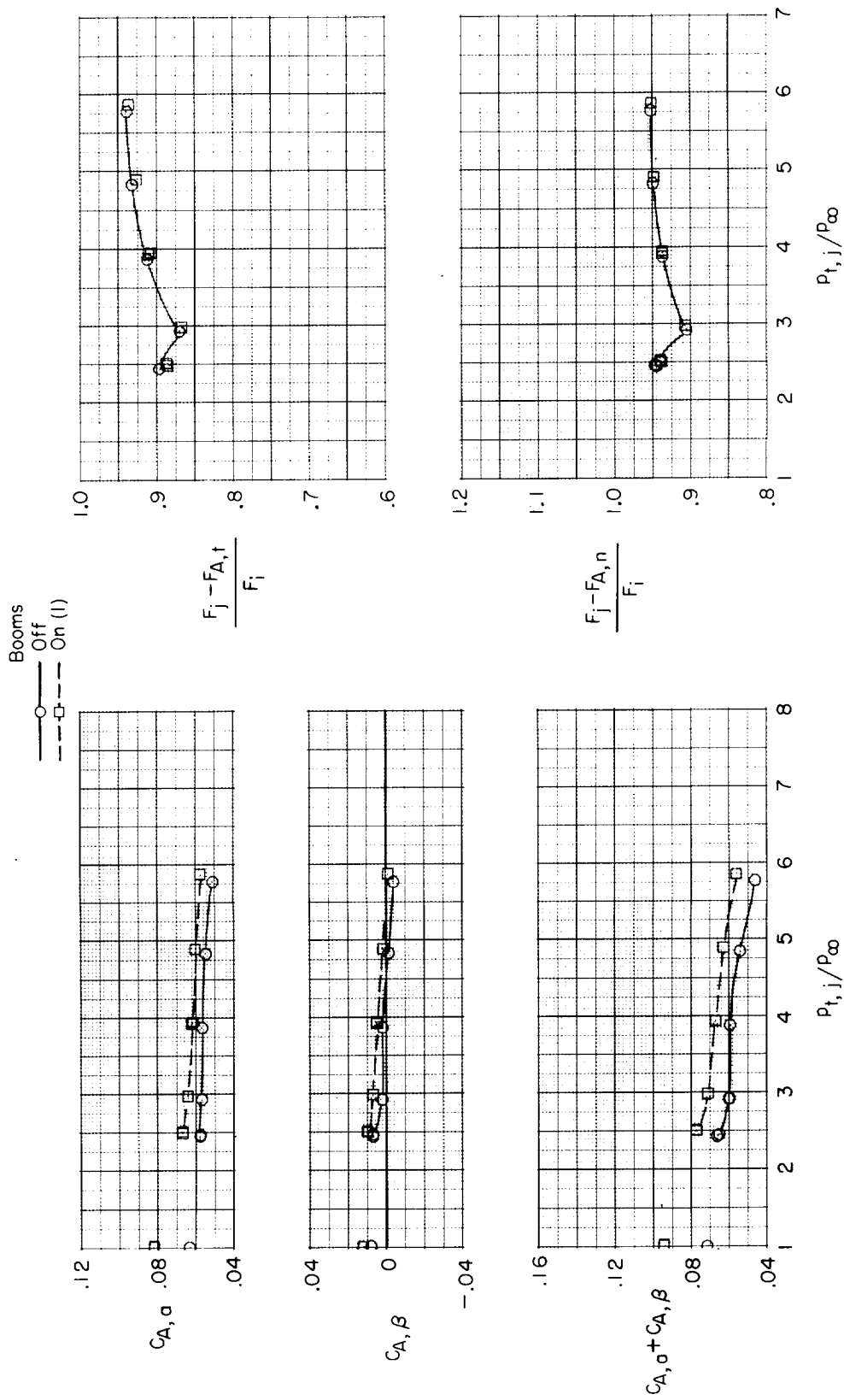
(i) $M = 2.01$.

Figure 17.- Concluded.



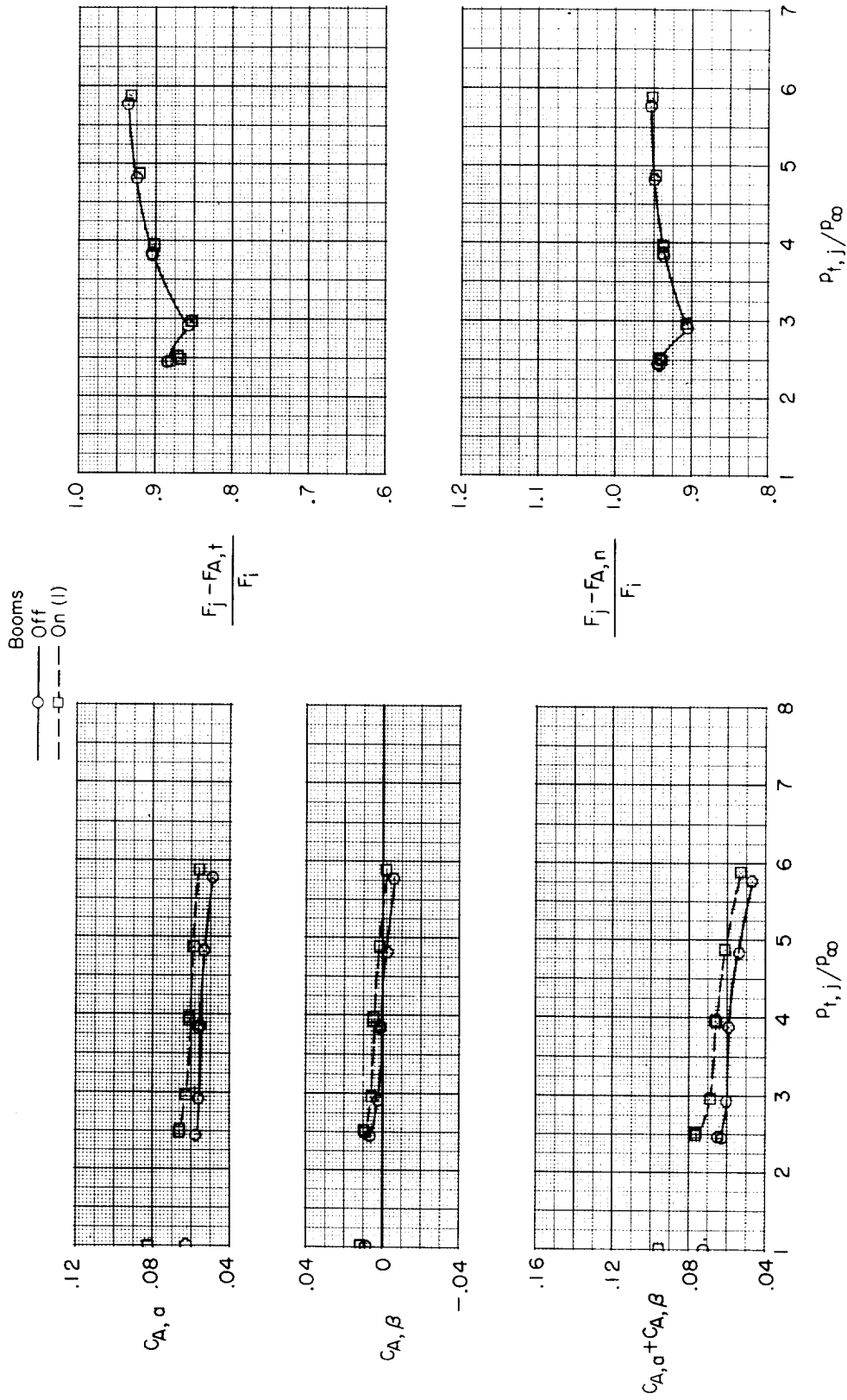
(a) $M = 0.60$.

Figure 18.- Effect of tail booms on performance of afterbody with extended interfering and shrouded-augmented iris nozzles.



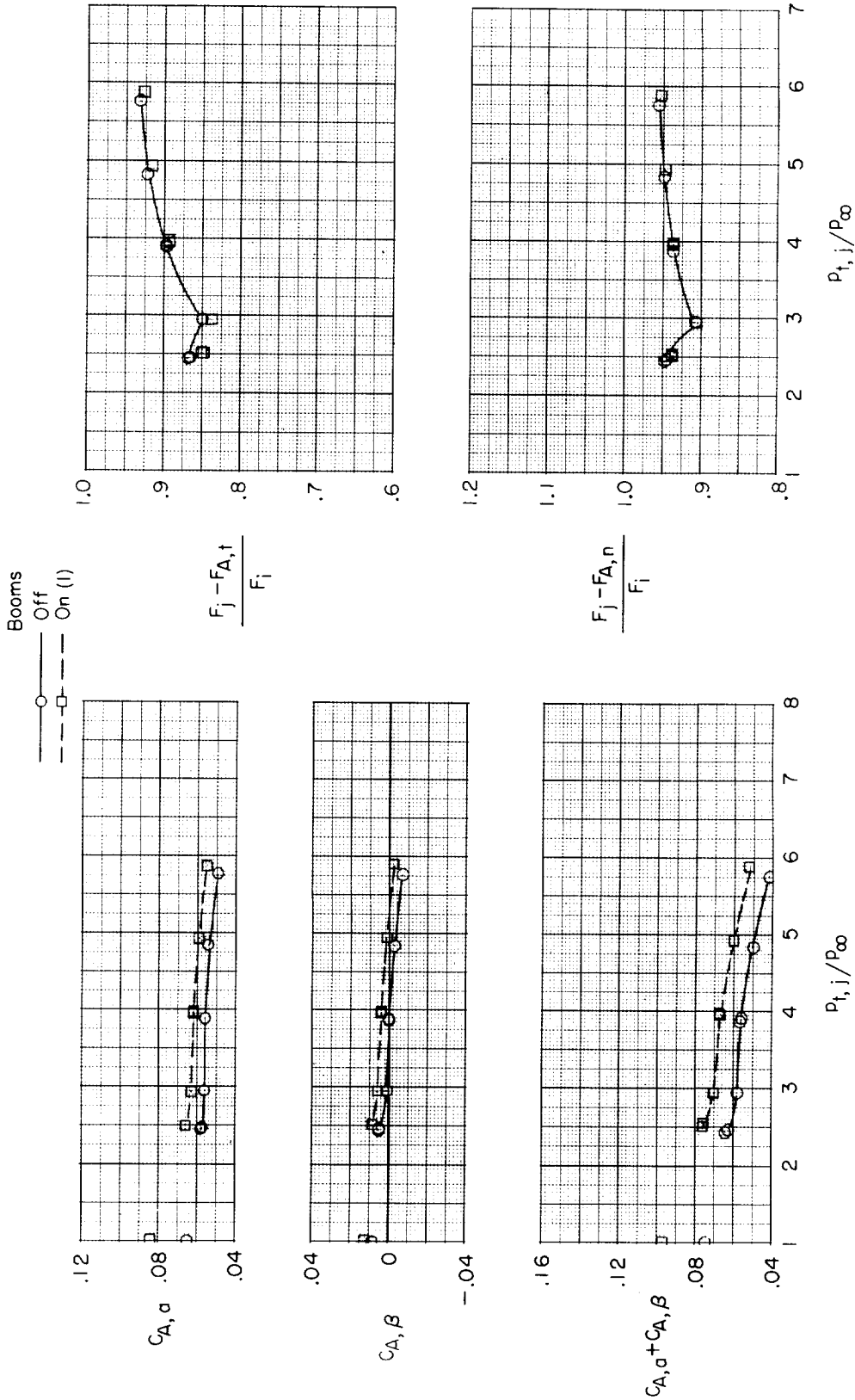
(b) $M = 0.70$.

Figure 18.- Continued.



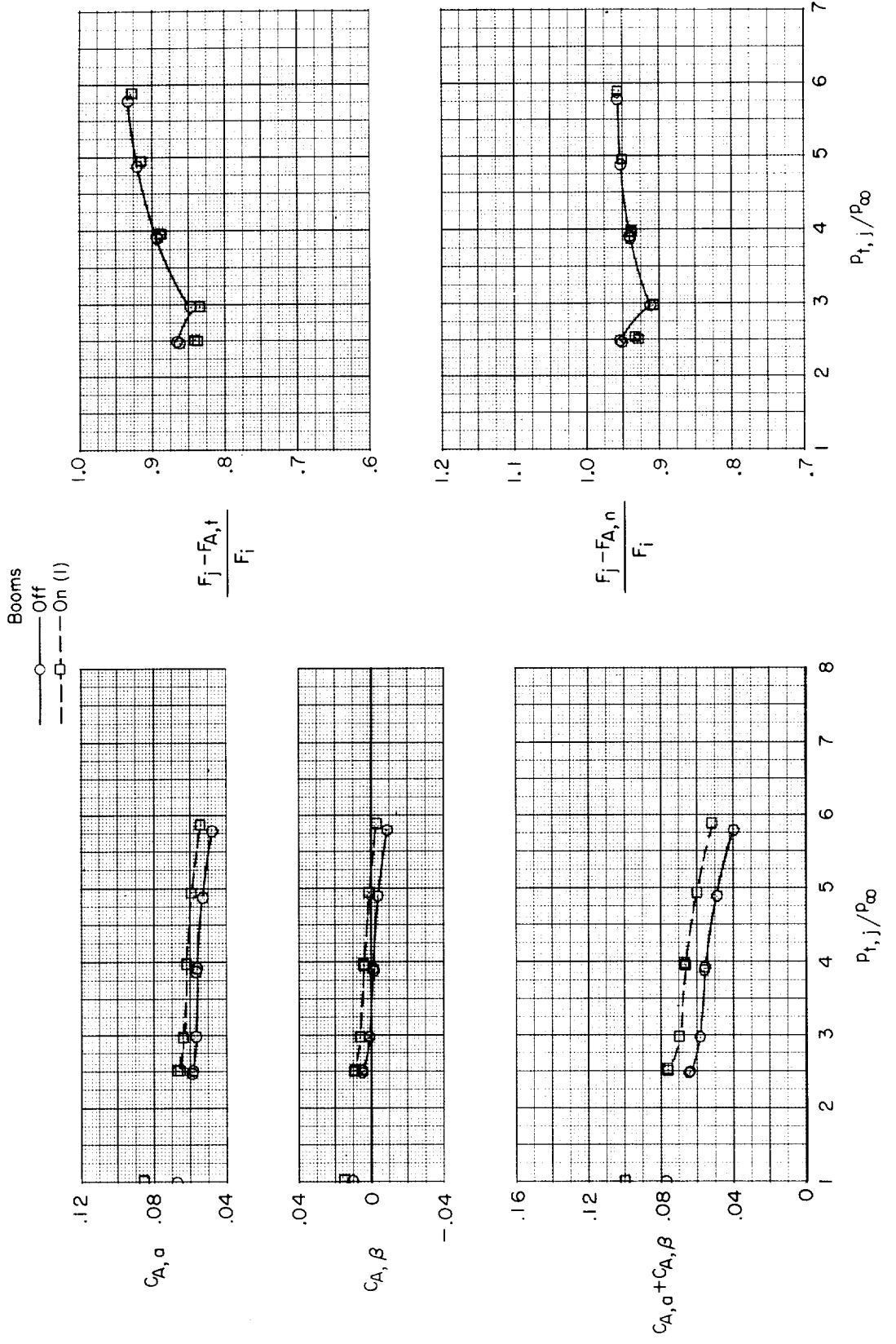
(c) $M = 0.80$.

Figure 18.- Continued.



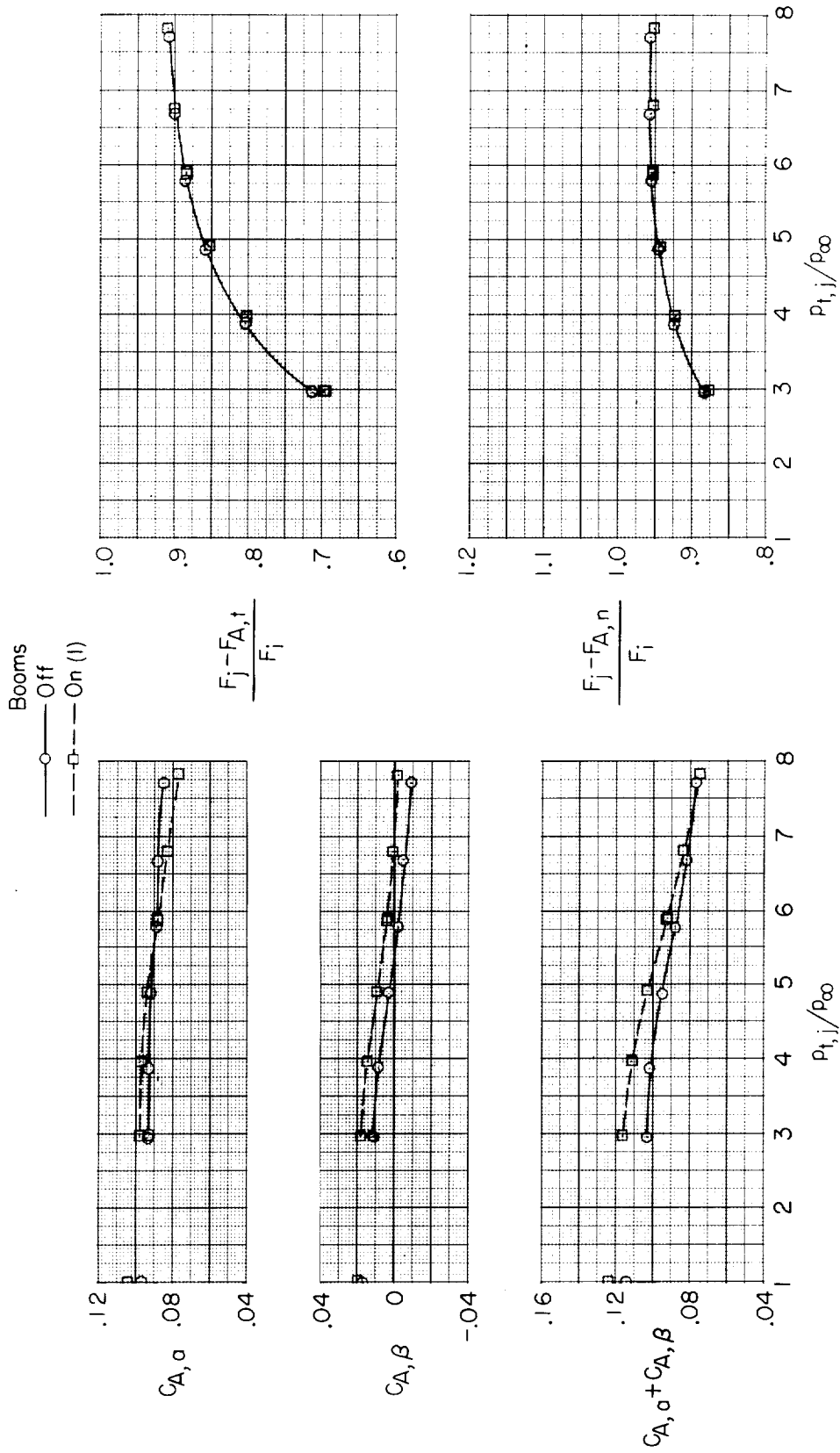
(d) $M = 0.90$.

Figure 18.- Continued.



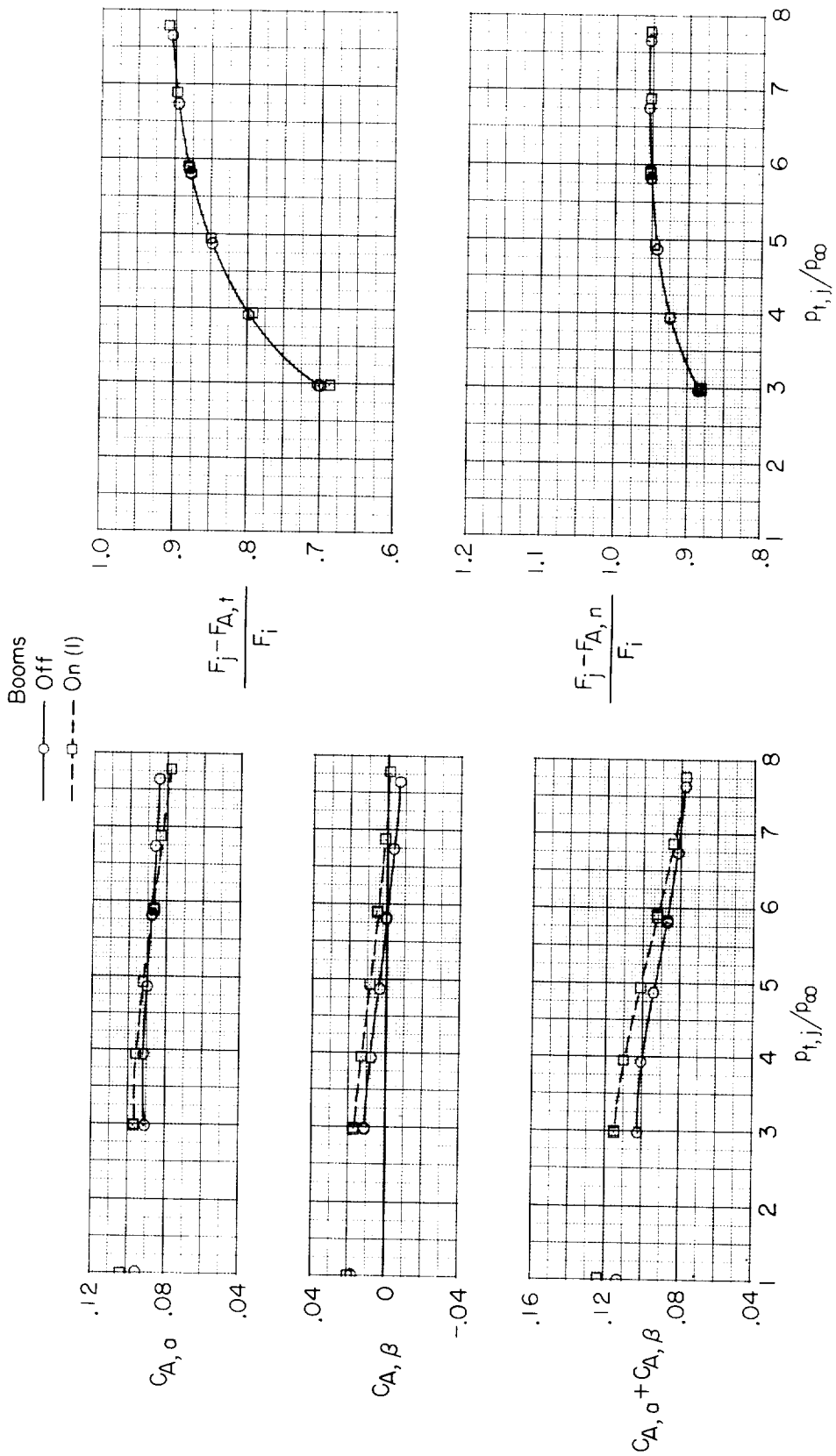
(e) $M = 0.95$.

Figure 18.- Continued.



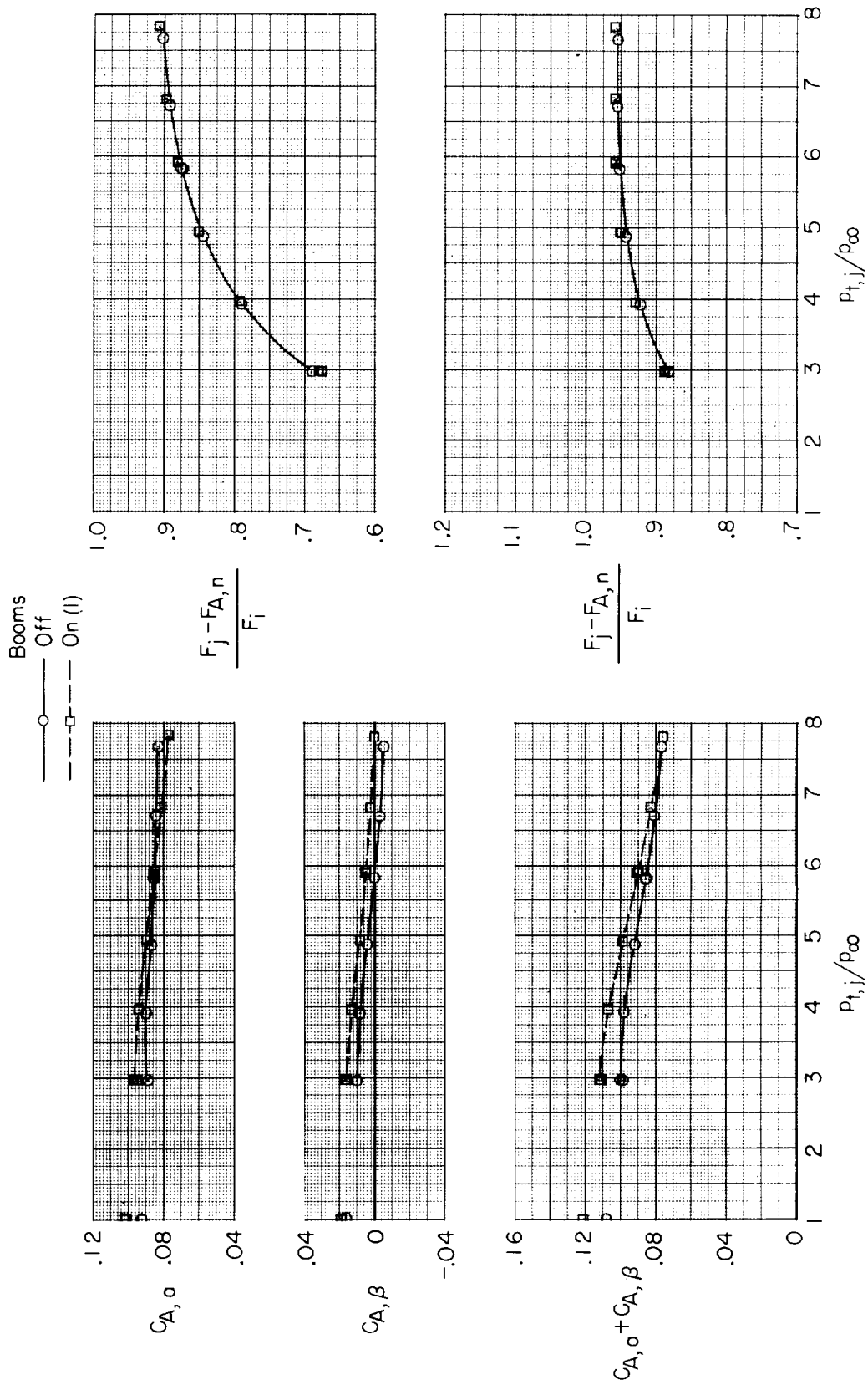
(f) $M = 1.20$.

Figure 18.- Continued.



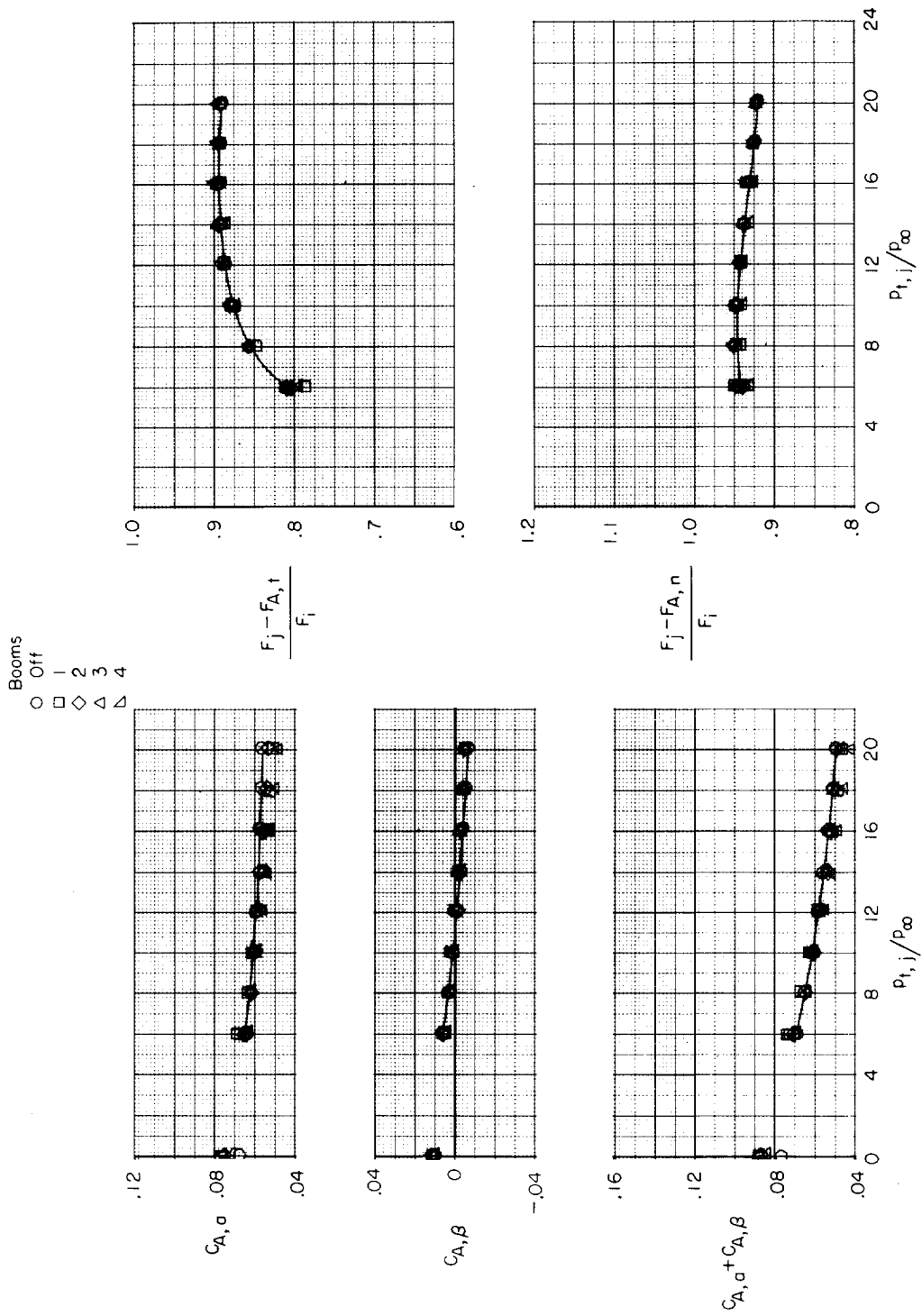
(g) $M = 1.25$.

Figure 18.- Continued.



(h) $M = 1.30$.

Figure 18.- Continued.



(1) $M = 2.01$.

Figure 18.- Concluded.

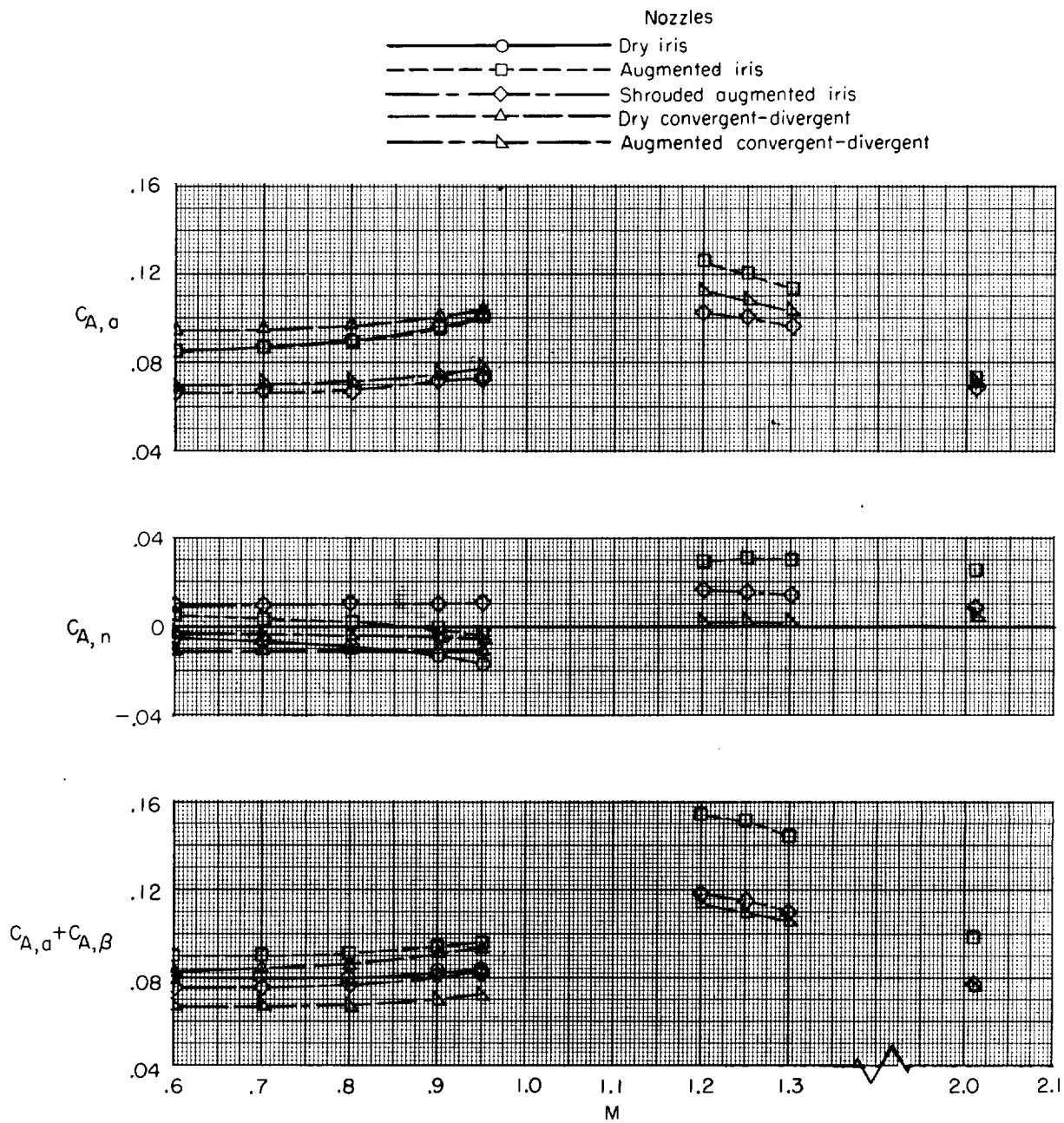


Figure 19.- Effect of nozzle shape on jet-off axial-force coefficients of afterbody with elliptical interfairing.

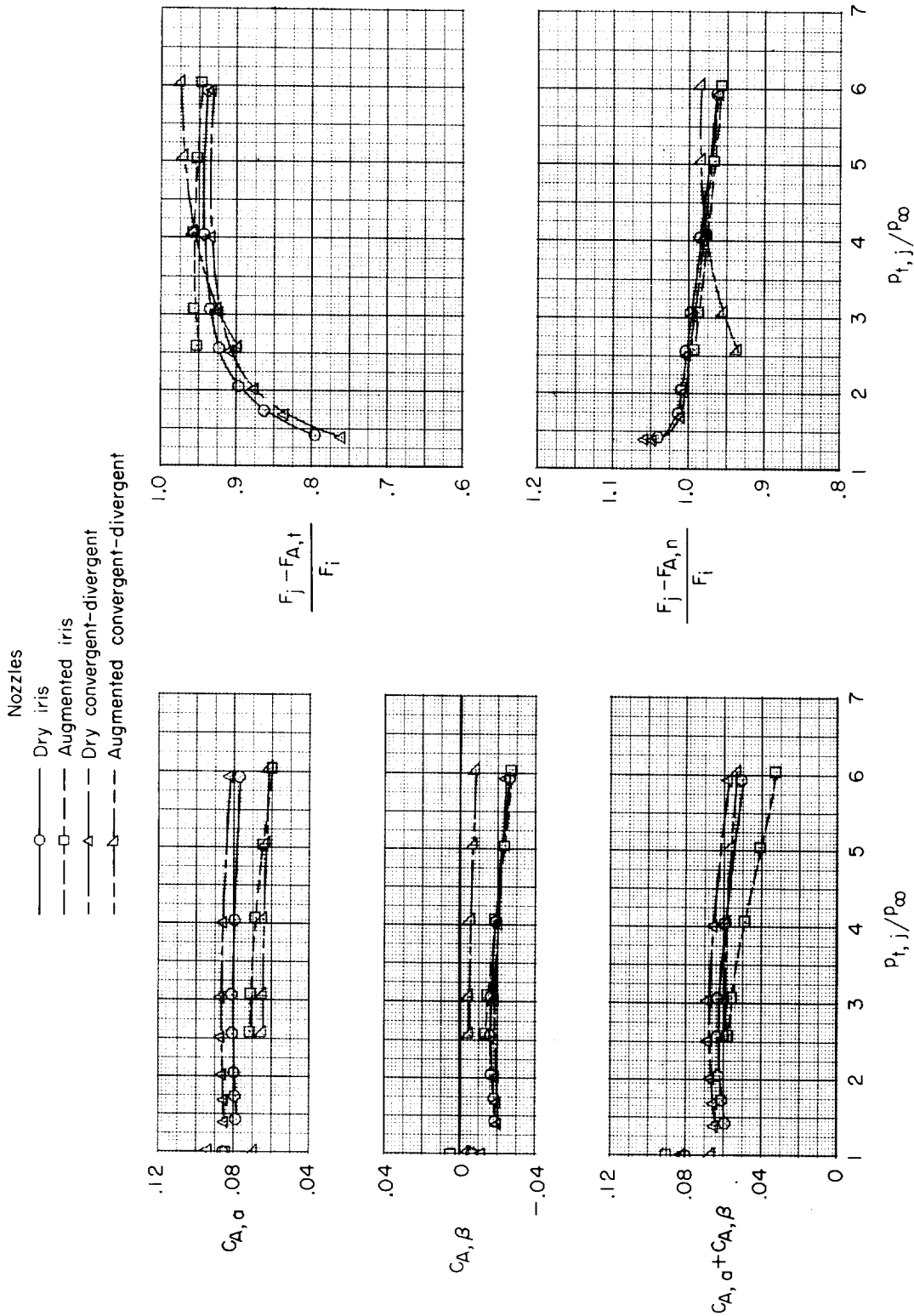
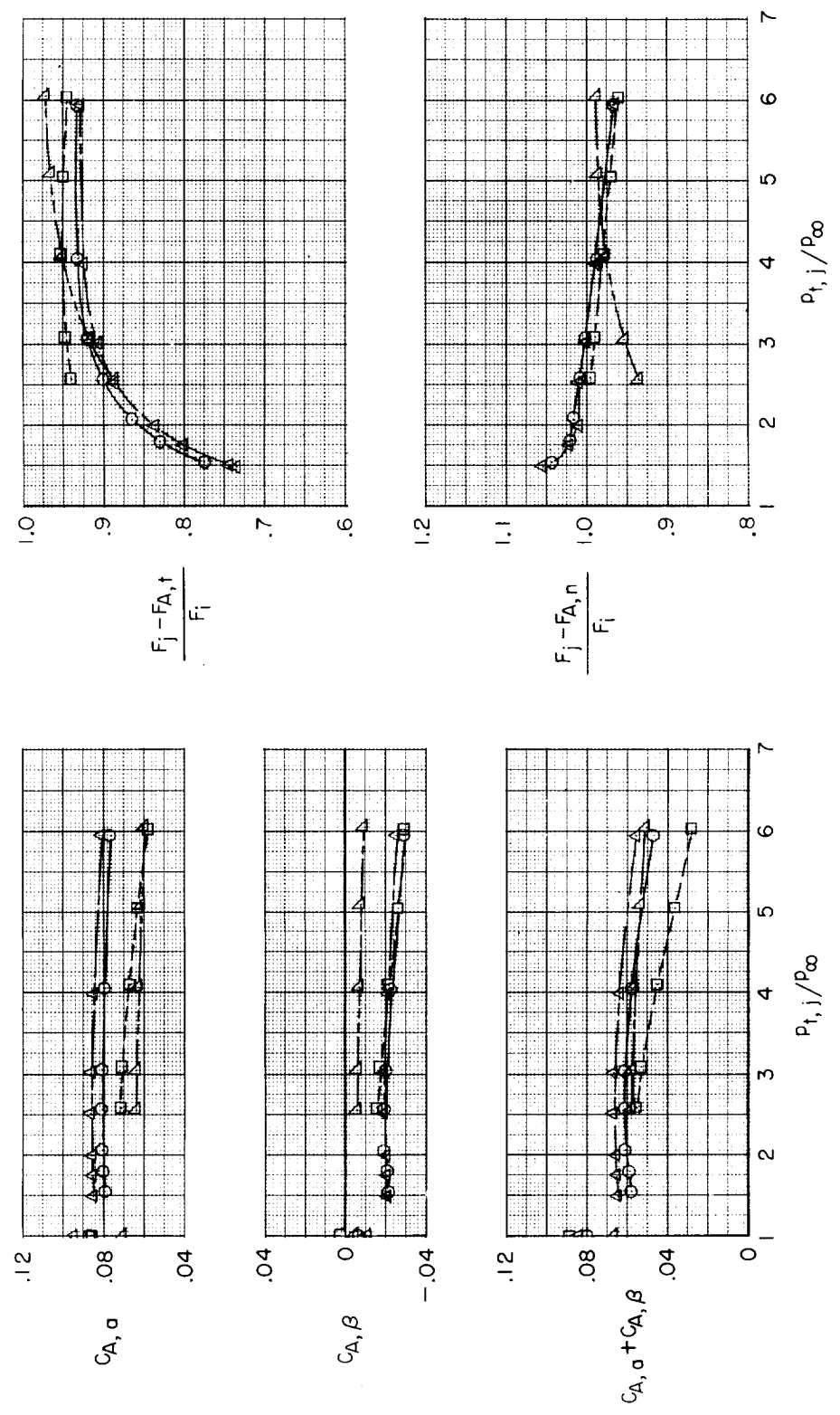


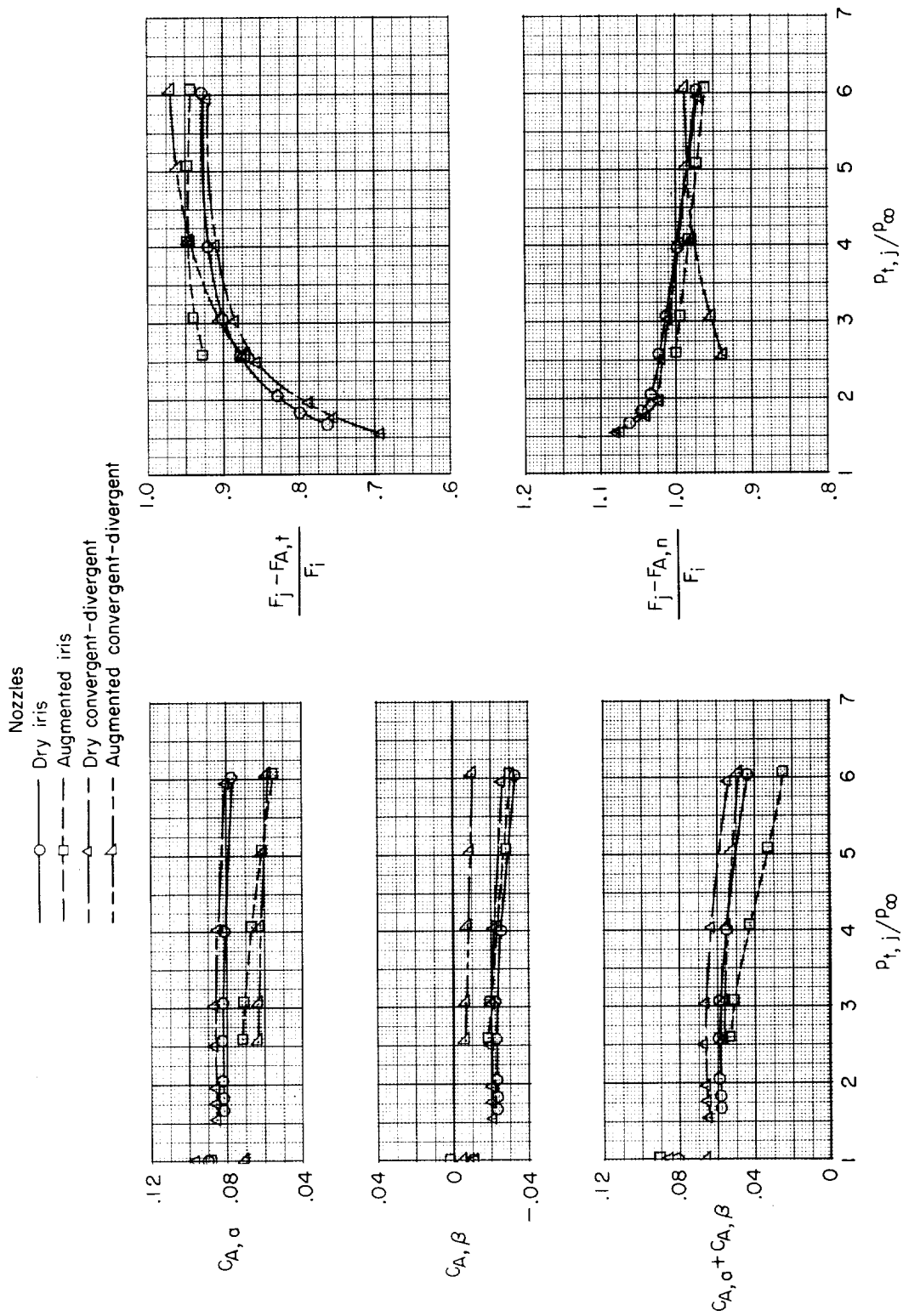
Figure 20.- Effect of nozzle configuration on performance at subsonic speeds of afterbody with elliptical interfairing.

- Nozzles
- Dry iris
 - -□- - Augmented iris
 - -△- - Dry convergent-divergent
 - -▽- - Augmented convergent-divergent



(b) $M = 0.70$.

Figure 20.- Continued.

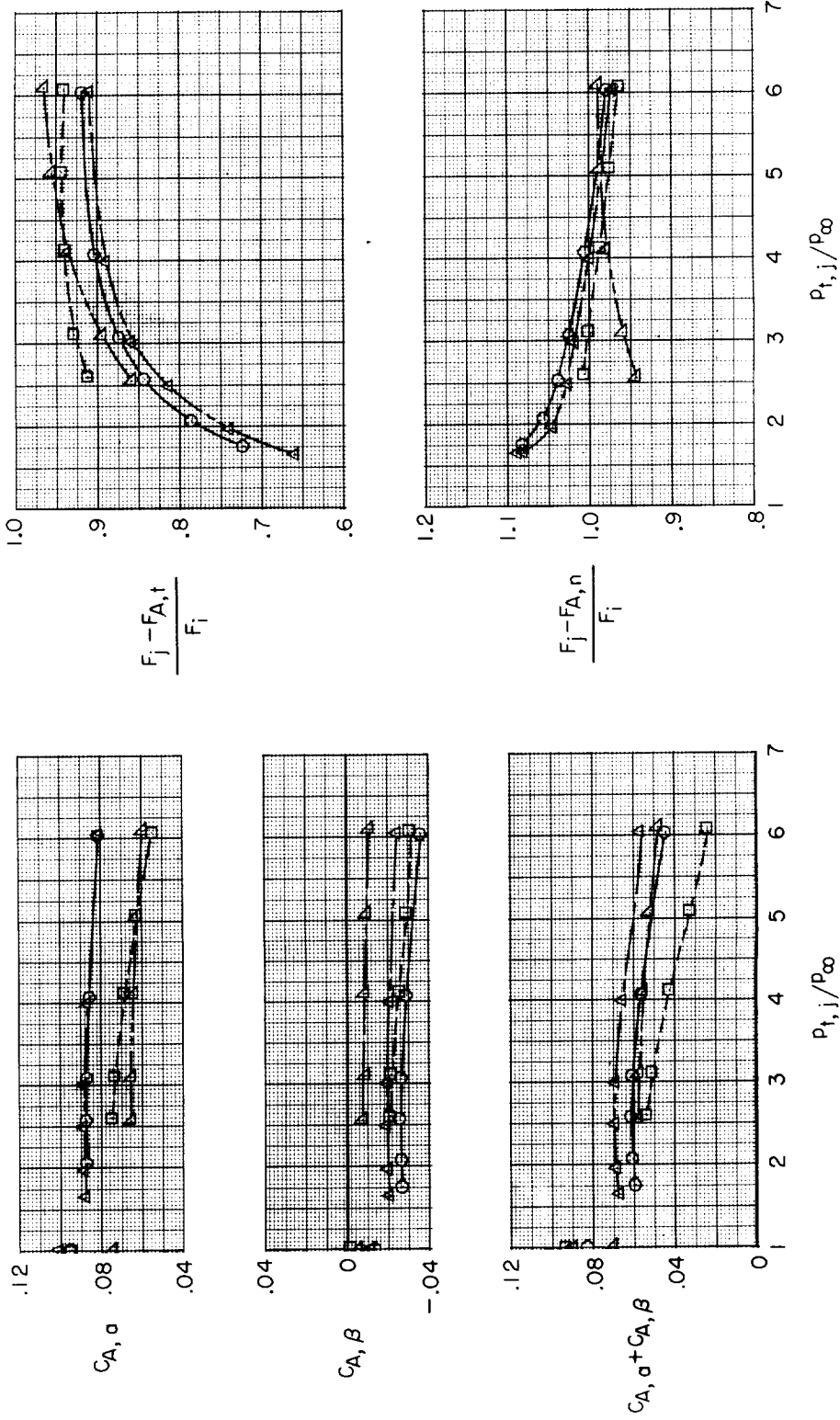


(c) $M = 0.80$.

Figure 20.- Continued.

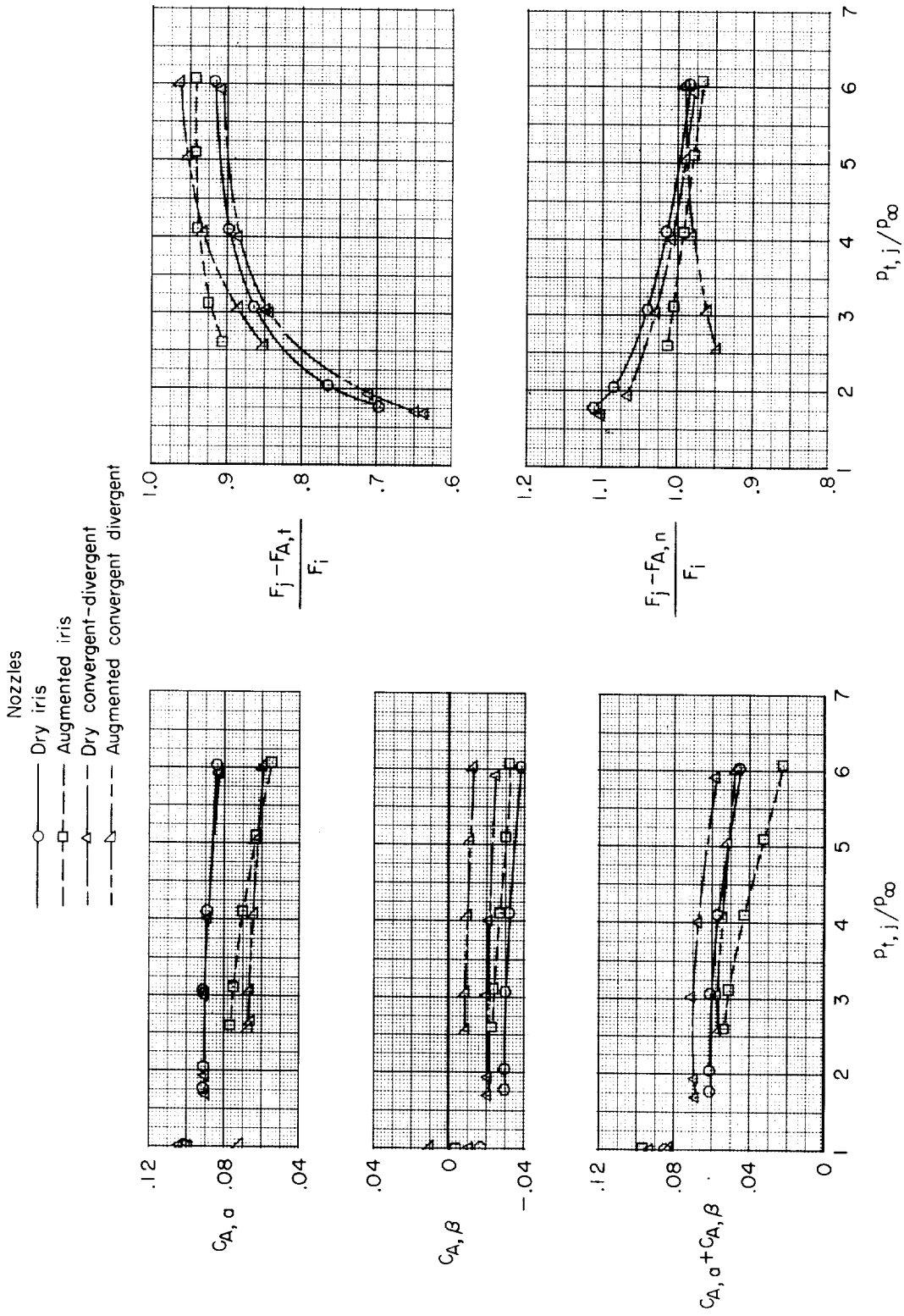
Nozzles

- Dry iris
- Augmented iris
- △— Dry convergent-divergent
- ◇— Augmented convergent-divergent



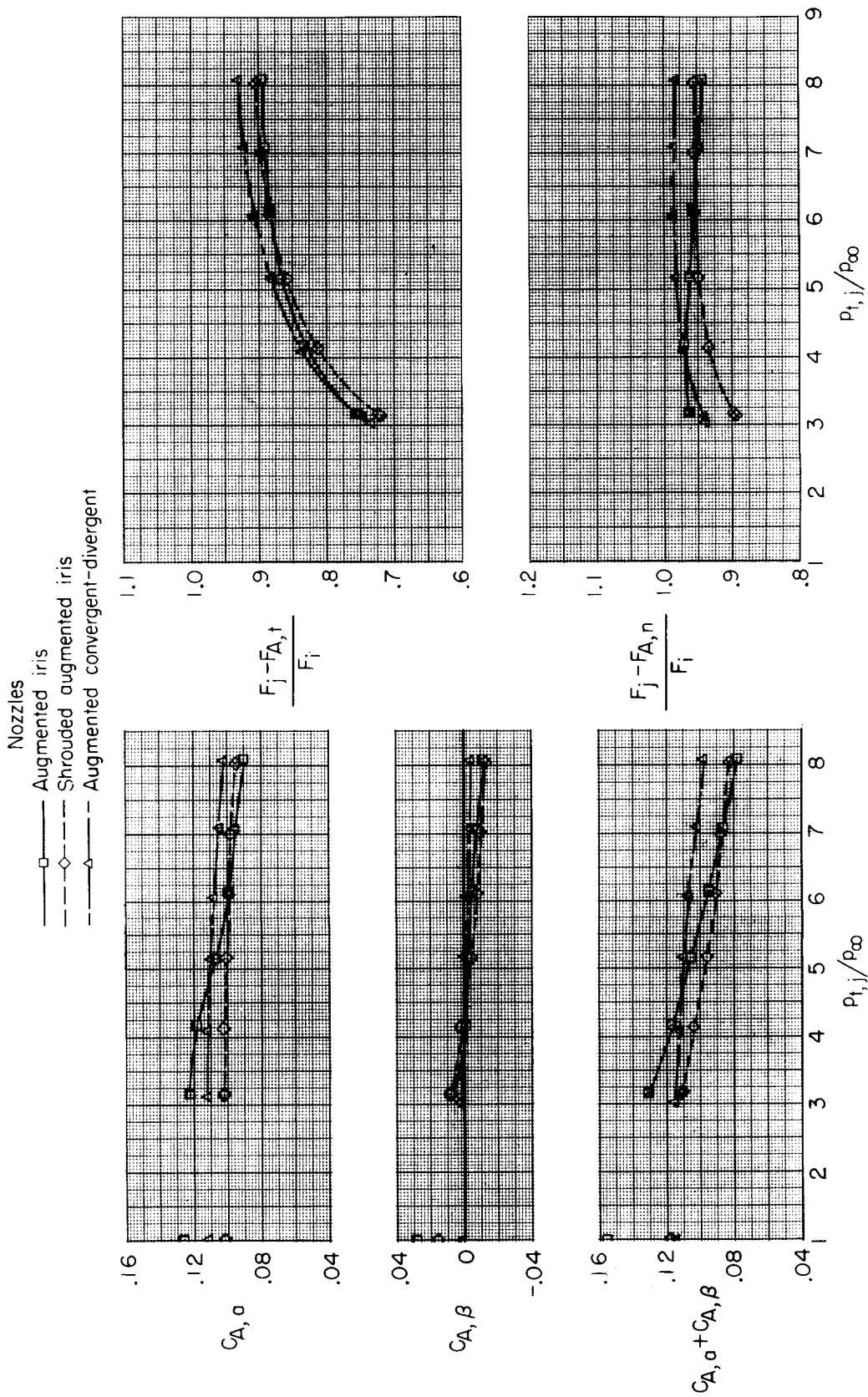
(d) $M = 0.90$.

Figure 20.- Continued.



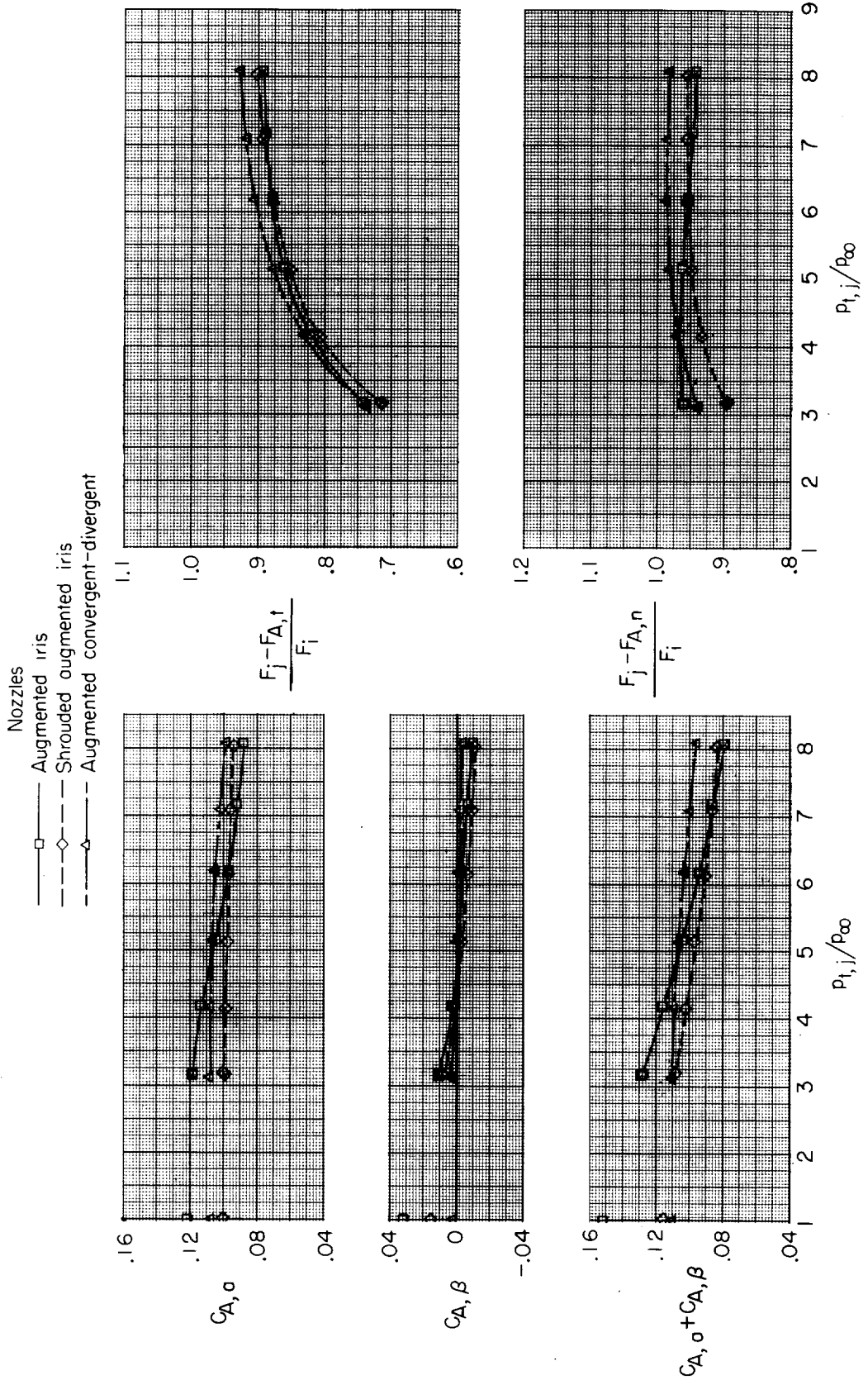
(e) $M = 0.95$.

Figure 20.- Concluded.



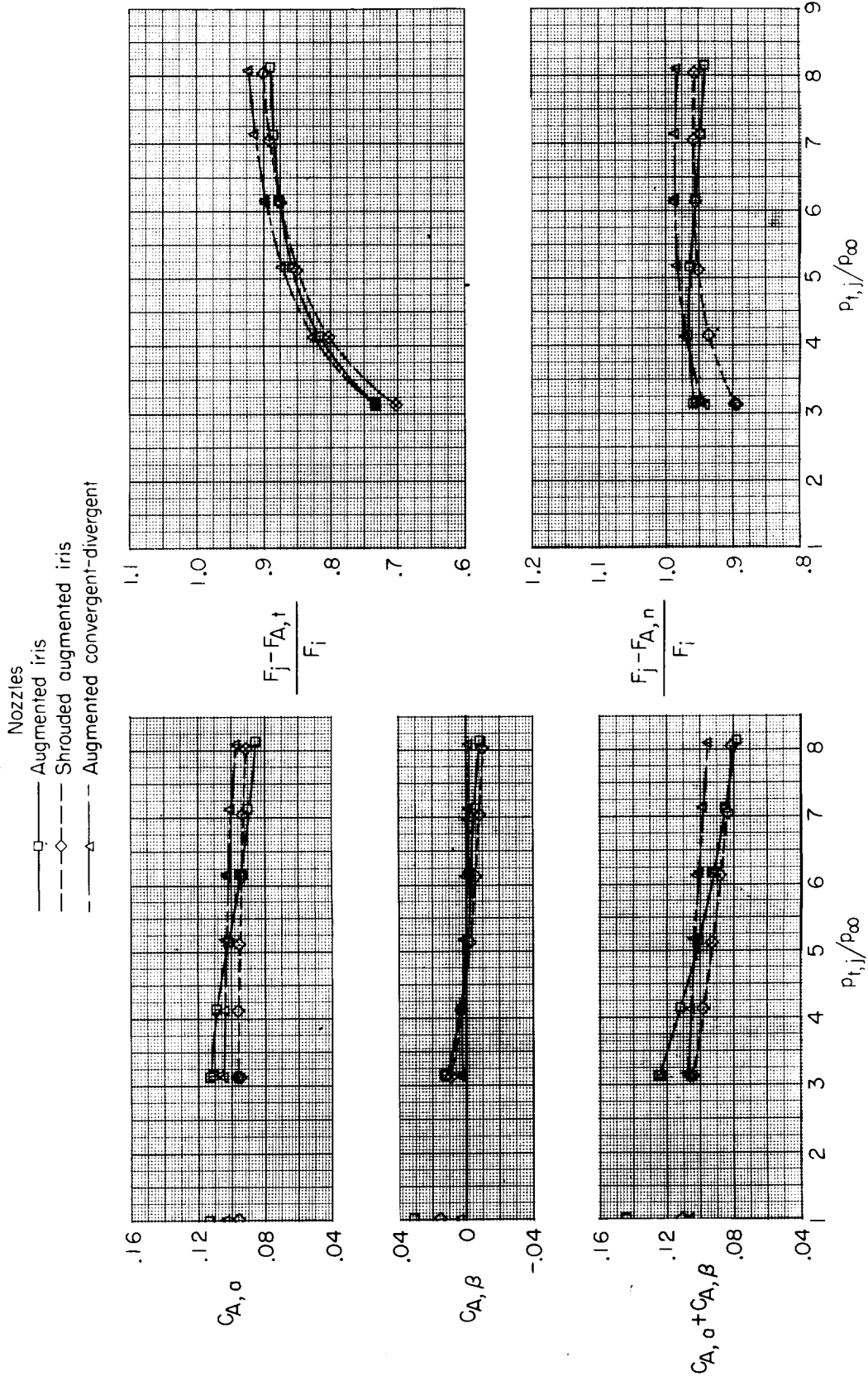
(a) $M = 1.20$.

Figure 21.- Performance of configurations with elliptical interfairings and various types of augmented nozzles.



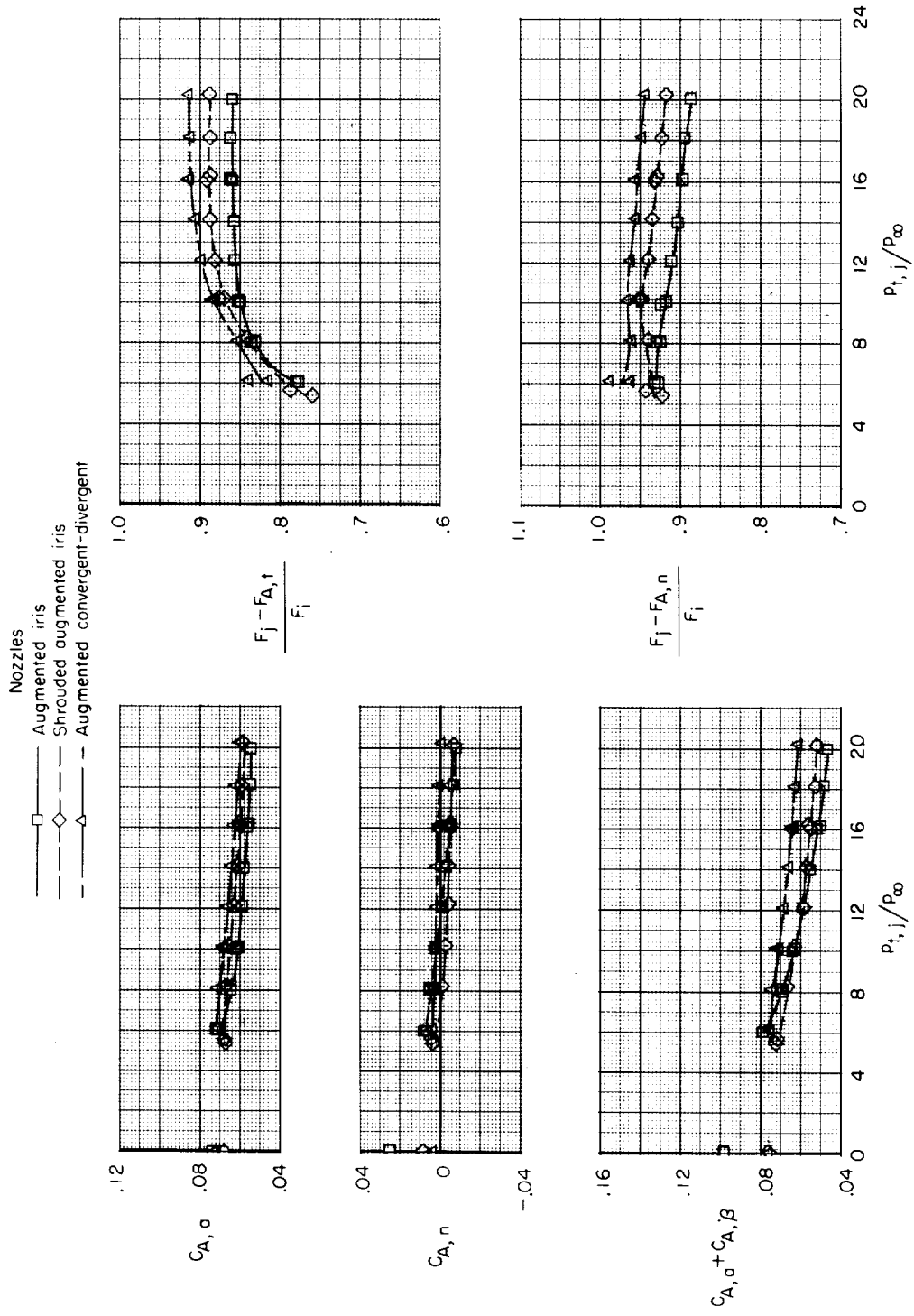
(b) $M = 1.25$.

Figure 21.- Continued.



(c) $M = 1.30$.

Figure 21.- Continued.



(d) $M = 2.01$.

Figure 21.- Concluded.

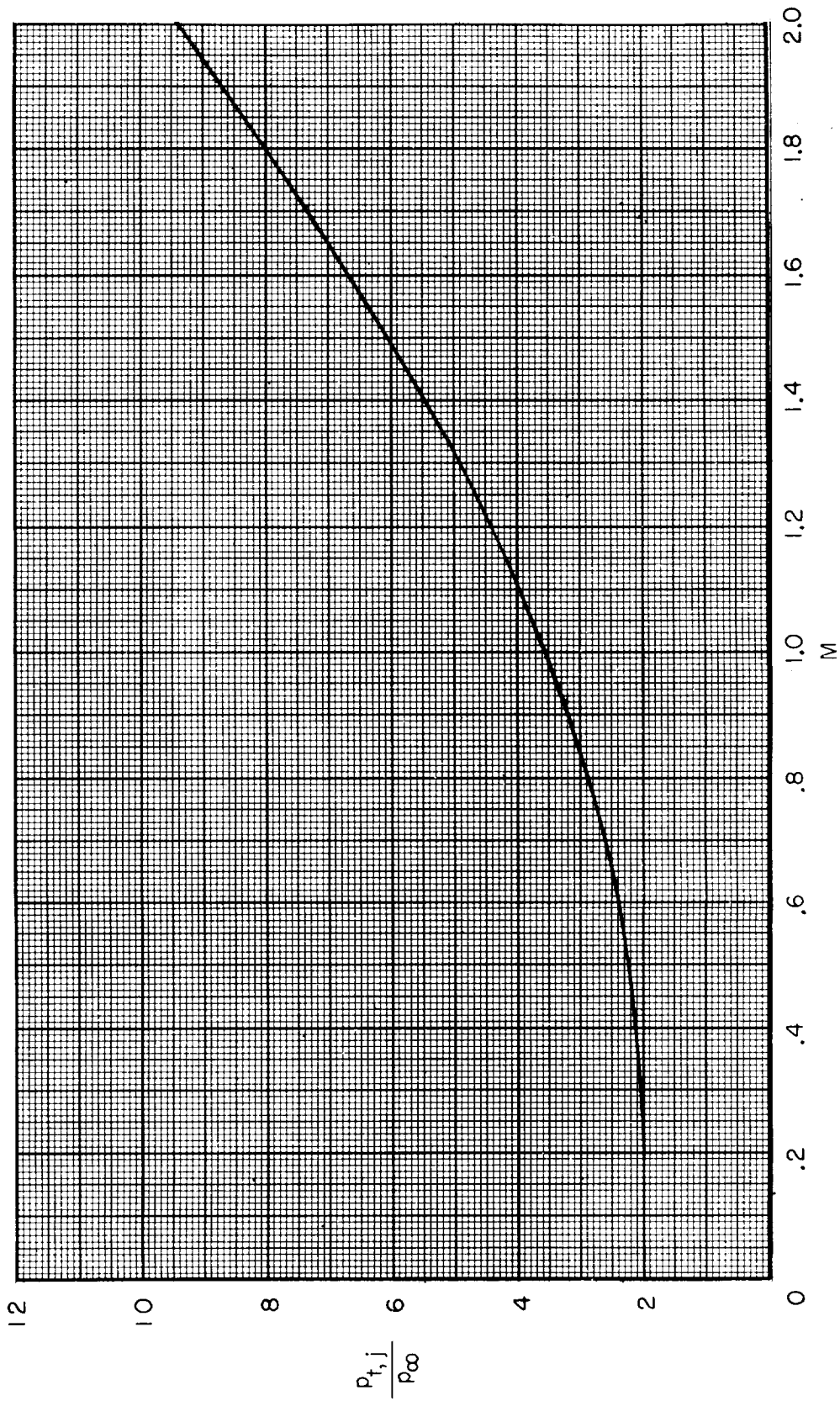
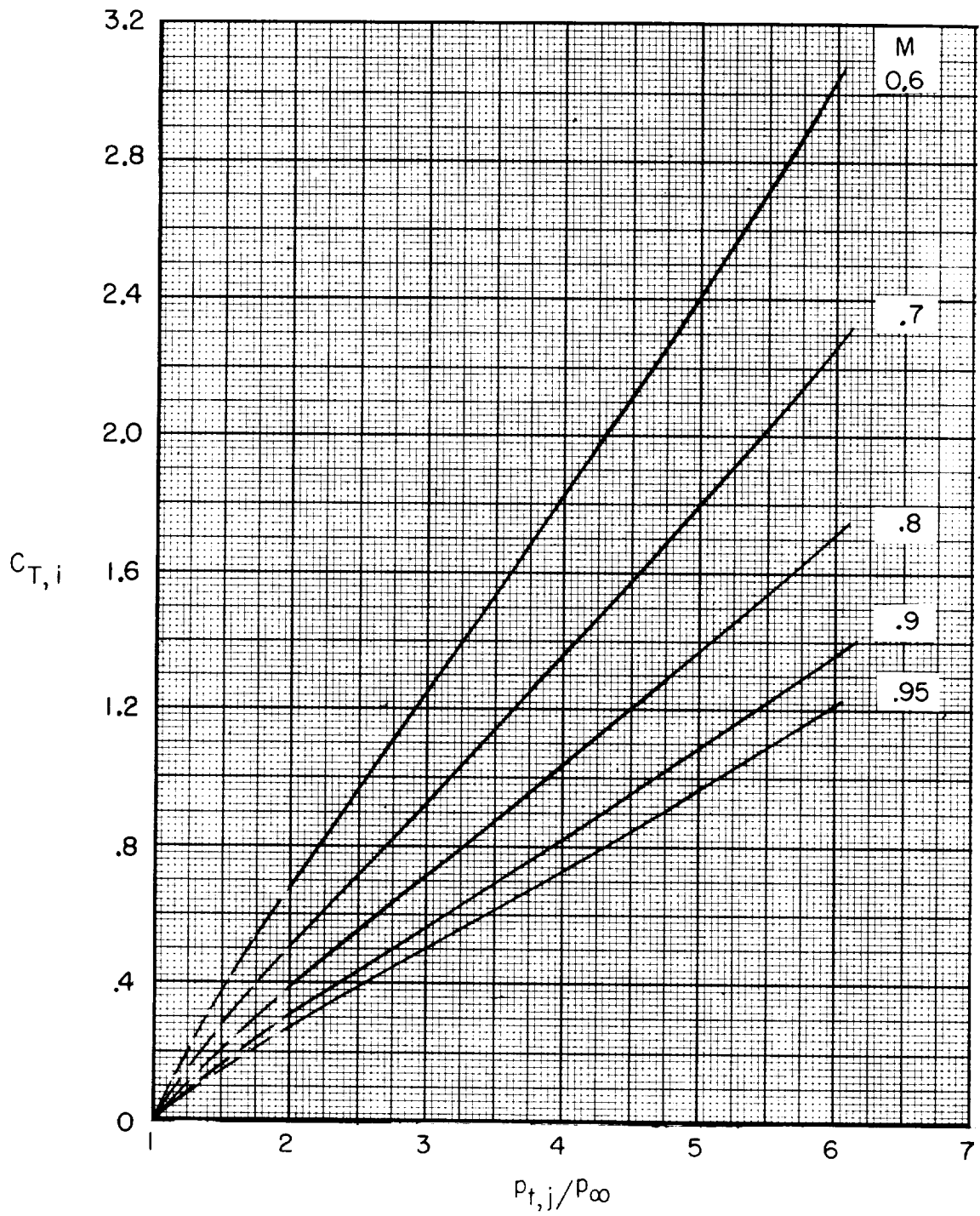
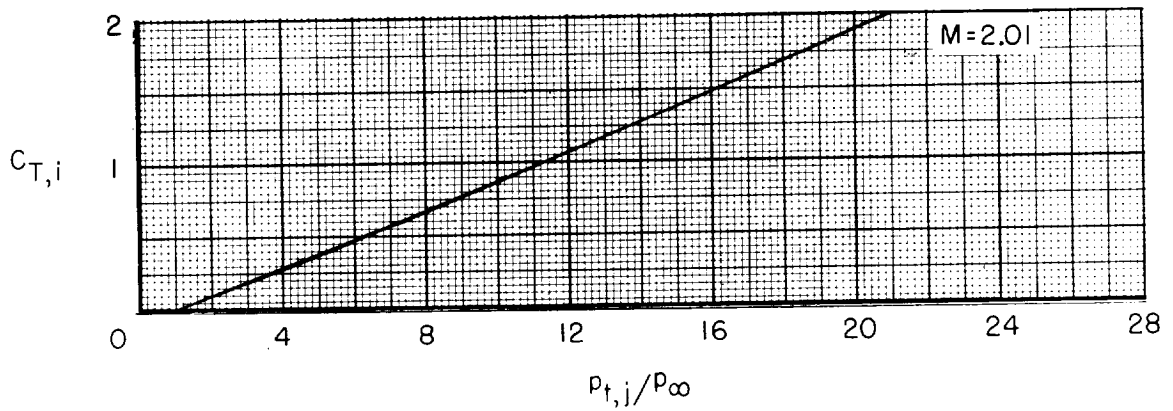
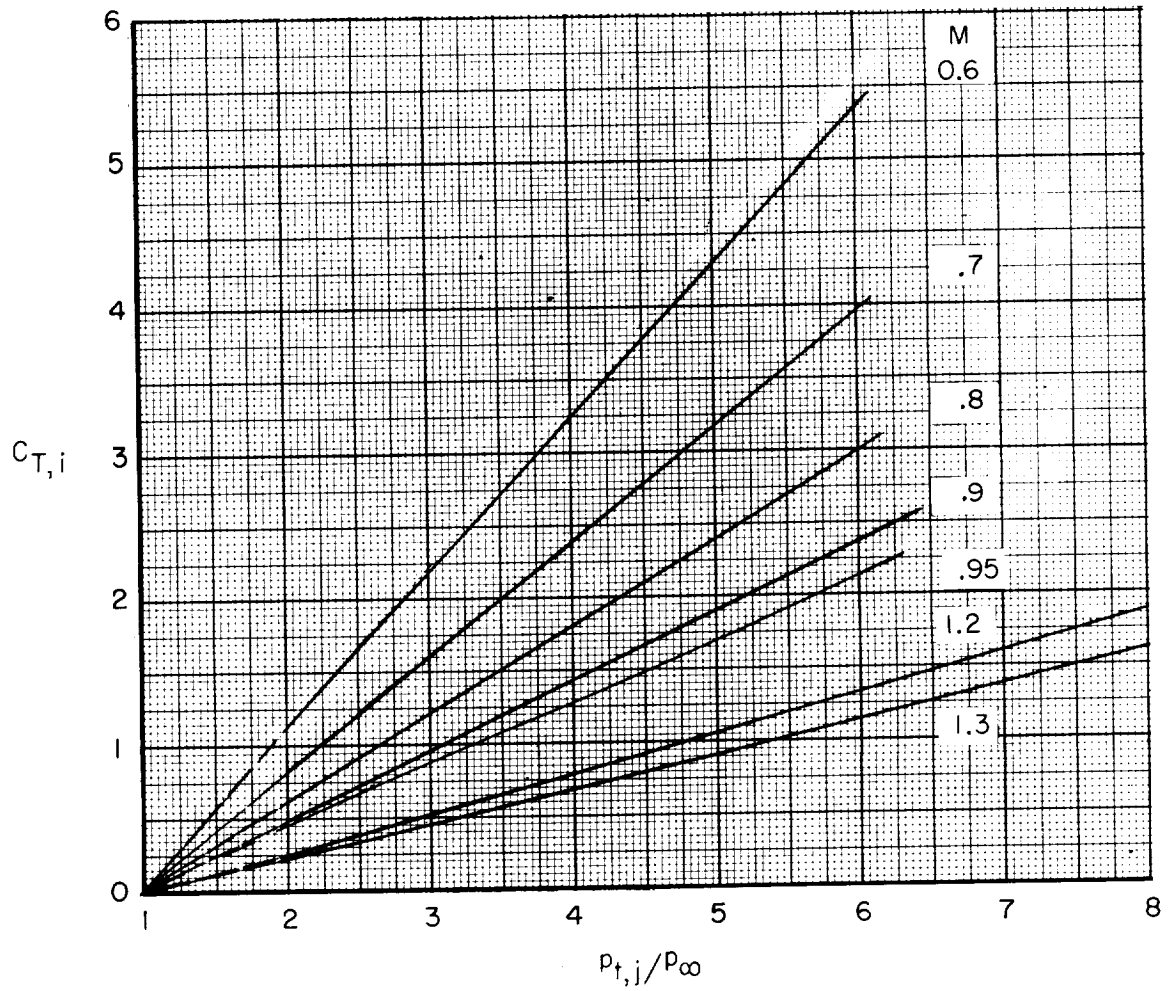


Figure 22.- Assumed jet-total-pressure-ratio schedule for turbofan engine.



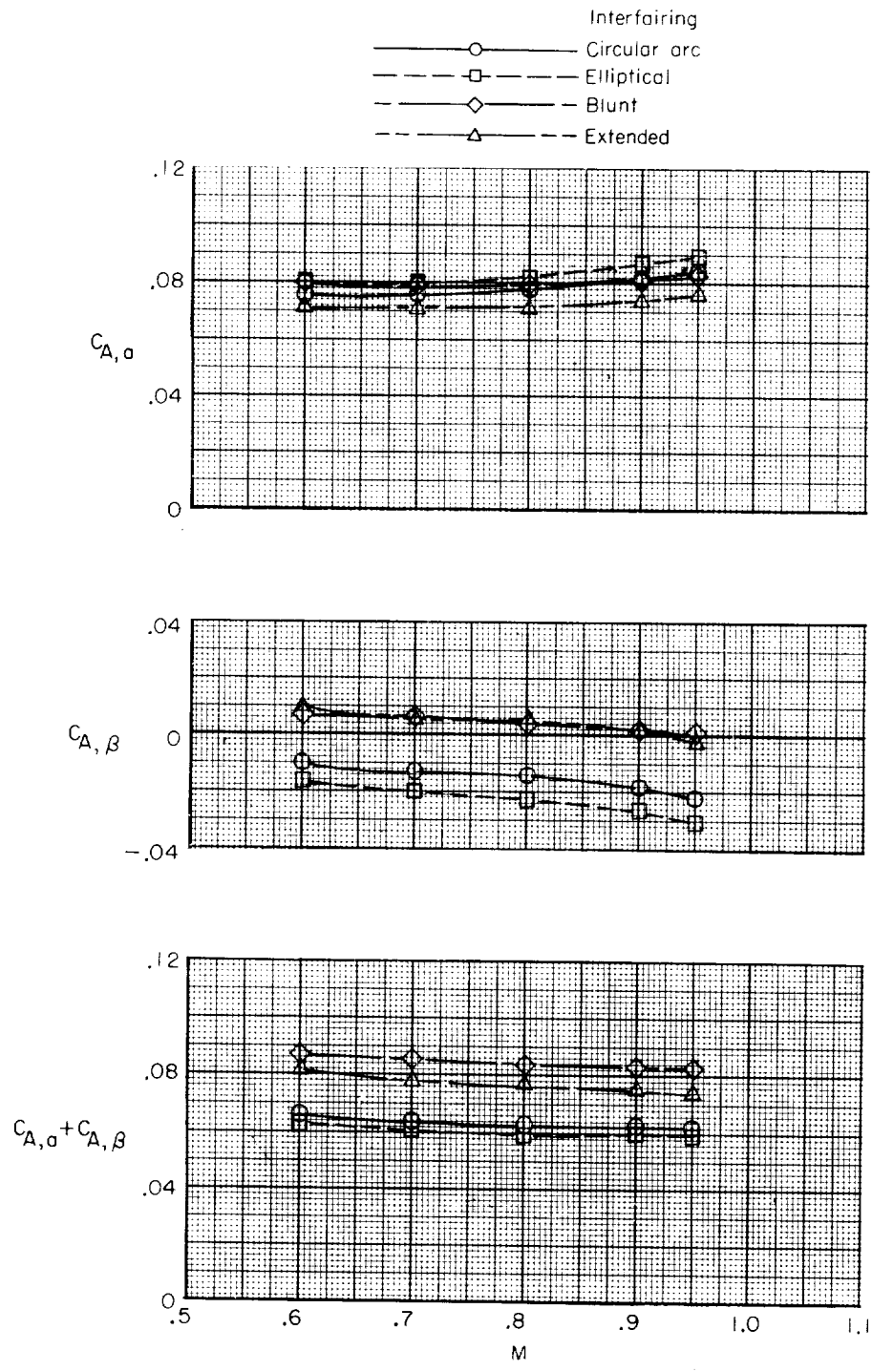
(a) Dry nozzles.

Figure 23.- Ideal aerodynamic thrust coefficient.



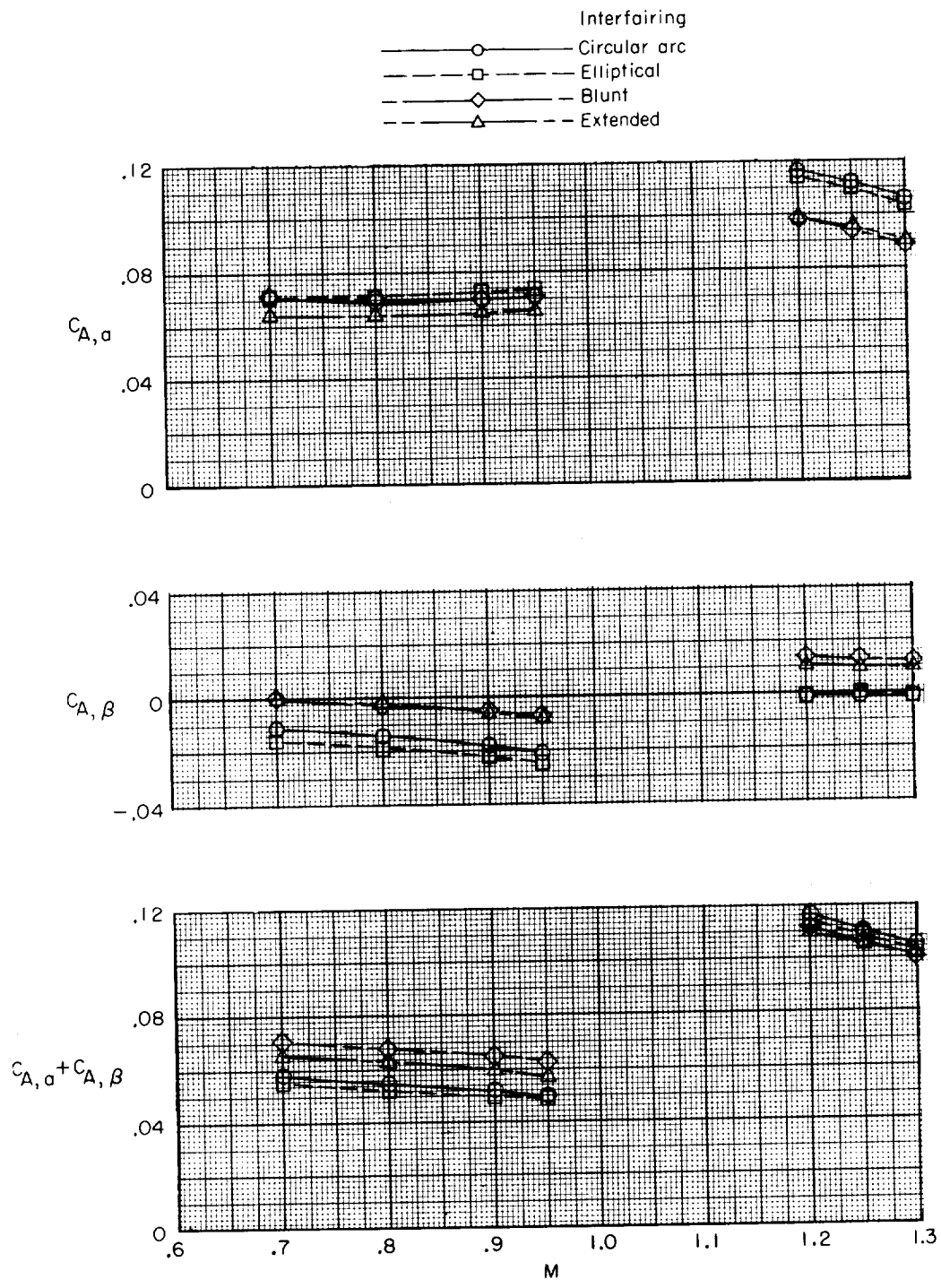
(b) Augmented nozzles.

Figure 23.- Concluded.



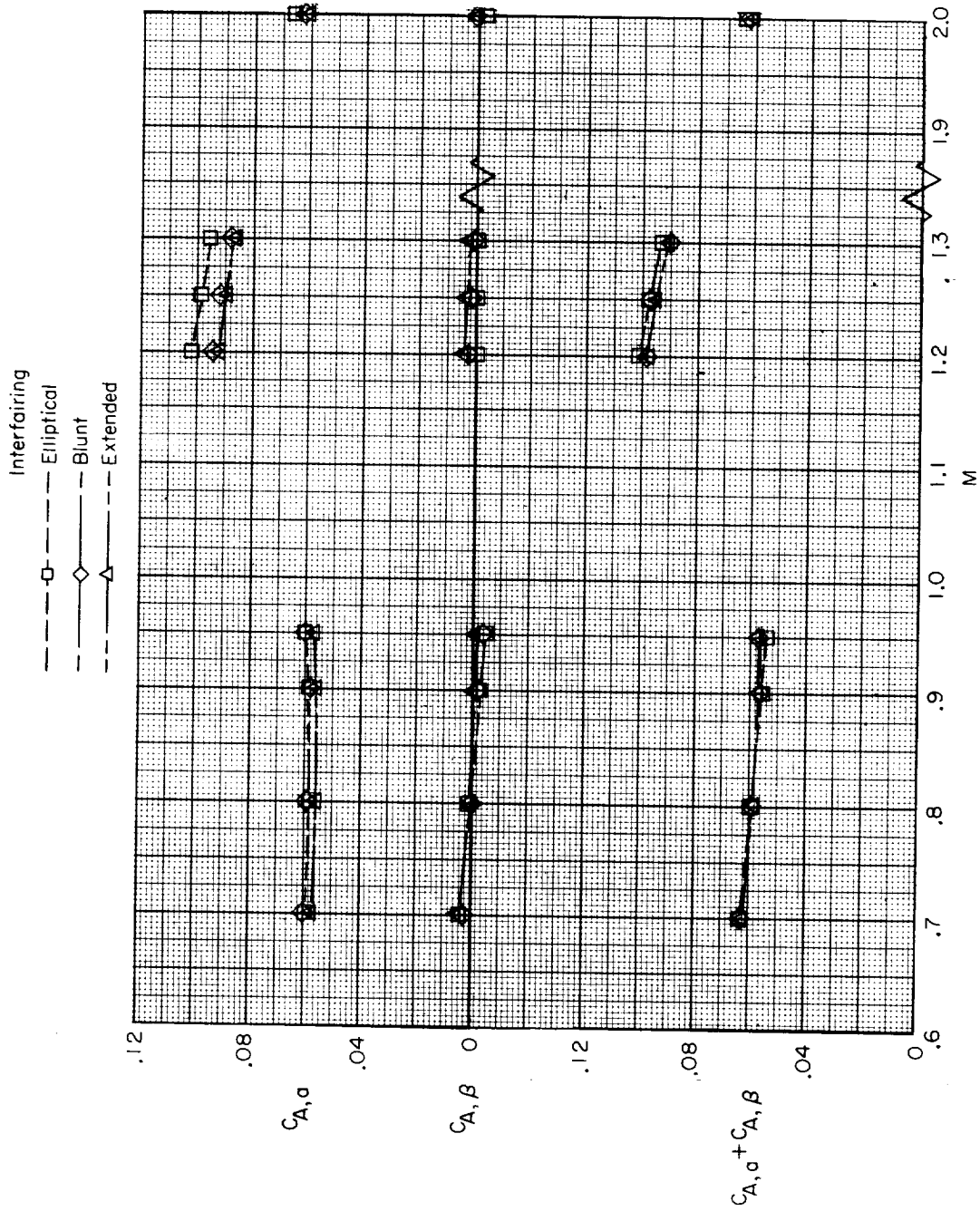
(a) Dry-power iris nozzles.

Figure 24.- Effect of interfairing shape on axial-force coefficients for scheduled jet-pressure ratios.



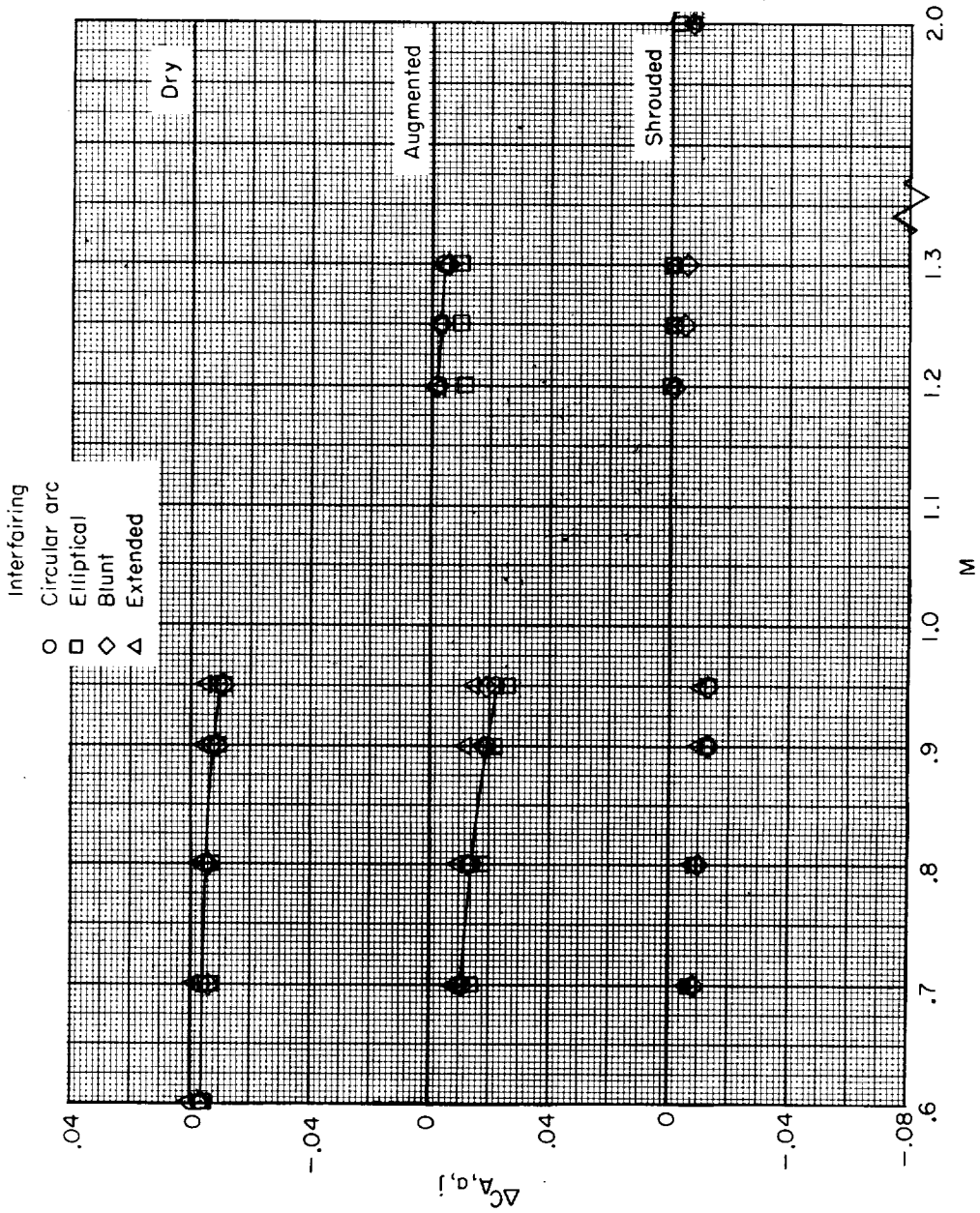
(b) Augmented-power iris nozzles.

Figure 24.- Continued.



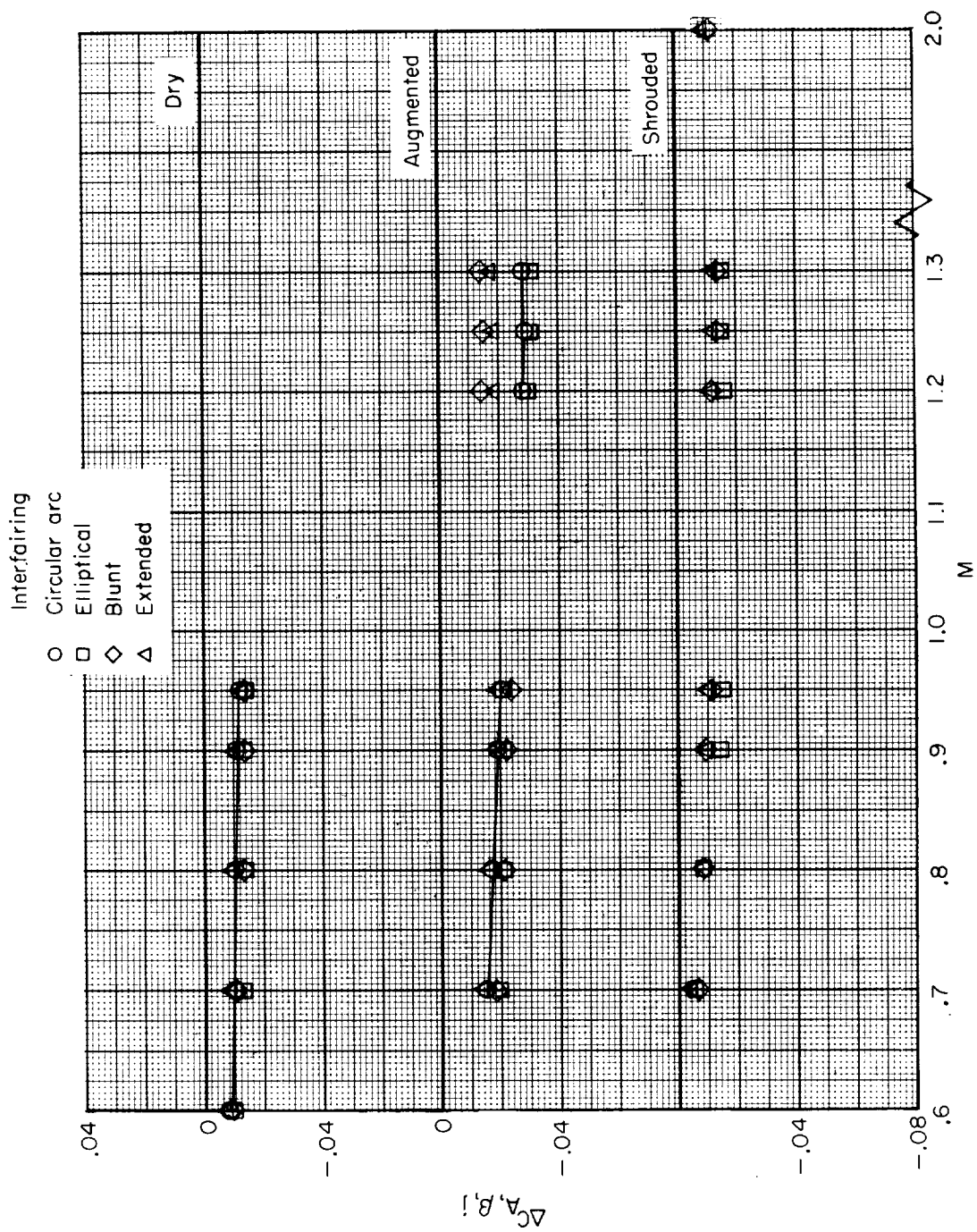
(c) Shrouded-augmented iris nozzles.

Figure 24.- Concluded.



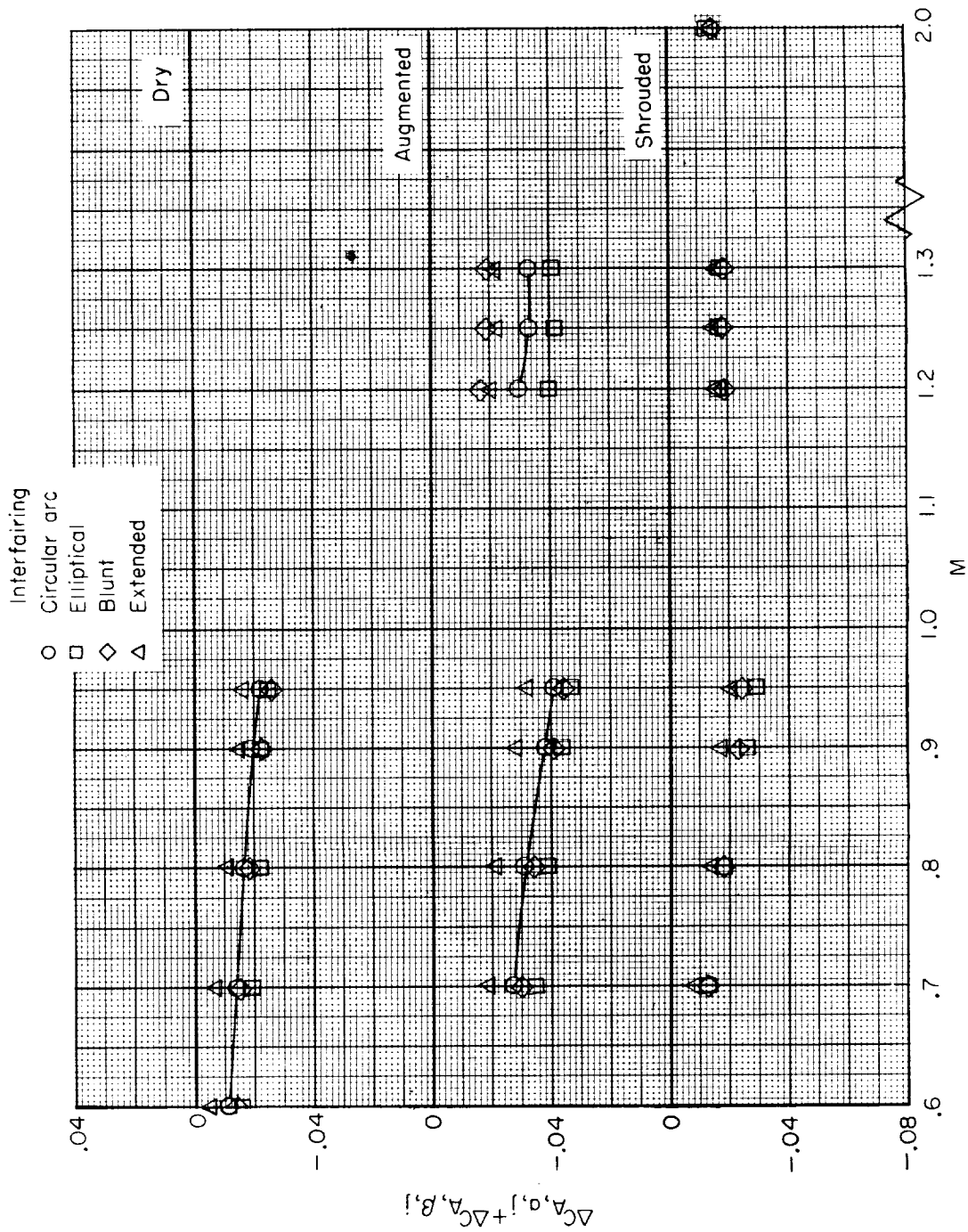
(a) Incremental afterbody-axial-force coefficients.

Figure 25.- Axial-force coefficient increments due to jet operation. Iris nozzles; scheduled jet-pressure ratios.



(b) Incremental nozzle-axial-force coefficients.

Figure 25.- Continued.



(c) Incremental total-axial-force coefficients.

Figure 25.- Concluded.

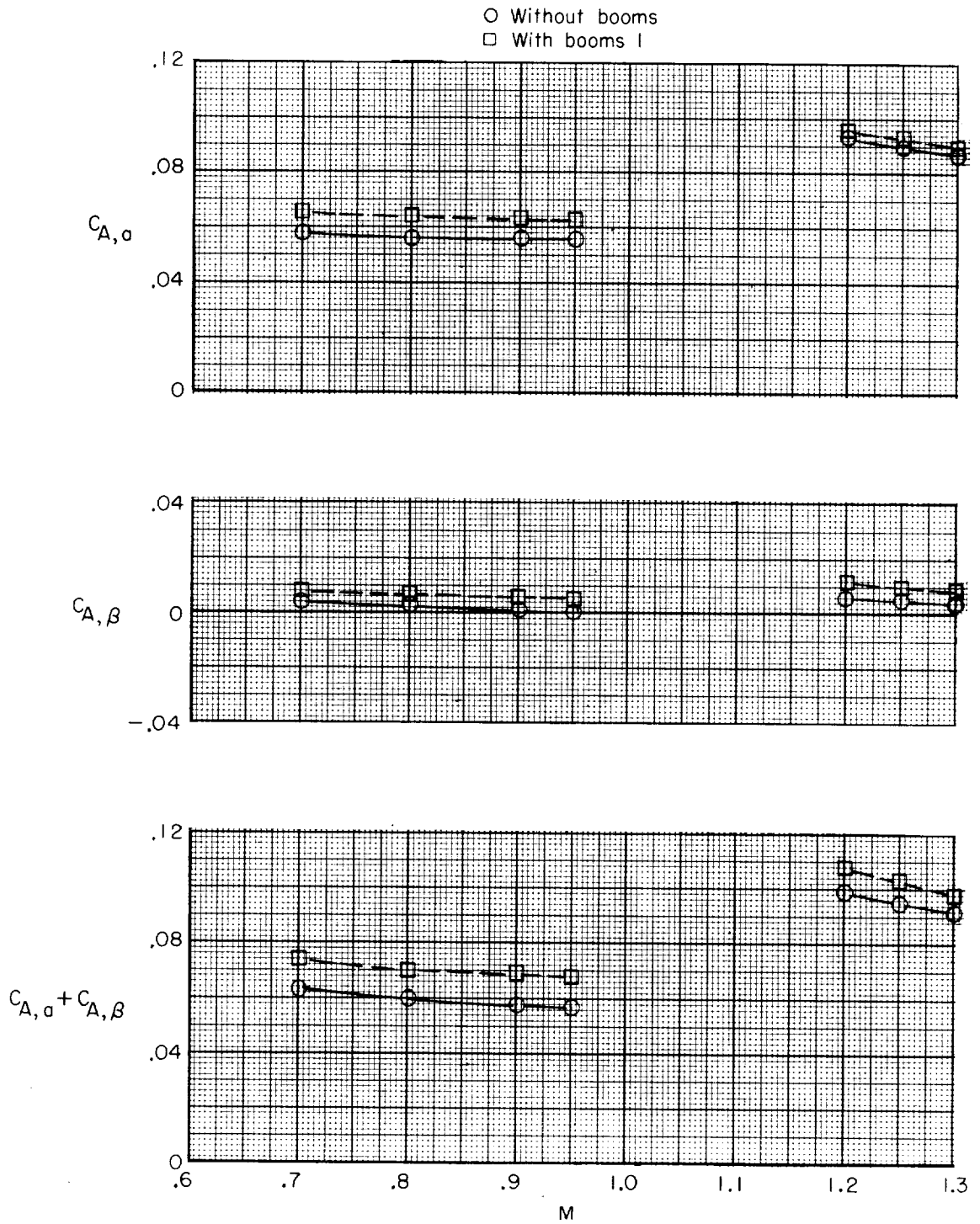
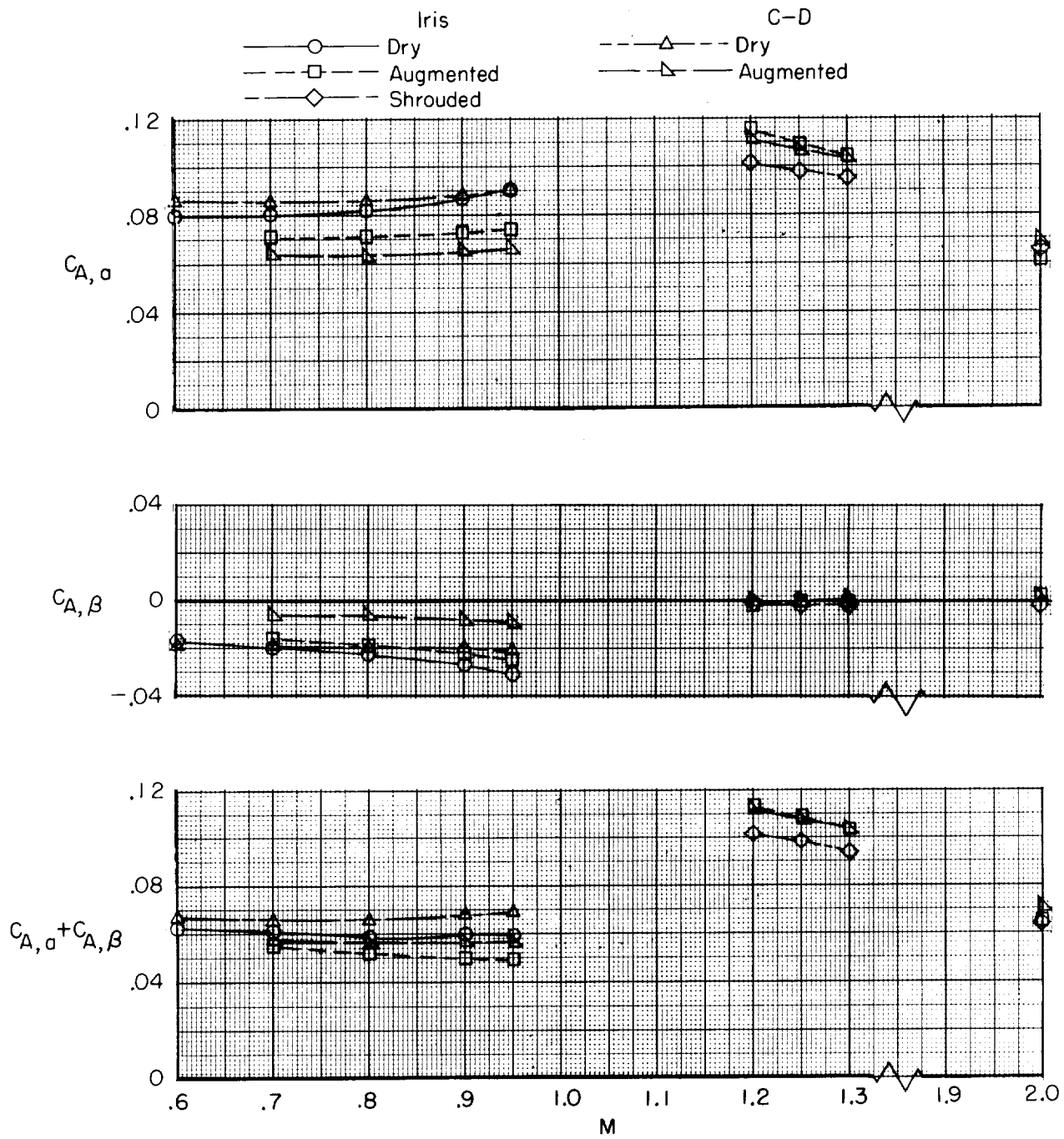
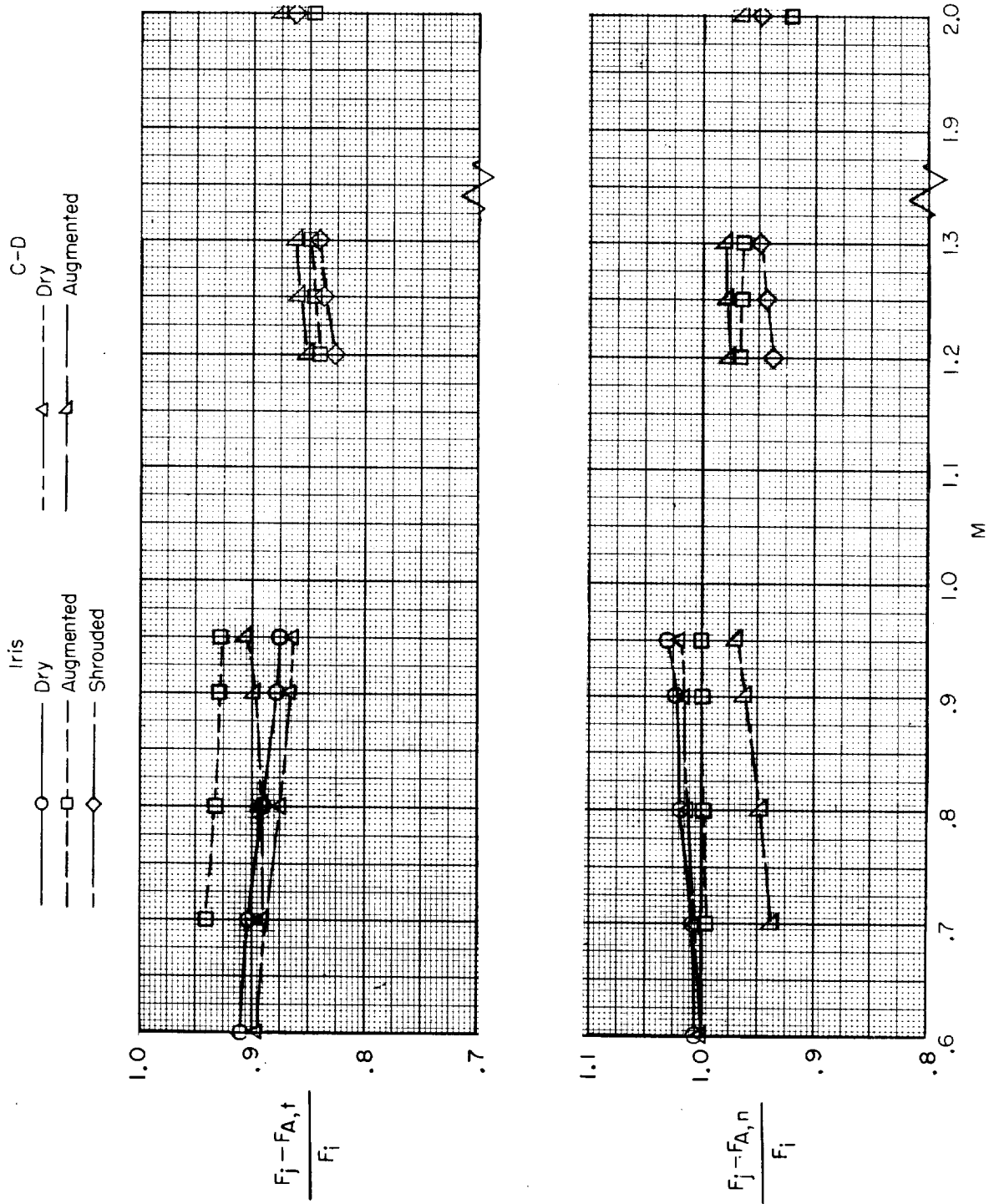


Figure 26.- Effect of booms on axial-force coefficients. Afterbody with extended interfairings and shrouded iris nozzles; scheduled jet-pressure ratios.



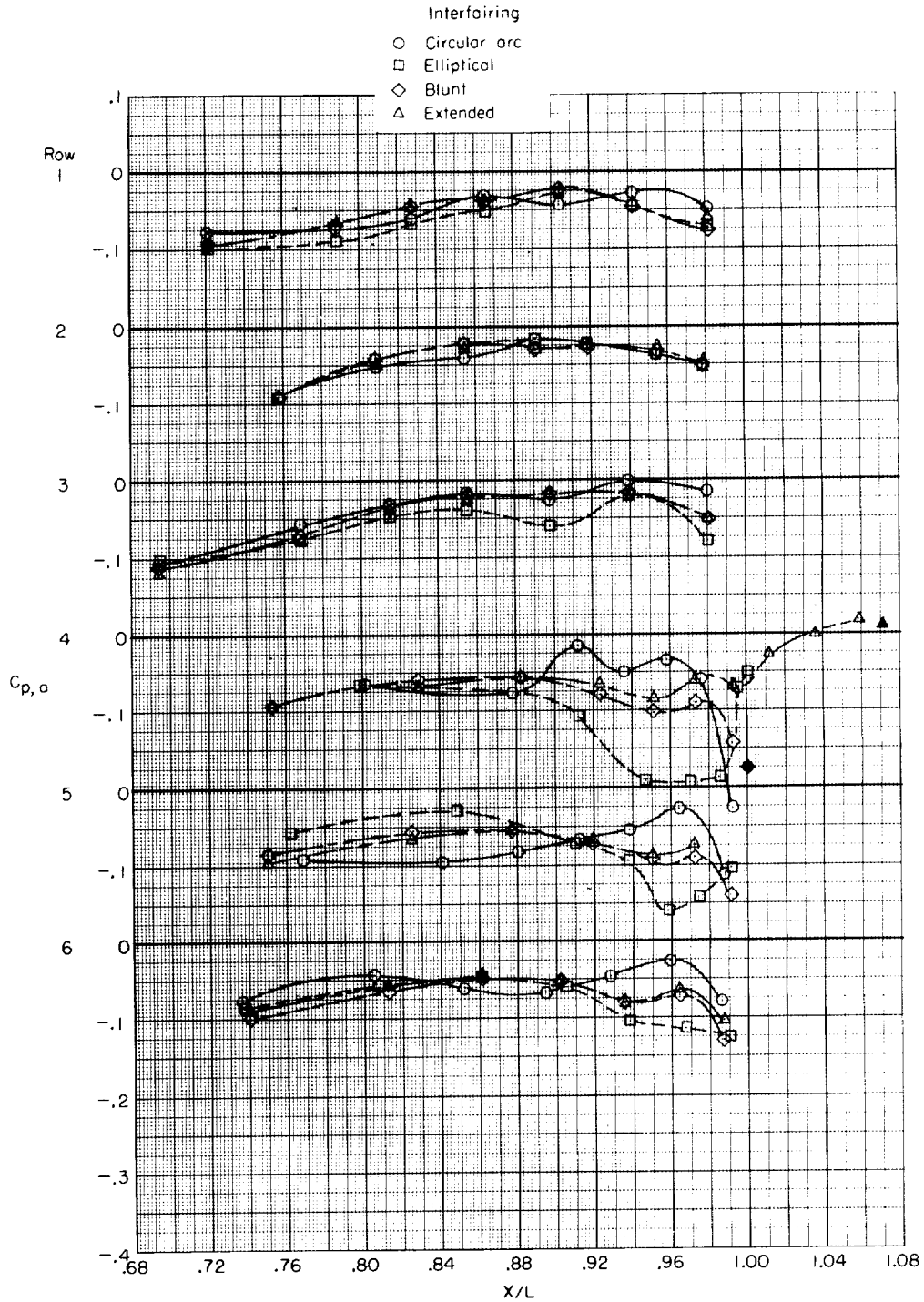
(a) Axial-force coefficients.

Figure 27.- Effect of nozzle type on afterbody performance. Elliptical interfairing; scheduled jet-pressure ratio.



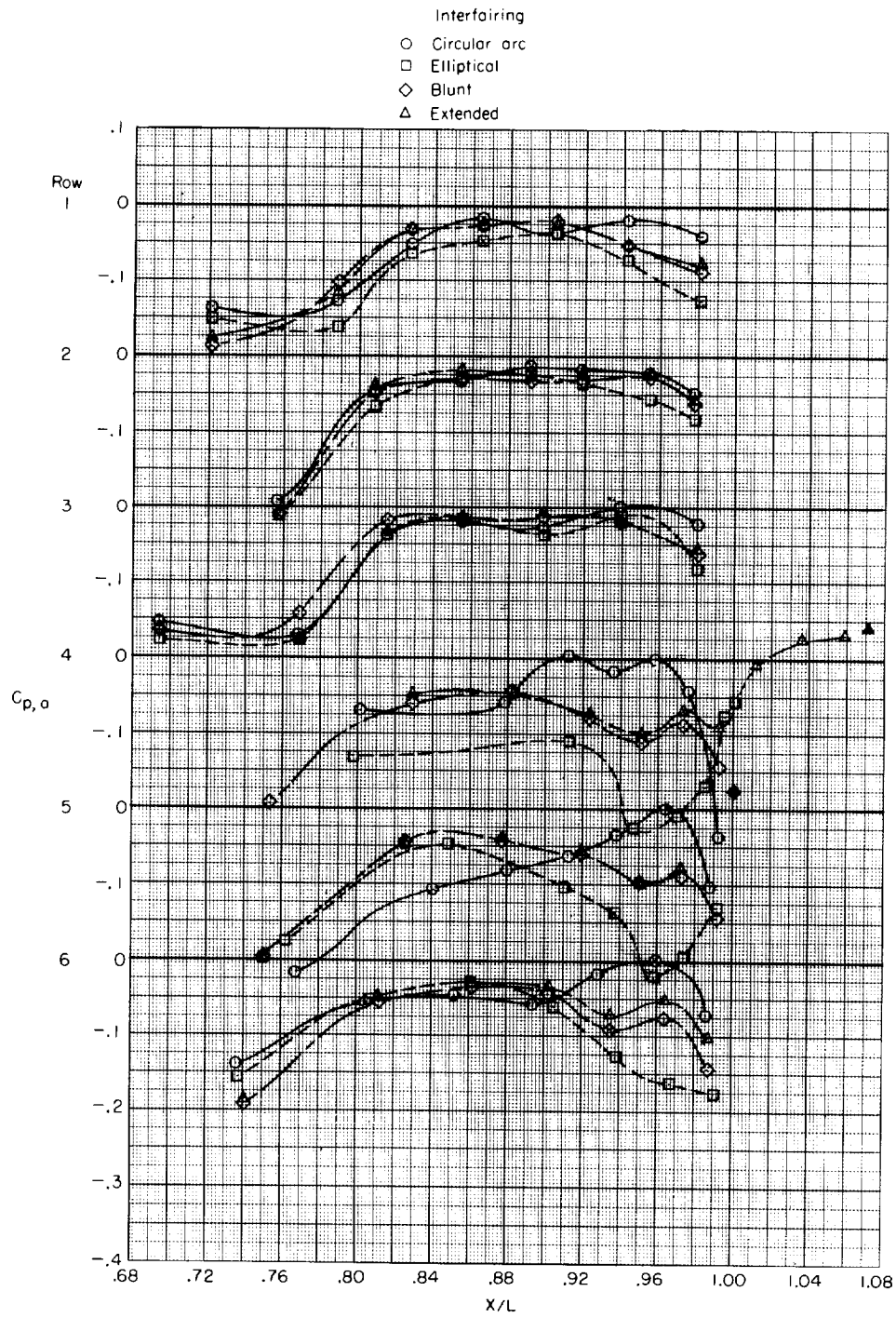
(b) Thrust-minus-axial-force ratios.

Figure 27.- Concluded.



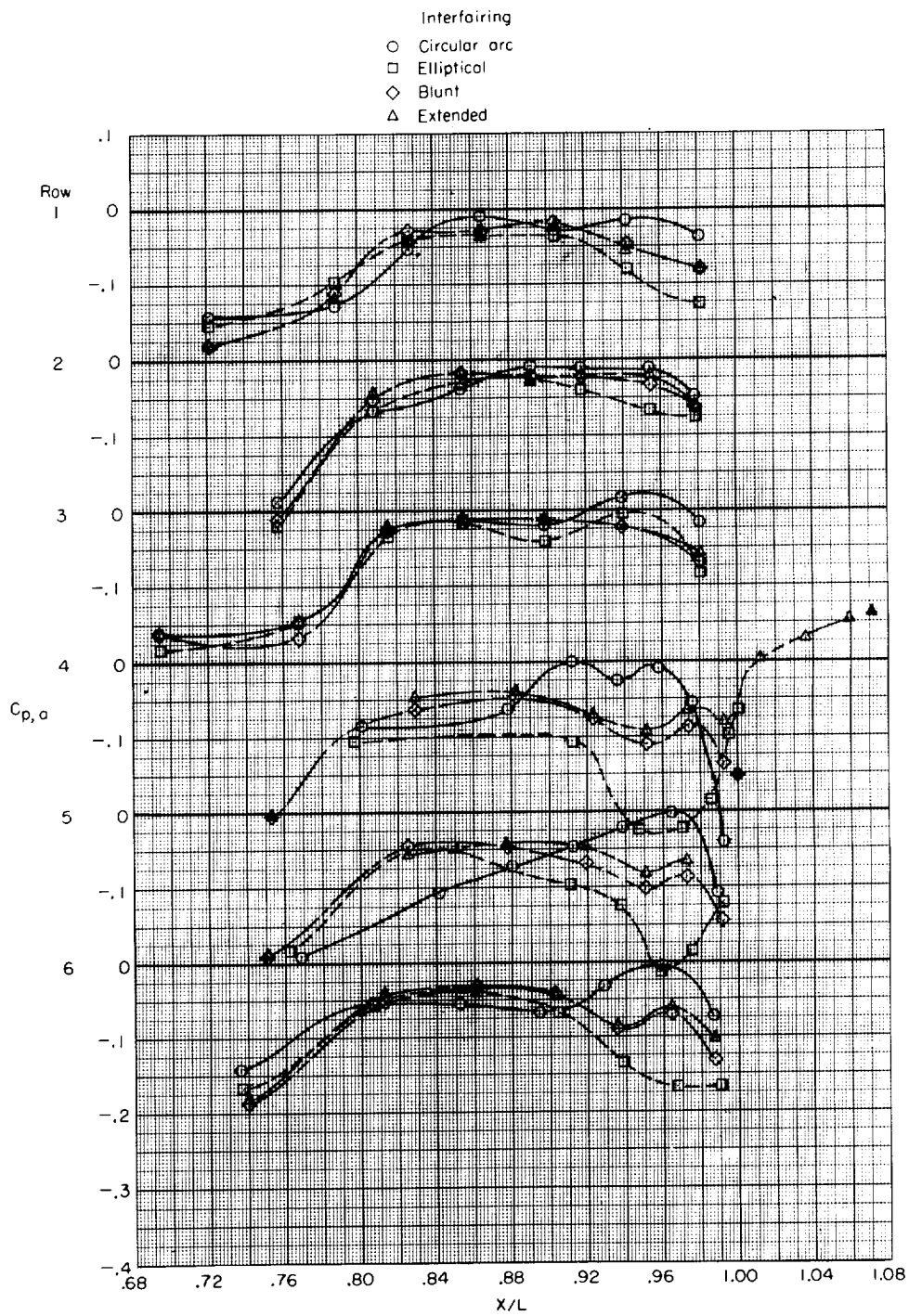
(a) Dry iris nozzles; $M = 0.60$.

Figure 28.- Effect of interfering shape on jet-off afterbody pressure distributions.



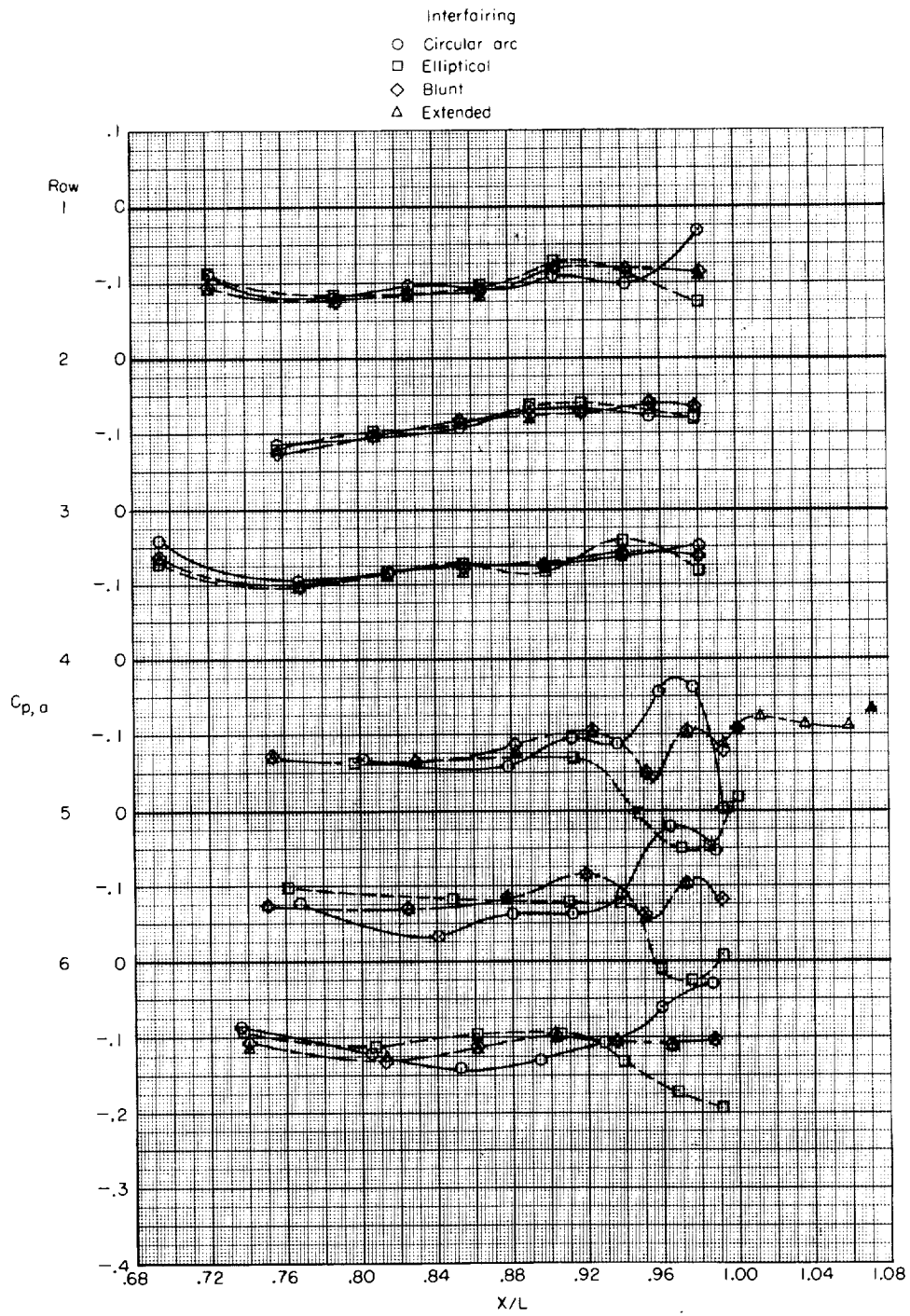
(b) Dry iris nozzles; $M = 0.95$.

Figure 28.- Continued.



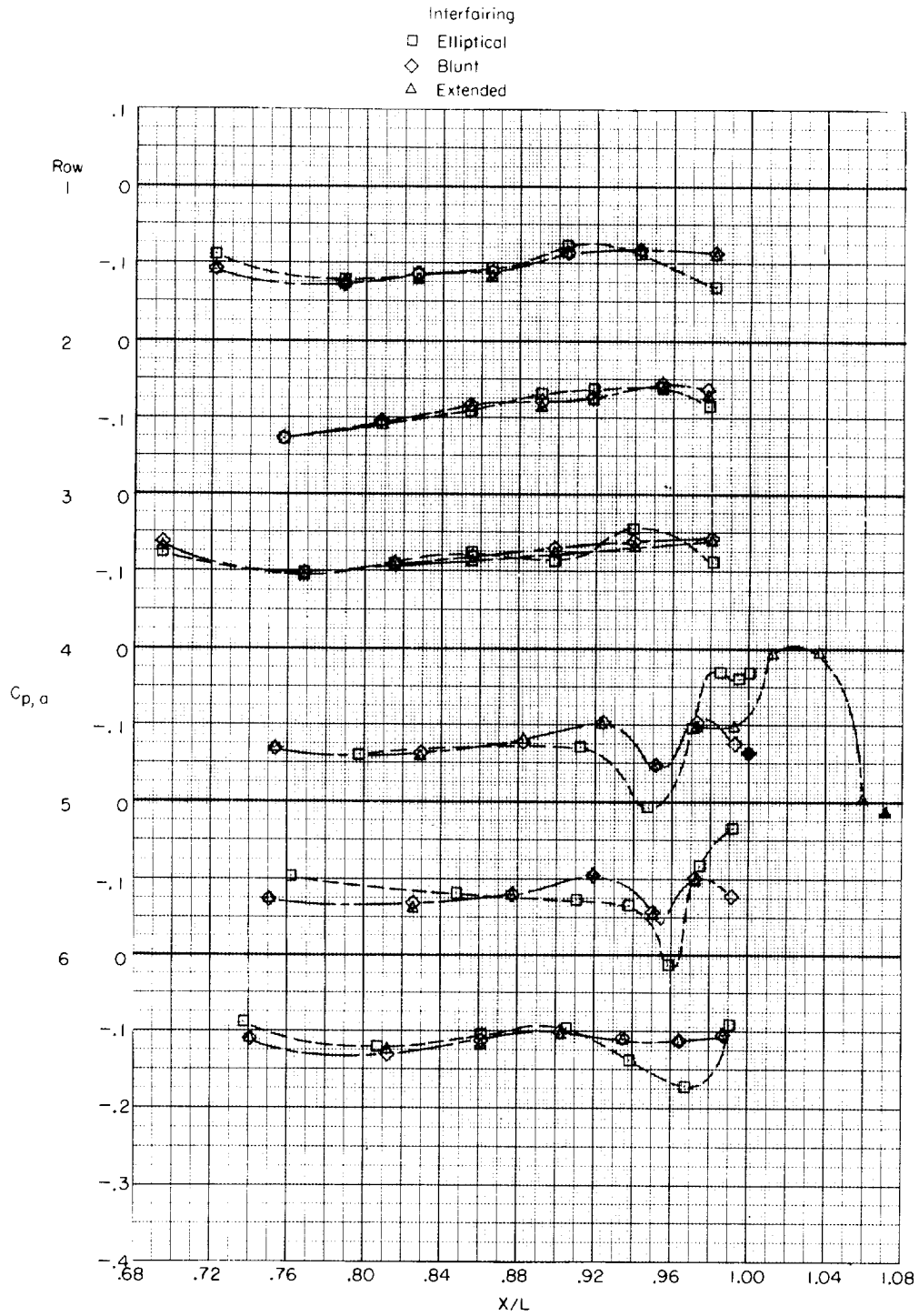
(c) Augmented iris nozzles; $M = 0.95$.

Figure 28.- Continued.



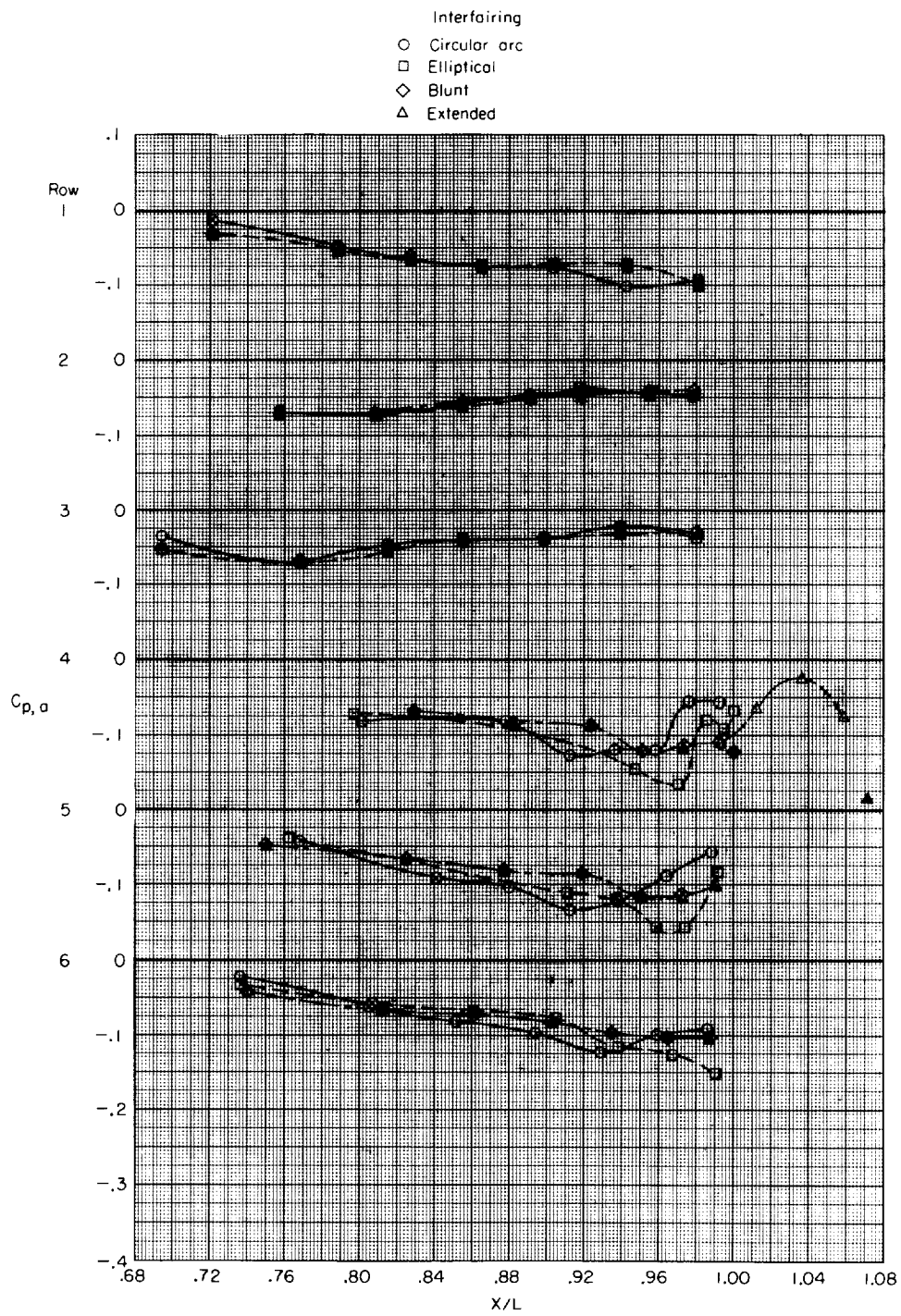
(d) Augmented iris nozzles; $M = 1.30$.

Figure 28.- Continued.



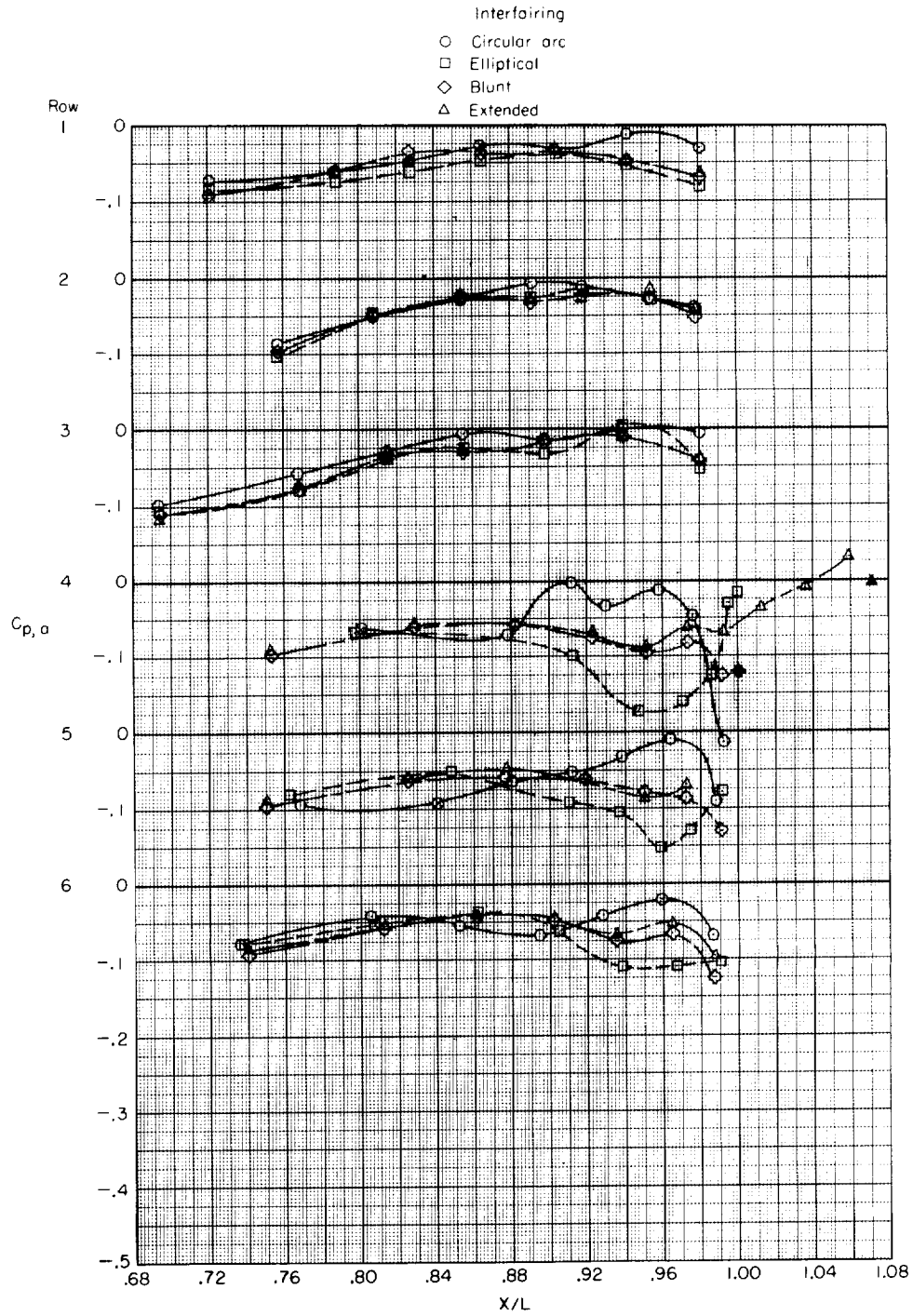
(e) Shrouded-augmented iris nozzles; $M = 1.30$.

Figure 28.- Continued.



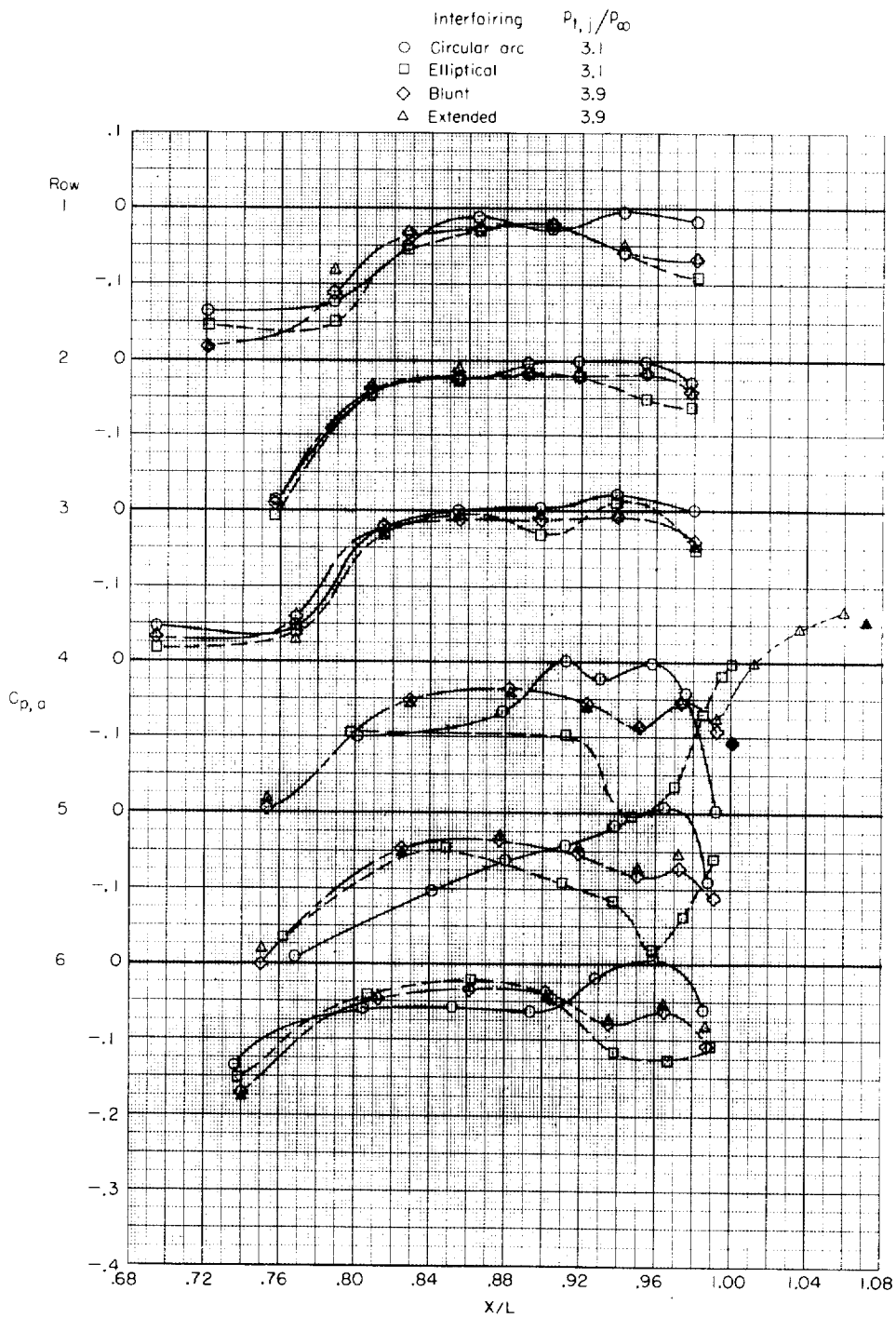
(f) Shrouded-augmented iris nozzles; $M = 2.01$.

Figure 28.- Concluded.



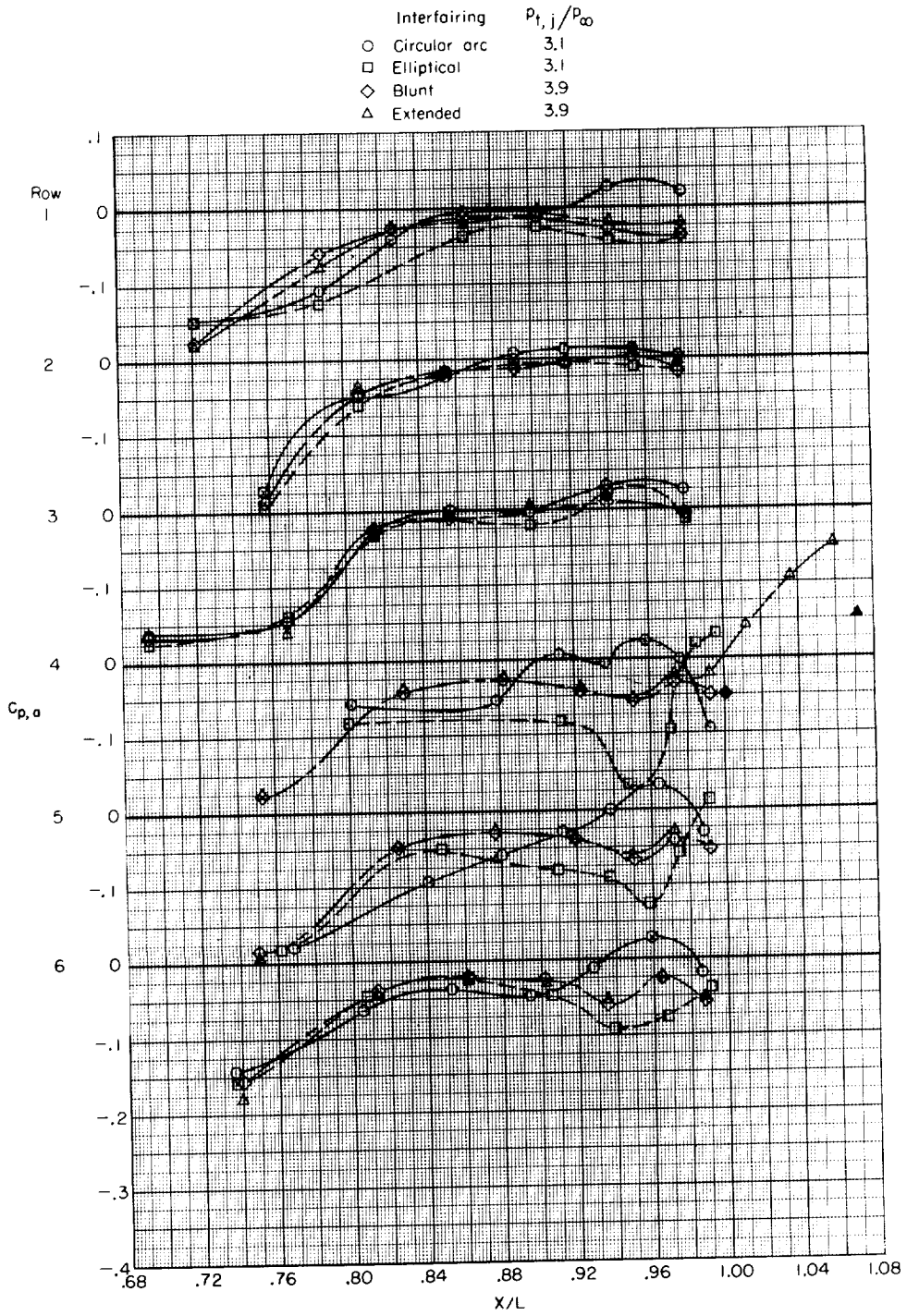
(a) Dry iris nozzles; $M = 0.60$; $p_{t,j}/p_{\infty} \approx 2.5$.

Figure 29.- Effect of interfering shape on afterbody-pressure distributions with jets on.



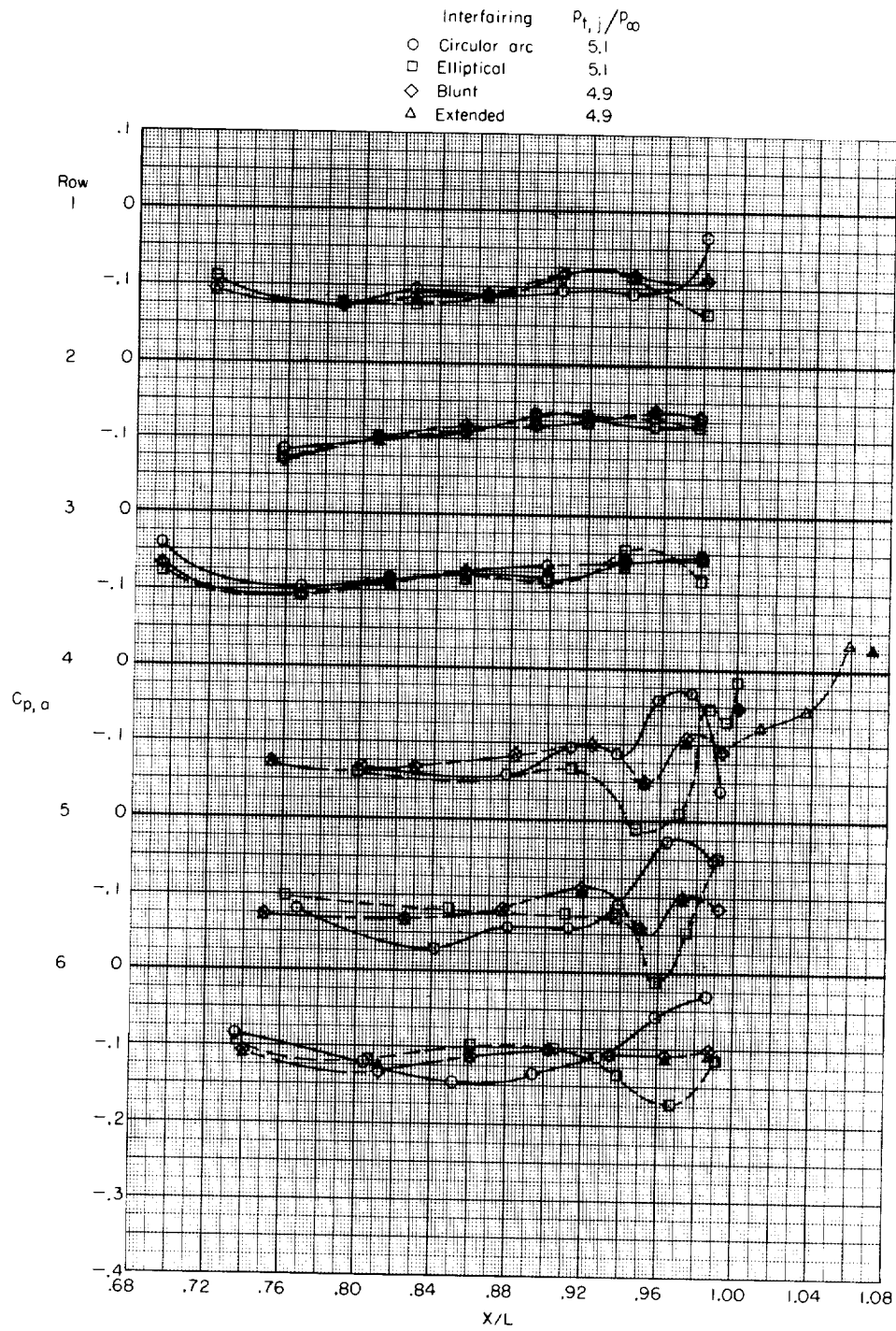
(b) Dry iris nozzles; $M = 0.95$.

Figure 29.- Continued.



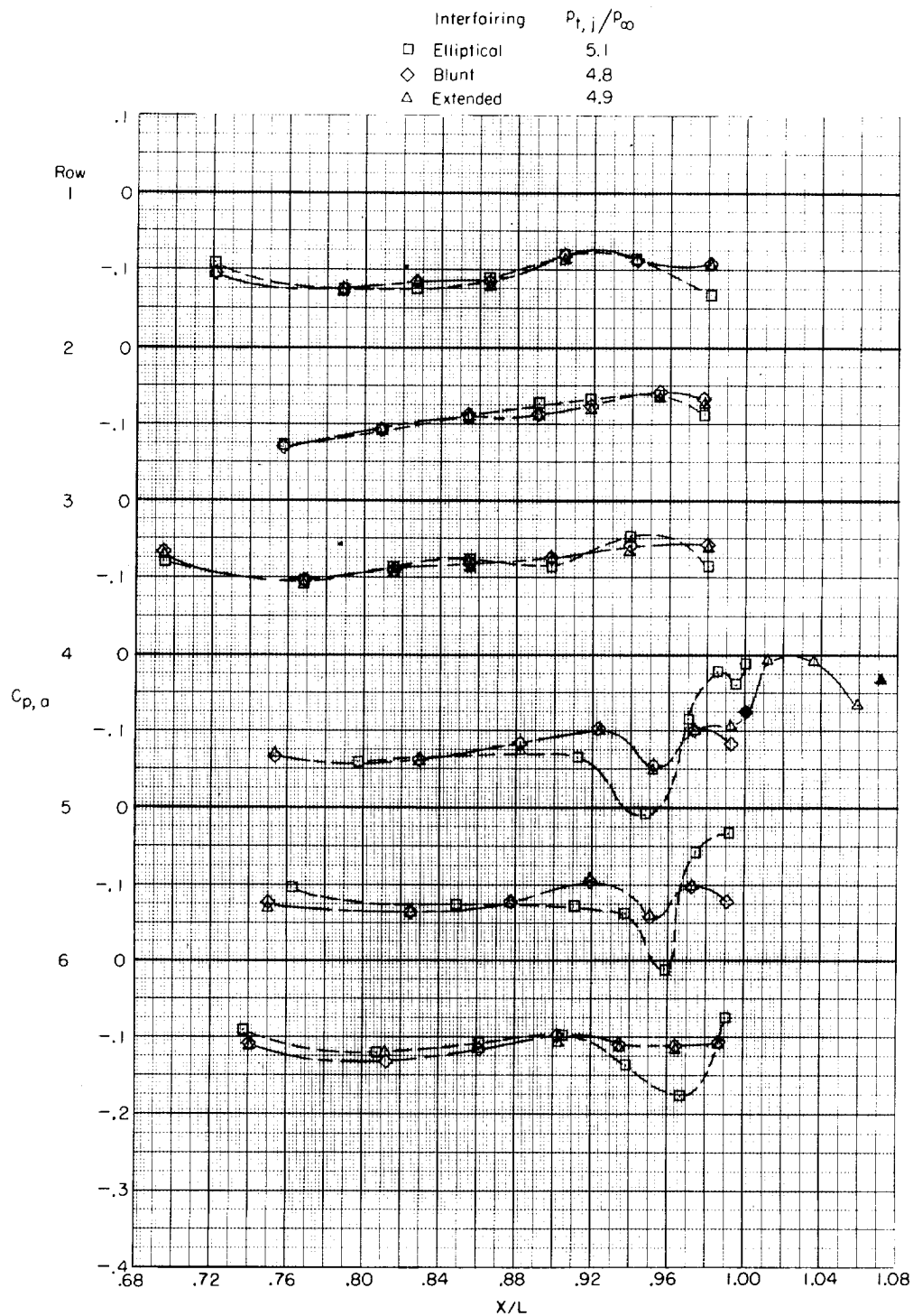
(c) Augmented iris nozzles; $M = 0.95$.

Figure 29.- Continued.



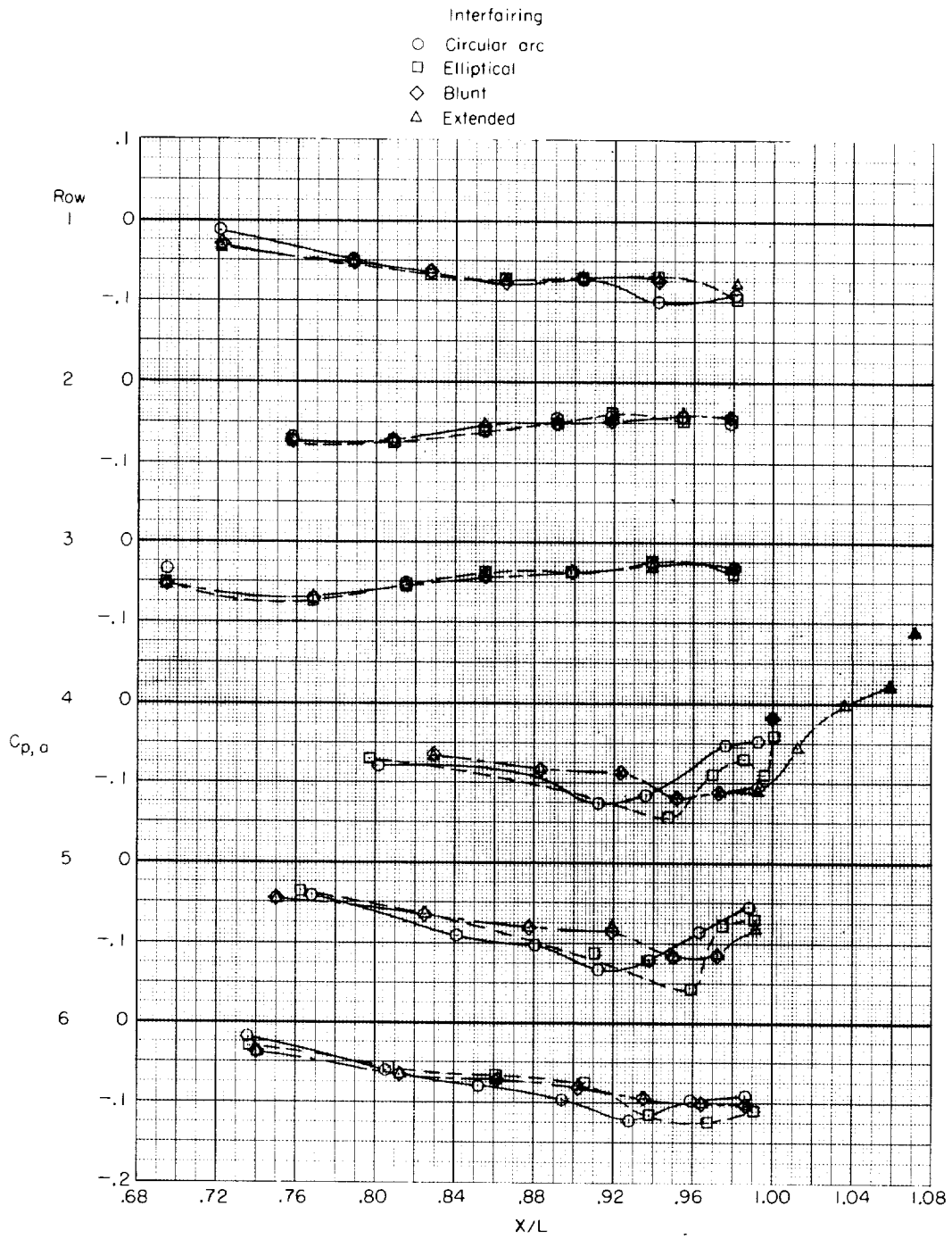
(d) Augmented iris nozzles; $M = 1.30$.

Figure 29.- Continued.



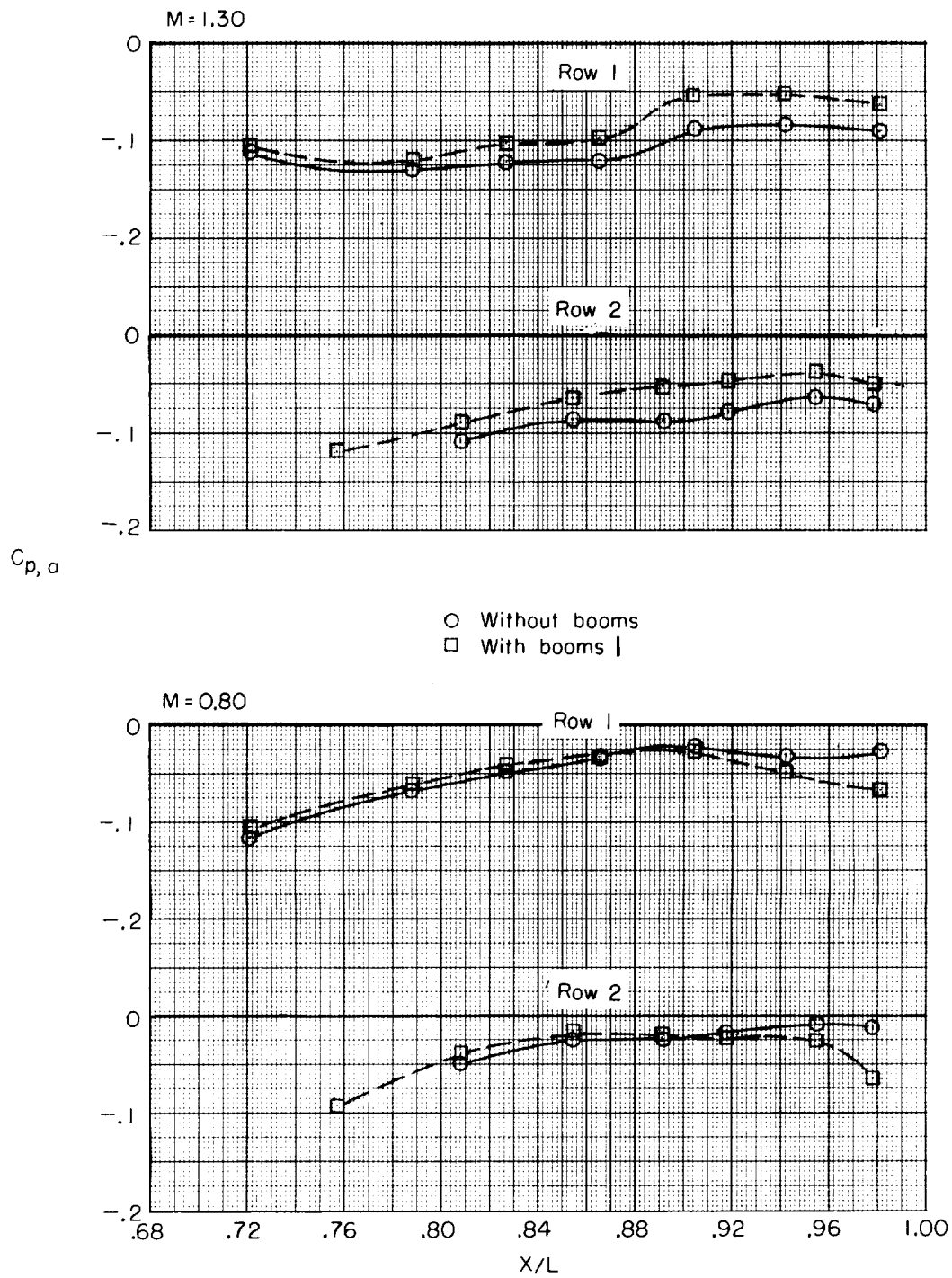
(e) Shrouded-augmented iris nozzles; $M = 1.30$.

Figure 29.- Continued.



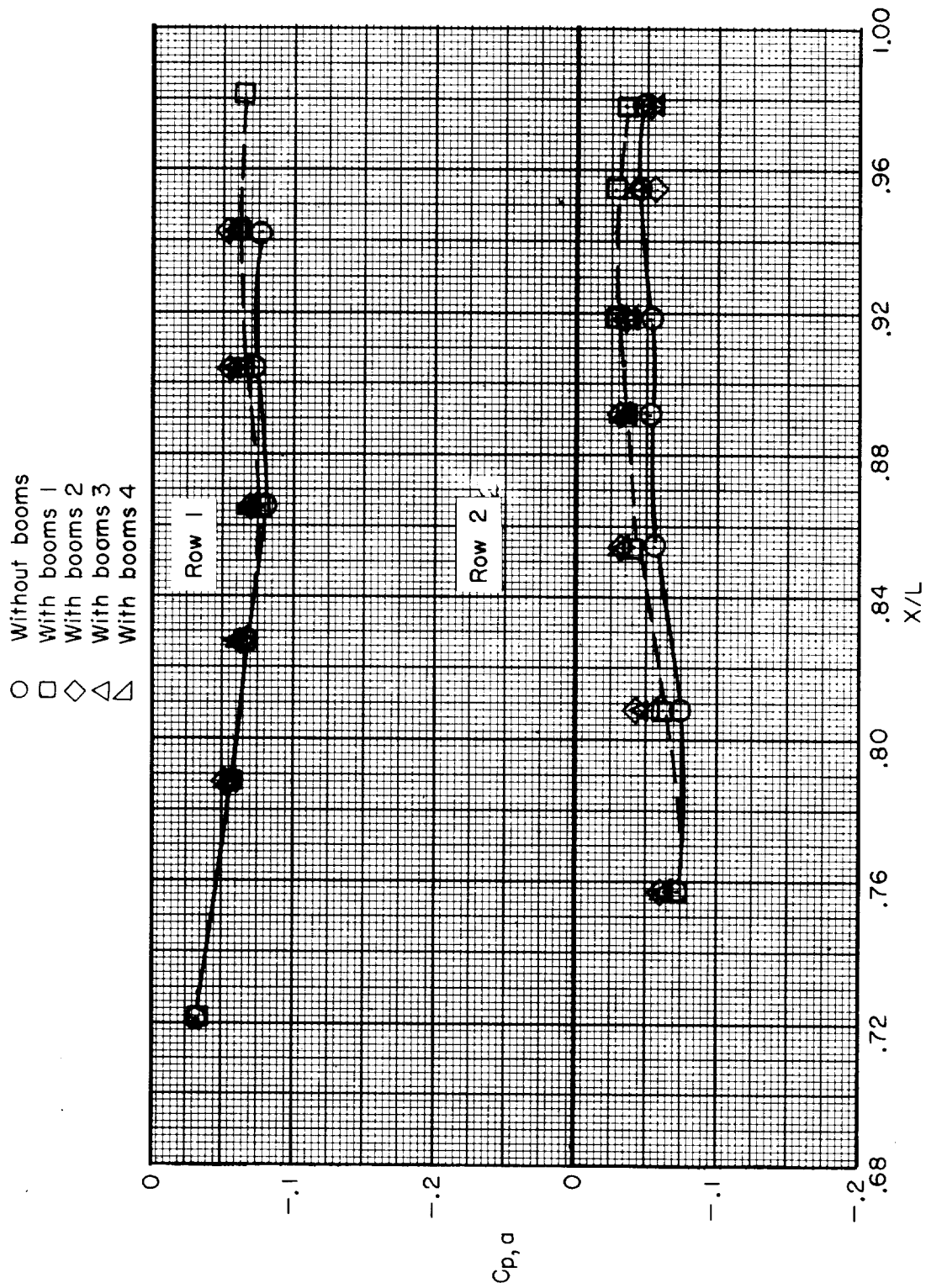
(f) Shrouded-augmented iris nozzles; $M = 2.01$; $p_{t, j}/p_{\infty} \approx 10.0$.

Figure 29.- Concluded.



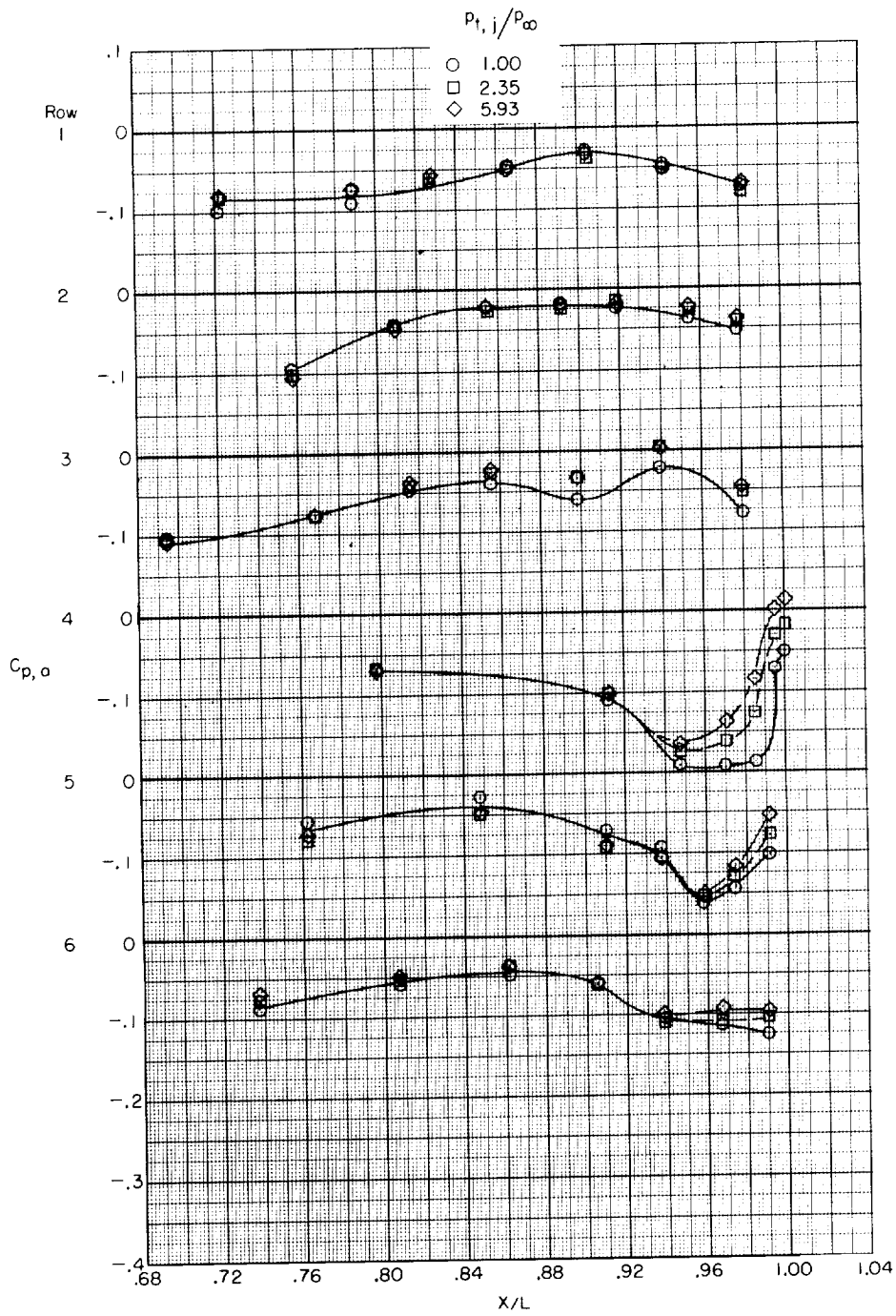
(a) Subsonic and transonic speeds.

Figure 30.- Effect of outboard booms on jet-off afterbody pressure distributions.



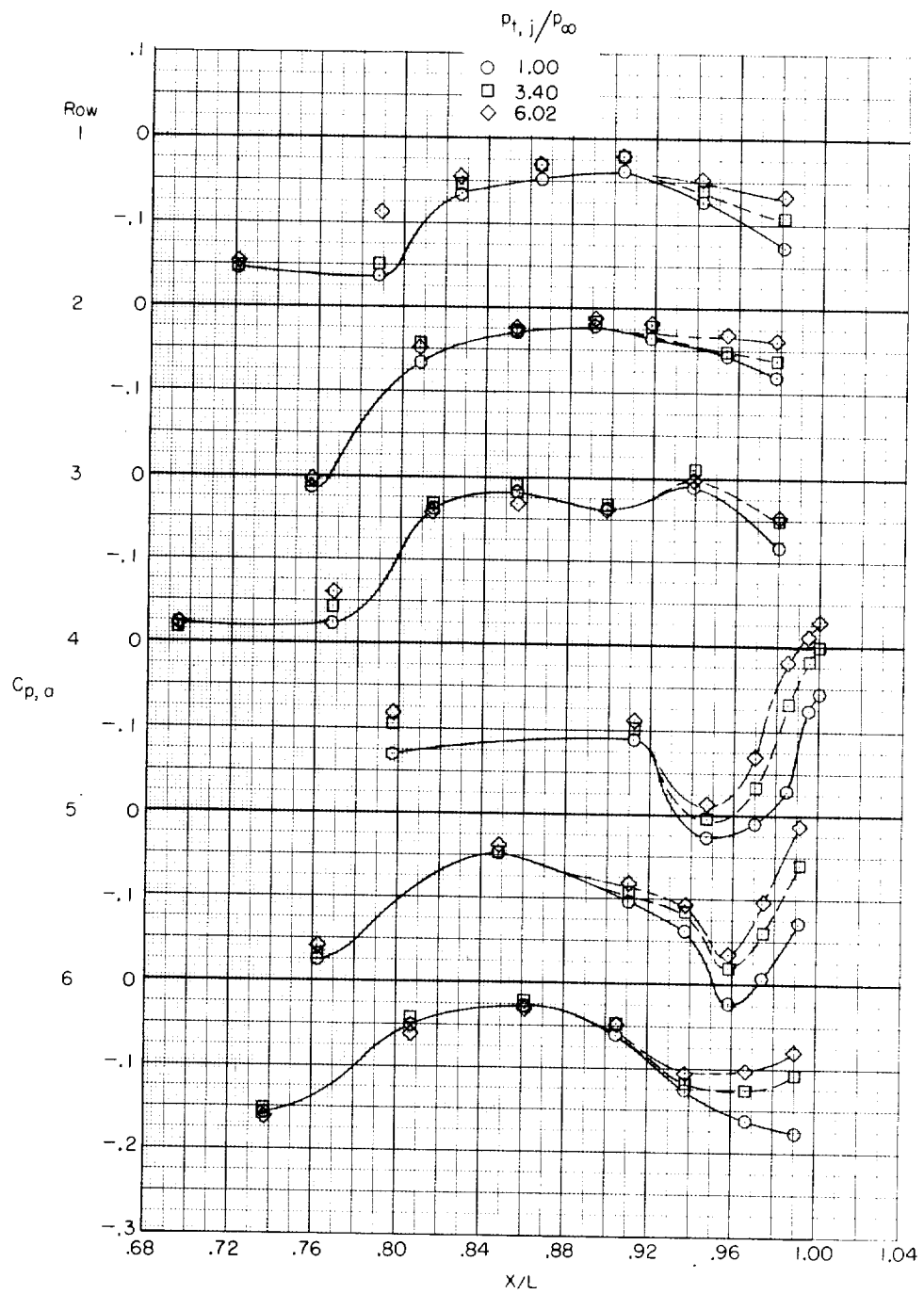
(b) $M = 2.01$.

Figure 30.- Concluded.



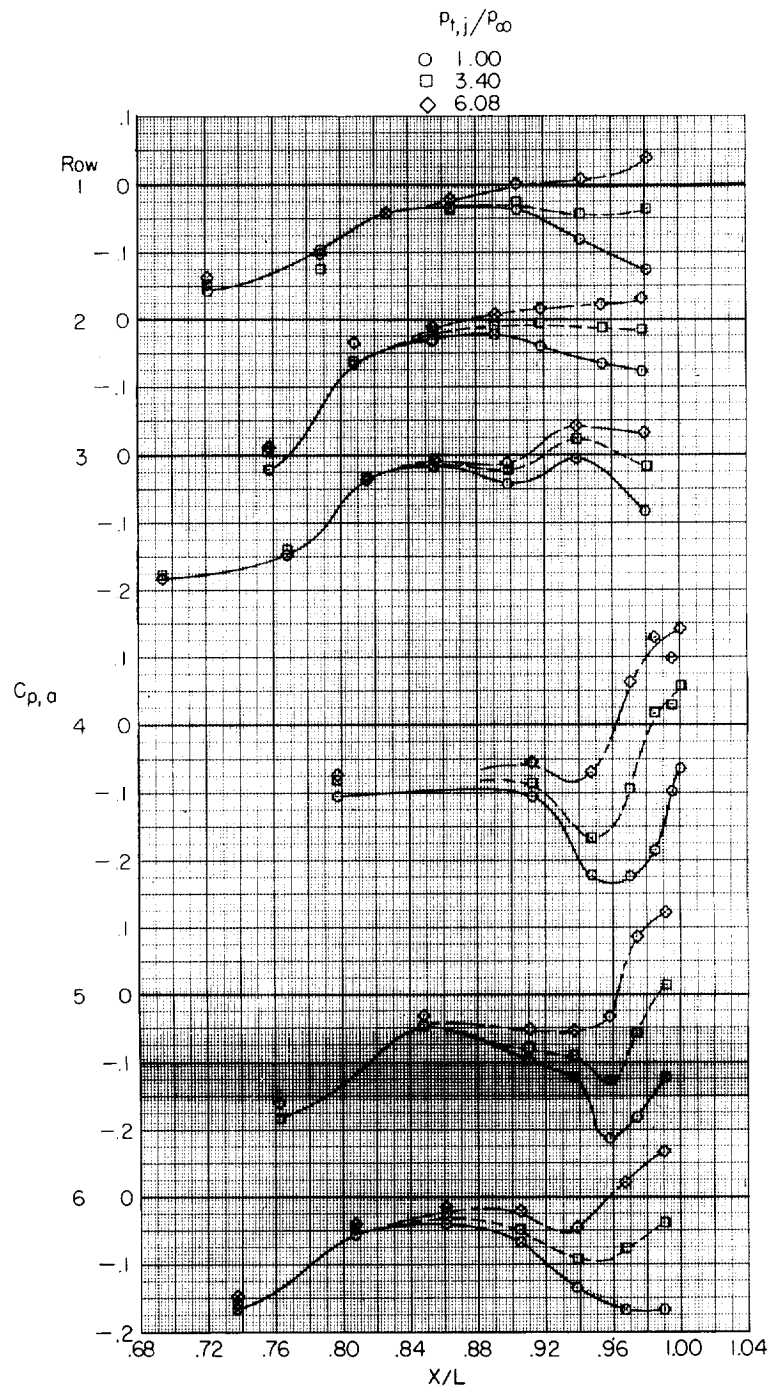
(a) Dry iris nozzles; $M = 0.60$.

Figure 31.- Effect of jet operation on pressure distribution of afterbody with elliptical interfairing and iris nozzles.



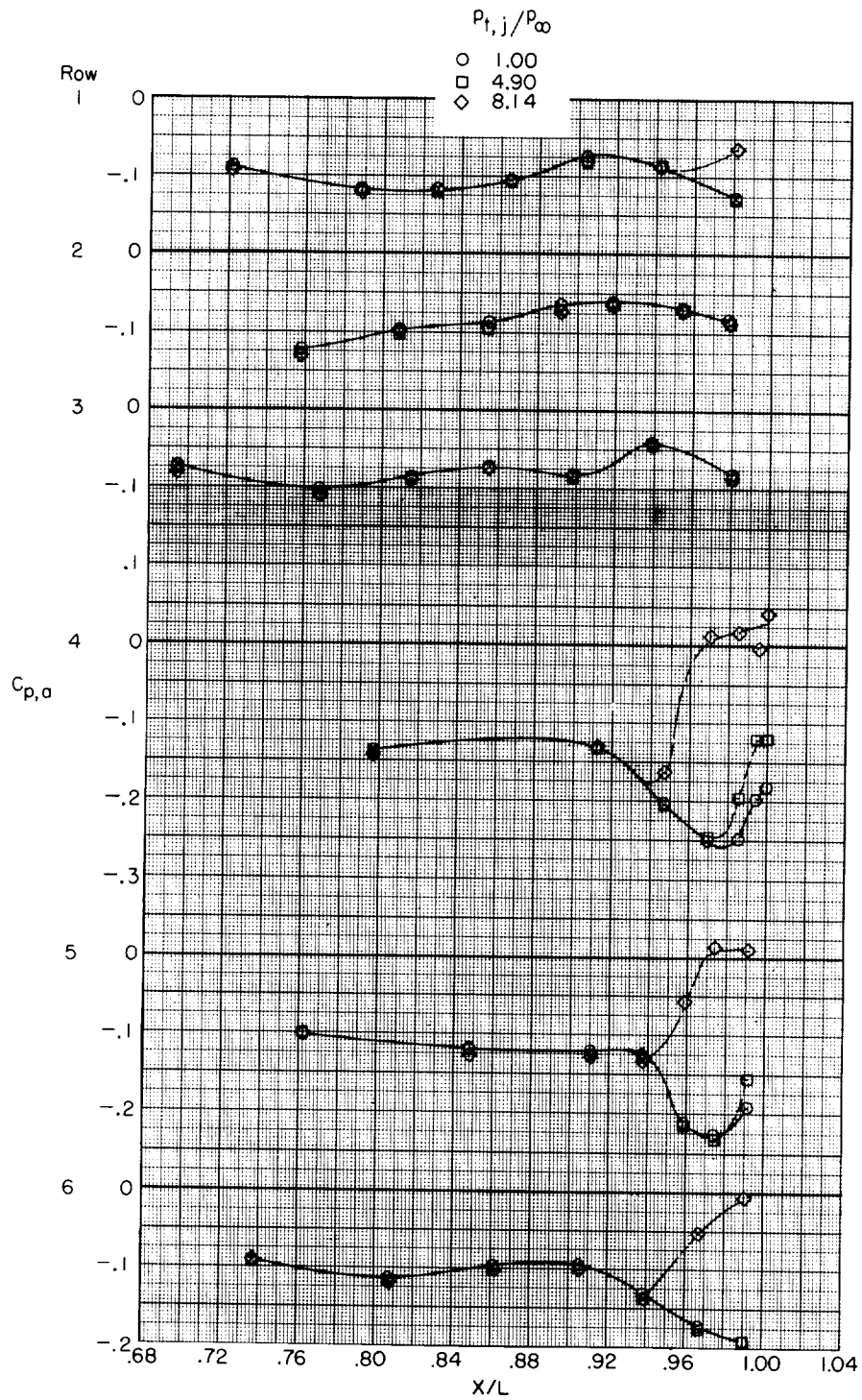
(b) Dry iris nozzles; $M = 0.95$.

Figure 31.- Continued.



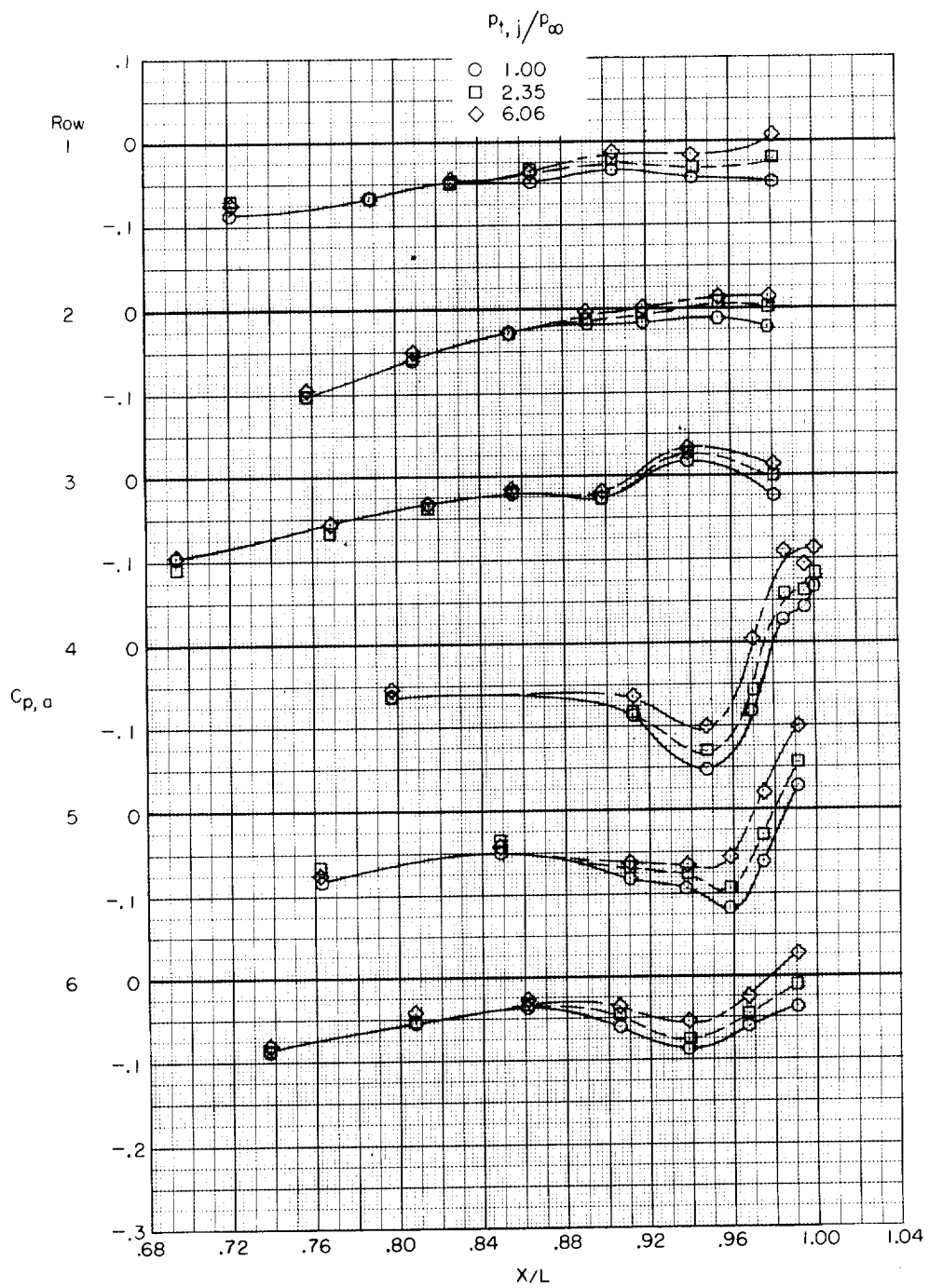
(c) Augmented iris nozzles; $M = 0.95$.

Figure 31.- Continued.



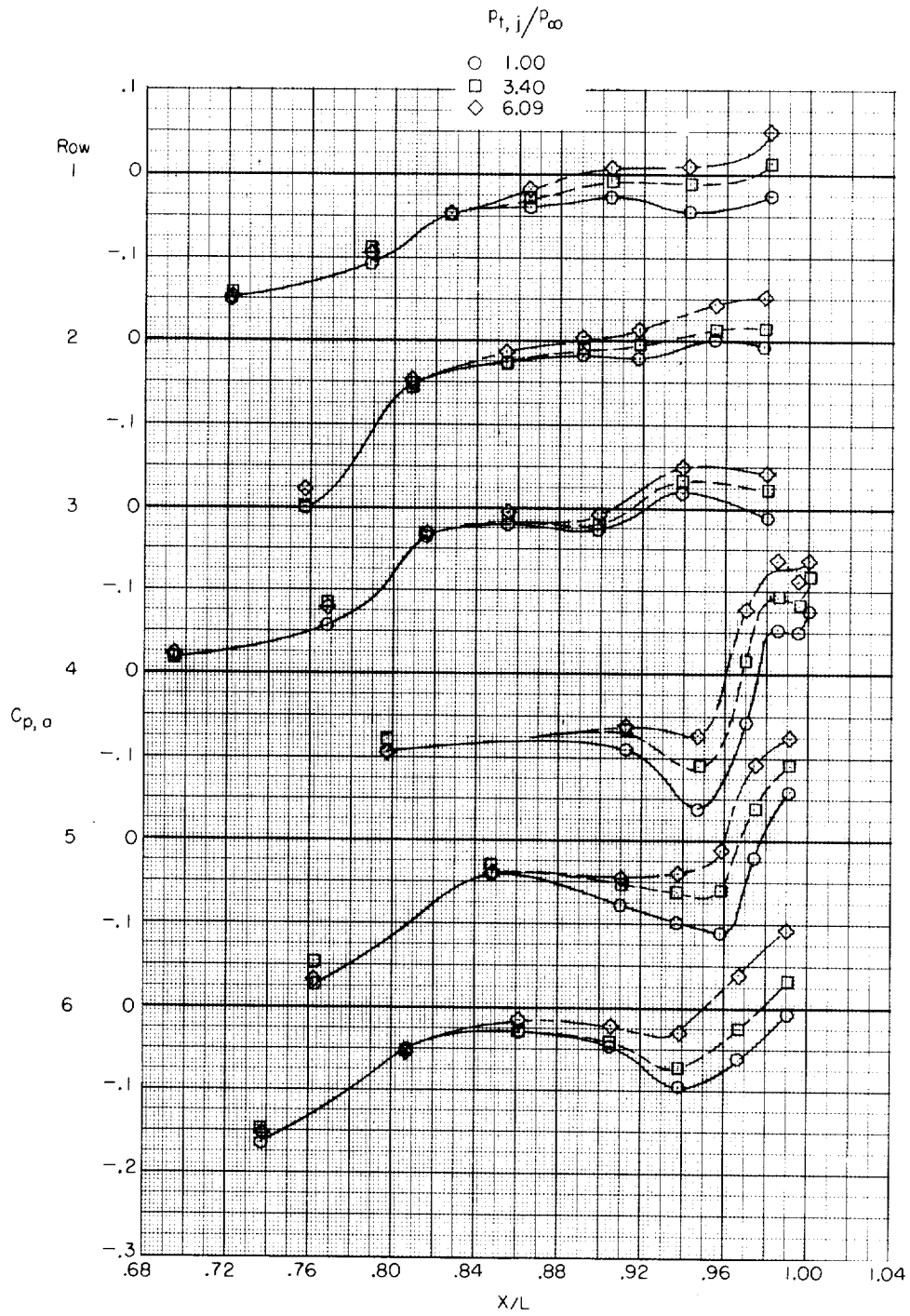
(d) Augmented iris nozzles; $M_j = 1.30$.

Figure 31.- Continued.



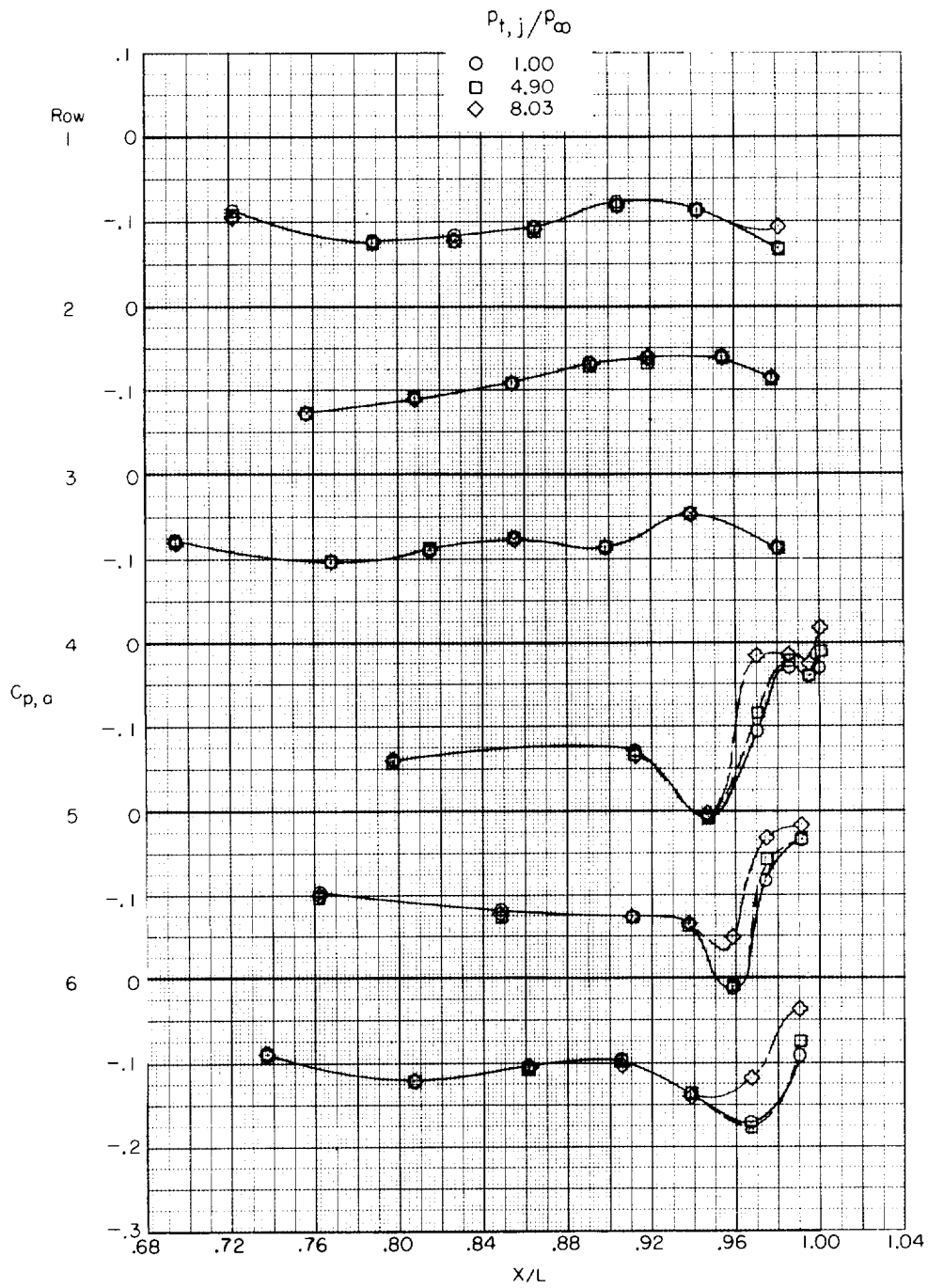
(e) Shrouded-augmented iris nozzles; $M = 0.60$.

Figure 31.- Continued.



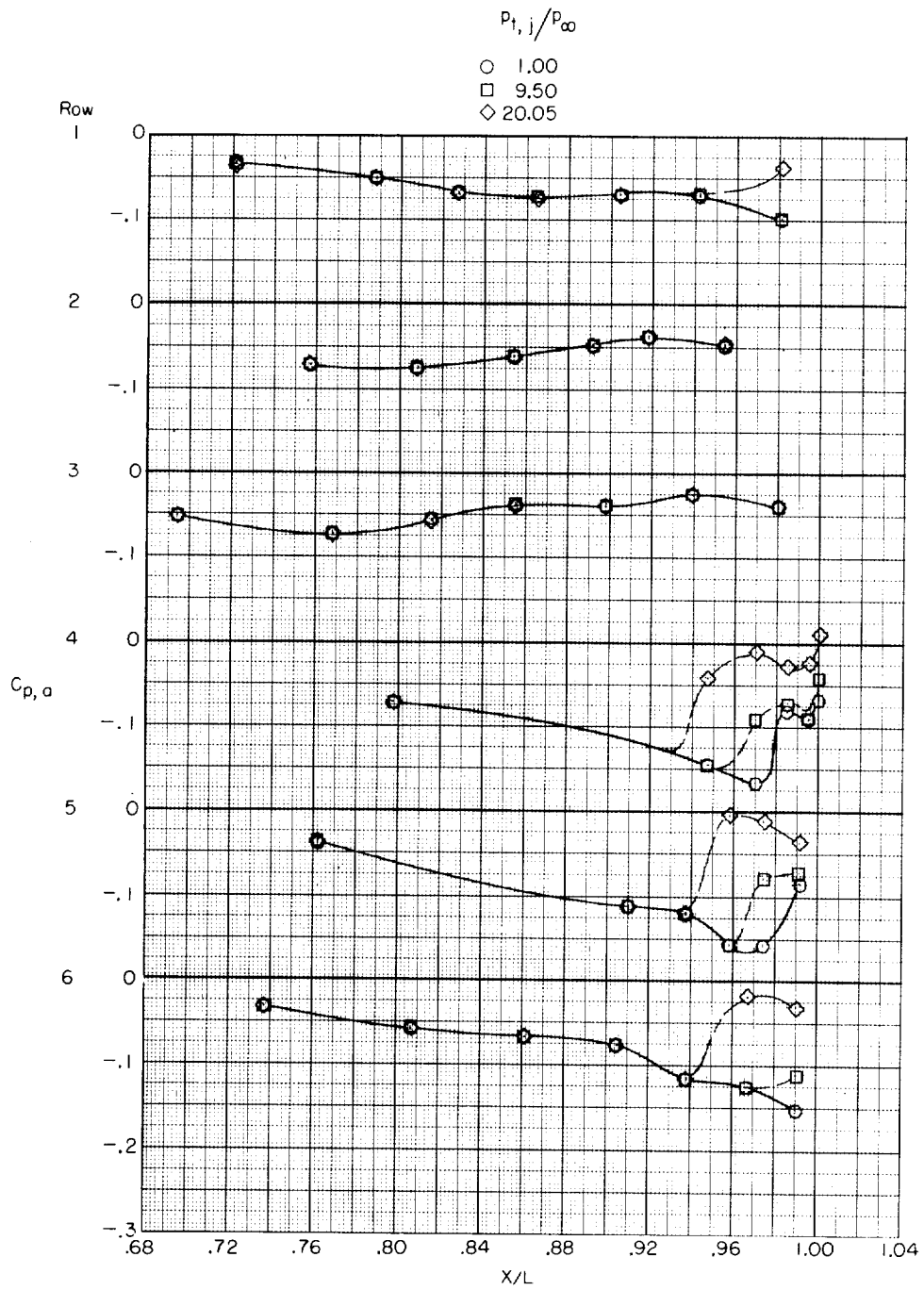
(f) Shrouded-augmented iris nozzles; $M = 0.95$.

Figure 31.- Continued.



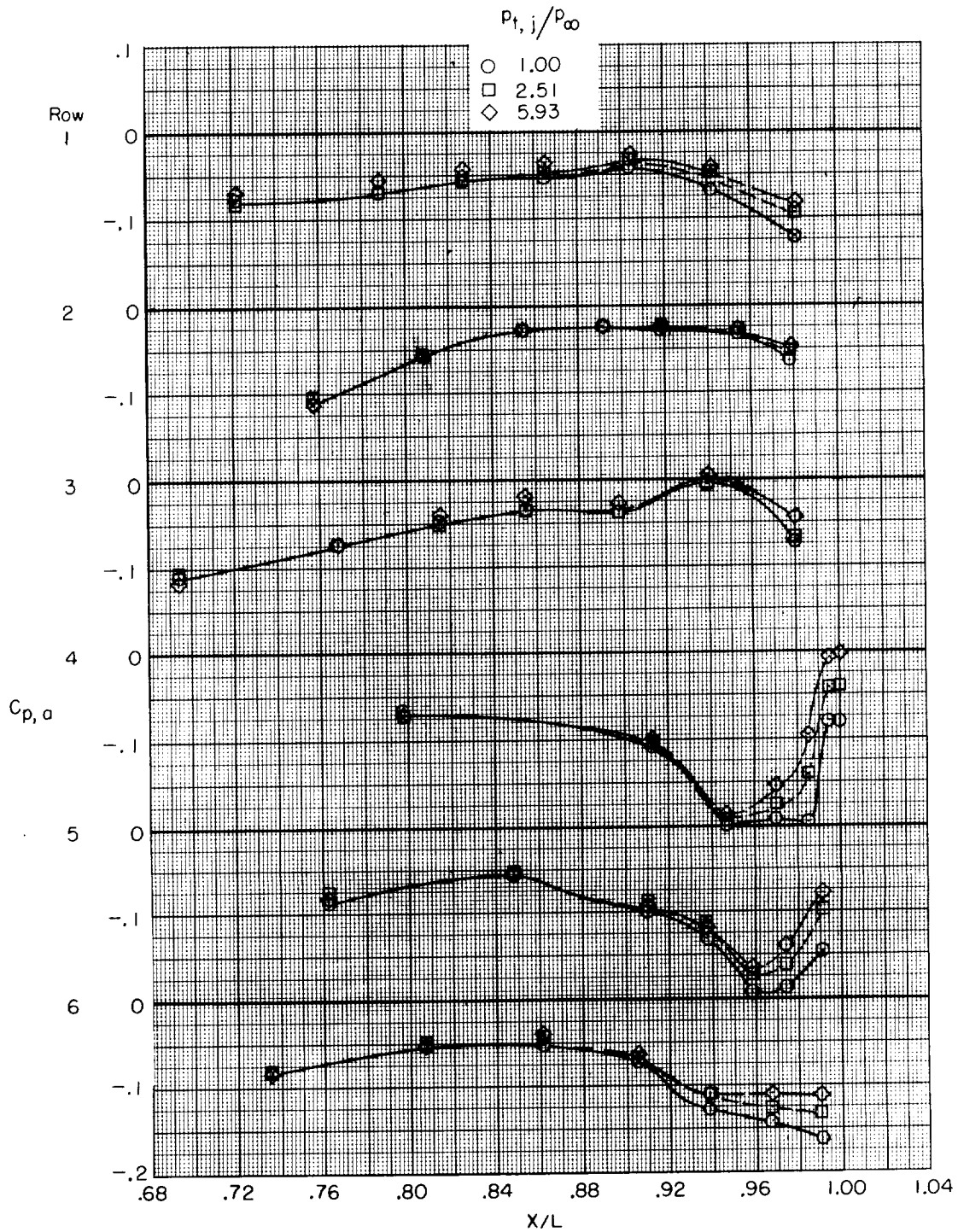
(g) Shrouded-augmented iris nozzles; $M = 1.30$.

Figure 31.- Continued.



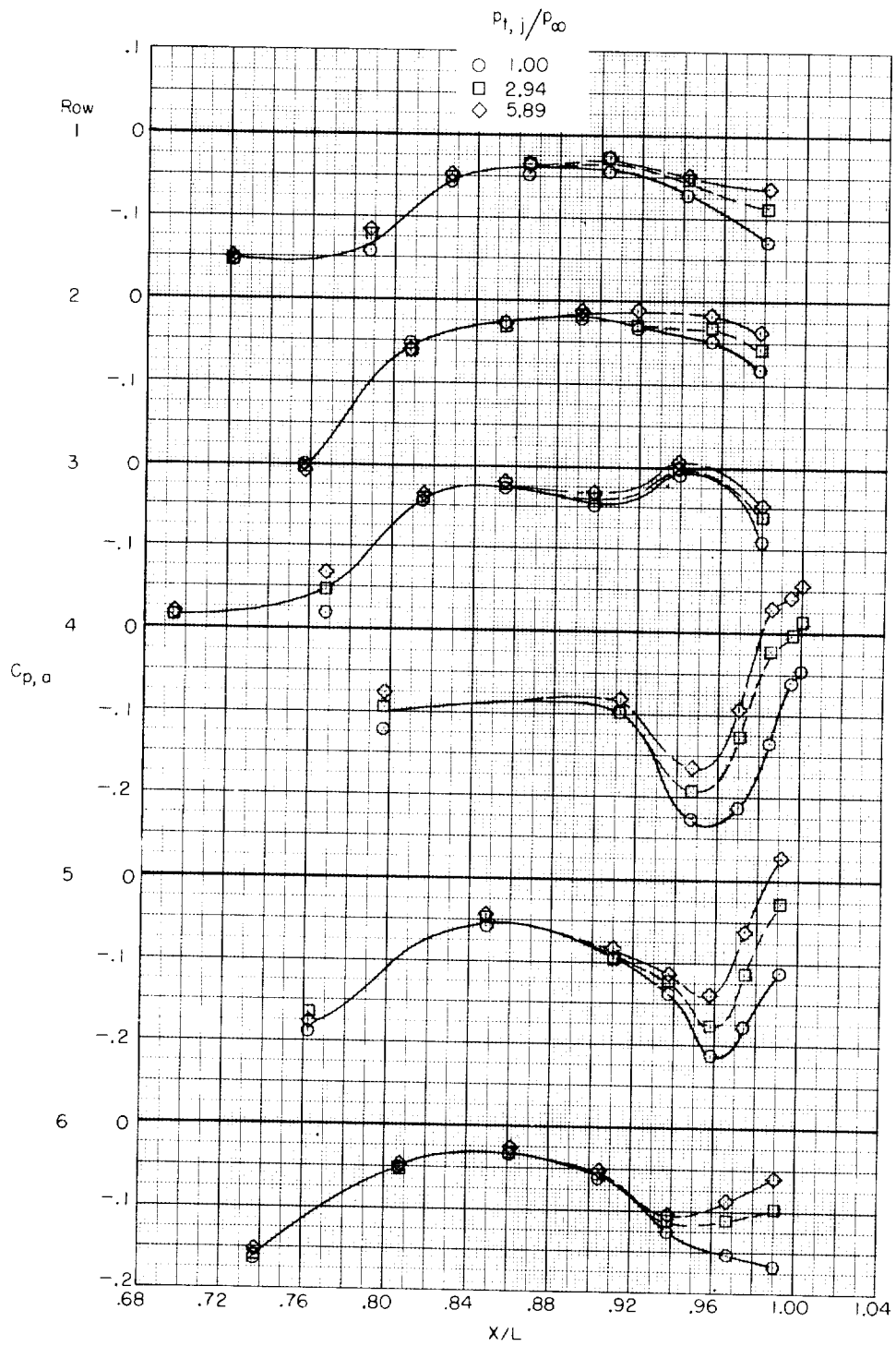
(h) Shrouded-augmented iris nozzles; $M = 2.01$.

Figure 31.- Concluded.



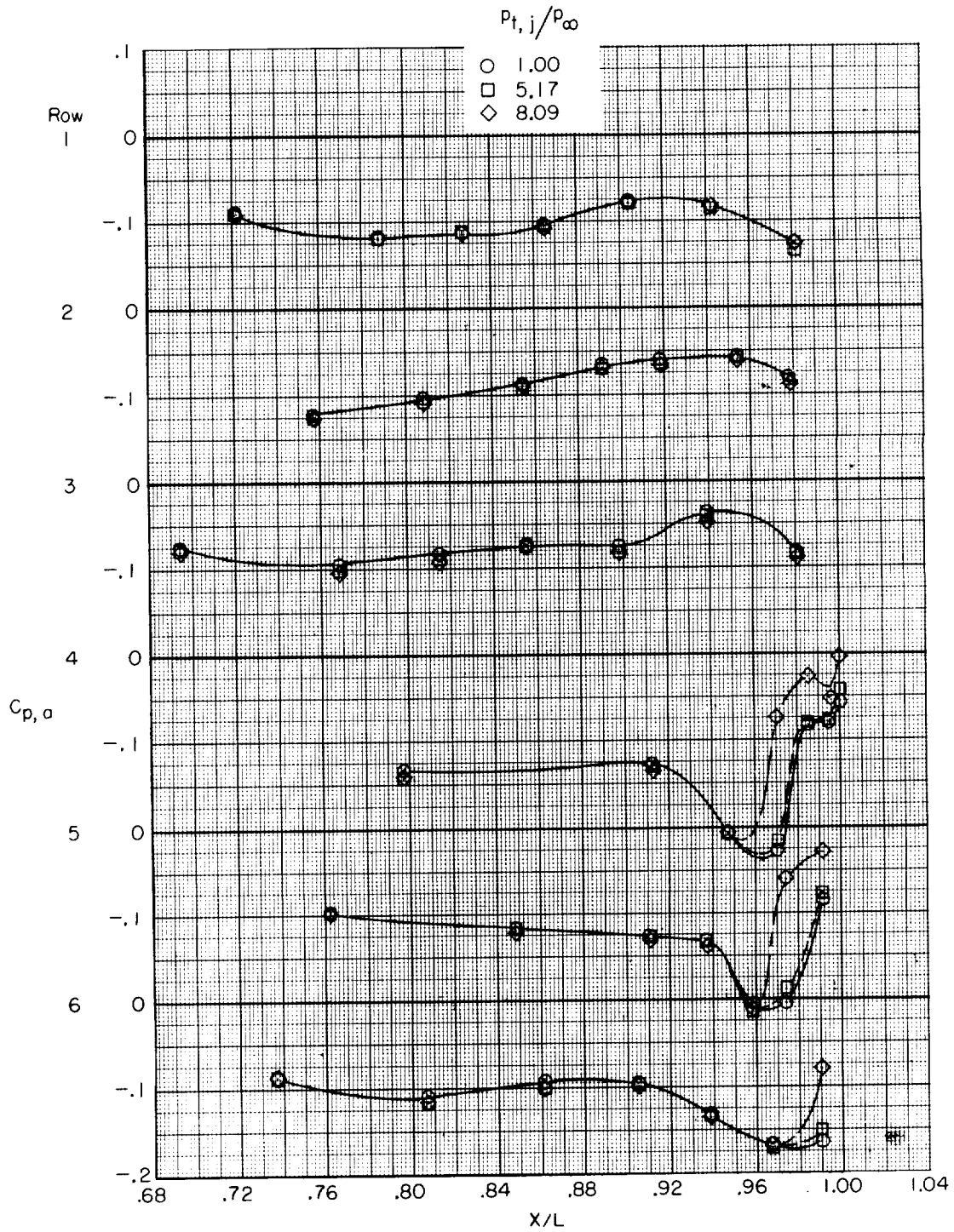
(a) Dry convergent-divergent nozzles; $M = 0.60$.

Figure 32.- Effect of nozzle power setting on pressure distributions for afterbody with elliptical interfering and convergent-divergent nozzles.



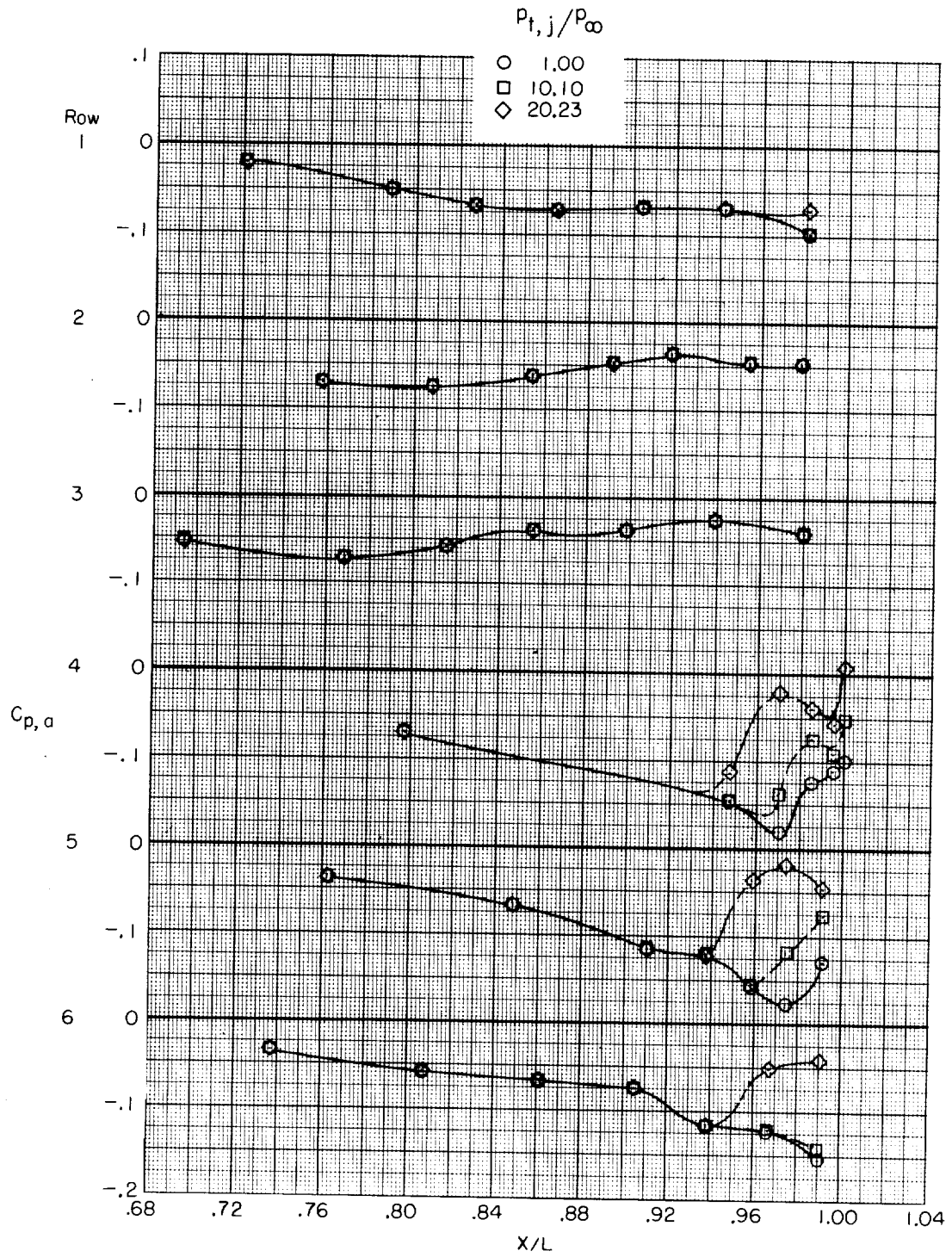
(b) Dry convergent-divergent nozzles; $M = 0.95$.

Figure 32.- Continued.



(c) Augmented convergent-divergent nozzles; $M = 1.30$.

Figure 32.- Continued.



(d) Augmented convergent-divergent nozzles; $M = 2.01$.

Figure 32.- Concluded.

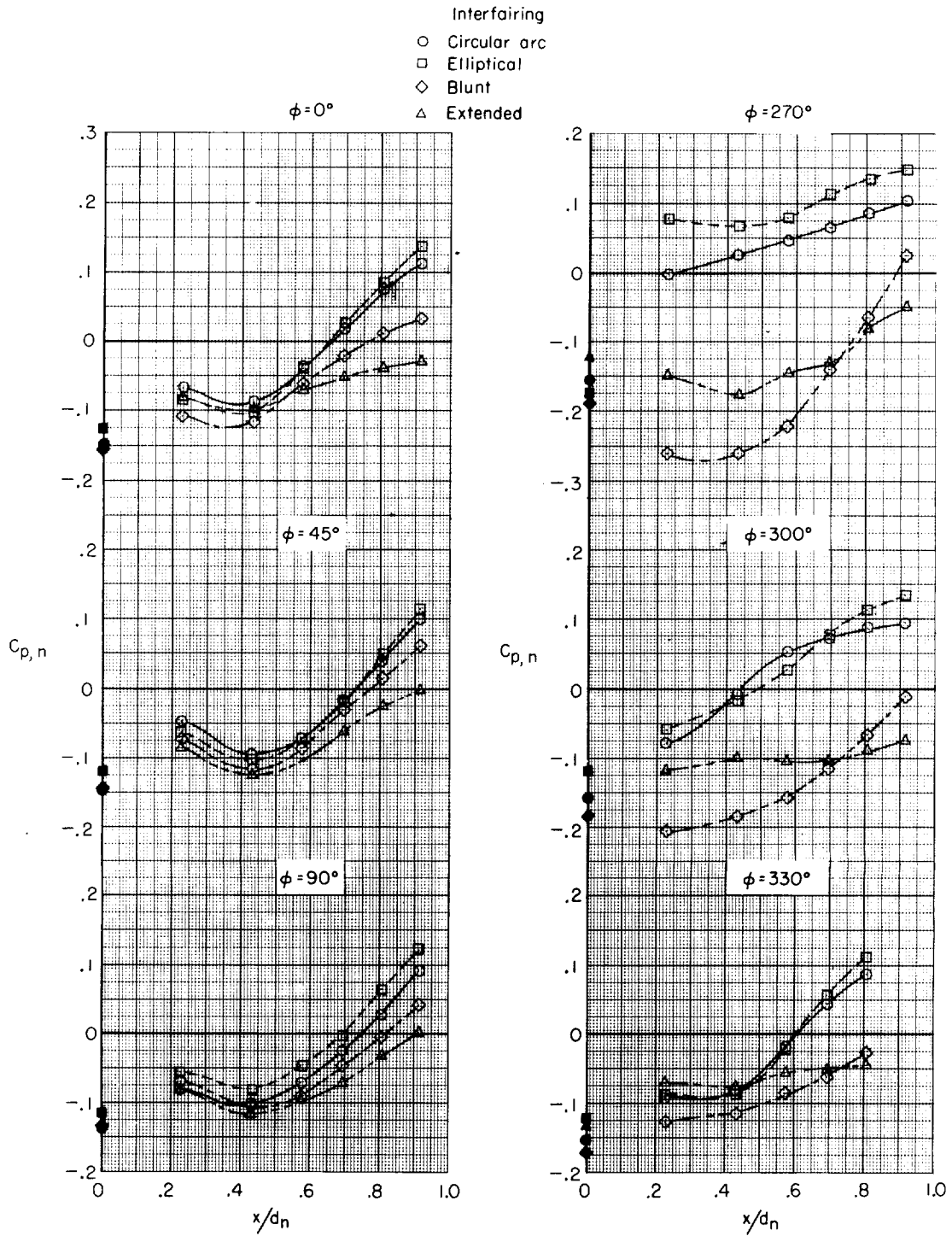


Figure 33.- Effect of interfairing shape on nozzle pressure distribution with jets off.

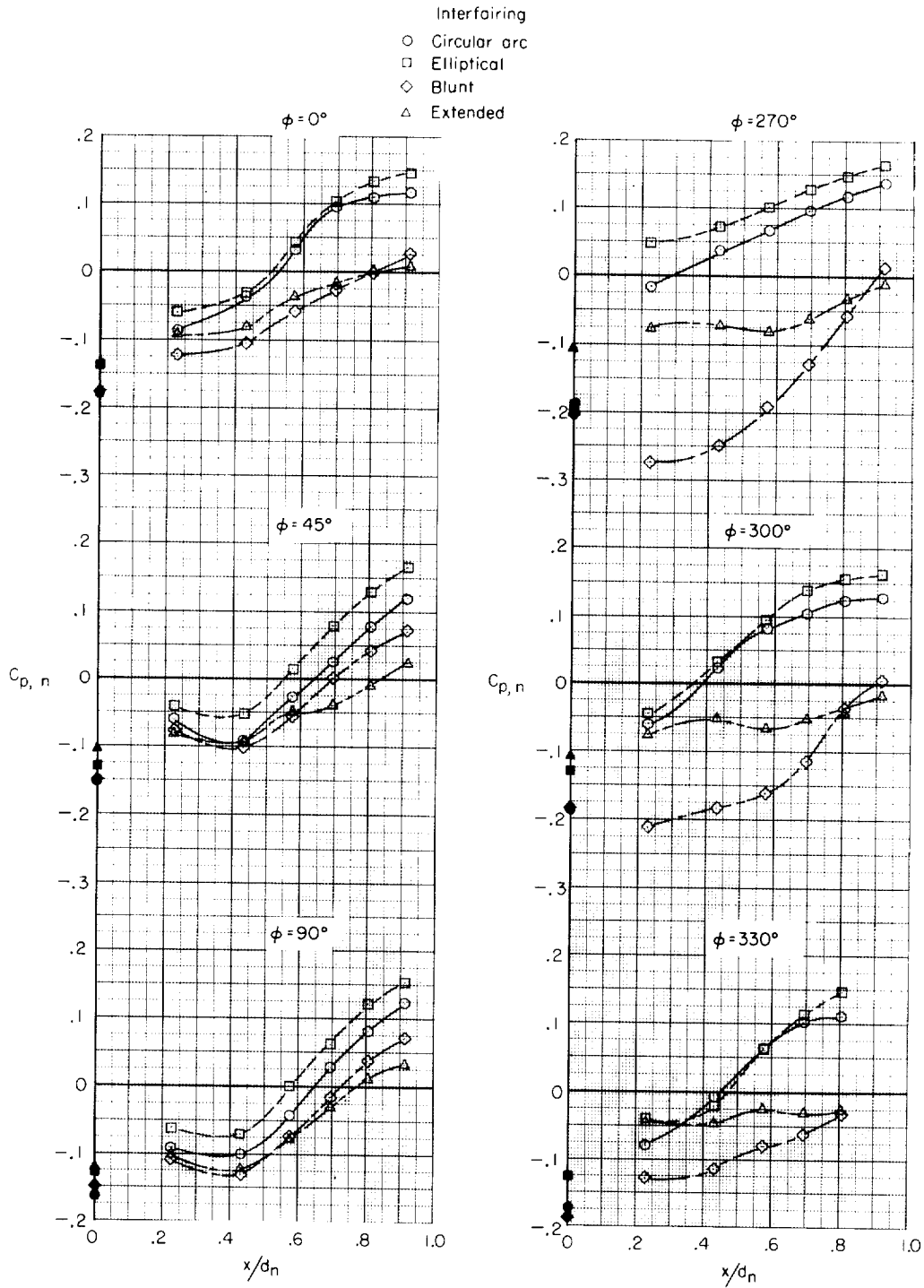
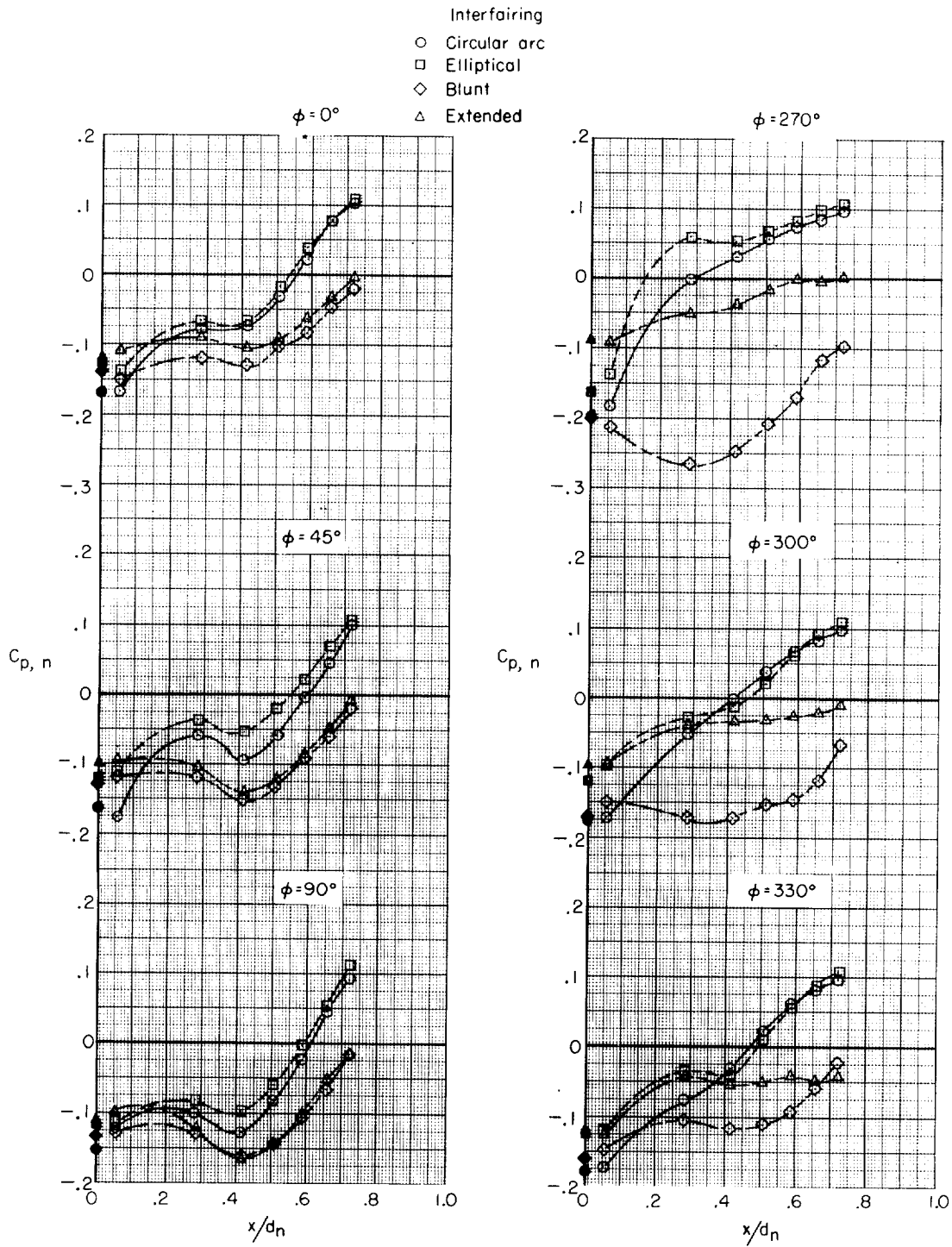
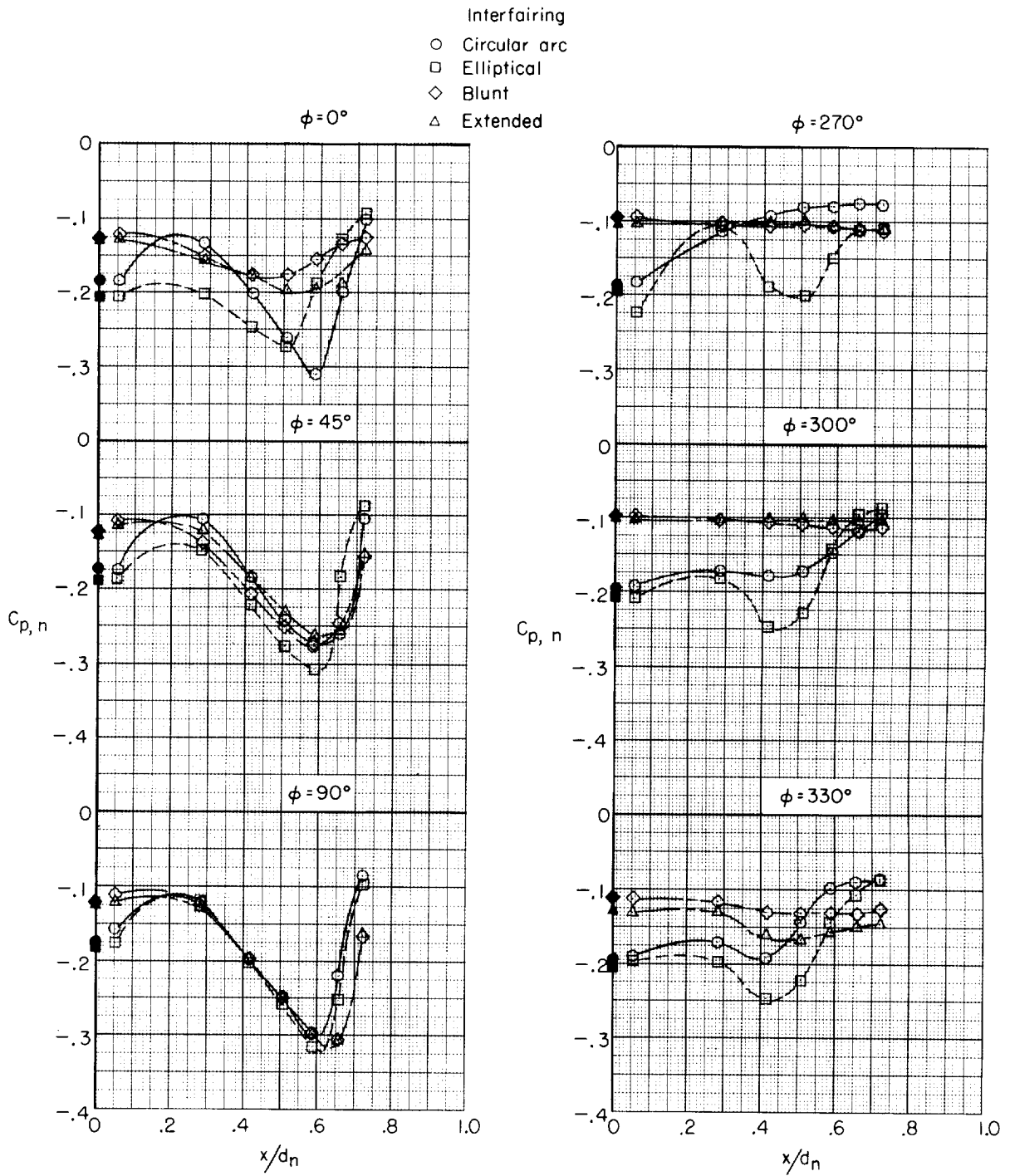


Figure 33.- Continued.



(c) Augmented iris nozzles; $M = 0.95$.

Figure 33.- Continued.



(d) Augmented iris nozzles; $M = 1.30$.

Figure 33.- Continued.

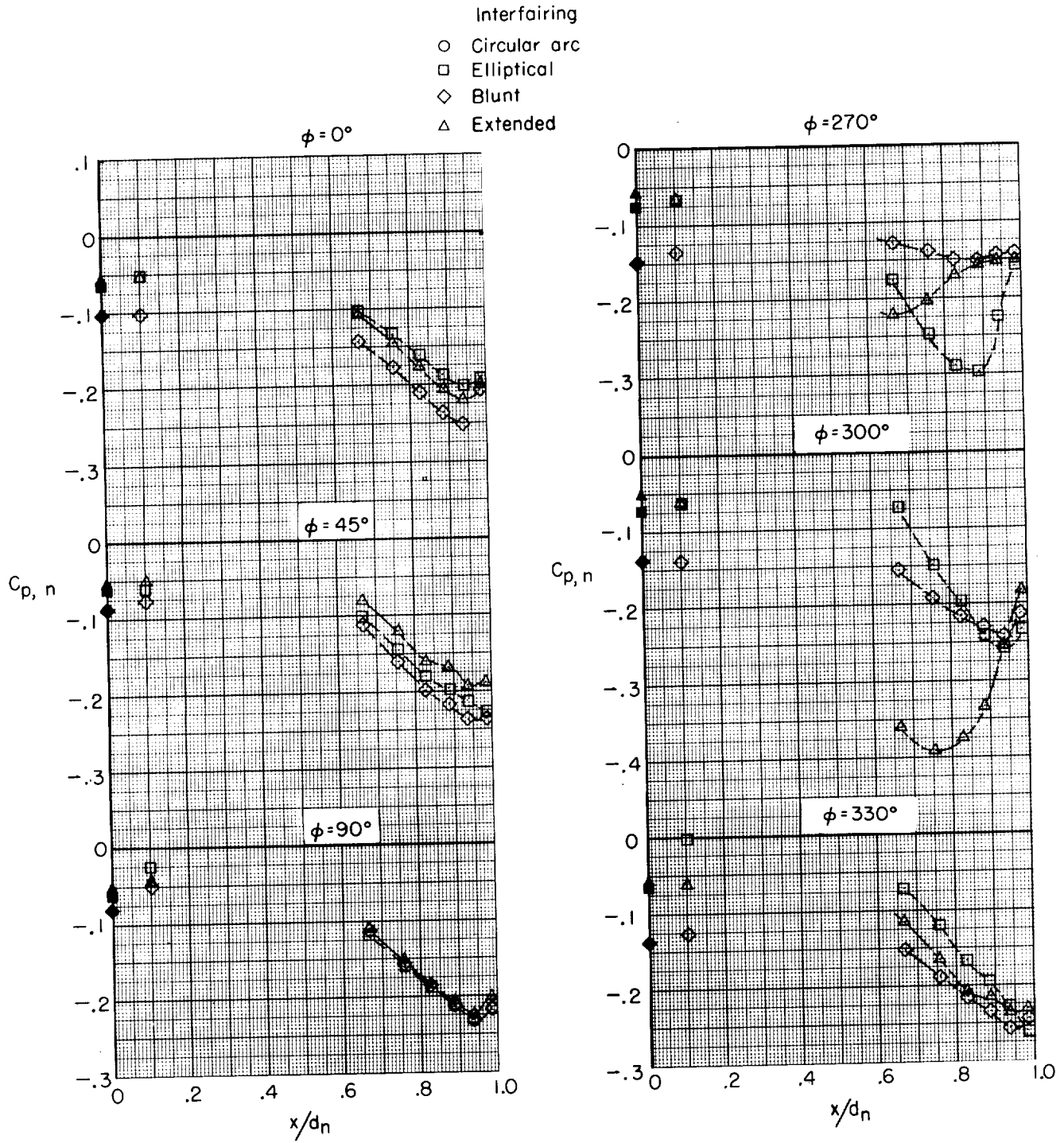
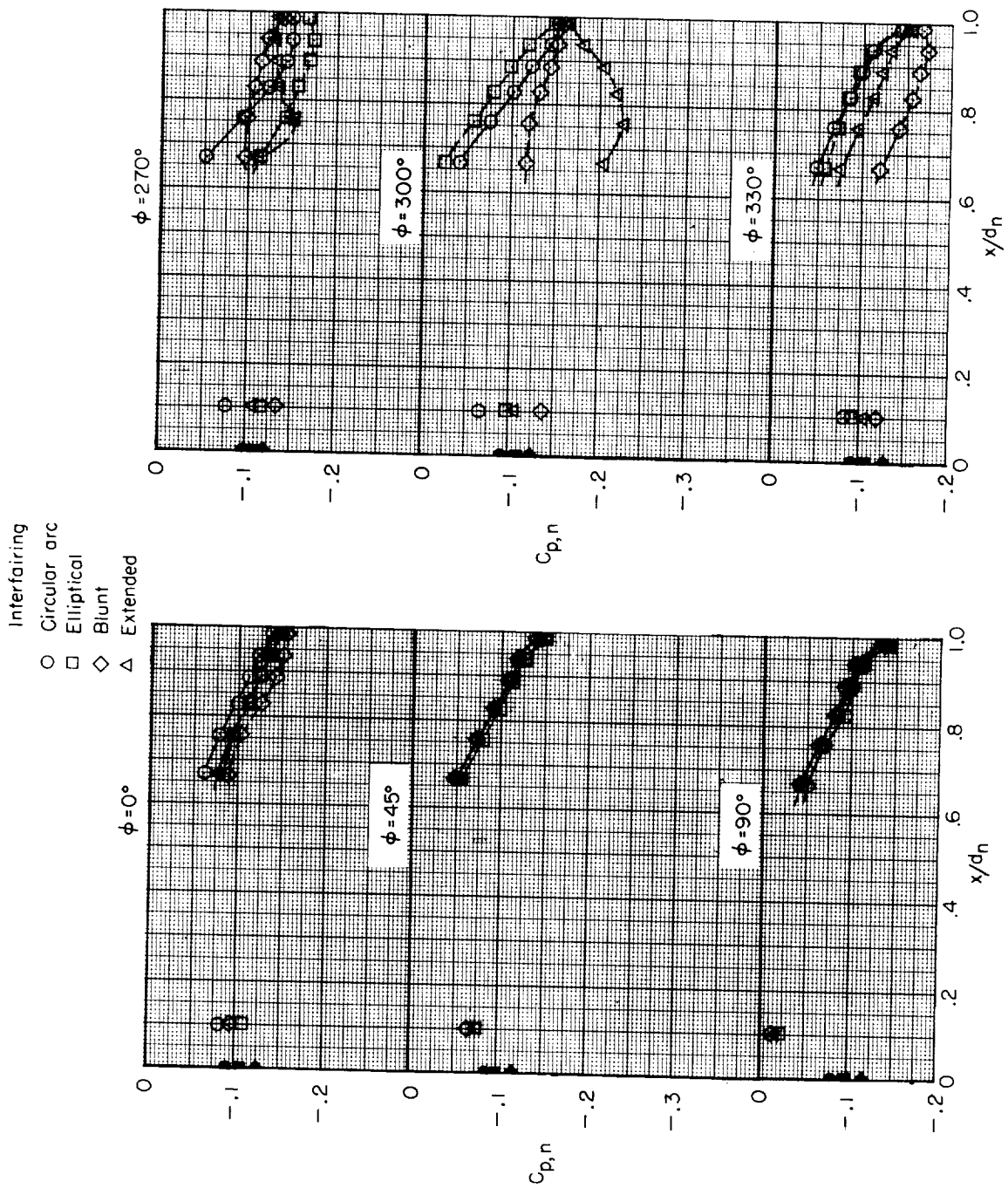
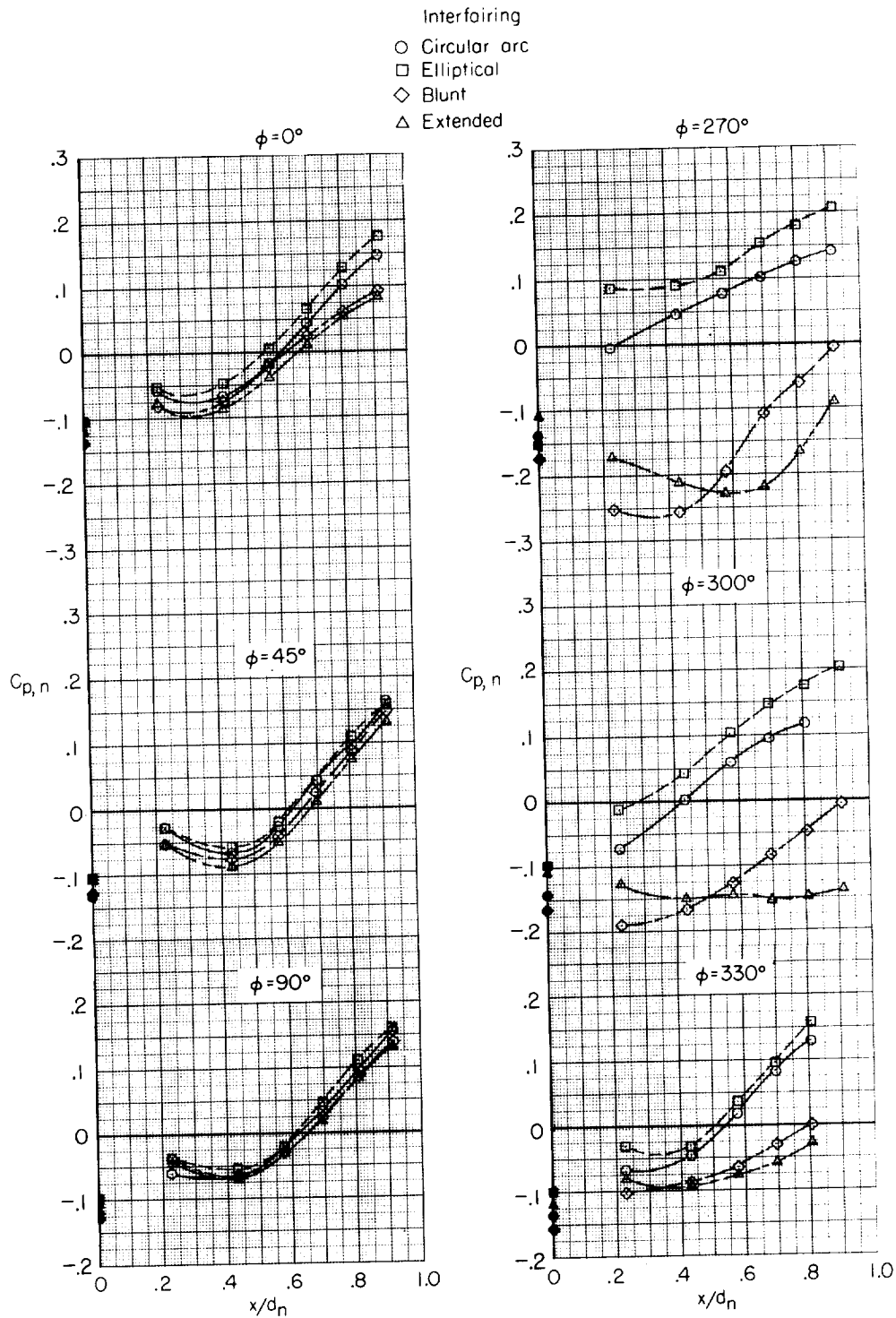


Figure 33.- Continued.



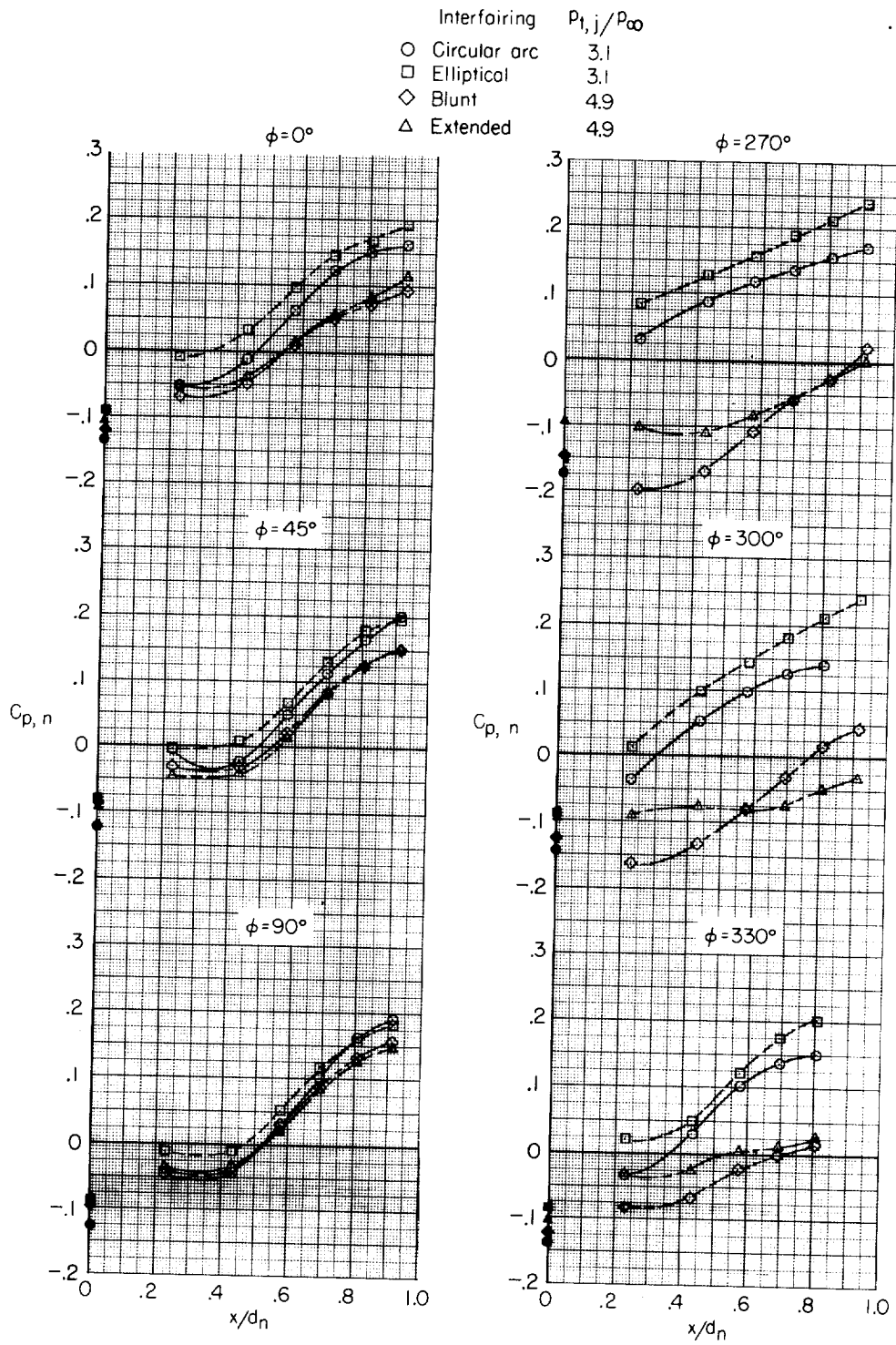
(f) Shrouded-augmented iris nozzles; $M = 2.01$.

Figure 33.- Concluded.



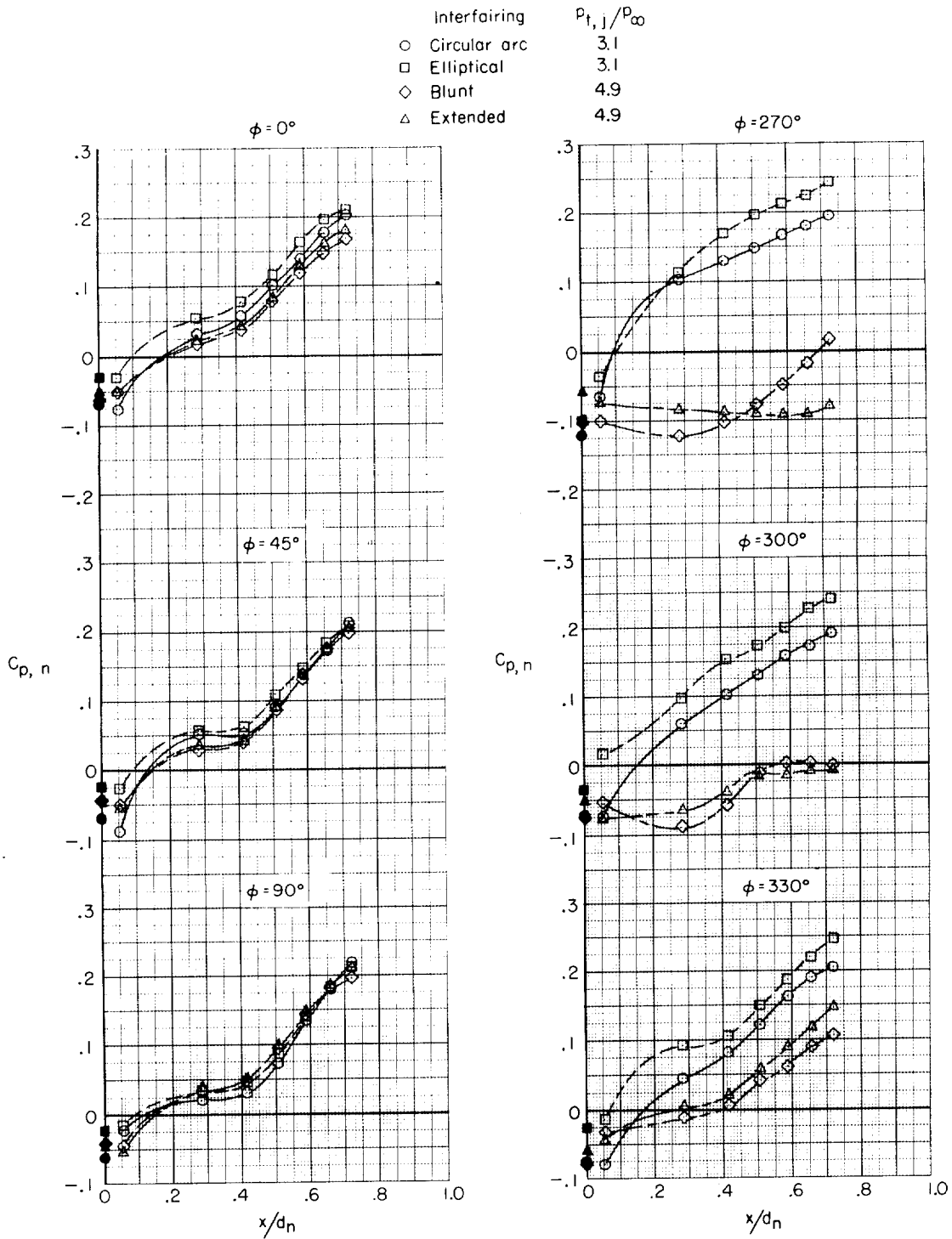
(a) Dry iris nozzles; $M = 0.60$; $p_{t,j}/p_{\infty} \approx 2.5$.

Figure 34.- Effect of interfering shape on nozzle pressure distributions with jets on.



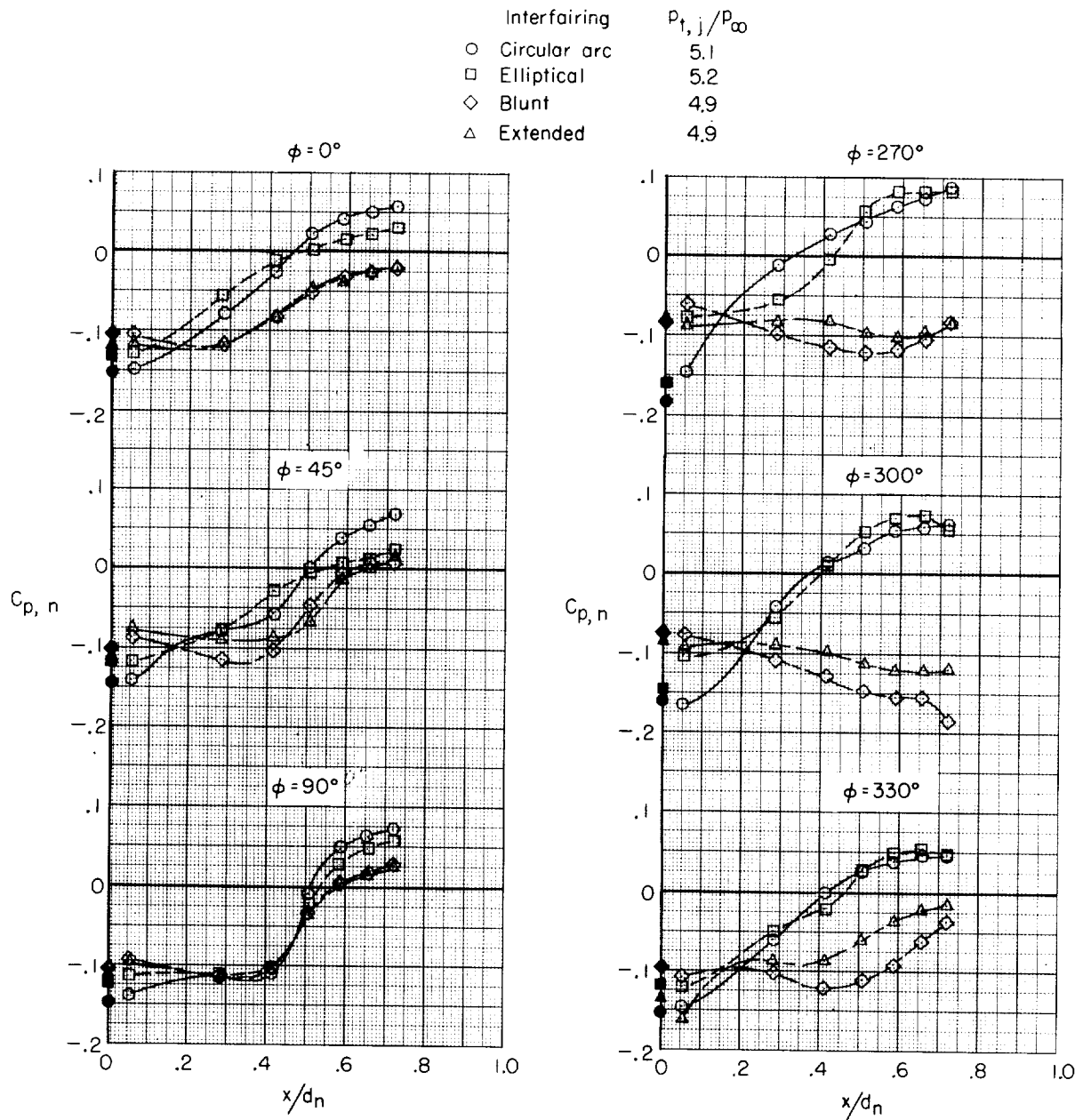
(b) Dry iris nozzles; $M = 0.95$.

Figure 34.- Continued.



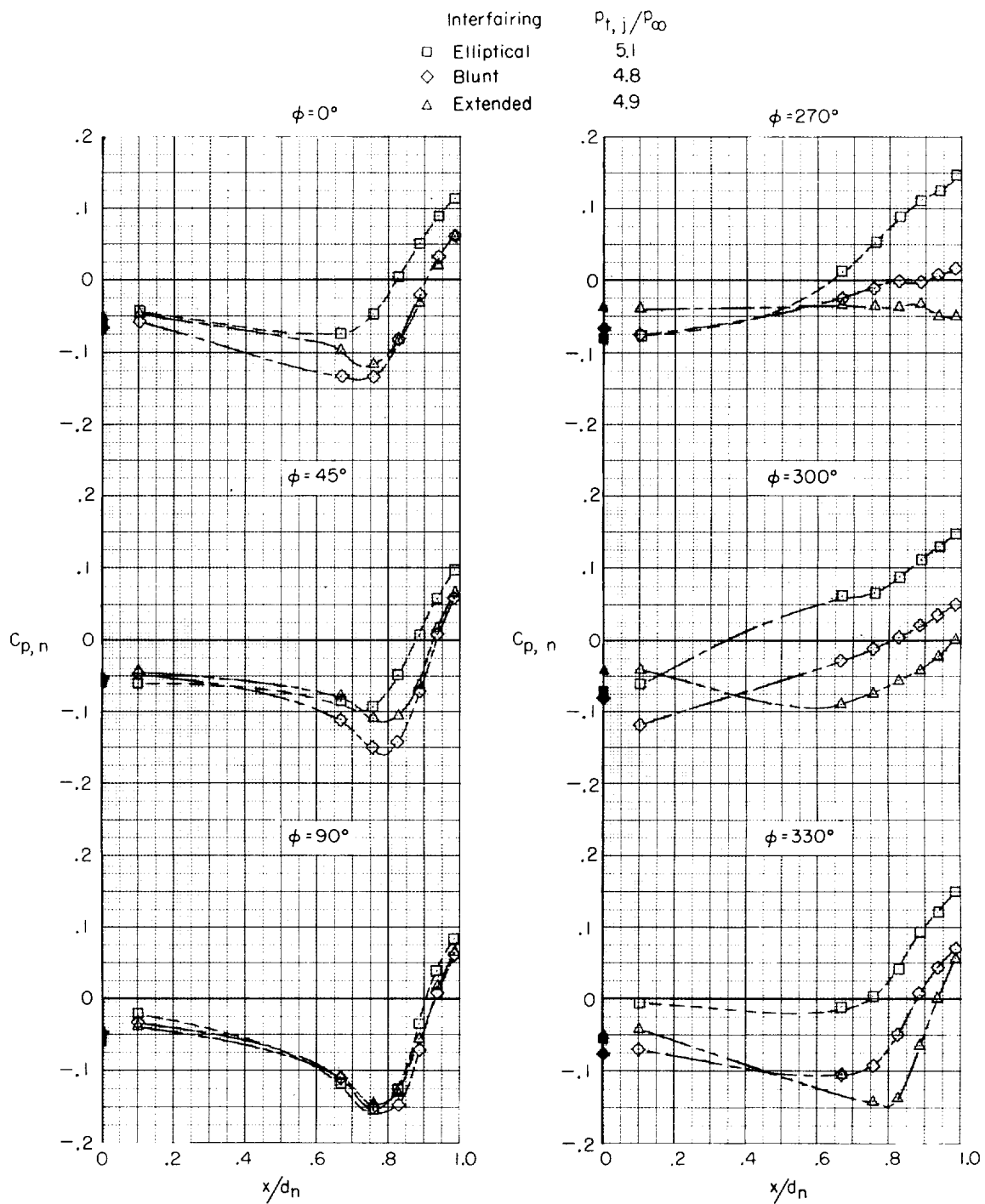
(c) Augmented iris nozzles; $M = 0.95$.

Figure 34.- Continued.



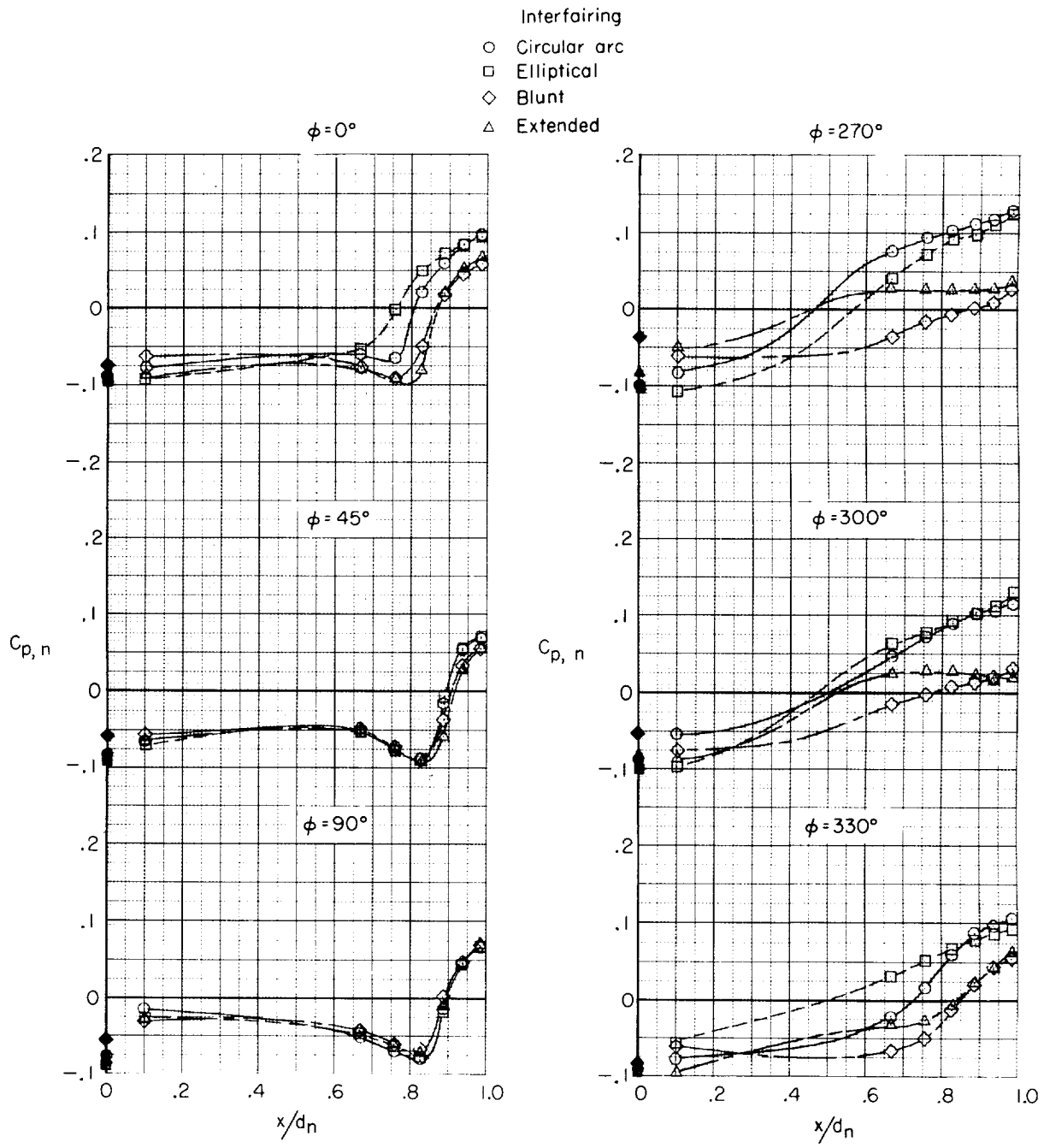
(d) Augmented iris nozzles; $M = 1.30$.

Figure 34.- Continued.



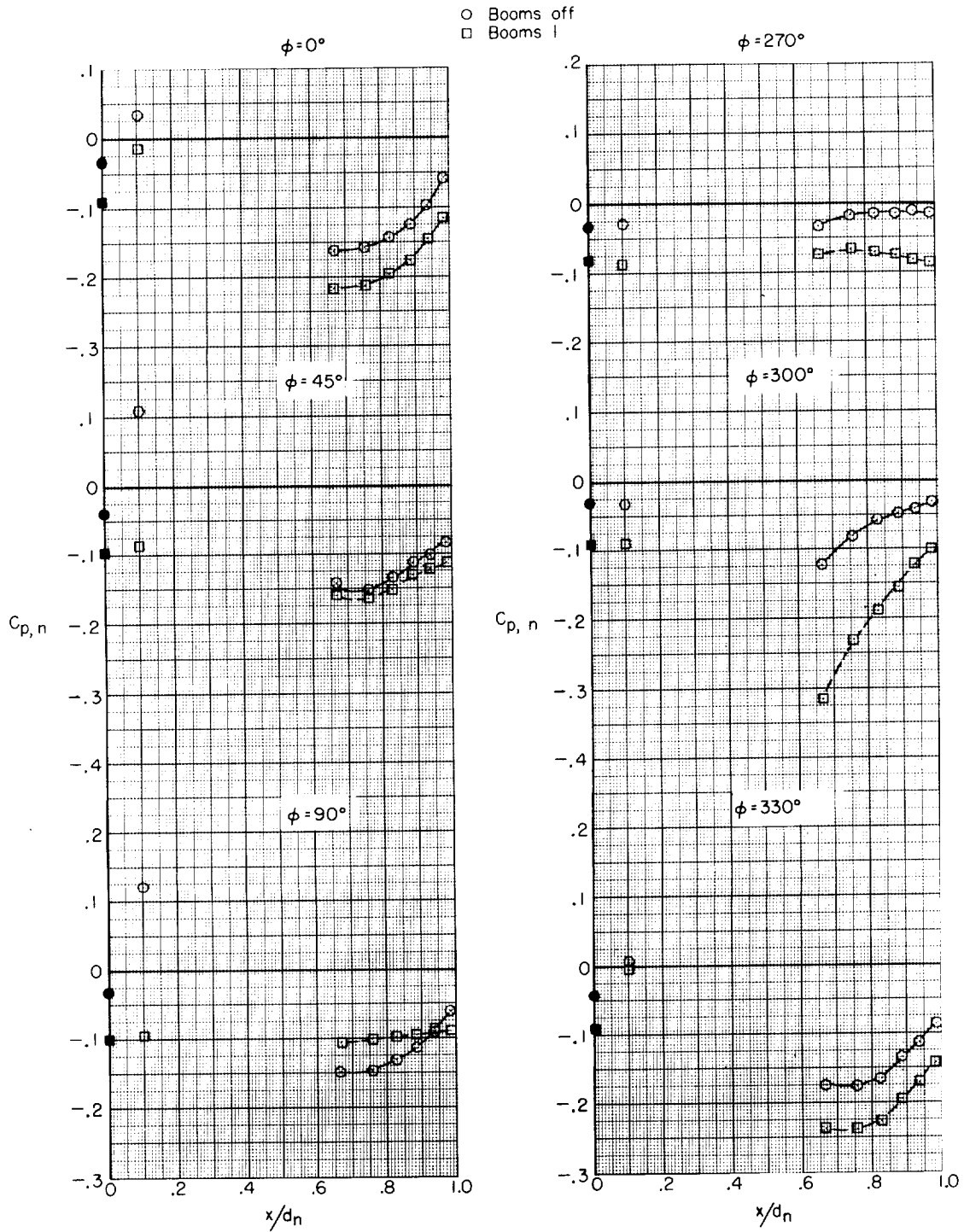
(e) Shrouded-augmented iris nozzles; $M = 1.30$.

Figure 34.- Continued.



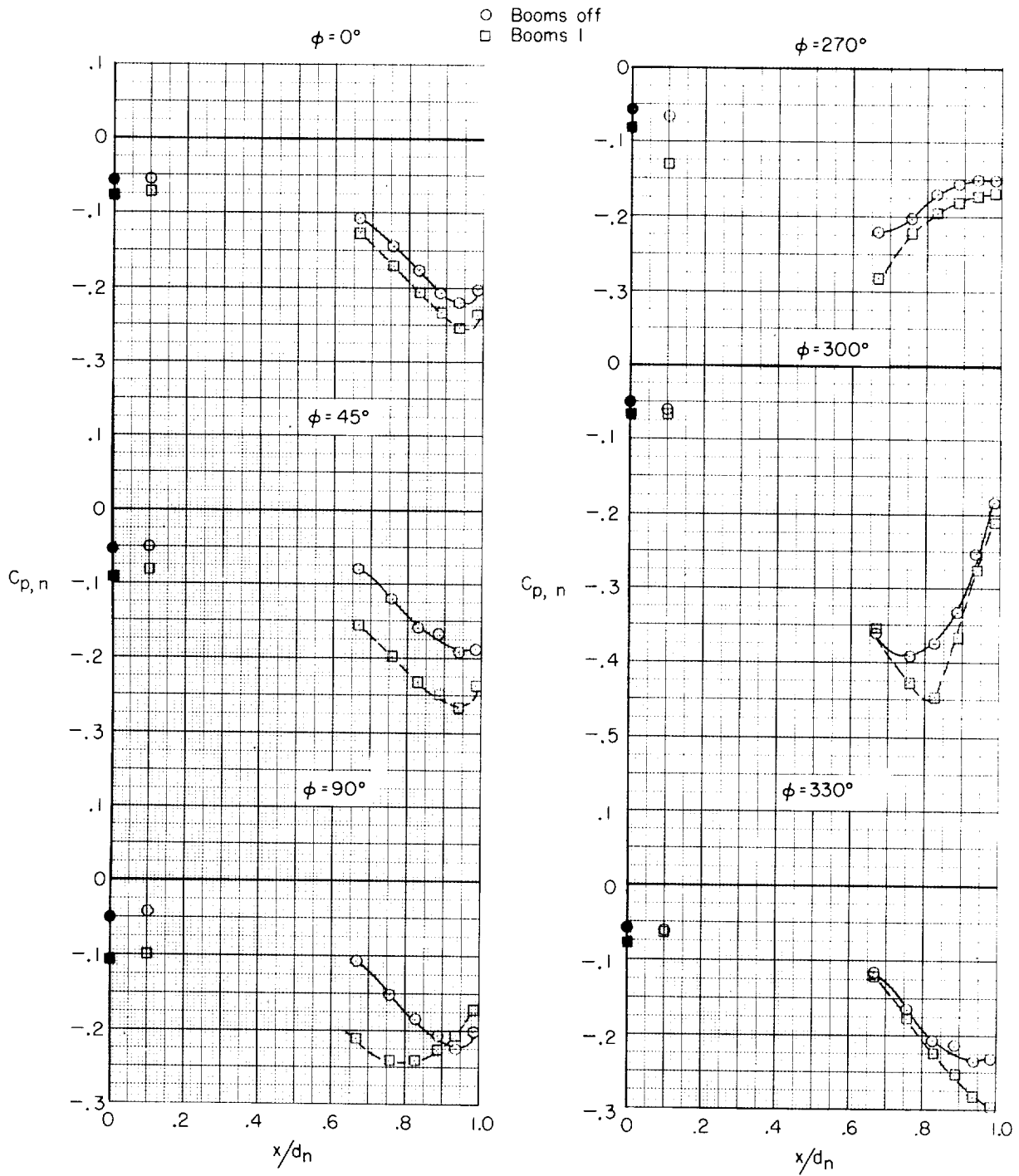
(f) Shrouded-augmented iris nozzles; $M = 2.01$; $p_{t,j}/p_{\infty} \approx 10.0$.

Figure 34.- Concluded.



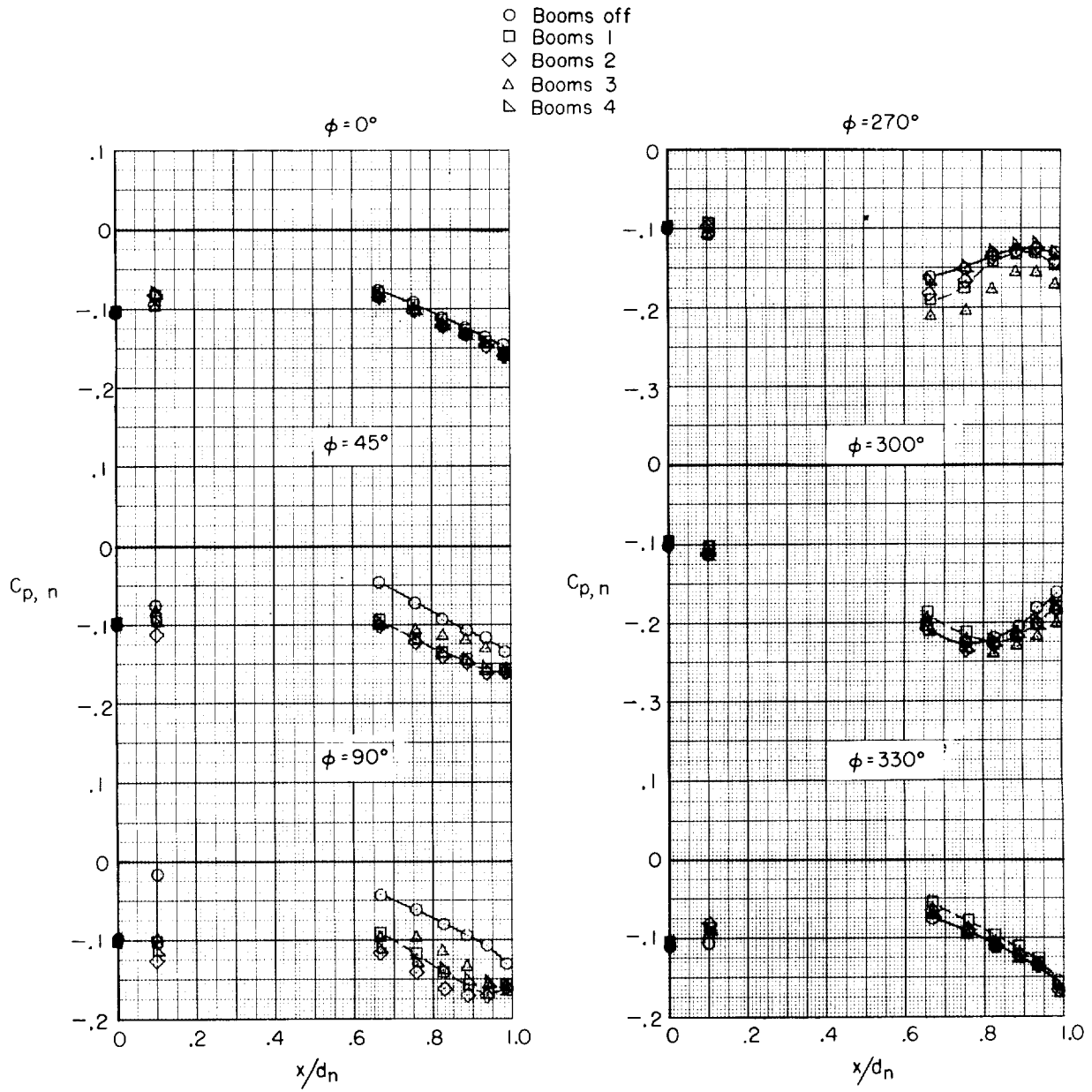
(a) $M = 0.80$.

Figure 35.- Effect of booms on pressure distribution over shrouded iris nozzles. Extended interfairing; jets off.



(b) $M = 1.30$.

Figure 35.- Continued.



(c) $M = 2.01$.

Figure 35.- Concluded.

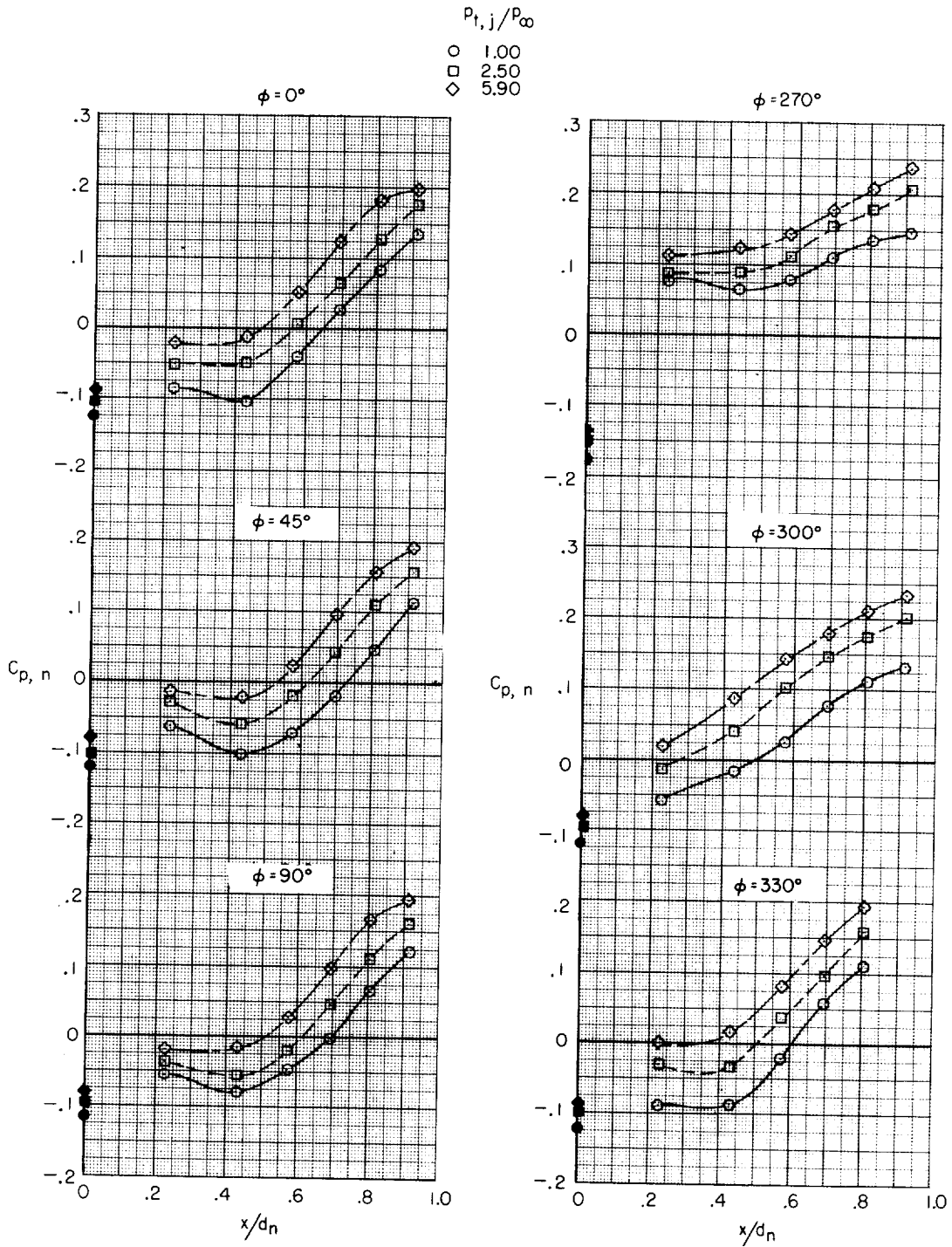
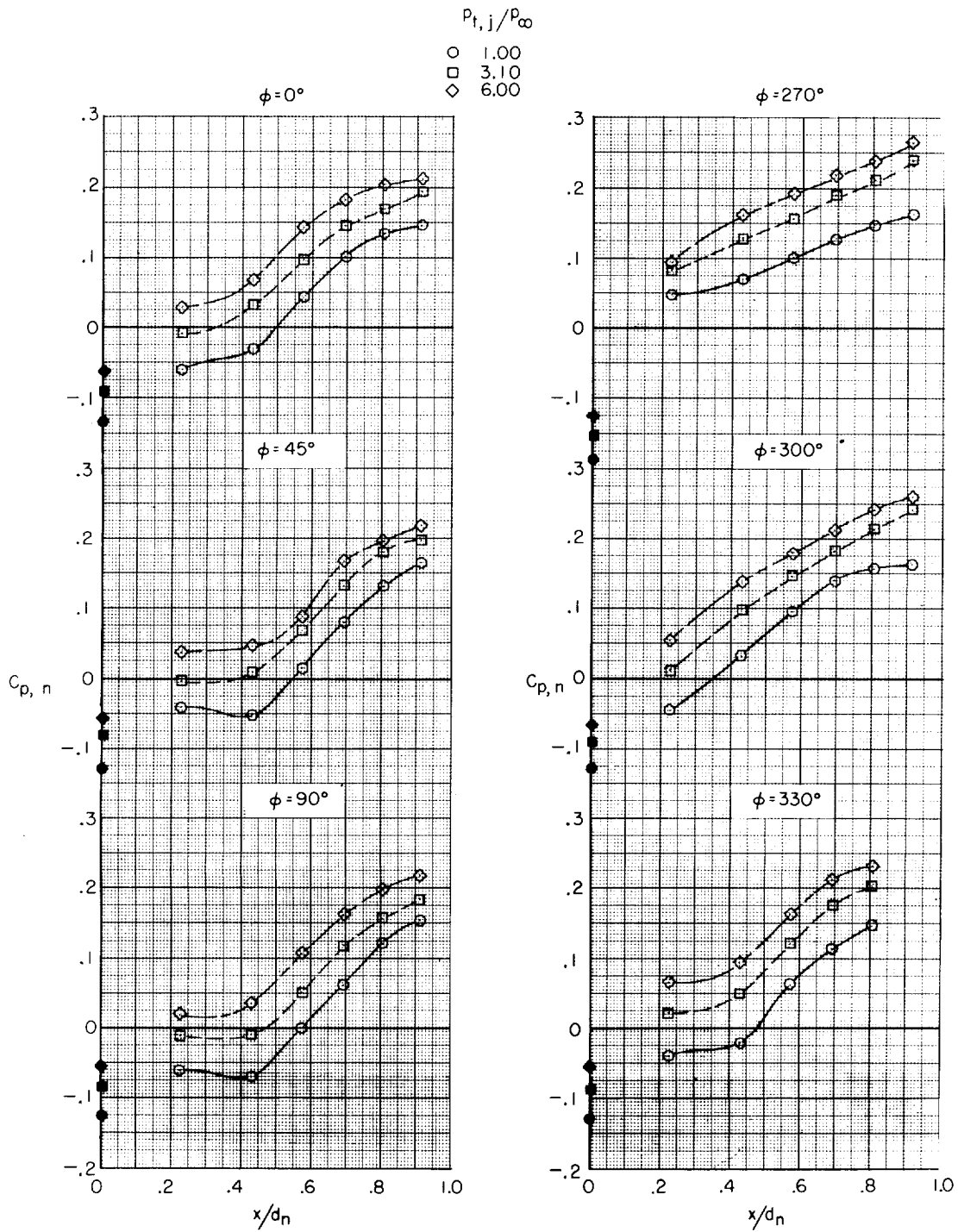
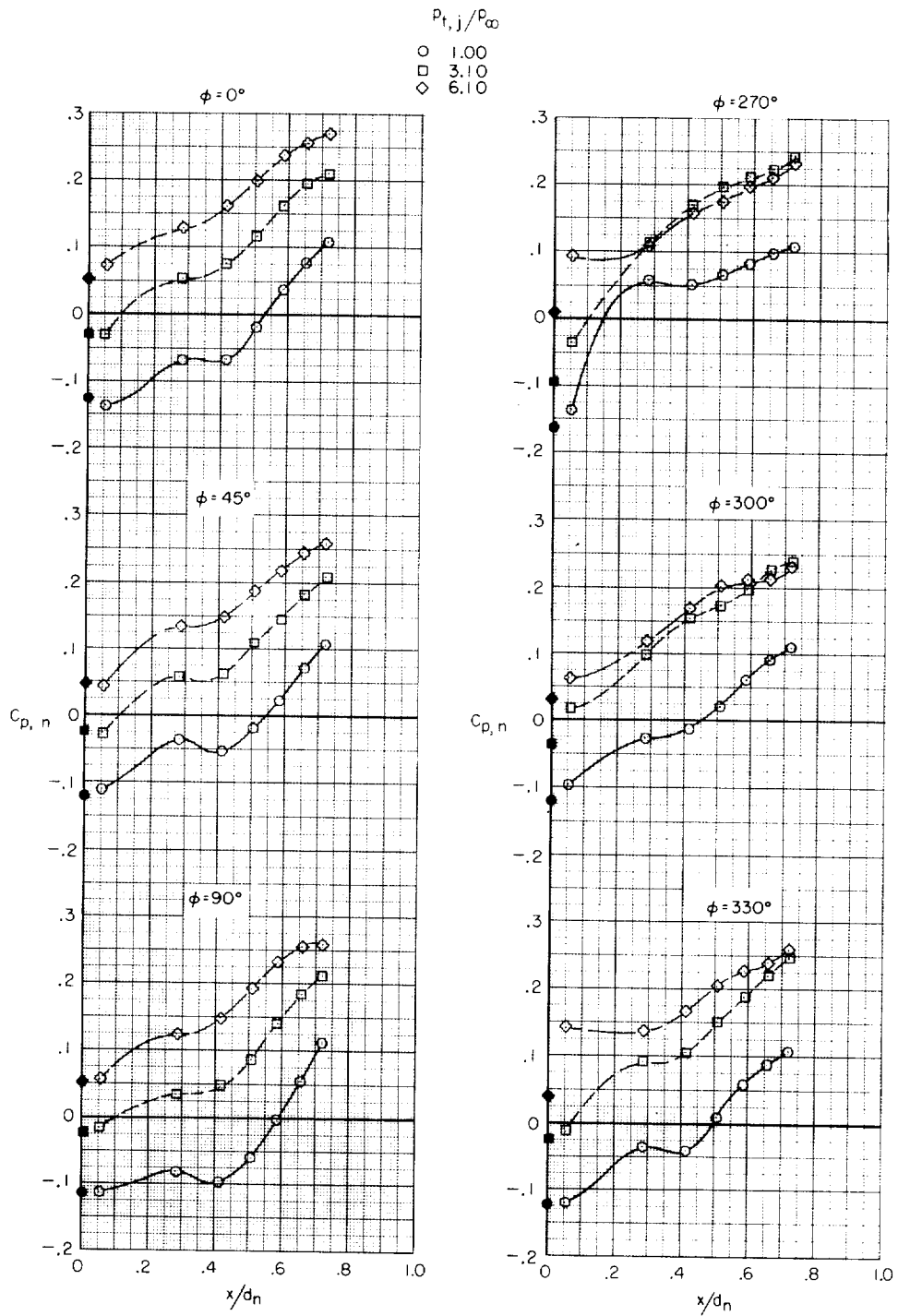


Figure 36.- Effect of jet operation on nozzle pressure distribution for afterbody with elliptical interfairing.



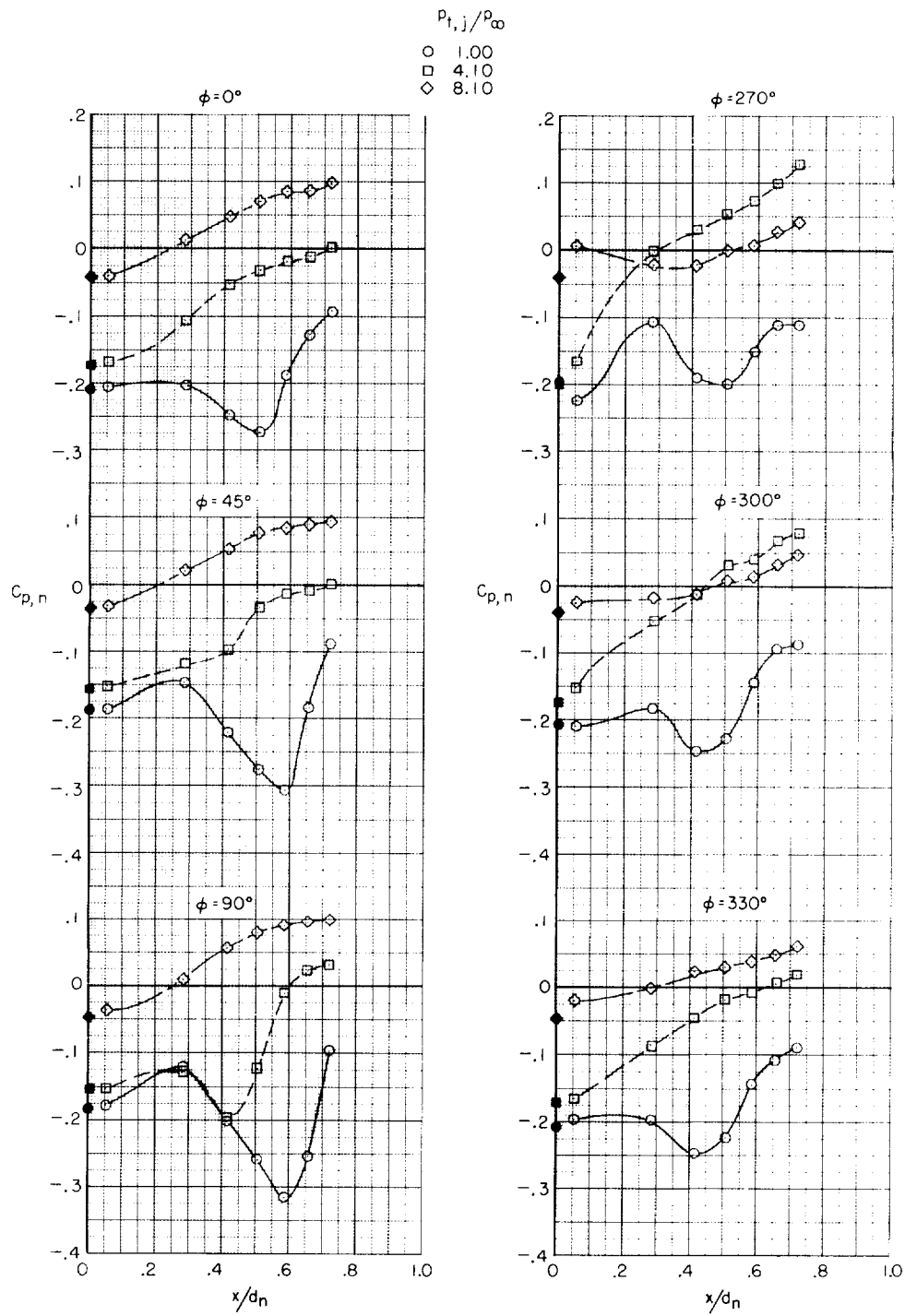
(b) Dry iris nozzles; $M = 0.95$.

Figure 36.- Continued.



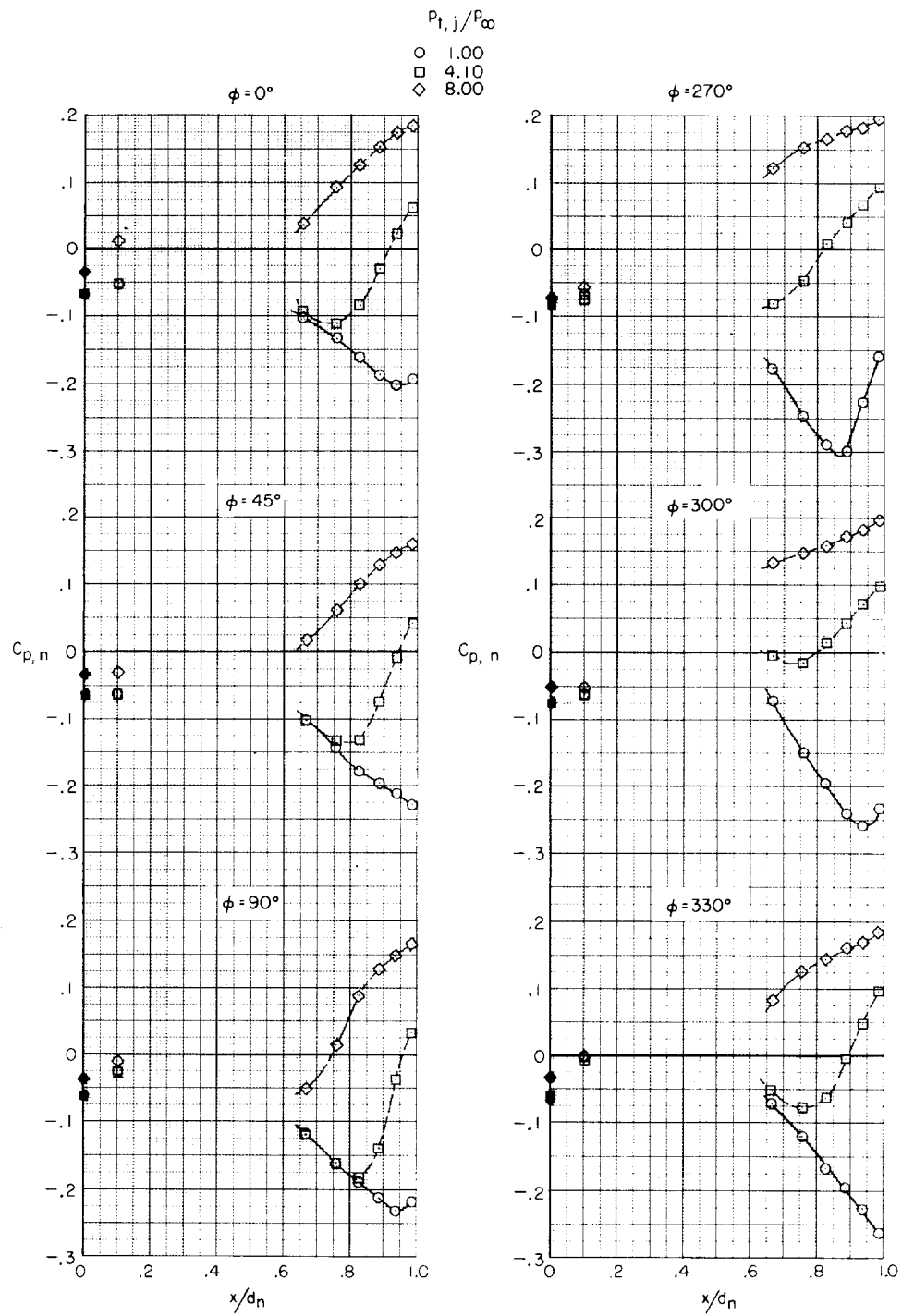
(c) Augmented iris nozzles; $M = 0.95$.

Figure 36.- Continued.



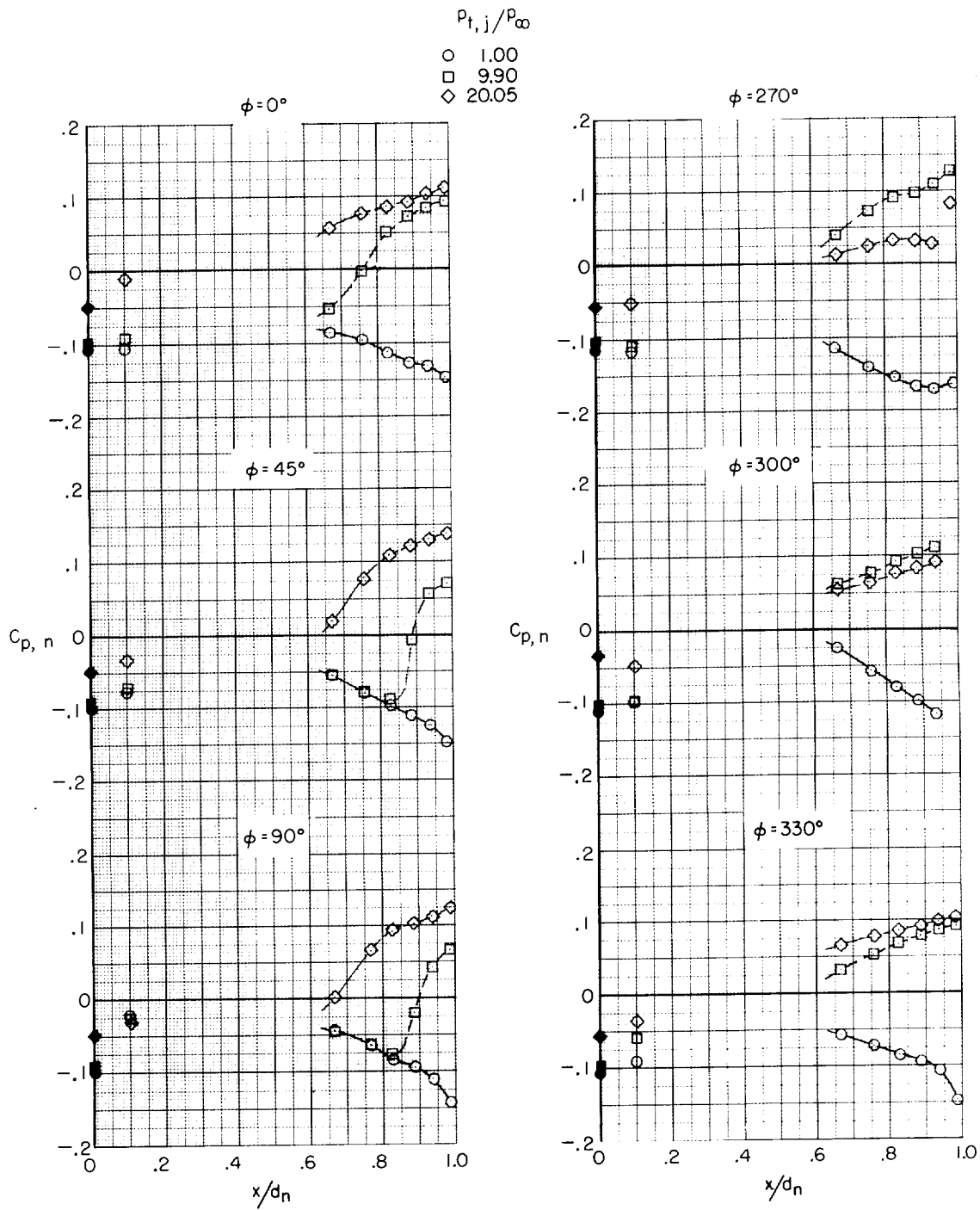
(d) Augmented iris nozzles; $M = 1.30$.

Figure 36.- Continued.



(e) Shrouded-augmented iris nozzles; $M = 1.30$.

Figure 36.- Continued.



(f) Shrouded-augmented iris nozzles; $M = 2.01$.

Figure 36.- Concluded.

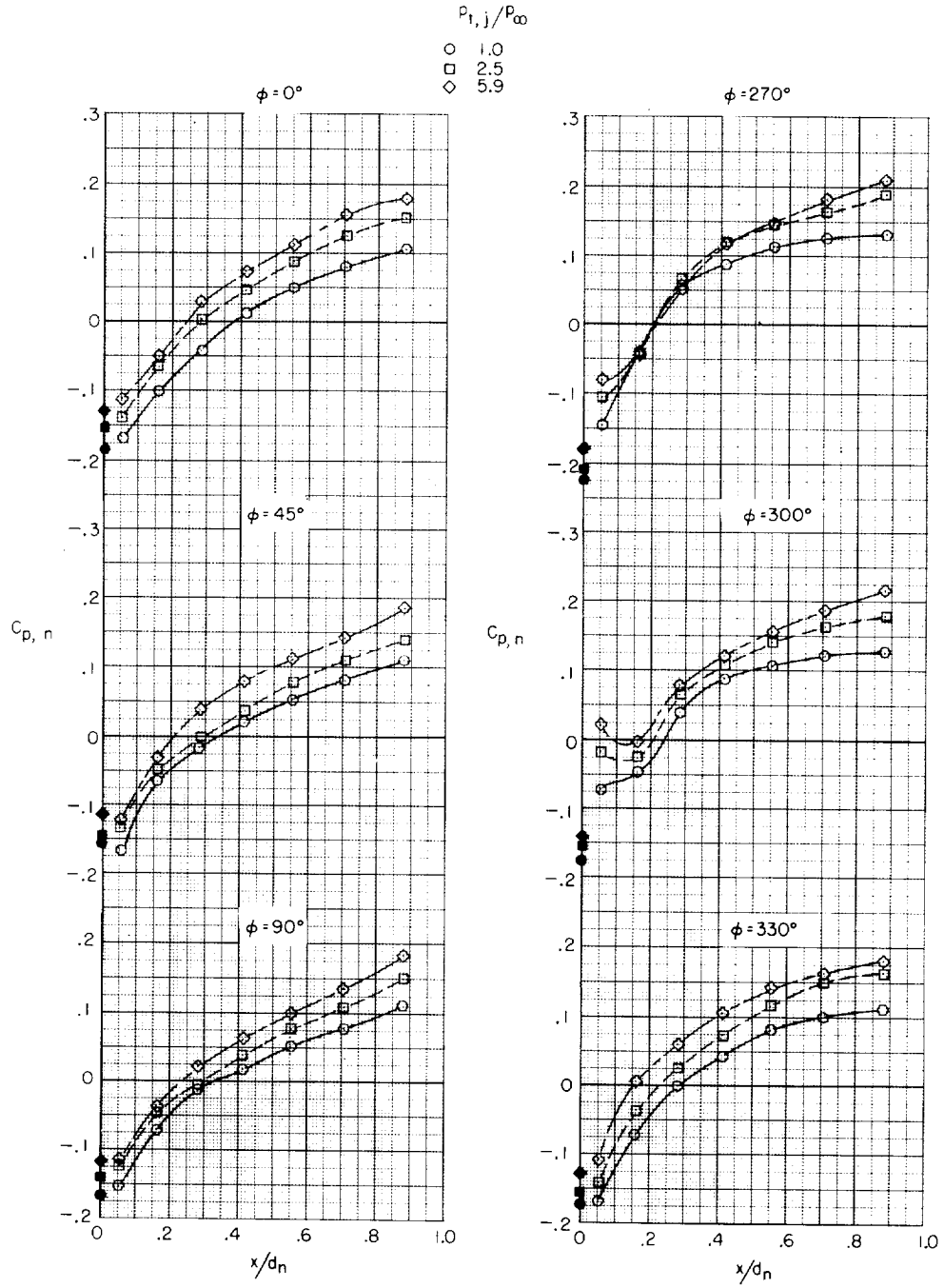
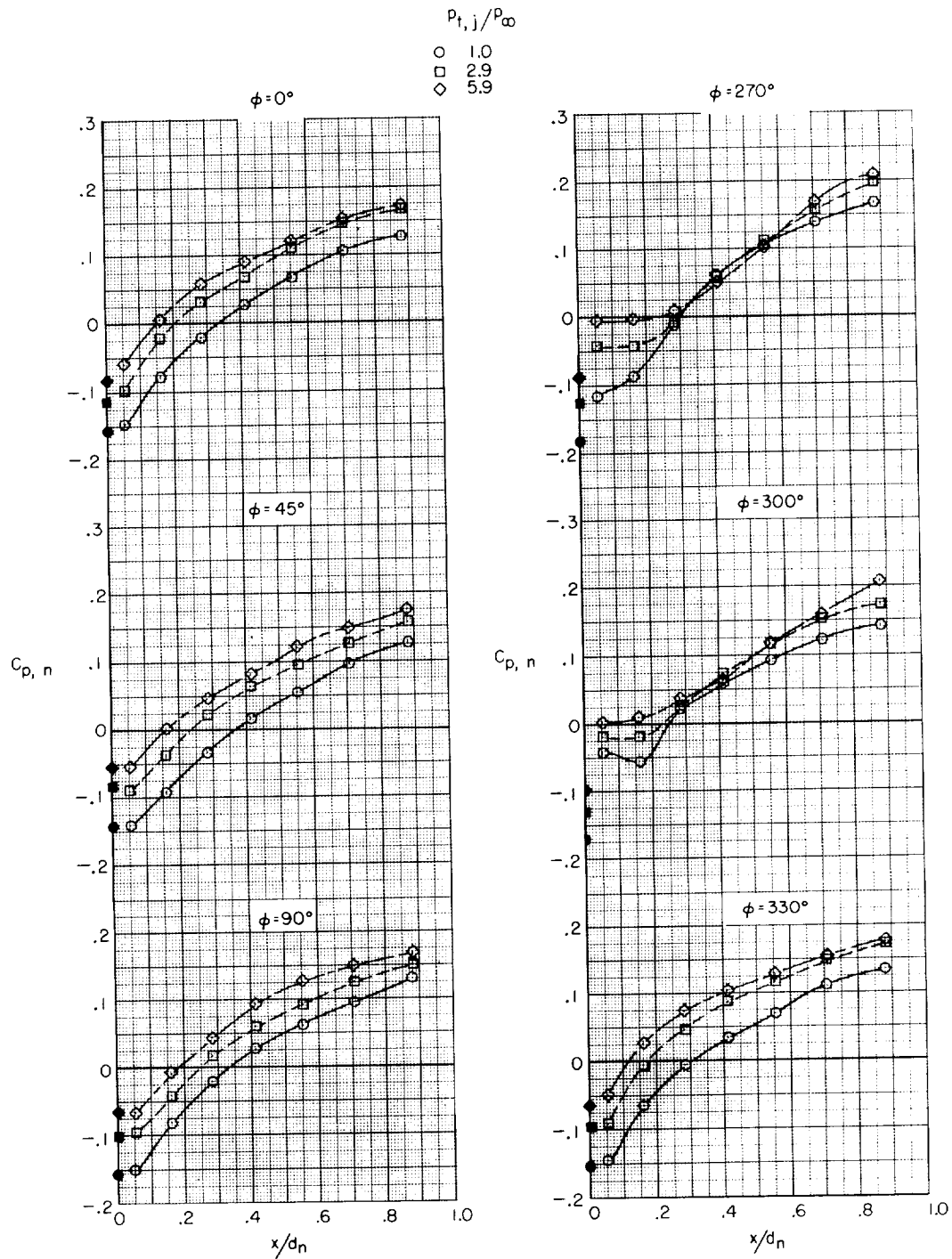
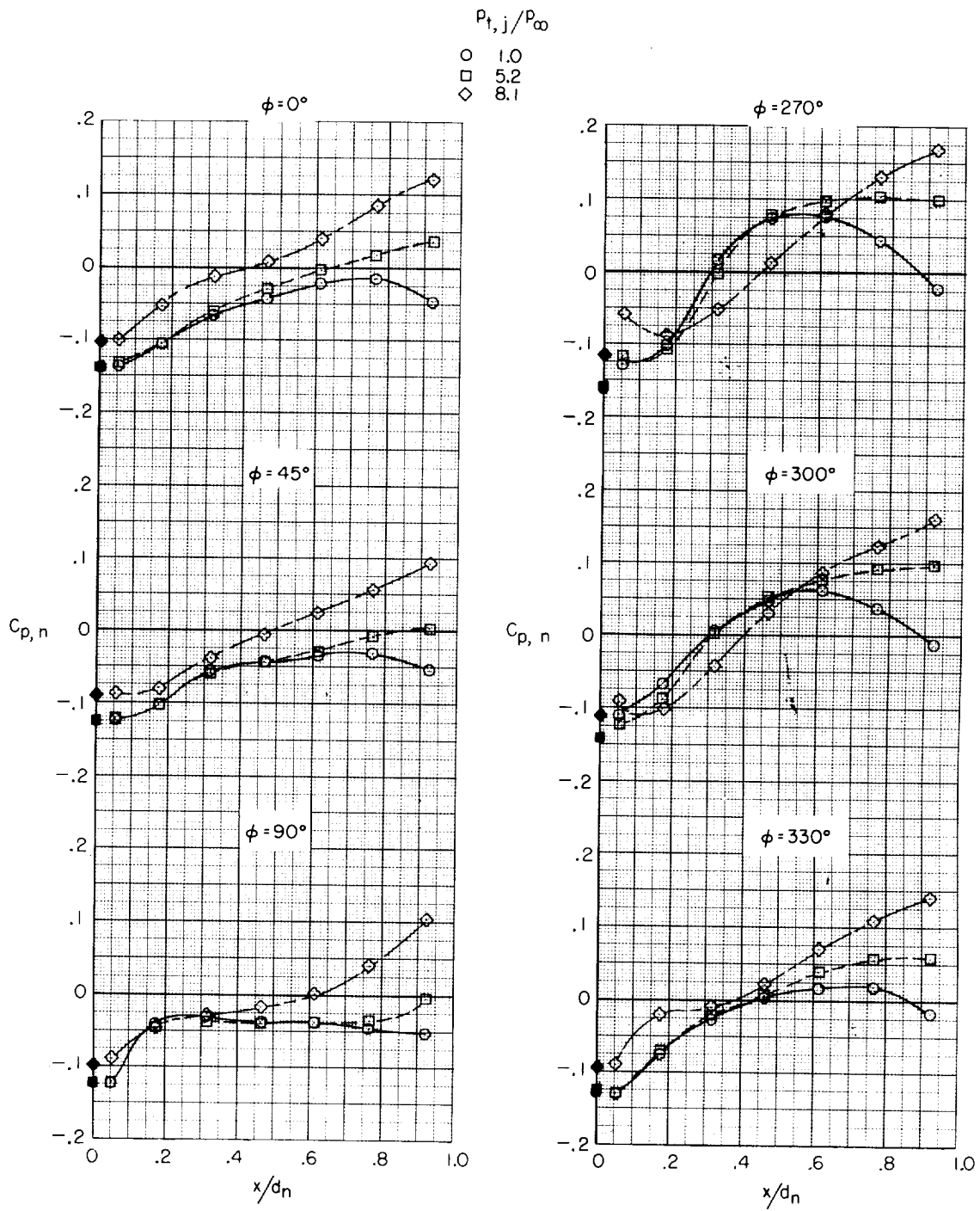


Figure 37.- Effect of jet operation on nozzle pressure distribution for afterbody with elliptical interfairing.



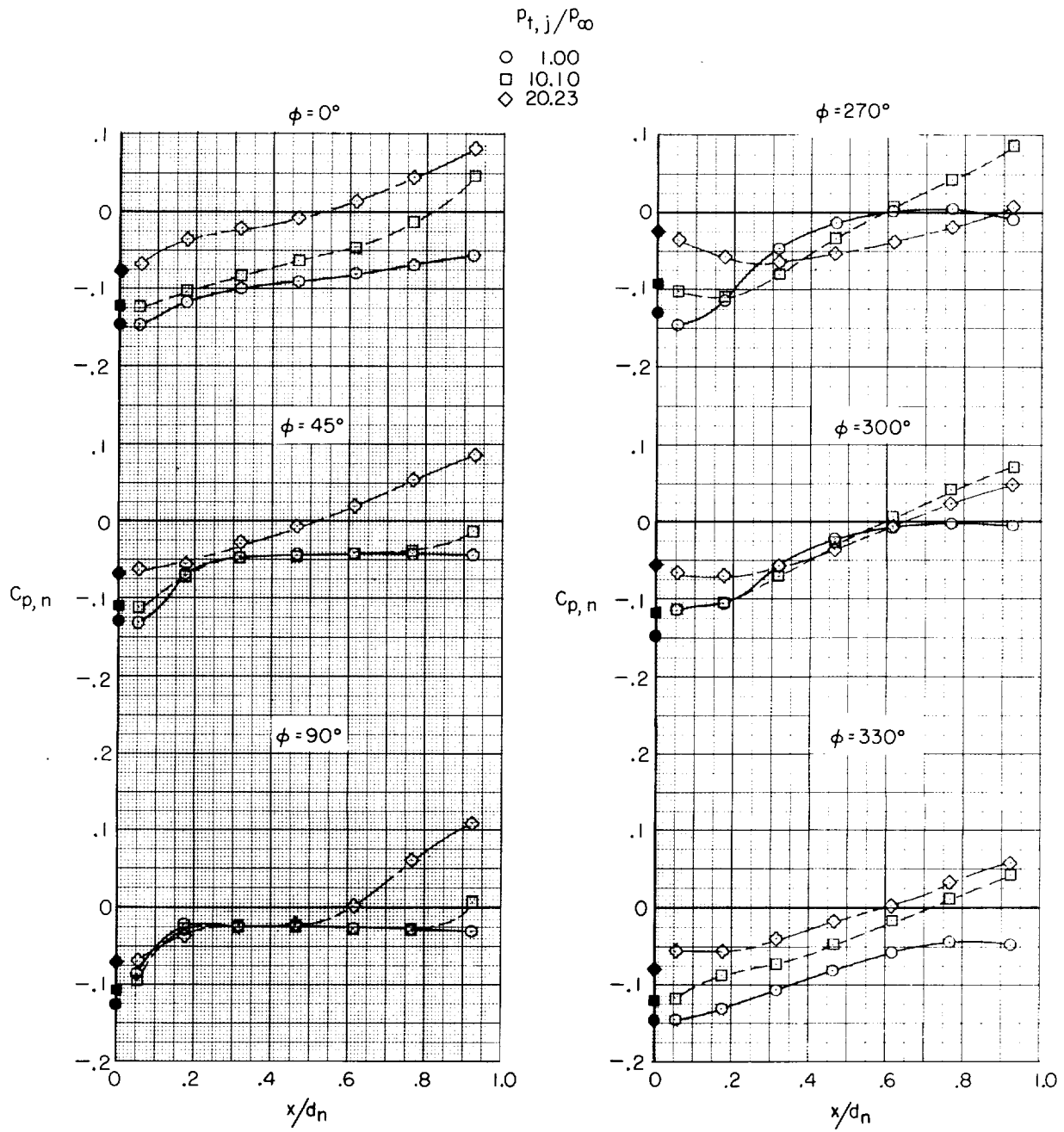
(b) Dry convergent-divergent nozzles; $M = 0.95$.

Figure 37.- Continued.



(c) Augmented convergent-divergent nozzles; $M = 1.30$.

Figure 37.- Continued.



(d) Augmented convergent-divergent nozzles; $M = 2.01$.

Figure 37.- Concluded.

